Spontaneous spin squeezing in a spinor Bose-Einstein condensate trapped on an atom chip

Théo Laudat

THÈSE DE DOCTORAT

de l'Université de recherche Paris Sciences et Lettres
PSL Research University

Préparée à l'Observatoire de Paris

Spontaneous spin squeezing in a spinor Bose-Einstein condensate trapped on an atom chip

Étude du phénomène de compression de spin dans un condensat de Bose-Enstein piégé sur microcircuit

École doctorale n°564

ECOLE DOCTORALE PHYSIQUE EN ILE DE FRANCE

Spécialité PHYSIQUE QUANTIQUE

COMPOSITION DU JURY :

Mme Jocelyne Guéna
Syrte-OBSPM, Présidente

Mme Isabelle Bouchoule
LCF-IOGS, Rapporteur

M Christian Gross
MPQ, Rapporteur

Mme Alice Sinatra
LKB-ENS, Membre du jury

M Jean-Philippe Brantut
EPFL, Membre du jury

M Noel Dimarcq
Syrte-OBSPM, directeur de thèse

M Carlos Garrido Alzar
Syrte-OBSPM, Membre invité

M Jakob Reichel
LKB-ENS, Membre invité

Soutenue par **Théo Laudat**
le 04 octobre 2017

Dirigée par **Noel Dimarcq**

l'Observatoire de Paris — SYRTE
Systèmes de Référence Temps-Espace

PSL RESEARCH UNIVERSITY PARIS

Contents

*****

Introduction

*****

FUNDAMENTAL research conducted in the laboratory can sometimes be challenging and frustrating, but one should not forget that it can also lead to great results with outstanding repercussions on our everyday life. The two most striking examples being the invention of transistors and lasers. The later in particular, developed in 1960 [1], enabled the possibility of cooling and trapping neutral atoms [2–4] and opened the door to a significant part of modern experimental atomic physics. Beside the obvious interest in understanding the structure of matter at the atomic level, where the physical laws are dominated by quantum mechanics, cold atoms techniques have also quickly become mature enough for applications and instrumental developments.

Atomic sensors and quantum metrology

Indeed, compared to more conventional technologies, cold atoms offer an alternative and often better performances concerning precision measurements and sensing [5,6]. Atomic sensors can be regrouped into four categories:

- *Atomic clocks:* Their goal is to probe the transition frequency between two atomic levels using an electromagnetic field. The time is then determined by counting the number of oscillation periods $\frac{\nu_{at}}{[1Hz]}$ contained in one second, ν_{at} being the considered atomic frequency. The oscillating field locked to the atomic transition thus acts as a time ruler, whose graduations are represented by one oscillation period. As a result, the higher the frequency the better the precision. A clock is characterized by its accuracy and stability that define the precision with which we know the spacing between the graduations and by how much these intervals fluctuates with respect to each other. While best quartz show a short term stability on the order of 10^{-13} at one second and a flicker floor in the low 10^{-14} after only a few seconds

[7], best atomic clocks now work in the 10^{-17} range at one second [8] and keep integrating in the low 10^{-18}. Their fractional uncertainty also lies in the 10^{-18} level [9]. These extremely precise devices begin to be interesting for fundamental research, as they start to be able to test the stability of fundamental constants [10], general relativity [11] and provide information regarding the exploration of dark matter [12].

- *Field sensors:* As atomic energy levels are sensitive to magnetic and/or electric fields, atoms can also be used as a field sensor. Similarly to working principle of atomic clocks, by monitoring the frequency changes of a given transition, it is possible to precisely measure the amplitude of the surrounding fields, after prior calibration [13–16].

- *Acceleration sensors:* Being massive objects, atoms are sensitive to forces and in particular to the inhomogeneous Earth gravitational field [17]. This gravitational acceleration, and more generally any kind of accelerations, can be probed locally with a Mach-Zehnder or Ramsey-Bordé interferometer [18, 19]. It consist in measuring the phase difference between two spatially separated and recombined atomic clouds, in the direction of acceleration. Indeed, during the separation the two clouds experience different accelerations and therefore accumulate different phases, resulting in an interference pattern. Such a gravimeter has been realized for the first time in 1991 [20] and many times since then [21–26], and now present better performances than conventional ballistic devices. Only the superconducting gravimeter surpasses the best atomic ones [27] in term of short term sensitivity.

- *Rotational sensors:* The same principle can be applied to measure rotational velocities. The spatial separation has then to take place in the plane orthogonal to the rotation vector, and this time the phase shift between the two atomic clouds is due to the so-called Sagnac effect [28]. The first atomic gyroscope, realized in 1991 [29], opened the way to atomic rotational sensing [30–34]. In contrast to conventional gyroscopes [35, 36], the atomic ones present better long term stabilities and constitute absolute references, meaning that they do not need specific calibration.

So far we only considered cold but non-degenerate atomic ensembles. Thanks to their very high phase-space density and macroscopic coherence properties [37], Bose-Einstein condensates (BEC) are very interesting candidates for atom interferometry [19, 38, 39]. Since their first observation in 1995 [40, 41], they have known an immediate success and have led to a large variety of fascinating experiments [42]. The more recent development of atom chip technologies [43, 44] has also greatly simplified the production and manipulation of BEC's, leading to a tremendous growth of on-chip interferometers in the last decade [45–49]. One of the ultimate goals would be to combine an atomic clock

with a set of gyroscopes and accelerometers on a chip in order to form an autonomous inertial navigation system applied for submarines and spacecrafts [6].

In all these atom interferometers the quantity of interest is the relative phase between two atomic ensembles, and it can only be probed through readout of the atomic state, which is subject to a fundamental noise: the quantum projection noise (QPN). The measurement of a coherent superposition of atomic states is performed by projecting it onto one of its eigenstates. Similarly to a coin-tossing game, the outcome of this measurement is subject to a statistical uncertainty, that is reduced by repeating the process many times, either successively or in parallel. The measurement uncertainty, called standard quantum limit (SQL) [50], then scales as $1/\sqrt{N}$, where N is the number of repetitions. This process actually limits nowadays best atomic sensors [33, 51]. While this rule cannot be overcome in the "classical" world, quantum mechanics provides some tools to further reduce this limit and opens the path to quantum metrology [52, 53]. As a matter of fact, quantum correlations and entanglement [54, 55] can in principle push away this limit down to the Heisenberg limit [56], for which the measurement uncertainty scales as $1/N$. This field of study has also known a tremendous success with several implementation of atomic systems working below the standard quantum limit with direct possible applications in atom interferometry and sensing [14, 57–63]. Here again, BEC's appear like perfect candidates for quantum metrology, since they inherently present non-linear interactions leading to spin squeezing [60, 61, 64–66]. This scientific breakthrough is at the very core of the second quantum revolution [67] recently supported by the European Union with a one billion euros flagship [68].

In the framework of developing increasingly more accurate and stable sensing devices for industrial or fundamental applications, the combination of atom chip technologies, Bose-Einstein condensates and entanglement protocols is not only appealing but also genuinely realistic, and could really revolutionize the world of sensing and precision measurement in the years to come. All of these metrological devices have several fundamental applications but they can also be combined in order to form an autonomous inertial navigation system. This assembly is made possible by the recent development of atom chip technologies. In that sense, the work presented here represents a small step towards the development and realization of applied quantum technologies.

Trapped atom clock on a chip (TACC)

The TACC project was, in 2006 and in collaboration between the LKB and SYRTE, initially designed to be a compact atomic clock, which interrogates Rubidium atoms magnetically trapped in the vicinity of an atom chip. The idea was to get a robust metrological device, working at the state of the art with a stability in the low $10^{-13}/\sqrt{s}$, and eventually contribute to the development of chip-based inertial sensors and space applications. The latest version of the clock exhibits a stability of 5.8×10^{-13} at one second with 20 000 atoms and a 5 s interrogation time [69].

This set-up is however not only a competitive compact clock but also a remarkable

platform for fundamental studies and complex manipulations of atoms and quantum states. For instance, it permitted in 2010 the experimental observation of an intricate and very general quantum mechanical phenomenon, called identical spin rotation effect (ISRE) [70]. Owing to the indistinguishability of particles, binary collisions can exchange the internal states of the two colliding atoms and lead to a an auto-synchronization of the atomic spins [71], resulting in extremely long coherence times (~ 58 s) and contrast revivals [72, 73]. This effect also enables the observation of spin waves and density-dependent frequency shifts [74, 75]. However, since the whole process is based on the symmetrization of the total wave-function, atoms cannot be in the same external state and have two different internal states at the same time. This is the reason why the ISRE cannot occur in Bose-Einstein condensates.

In this manuscript, we propose to study another very general quantum mechanical feature that is spin squeezing [76, 77]. In 2001, a proposal suggested to use the elastic collisions happening in a spinor BEC in order to generate an interaction-mediated spin squeezing [78]. This process lies on the different collisional properties of the two internal states occupied by the BEC, and in the case of ^{87}Rb, some tricks have to be applied in order to tune these interactions. This has been successfully achieved twice in 2010, by using either a Feshbach resonance in an optical lattice potential [60], or a state-dependent microwave potential in a magnetic trap on a chip [61]. Both methods showed a significant reduction of the relative number fluctuations between the two states below the SQL, and good enough phase coherence to actually get use of this squeezing [13,79]. Here, were propose to benefit from the inherent mean field dynamics of a dual-component BEC leading to a spontaneous spatial separation and recombination of the two states [80–83]. During the separation, the non-linear interaction considerably increases resulting in significant spontaneous spin squeezing [84]. Not only this method could significantly improve the sensitivity of BEC-based interferometers, but it also comes within the framework of multi-particle entanglement which is a fascinating open topic in itself.

The idea here is thus to get use of our atom chip to benefit from the metrological environment provided by TACC to observe a reduction of the phase measurement uncertainty .

The manuscript is organized as follows:

- We begin by introducing all the concepts involved in the operation of a trapped atom clock on a chip. The basic principles of magnetic trapping on an atom chip, atom-field interaction and atomic clocks will be briefly reviewed. A a key element of the study, Bose-Einstein condensates will then be theoretically described in the regime used experimentally. Subsequently, the concept of spin squeezing for metrology will be introduced and its implementation through inter-atomic interactions will be tackled.

- The second chapter consists of a rapid overview of the experimental set-up including the chip, the laser system and the interrogation signals. The temporal sequence,

from the trapping and cooling to the interrogation and detection of the atoms will also be presented. Some preliminary results concerning the characterization of our Bose-Einstein condensates and their oscillation inside the trap will be exhibited thereafter.

- The third chapter deals with the detection system. As it is our only way to probe the atoms, great care has been devoted to its optimization and calibration. The basics of time of flight absorption imaging and atom number estimation will be reviewed. A newly implemented double state detection scheme, allowing the simultaneous detection of the two clock states with a single light pulse, will be subsequently presented and characterized. Finally, the performances of the imaging system in terms of accuracy and stability will be challenged.

- The fourth chapter is dedicated to the study of the spontaneous state-dependent spatial dynamics occurring in a spinor Bose-Einstein condensate, and eventually leading to spin squeezing. A theoretical model used to numerically reproduce the experimental data will be introduced. Then, a Ramsey-type interferometric protocol will be implemented to thoroughly study this phenomenon through two features: the contrast and the central frequency of the interferometer. The initial scheme will be modified in order to increase its sensitivity in the presence of significant asymmetric population losses. The influence of several parameters such as the trapping frequencies and atom numbers on the dynamics will also be studied.

- The fifth chapter addresses the realization of the atomic state tomography and spin squeezing measurement. Thank to the spatial dynamics, non-linear interactions will twist the spin noise distribution of the atomic state, resulting in a squeezed spin state. A protocol will be implemented in order to probe the spin distribution and exhibit a reduced atomic noise. Different sources of instability will finally be analyzed using a clock measurement, to explain our measured squeezing parameter.

Chapter 1

Theory of a trapped atom clock on a chip

*****

This chapter draws up the main aspects of the TACC experiment and provides all the theoretical tools required to explain the experimental methods and observations. It starts by reviewing the different physical mechanisms involved in a trapped atom clock on a chip such as magnetic trapping, Zeeman shifts, atom field interaction, atom loss processes and so on. Some theoretical tools concerning the time evolution of an atomic state are also developed in order to support the experimental data later on. Then the basic principles of atomic clocks are presented making the link with the current status of the experiment. The connection with atom interferometry is made to illustrate our interest for spinor Bose-Einstein condensates and quantum metrology. This degenerate state of matter is then theoretically described under the mean-field formalism and in the case of a cigar-shaped harmonic trapping. Finally, the spontaneous state-dependent spatial dynamics of condensed Rubidium atoms is exploited to generate spin squeezing through the one-axis-twisting Hamiltonian.

1.1 Magnetic trapping on atom chips

Theoretically proposed [85] and experimentally realized [86] in the early eighties, the idea of magnetic trapping for neutral atoms has become a cornerstone for nowadays ultracold physics. Combined with the versatility of on-chip micro-circuits, it enables the precise confinement and manipulation of atomic gases paving the way for the study of numerous physical phenomena [43, 44]. This section is a brief introduction to magnetic trapping of neutral atoms on an atom chip. The fundamental aspects of the interaction between an atom and a magnetic field, as well as the generation of such trapping field in the context of the TACC experiment are presented.

1.1.1 Atom chip technology

The heart of the TACC experiment is a micro-fabricated chip, displayed on figure 1.1, whose working principle and applications are thoroughly detailed in [44,87,88]. The most widely used atom chip technology consist of micro-fabricated conductive wires deposited on an insulated substrate [43, 89, 90]. The two main advantages of such a device are its compactness and its versatility. Indeed, in the framework of lab-on-chip technologies, it is possible to concentrate most of the tools required to interact with the atoms in a relatively small area [91]. A good example of such versatility is the addition on top of the "standard" trapping wires of a coplanar wave-guide whose purpose is to generate the microwave magnetic field that interrogates the atoms. Furthermore, the currently on-going next generation of the experiment also includes a pair of fibred Fabry-Pérot cavities [92], increasing the possible atomic manipulations and getting closer to a lab-on-chip realization. One of the final possible applications being the implementation of a robust and portable inertial sensor combining an on-chip atomic clock with on-chip gyroscopes [93, 94] and gravimeters [95, 96].

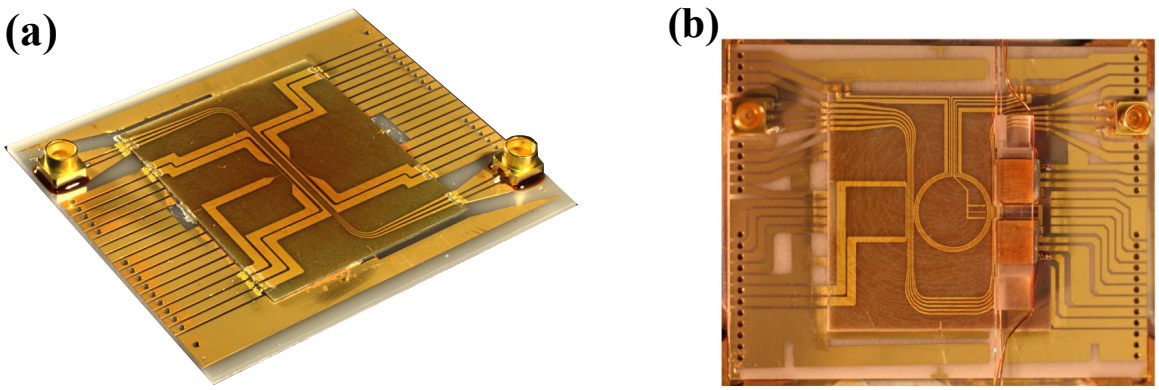

Figure 1.1: **TACC atom chips.** Micro-fabricated circuits used in the present experiment **(a)** and new configuration with integrated fibered micro-cavities **(b)**. Both chips present a coplanar wave-guide, whose connectors are visible, used to generate the MW interrogation field. The new configuration also possesses a circular structure to transport the atoms towards a pair of optical fiber cavities, whose common bridge is visible on its right side.

Let's now have a look at the interaction between an atom and a static magnetic field.

1.1.2 Physical principle of magnetic trapping

A neutral atom subject to a small[1] external magnetic field $\overrightarrow{B}$ experiences a potential which can be written to first order as

$$V = -\overrightarrow{\mu}.\overrightarrow{B} = \mu_B g_F m_F \|\overrightarrow{B}\|, \tag{1.1}$$

where μ_B is the Bohr magneton, g_F is the Landé g-factor of the angular momentum state F, and m_F is the magnetic quantum number resulting from the projection of $\overrightarrow{F}$ onto $\overrightarrow{B}$. The trapping or repulsive nature of the potential depends on the sign of $g_F m_F$. If it is positive, then the atoms will be attracted toward a minimum of the magnetic field and conversely. Yet, local maxima of the magnetic field in source-free regions are forbidden by the Maxwell equations [97]. Therefore, only "low-field seekers" ($g_F m_F > 0$) can be trapped. Such states are represented in red on figure 1.5. This reasoning assumes an adiabatic evolution of the atoms in the magnetic potential. Otherwise, if the atomic spin does not adiabatically follow the local direction of the magnetic field, it can topple into a repulsive or non trapping state and be ejected from the trap. Such spin-flip losses are called Majorana losses [98–100]. To avoid them, magnetic field direction variations have

[1] The resulting potential has to be smaller than the hyperfine splitting.

to be slower than the Larmor frequency:

$$|\frac{d}{dt}\left(\frac{\overrightarrow{B}}{\|\overrightarrow{B}\|}\right)| << \omega_L = \frac{\mu_B|g_F|}{\hbar}\|\overrightarrow{B}\|. \tag{1.2}$$

The left term of equation (1.2) is generally smaller than the maximum trapping frequency. This condition gives then a higher bound on the achievable trapping frequencies [86].

1.1.3 Magnetic trap basics

The main goal is thus to create a magnetic field distribution containing a local minimum. The two simplest ways to generate a trap are either to use a pair of coils in the anti-Helmoltz configuration [86] or, as illustrated on figure 1.2, to combine the field of a current carrying wire with a homogeneous bias field created by a pair of coils in the Helmoltz configuration for instance. Such linear quadrupole traps are often used for generating a Magneto-Optical Trap [101]. The main problem is that the magnetic field strength vanishes at the trap center preventing condition (1.2) from being satisfied. It can be shown that a quadratic confinement is required to get a finite magnetic field at the trap center [102]

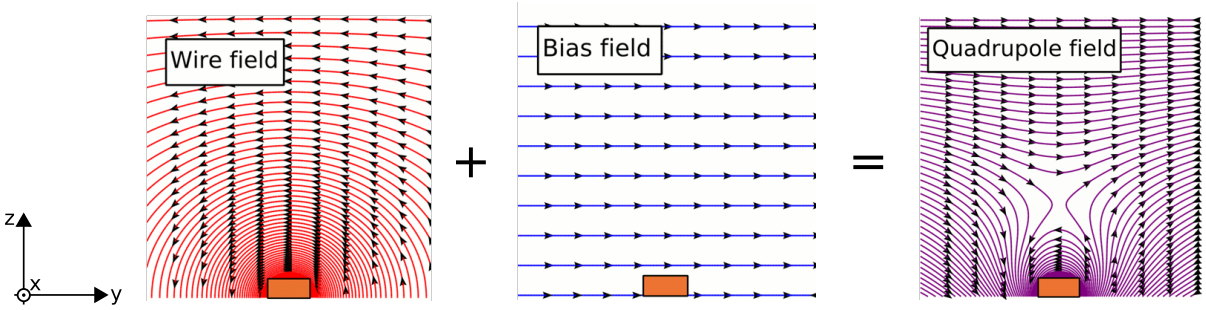

Figure 1.2: **Principle of a quadrupole magnetic trap.** The combination of the field radiated by a current carrying wire and a homogeneous bias field results in a quadrupole field that presents a local minimum inside which atoms can be trapped. Taken from [103].

This problem can be circumvented by using dynamic traps such as TOP[2] traps [104] or static traps involving a more complex combination of current carrying wires and static fields such as the widely used Ioffe-Pritchard traps [85, 105]. The dimple trap, presented in figure 1.3, is a particular kind of Ioffe-Pritchard traps that is used in TACC.

It is moreover possible to theoretically predict the trapping parameters (position, depth, frequencies) from a given geometry, currents and bias fields. Indeed, the magnetic field generated by a rectangular wire ($x_1 \leq x \leq x_2$, $y_1 \leq y \leq y_2$, $z_1 \leq z \leq z_2$) carrying a DC current is derived using the Biot-Savart law [106]

[2]time-averaged orbiting potential.

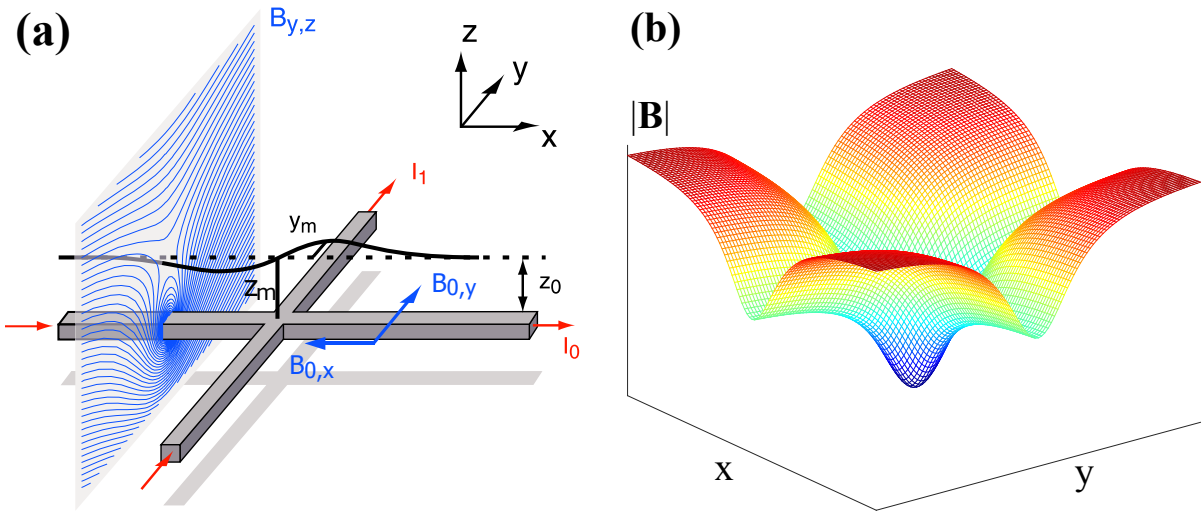

Figure 1.3: **Dimple trap. (a)** Three dimensional Ioffe-Pritchard trap generated by two crossing wires and a combination of two bias fields. The resulting field in the y-z plane is shown. Adapted from [89]. **(b)** Magnetic field strength in the x-y plane.

$$\overrightarrow{B}(\mathbf{r}) = \frac{\mu_0}{2\pi}\int_{x_1}^{x_2} \mathrm{d}x' \int_{y_1}^{y_2} \mathrm{d}y' \int_{z_1}^{z_2} \mathrm{d}z' \frac{\overrightarrow{j} \times (\overrightarrow{r} - \overrightarrow{r}')}{|\overrightarrow{r} - \overrightarrow{r}'|^3}, \tag{1.3}$$

where $\overrightarrow{j}$ is the current density flowing through the wire and μ_0 is the magnetic permeability. The fields radiated by the different wires and coils are then summed and the minimum of the norm $B(\mathbf{r}) = \sqrt{B_x^2 + B_y^2 + B_z^2}$ is found by looking for the zeros of its gradient $|\nabla \overrightarrow{B}| = \sqrt{(\frac{\partial B}{\partial x})^2 + (\frac{\partial B}{\partial y})^2 + (\frac{\partial B}{\partial z})^2}$. This gives access to the position of the trap center $\{x_m, y_m, z_m\}$ corresponding to $|\nabla \overrightarrow{B}(x_m, y_m, z_m)| = 0$. The other trap parameters (frequencies and axes) are found by deriving the Taylor expansion of the field around the stationary point and diagonalizing the resulting second order Hessian matrix[3] [107, 108]

$$M = \begin{bmatrix} \frac{\partial^2 B(x_m,y_m,z_m)}{\partial x^2} & \frac{\partial B(x_m,y_m,z_m)}{\partial x \partial y} & \frac{\partial B(x_m,y_m,z_m)}{\partial x \partial z} \\ \frac{\partial B(x_m,y_m,z_m)}{\partial y \partial x} & \frac{\partial^2 B(x_m,y_m,z_m)}{\partial y^2} & \frac{\partial B(x_m,y_m,z_m)}{\partial y \partial z} \\ \frac{\partial B(x_m,y_m,z_m)}{\partial z \partial x} & \frac{\partial B(x_m,y_m,z_m)}{\partial z \partial y} & \frac{\partial^2 B(x_m,y_m,z_m)}{\partial z^2} \end{bmatrix}, \tag{1.4}$$

The off diagonal terms correspond to a three-dimensional rotation of the trap axes. In the eigenvectors basis, the magnetic field takes the expected harmonic the form

$$B(\mathbf{r}) \approx B_m + \frac{m}{\mu}\left(\omega_X^2 \frac{(X - x_m)^2}{2} + \omega_Y^2 \frac{(Y - y_m)^2}{2} + \omega_z^2 \frac{(Z - z_m)^2}{2}\right), \tag{1.5}$$

[3] By definition the first order terms vanish at the stationary point.

where $B_m = B(x_m, y_m, z_m)$ is the field at the trap bottom and $\frac{1}{2\pi}\{\omega_X, \omega_Y, \omega_Z\}$ are the trapping frequencies along the eigen-axes X, Y, Z.

In the case of the dimple trap and for infinitely thin wires, analytical formulas can be found in the appendix of [87]. More details about magnetic traps associated to TACC and the inclusion of gravity and gravitational sag can be found in [92, 103].

1.1.4 A pseudo-magic trap

In the context of implementing an atomic clock with high metrological requirements, magnetically trapped atoms may not appear like the most efficient solution. Indeed, in the trap, the atoms will experience an unstable frequency shift, called Zeeman shift, which depends on their internal state and position. Indeed, a magnetic field B displaces the energy levels according to the Breit-Rabi formula [109, 110]

$$E_{F,m_F} = -\frac{E_{hfs}}{2(2I+1)} + \mu_B g_I m_F B \pm \frac{E_{hfs}}{2}\sqrt{1 + \frac{4m_F X}{2I+1} + X^2}, \tag{1.6}$$

where $X = \frac{\mu_B(g_J - g_I)B}{E_{hfs}}$ and $E_{hfs} = A_{hfs}(I + 1/2)$, with I = 3/2 and J = 1/2. The hyperfine energy levels for the ground state of ^{87}Rb are displayed on figure 1.4 (a).

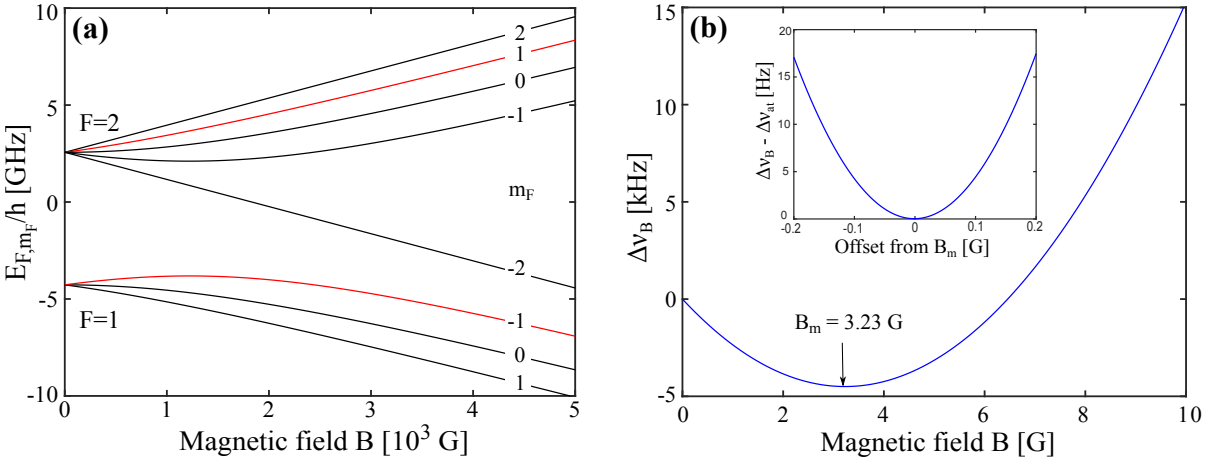

Figure 1.4: **Zeeman energy shifts. (a)** Energy level shifts due to a static magnetic field according to Eq. (1.6). The clock states are represented in red. **(b)** Frequency shift of the clock transition defined as $\Delta\nu_B = (E_{2,1} - E_{1,-1} - E_{hfs})/h$. The smooth region around $B_m \approx 3.229$ G is shown in the inset.

A clever choice of the clock states can nonetheless minimize this issue. As a matter of fact, in the case of the ground state ($5^2S_{1/2}$) of ^{87}Rb, states $|1\rangle = |F = 1, m_F = -1\rangle$ and $|2\rangle = |F = 2, m_F = 1\rangle$ have the same magnetic moment which makes the transition frequency insensitive to magnetic fields to first order. Only the second order Zeeman

shift contributes and it can be shown that there is a pseudo-magic[4] field for which the transition frequency does not depend on magnetic field fluctuations [111, 112] (cf figure 1.4 (b)). More quantitatively, around this magic field the transition frequency reads [113],

$$\Delta\nu_B = \frac{E_{2,1}(B) - E_{1,-1}(B)}{2\pi\hbar} = \nu_{at} + \Delta\nu_{at} + \beta(B(\mathbf{r}) - B_m)^2, \tag{1.7}$$

where $\nu_{at} = 6.834682610$ GHz is the non-perturbed atomic frequency, $\Delta\nu_{at} = -4497.34$ Hz is the systematic frequency shift at the magic field $B_m = 3.22892$ G and $\beta = 431.3596$ Hz.G^{-2} [103, 110]. This justifies the choice of the two clock states represented on figure 1.5.

To go a bit further, let's now consider the spatial extension of the atomic cloud. For instance, non-degenerate thermal clouds have a size which is related to their temperature $\sigma_i = \sqrt{\frac{k_B T}{m\omega_i}}$, where $i = x, y, z$ is the spatial coordinate. This means that the Zeeman shift is inhomogeneous over the cloud extension, hence the interest in cold atoms[5]. Namely, the spatial dependence of the magnetic field combined with the action of gravity lead to a position-dependent frequency shift [114]

$$\Delta\nu_B(x, y, z) = \frac{\beta m^2}{\mu_B^2}\left(\omega_x^2 x^2 + \omega_y^2 y^2 + \omega_z^2 z^2 - 2gz + \delta B\frac{\mu_B}{m}\right)^2, \tag{1.8}$$

where $\delta B = B(0) - B_m$ is the offset between the bottom field and the magic field, and g is the gravitational acceleration. Besides, in trapped atomic ensembles, there is another position-dependent frequency shift arising from atom-atom interactions. This shift, called collisional shift, can be written in the case of thermal atoms [111, 112]

$$\Delta\nu_{coll}(x, y, z) = \frac{2\hbar}{m} n(x, y, z)[a_{22} - a_{11} - (2a_{12} - a_{22} - a_{11})f(x, y, z)], \tag{1.9}$$

where $f = \frac{n_1 - n_2}{n}$ is the population imbalance between the two states, a_{ij} is the s-wave scattering length and n is the standard atomic density given by the Maxwell-Boltzmann distribution. As it was shown in [114], these two shifts are on the same order of magnitude and a particular value of δB can be found in order to minimize the overall frequency shift averaged over the cloud size. This method was used to minimize the dependence of the clock frequency on the atom temperature and magnetic field fluctuations [69]. In the case of Bose-Einstein condensates, because of their very high densities ($\sim 10^{19}$ atoms.m^{-3}) and small sizes, the spatial dependency of the Zeeman shift becomes negligible compared to the collisional shift and no such optimization is possible.

1.2 Atom-field interaction

While static fields are used to trap atoms, oscillating fields are used to interrogate them. Indeed, a significant part of our knowledge on atoms comes from the study of

[4] The designation of "pseudo"-magic field refers to the presence of a residual systematic shift $\Delta\nu_{at}$.

[5] The smaller the could, the smaller the inhomogeneity.

its interaction with an electromagnetic field. This complex coupling leads to a large variety of physical phenomena that can be theoretically predicted and experimentally observed [115]. The study of such phenomena requires either a semi-classical (atom cooling and trapping [116], manipulation of atomic clocks [117]), or fully quantum mechanical formalism (spontaneous emission [115], cavity quantum electrodynamics [118], polarization-entangled photon pairs emitted in an atomic radiative cascade [119]). In this manuscript, the semi-classical approach is powerful enough to describe most of our experimental observations and this is why we will restrict ourselves to it.
We will thus see in this section, how we can use oscillating fields to control the atomic state. This interaction will be described under the density matrix formalism through the resolution of the Bloch equations. A simple analytic expression for a system without atom losses, will be derived and used to access the temporal evolution of the density matrix elements after arbitrarily complex interrogation sequences. The generalization of the Bloch equations with many-body losses will also be tackled and the geometrical representation of the atomic state on the Bloch sphere will be introduced.

1.2.1 Dipolar coupling

A two-level atom, with states $|1\rangle$ and $|2\rangle$ as depicted on figure 1.5, exposed to an oscillating magnetic field of angular frequency ω can be described by the following Hamiltonian.

$$\hat{H} = \hat{H}_0 + \hat{H}_{int} = \frac{\hbar}{2}\begin{pmatrix}\omega_{at} & 0\\ 0 & -\omega_{at}\end{pmatrix} + \hbar\begin{pmatrix}0 & V_{12}\\ V_{21} & 0\end{pmatrix}, \tag{1.10}$$

in the $\{|1\rangle, |2\rangle\}$ basis where

$$V_{12} = \frac{\Omega_R}{2}e^{-i(\omega t+\phi_{lo})} + \frac{\Omega_R^*}{2}e^{i(\omega t+\phi_{lo})} \tag{1.11}$$

$$= \Omega_R \cos(\omega t + \phi_{lo}) \tag{1.12}$$

$$= \frac{b_1 + ib_2}{2}e^{-i\omega t} + h.c. \tag{1.13}$$

with $b_1 = \Omega_R \cos(\phi_{lo})$ and $b_2 = -\Omega_R \sin(\phi_{lo})$ and

$$\Omega_R = \frac{g_F\mu_B}{\hbar}B\overrightarrow{e}.\langle F', m_{F'}|\hat{\overrightarrow{F}}|F, m_F\rangle, \tag{1.14}$$

is the one-photon Rabi frequency with $\overrightarrow{B} = Be^{i(\omega t+\phi_{lo})}\overrightarrow{e} + c.c.$. The coupling constants and the matrix elements can be found in [110]. As $\Delta(m_F) = 2$, the transition $|1\rangle \leftrightarrow |2\rangle$ cannot be driven with a single photon transition. This is the reason why a two-photon drive composed of a microwave and radio-frequency fields, is used. The resulting two-photon Rabi frequency reads [120]

$$\Omega_R = \frac{\Omega_{MW}\Omega_{RF}}{2\Delta}, \tag{1.15}$$

where $\Delta \approx 500$ kHz is the detuning with respect to the intermediate state $|F = 2, m_F = 0\rangle$. For the considered atomic transition, the two one-photon Rabi frequencies read[6] [103]

$$\Omega_{MW} = \frac{g_J \mu_B}{2\hbar} B_{MW} \text{ and } \Omega_{RF} = \frac{g_J \mu_B \sqrt{3}}{2\hbar} B_{RF}. \tag{1.16}$$

This interrogation field enables us to control the internal state of the atoms and is therefore a key element in the atomic clock operation. Let's now have a look at the theoretical description of such coupling between an oscillating electromagnetic field and the atoms.

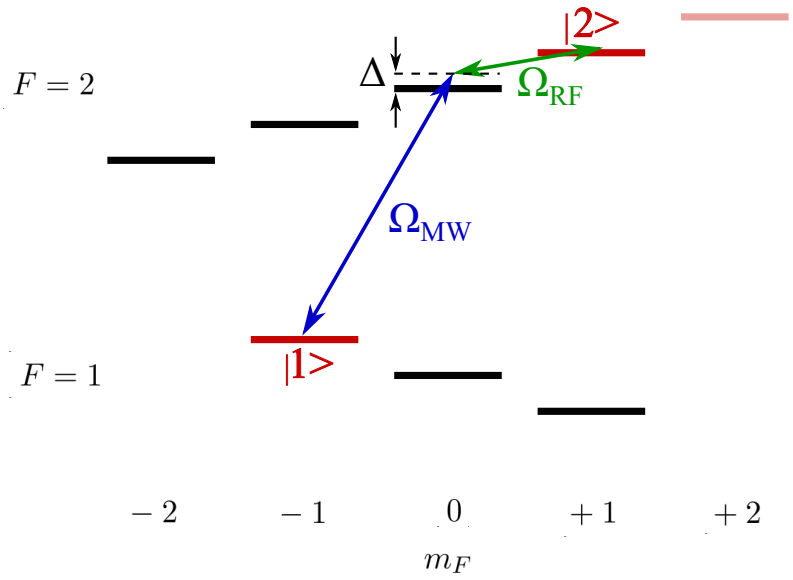

Figure 1.5: **Zeeman sub-levels of the $5^2S_{1/2}$ manifold of ^{87}Rb.** The microwave (blue) and radio-frequency (green) photons and the trapping levels (red) are represented. The detuning of the interrogation fields with the intermediate state is by $\Delta \approx 500$ kHz.

1.2.2 Time evolution of the atomic state

In contrast to single elementary particles, an ensemble of atoms is better described in terms of populations and coherences using the statistical density matrix elements [121]. The temporal evolution of the system is governed by the Liouville-Von Neumann equation [122]:

$$i\hbar \frac{d\rho}{dt} = [\hat{H}, \rho], \tag{1.17}$$

[6] This is only true if the two fields are perfectly circularly polarized, otherwise some corrections have to be taken into account [16, 113].

where ρ is the density matrix: $\begin{pmatrix}\rho_{11} & \rho_{12}\\ \rho_{21} & \rho_{22}\end{pmatrix}$, with $\rho_{11}+\rho_{22}=1$ and $\rho_{12}=\rho_{21}^{*}$. Using the Hamiltonian (1.10), equation (1.17) leads to the following set of coupled differential equations

$$\begin{cases} i\dot{\rho}_{11} = V_{12}\rho_{21} - V_{21}\rho_{12} \\ i\dot{\rho}_{12} = V_{12}(\rho_{22}-\rho_{11}) + \rho_{12}\omega_{at} \\ i\dot{\rho}_{21} = -V_{21}(\rho_{22}-\rho_{11}) + \rho_{21}\omega_{at} \\ i\dot{\rho}_{22} = -V_{12}\rho_{21} + V_{21}\rho_{12} \end{cases} . \tag{1.18}$$

An analytical solution of the form $\rho_{12}=\frac{1}{2}(a_1(\tau)+ia_2(\tau))e^{-i\omega t}$ and $\rho_{11}-\rho_{22}=a_3(\tau)$ can be derived where τ is the interaction time. It is worthy to note that at this point the length of the vector $\mathrm{a}=(a_1\ a_2\ a_3)^{\intercal}$ is conserved. For arbitrary detunings, pulse durations and Rabi frequencies, it can be shown that the temporal evolution of the atomic state reads

$$\begin{pmatrix}a_1(\tau)\\ a_2(\tau)\\ a_3(\tau)\end{pmatrix} = \mathrm{R}(b_1,b_2,\Delta,\tau)\begin{pmatrix}a_1(0)\\ a_2(0)\\ a_3(0)\end{pmatrix}, \tag{1.19}$$

with $\mathrm{R}(b_1,b_2,\Delta,\tau)=$

$$\begin{pmatrix} \cos(\Omega\tau)+2\frac{b_1^2}{\Omega^2}\sin^2(\frac{\Omega\tau}{2}) & -\frac{\Delta}{\Omega}\sin(\Omega\tau)+2\frac{b_1b_2}{\Omega^2}\sin^2(\frac{\Omega\tau}{2}) & -\frac{b_2}{\Omega}\sin(\Omega\tau)-2\frac{b_1\Delta}{\Omega^2}\sin^2(\frac{\Omega\tau}{2}) \\ \frac{\Delta}{\Omega}\sin(\Omega\tau)+2\frac{b_1b_2}{\Omega^2}\sin^2(\frac{\Omega\tau}{2}) & \cos(\Omega\tau)+2\frac{b_2^2}{\Omega^2}\sin^2(\frac{\Omega\tau}{2}) & \frac{b_1}{\Omega}\sin(\Omega\tau)+2\frac{b_2\Delta}{\Omega^2}\sin^2(\frac{\Omega\tau}{2}) \\ \frac{b_2}{\Omega}\sin(\Omega\tau)-2\frac{b_1\Delta}{\Omega^2}\sin^2(\frac{\Omega\tau}{2}) & -\frac{b_1}{\Omega}\sin(\Omega\tau)-2\frac{b_2\Delta}{\Omega^2}\sin^2(\frac{\Omega\tau}{2}) & \cos(\Omega\tau)+2\frac{\Delta^2}{\Omega^2}\sin^2(\frac{\Omega\tau}{2}) \end{pmatrix} \tag{1.20}$$

where $\Omega=\sqrt{\Omega_R^2+\Delta^2}$ and $\Delta=\omega-\omega_{at}$. With that formalism, the expression of the population in the excited state simply reads

$$P_2(\tau)=\frac{1}{2}\left(1-\frac{a_3(\tau)}{a_3(0)}\right). \tag{1.21}$$

As we will see later, the form of equation (1.19) allows the quick derivation of the populations after an arbitrary sequence of interrogation pulses and free evolution times.

1.2.3 Inclusion of atom losses

Equations (1.17) and (1.18) are however well suited only in a perfect world inside which the atoms remain trapped forever. In practice, the duration of the experimental sequence is limited by the atoms lifetime. Indeed, a trapped atom is subject to several loss mechanisms: Majorana losses, collisions with background gas, spin-exchange collisions and spin-dipole interactions. [123]. Because of the sufficiently strong magnetic fields

used in this experiment and according to equation (1.2), Majorana spin flips can be safely neglected. The resulting populations decay is described by the two rate equations

$$\begin{aligned}\frac{dn_1}{dt} &= -\gamma_{bck} n_1 - \gamma_{12} n_1 n_2 - \gamma_{111} n_1^3 \\ \frac{dn_2}{dt} &= -\gamma_{bck} n_2 - \gamma_{12} n_1 n_2 - \gamma_{22} n_2^2\end{aligned} \tag{1.22}$$

Let's now have a closer look at the different inelastic processes involved in our system.

One-body collisions Collisions with the background gas, whose loss rate γ_{bck} depends on the pressure in the vacuum cell. This is why considerable efforts are constantly made in order to improve the quality of the vacuum level and minimize the effect of this loss channel. Note that these one-body losses are independent from the atom density.

Two-body collisions Some states, such as state $|2\rangle$ can undergo spin flip collisions. If two atoms in $|2\rangle$ collide, the spins can be modified according to $|2,1\rangle + |2,1\rangle \rightarrow |2,0\rangle + |2,2\rangle$ because of conservation of the spin moment m_F. The corresponding two-body loss rate depends linearly on the atom density in state $|2\rangle$ with $\gamma_{22} = 8.1(3) \times 10^{-14}$ cm^3/s [124]. Note that this is the dominant loss process for this clock state. Atom loss through spin-dipole interaction is much smaller [123] and will be neglected here. The same process can happen between two atoms in a superposition of states: $|1,-1\rangle + |2,1\rangle \rightarrow |1,0\rangle + |2,0\rangle$ with a smaller rate constant $\gamma_{12} = 1.51(18) \times 10^{-14}$ cm^3/s [124].

Three-body recombination If three atoms collide, a molecule can be formed with a kinetic energy usually larger than the trap depth leading to the loss of these three atoms. The corresponding three-body decay rate $\gamma_{111} = 5.8(1.9) \times 10^{-30}$ cm^6/s [125] is now proportional the the density square. Our atom density is however too small to observe this loss process which will then be neglected in the following.

Extension of the Liouville-von Neumann equation Considering the discussed many-body losses, equation (1.17) is no longer appropriate to describe the open system, and the system-bath interaction has now to be described by the Markovian master equation [126, 127]. The calculations performed in [128] showed that the time evolution of the density matrix elements under many-body losses is well described by

$$\begin{cases} i\dot{\rho}_{11} = V_{12}\rho_{21} - V_{21}\rho_{12} - i[\gamma_{bck}\rho_{11} + \Gamma_{12}\rho_{11}\rho_{22}] \\ i\dot{\rho}_{12} = V_{12}(\rho_{22} - \rho_{11}) + \rho_{12}\omega_{at} - i[\kappa_1\rho_{12} + \kappa_2\rho_{11}\rho_{12} + \kappa_3\rho_{22}\rho_{12}] \\ i\dot{\rho}_{21} = -V_{21}(\rho_{22} - \rho_{11}) + \rho_{21}\omega_{at} - i[\kappa_1\rho_{21} + \kappa_2\rho_{11}\rho_{21} + \kappa_3\rho_{22}\rho_{21}] \\ i\dot{\rho}_{22} = -V_{12}\rho_{21} + V_{21}\rho_{12} - i[\gamma_{bck}\rho_{22} + \Gamma_{12}\rho_{11}\rho_{22} + \Gamma_{22}\rho_{22}^2] \end{cases}, \tag{1.23}$$

with

$$\kappa_1 = \frac{2\gamma_{bck} + \gamma_d}{2},\ \kappa_2 = \frac{\Gamma_{12}}{2},\ \kappa_3 = \frac{\Gamma_{22} + \Gamma_{12}}{2}, \tag{1.24}$$

where γ_d is a phenomenological decoherence rate, $\Gamma_{ij} = n_0\gamma_{ij}^{thermal} = 2n_0\gamma_{ij}^{BEC}$ is the decay constant due to two-body collisions between states $|i\rangle$ and $|j\rangle$, n_0 is the total atom number density at $t = 0$. The factor 2 accounts for the different counting statistics of condensed and non-condensed bosons [125,129]. It is moreover worth noting that system (1.23) has been adapted to our situation for which the one-body losses, identical for the two states, are due to collisions with the background gas. Furthermore, only state $|2\rangle$ is sensitive to two-body losses[7] and our densities are not high enough to observe three-body losses in either state.
Equations (1.23) can be numerically solved and will be used to explain and model our system, including spin rotations during the squeezing sequence in section 5.2.

1.2.4 Bloch sphere representation

The Bloch sphere [130] is a powerful tool to visualize the spins evolution during any kind of interrogation sequence. It can therefore provide a nice geometrical and intuitive interpretation of what happens during the experimental sequence. In this representation, the individual spin vector operator $\hat{s}$ is defined by:

$$\hat{s} = \begin{pmatrix} \hat{s}_x \\ \hat{s}_y \\ \hat{s}_z \end{pmatrix} \text{ with } \begin{cases} \hat{s}_x = (|1\rangle\langle 2| + |2\rangle\langle 1|)/2 \\ \hat{s}_y = (|2\rangle\langle 1| - |1\rangle\langle 2|)/2i \\ \hat{s}_z = (|2\rangle\langle 2| - |1\rangle\langle 1|)/2. \end{cases} \tag{1.25}$$

It can be easily shown that this operator satisfies the commutation relation $[\hat{s}_i, \hat{s}_j] = i\epsilon_{i,j}\hat{s}_k$ where $\epsilon_{i,j}$ is the Levi-Civita symbol and i, j, k refer to the spatial coordinates. It can can therefore be considered as a spin-$\frac{1}{2}$ angular momentum operator. Let's note here that the expectation value of this operator is called Bloch vector and can be linked to the density matrix elements via

$$\begin{cases} s_x(t) = [\rho_{21}(t)e^{-i\omega t} + \rho_{12}(t)e^{i\omega t}]/2 \ \ (\equiv Re(\rho_{12}(t)e^{i\omega t})) \\ s_y(t) = [i\rho_{21}(t)e^{-i\omega t} - i\rho_{12}(t)e^{i\omega t}]/2 \ \ (\equiv Im(\rho_{12}(t)e^{i\omega t})) \\ s_z(t) = [\rho_{22}(t) - \rho_{11}(t)]/2. \end{cases} \tag{1.26}$$

A second vector, called Rabi vector, is also defined to represent the interaction of such a spin with an external field [131]

$$\overrightarrow{\Omega} = \begin{pmatrix} \Omega_R \cos(\phi_{lo}) \\ -\Omega_R \sin(\phi_{lo}) \\ -\Delta \end{pmatrix} \tag{1.27}$$

[7] state $|1\rangle$ being a stretched state.

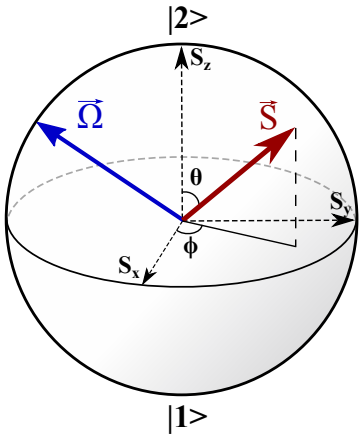

Figure 1.6: **Bloch sphere.** Bloch sphere representation defined by the three spin components. The collective spin S is defined by its length and the two angles θ and ϕ. Its interaction with a driving field induces rotations around the Rabi vector Ω according to Eq. (1.28).

The rotating terms $e^{\pm i\omega t}$ in equation (1.26) have been added here in order to express the Bloch vector in the rotating frame inside which the Rabi vector is stationary. The temporal evolution of the Bloch vector is then described by

$$\frac{d}{dt}\overrightarrow{s} = \overrightarrow{\Omega} \times \overrightarrow{s}. \tag{1.28}$$

In that representation, an atomic state can be fully described by the two angles θ and ϕ shown on figure 1.6

$$|\psi\rangle \equiv |\theta, \phi\rangle = \sin(\theta/2)e^{\frac{i\phi}{2}}|1\rangle + \cos(\theta/2)e^{-\frac{i\phi}{2}}|2\rangle \tag{1.29}$$

An important feature that will be used later in the manuscript is that the z-component of the Rabi vector is determined by the frequency difference between the local oscillator and the atomic resonance. This means that for a non-zero detuning the Rabi vector leaves the equator plane and prevents the spins from reaching the poles.

This reasoning can be extended to an ensemble of N two-level atoms that have coherently interacted with a resonant field. In that case, the collective pseudo-spin is simply defined as the sum of all the individual spins : $\hat{S}_k = \sum_{i=1}^{N} \hat{s}_{k,i}$ for $k = x, y, z$, and has a well defined length $|\langle \mathbf{S} \rangle| = \frac{N}{2}$.

1.3 Working principle of atomic clocks

Suggested by I. Rabi in 1945 and implemented at NIST for the first time in 1958 [132], atomic clocks have known a spectacular development all around the world with the

implementation of atomic fountains [133,134], optical clocks [10] ion clocks [135] or other compact atomic clocks [69,136]. They indeed provide the so far most stable and accurate measurement of time. Of course the expectations and goals of each of these clocks are different but the general guideline is to increase the precision and stability of the time measurement, either for fundamental purposes (general relativity tests [11], monitoring fundamental constant [137], dark matter investigations [12]) or industrial developments (satellite navigation systems [138], telecommunication, deep space navigation [139]).
In this section are presented the basic working principles of an atomic clock, including the detailed interrogation schemes and stability estimation. Being the metrological tool enabling the work presented in this manuscript, the current status of TACC is also briefly addressed.

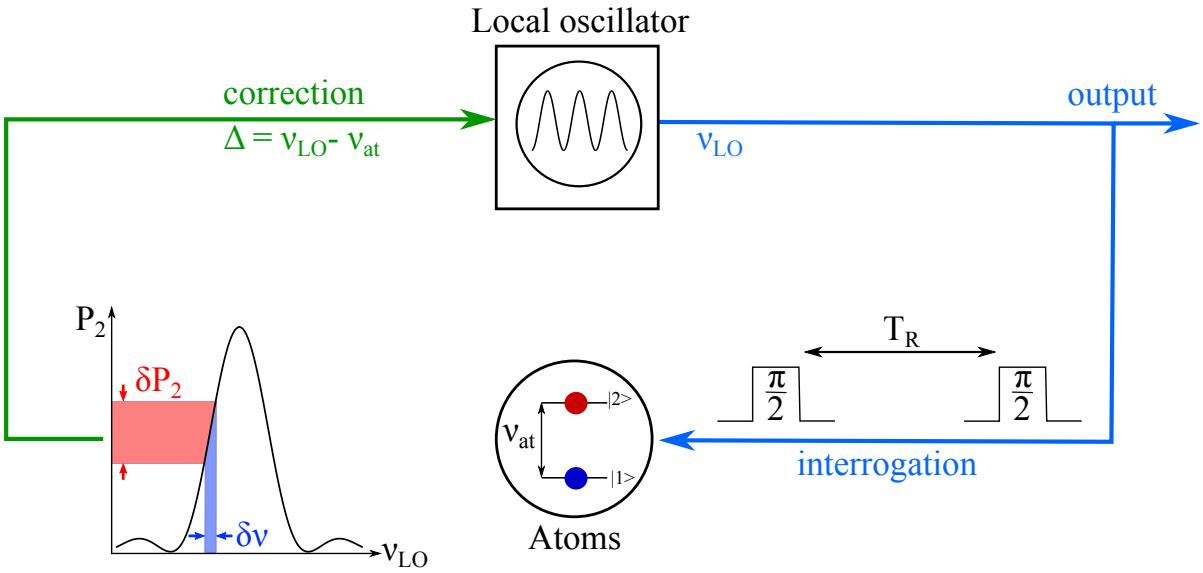

Figure 1.7: **Working principle of an atomic clock.** An oscillator provides an unstable signal which is compared to an atomic reference using a particular interrogation scheme. The resulting error signal is subsequently used to correct the oscillator and greatly improve its stability.

1.3.1 Basic principle

There exist two kinds of time-measurement devices: the active clocks, where the atoms emit a radiation at a well defined frequency (hydrogen maser [140]), and the passive clocks, where an atomic transition is used to correct the frequency of an oscillator (atomic fountains, optical lattice clocks and so on). The principle of a passive atomic clock is very similar to a musician following the beats of a metronome. Indeed, as the beginner musician tries to synchronize its rhythm with the beats of a metronome, the unstable local oscillator is locked on the atomic frequency. More specifically, the unlocked local

oscillator (laser, microwave synthesizer) provides an unstable signal while, until proven otherwise, an unperturbed atom is an infinitely stable frequency reference [137, 141]. The link between the two is realized by the interrogation that converts their frequency difference into a measurable quantity, the transition probability for instance. Every cycle, by monitoring the changes in P_2, one can deduce the corresponding frequency change and correct the local oscillator frequency accordingly. That way, the output frequency of the local oscillator is stabilized on the atomic reference.

1.3.2 Interrogation schemes

Two main interrogation schemes are currently used in atomic clocks: the Rabi [142] and Ramsey [143, 144] spectroscopy.

Rabi spectroscopy: It consists in applying a single near-resonant interrogation pulse that will put the atoms, initially in the ground state $|1\rangle$, in a coherent superposition. Using equation (1.20) with $\mathrm{a}(0) = (0\ 0\ 1)^{\intercal}$, one easily finds the evolution of the population in the excited state $|2\rangle$

$$P_2(\Omega_R, \Delta, \tau) = \frac{\Omega_R^2}{\Omega^2} \sin^2\left(\frac{\Omega\tau}{2}\right). \tag{1.30}$$

The evolution of the transition probability P_2 in the frequency and temporal domains are displayed on figure 1.8.

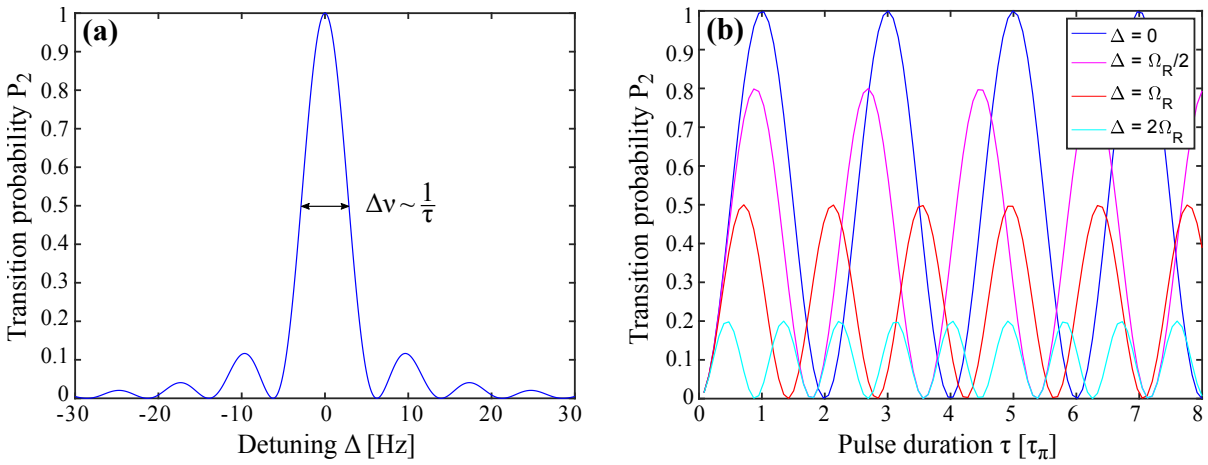

Figure 1.8: **Rabi interrogation. (a)** Rabi spectroscopy for a π-pulse i.e. $\tau_\pi = \frac{1}{2\Omega}$ with $\Omega_R \approx 2\pi \times 3.6$ Hz. **(b)** Temporal Rabi oscillation for various detunings. At resonance, a π-pulse brings all the atoms in the excited state and the transition probability P_2 oscillates at a frequency $\Omega_R/2$. On the other hand, in a presence of a detuning Δ, the contrast of the oscillation decreases while its frequency increases.

As shown on figure 1.8 (a), the width of the spectroscopy line scales as $1/\tau$. This means that in order to increase the clock sensitivity and therefore its stability, the interrogation pulse duration has to be increased. Unfortunately, this might give rise to some issues. For instance, when the drive is on, the energy levels are shifted (AC Zeeman or Stark shifts) and the frequency depends on the interrogation power which is often hard to precisely control for long times. Furthermore, inhomogeneities of the driving field amplitude over the atomic cloud cause dephasing and eventually an inhomogeneous broadening of the transition line. The Ramsey interrogation scheme is a widely used way to minimize these effects while increasing the interrogation time, and hence the clock stability.

Ramsey spectroscopy: In this scheme, illustrated in figure 1.9, two interrogation pulses separated by a free evolution time[8] T_R are applied. If the atomic ensemble is subject to frequency inhomogeneities (differential light-shifts, collisions, and so on), then the individual spins will rotate at different rates leading to dephasing during the free evolution time. The detuning (identical for the two pulses) is usually set so that the collective spin covers one quarter of the equator of the Bloch sphere and ends up aligned with the Rabi vector. The detection pulse then converts the accumulated phase into populations.

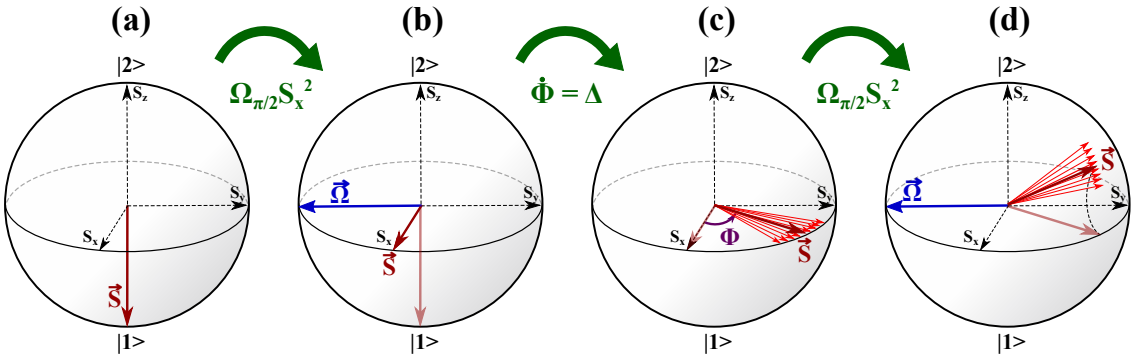

Figure 1.9: **Illustration of the Ramsey interrogation on the Bloch sphere. (a)** The atoms are initially prepared in $|1\rangle$. **(b)** A first near-resonant $\frac{\pi}{2}$-pulse (called preparation pulse) is applied to put them in a coherent superposition. **(c)** The interrogation fields are turned off and the spins rotate along the equator at a rate Δ, leading to an overall accumulated phaseshift $\Phi = 2\pi \int_0^{T_R} \Delta \mathrm{dt}$. **(d)** A second $\frac{\pi}{2}$-pulse (detection pulse) is applied to close the interferometer and convert the accumulated phase into P_2.

The resulting transition probability can be derived by applying equation (1.20) for the three parts of the sequence: preparation pulse, free evolution and detection pulse,

[8] also called interrogation or Ramsey time

with all the atoms starting in state $|1\rangle$ (a(0) = (0 0 1)$^\intercal$):

$$\begin{pmatrix} a_1(\tau_1 + T_R + \tau_2) \\ a_2(\tau_1 + T_R + \tau_2) \\ a_3(\tau_1 + T_R + \tau_2) \end{pmatrix} = \mathrm{R}(\Omega_R\cos(\phi_{lo}), -\Omega_R\sin(\phi_{lo}), \Delta, \tau_2)\mathrm{R}(0, 0, \Delta, T_R)\mathrm{R}(\Omega_R, 0, \Delta, \tau_1)\mathrm{a}(0) \tag{1.31}$$

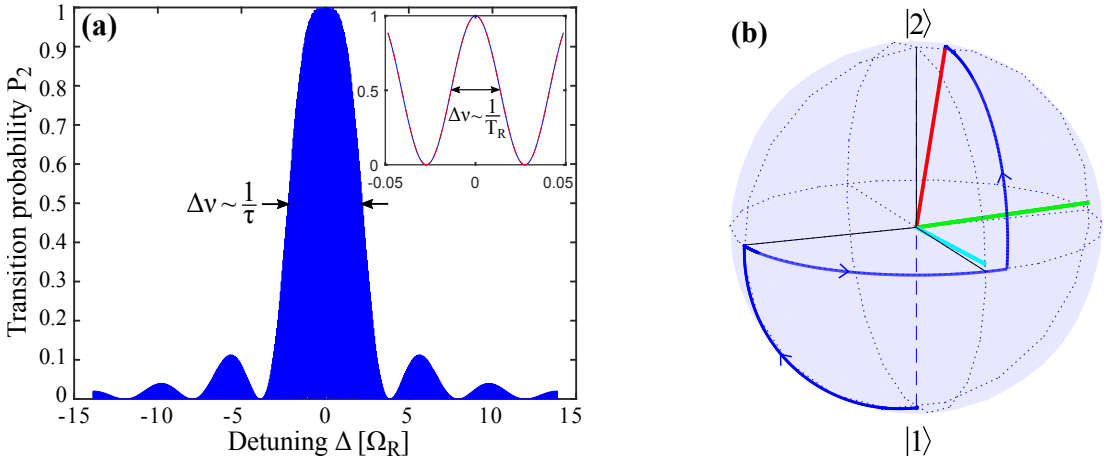

Figure 1.10: **Ramsey interrogation. (a)** Ramsey spectroscopy for two $\frac{\pi}{2}$-pulses i.e. $\tau_\pi = \frac{1}{2\Omega_R}$ with $\Omega_R \approx 2\pi \times 3.6$ Hz and $T_R = 5$s. The inset is a zoom of the central fringe and the red dashed line corresponds to equation (1.33). **(b)** Bloch sphere representation of the Bloch vector trajectory during a Ramsey sequence with $\phi_{lo} = -90°$ and $\Phi \approx 90°$. The cyan and green lines are respectfully the first and second Rabi vectors, the red line represents the final position of the Bloch vector and the blue line corresponds to the collective spin trajectory.

For arbitrary pulse durations, developing equation (1.31) leads to

$$\begin{aligned} a_3 = {} & \frac{\Omega_R^2}{\Omega^2}\cos(\Delta T_R + \phi_{lo})\left[\frac{4\Delta^2}{\Omega^2}\sin^2\left(\frac{\Omega\tau_1}{2}\right)\sin^2\left(\frac{\Omega\tau_2}{2}\right) - \sin(\Omega\tau_1)\sin(\Omega\tau_2)\right] \\ & + \frac{2\Omega_R^2\Delta}{\Omega^3}\sin(\Delta T_R + \phi_{lo})\left[\sin(\Omega\tau_1)\sin^2\left(\frac{\Omega\tau_2}{2}\right) + \sin(\Omega\tau_2)\sin^2\left(\frac{\Omega\tau_1}{2}\right)\right] \\ & + \frac{1}{\Omega^4}(\Omega_R^2\cos(\Omega\tau_1) + \Delta^2)(\Omega_R^2\cos(\Omega\tau_2) + \Delta^2) \end{aligned} \tag{1.32}$$

In the standard case of two $\frac{\pi}{2}$-pulses and close to resonance ($\Delta << \Omega_R$), equation (1.32) can be simplified a lot, and using equation (1.21) we retrieve the well known transition probability[9]

$$P_2(\Delta, T_R) = \frac{1}{2}(1 + \cos(\Delta T_R)). \tag{1.33}$$

[9]Note that no decoherence source has been taken into account yet.

Unlike the Rabi interrogation, the relevant time defining the width of the resonance line corresponds to the free evolution time T_R during which, in principle, no resonant field is sent to the atoms.

In both schemes, the precision of the frequency measurement will depend on the stability of the interrogation parameters (Rabi frequency and detuning) and the environment surrounding the atoms (spurious fields, temperature, pressure). The next section makes the link between the clock stability and these different noise sources.

1.3.3 Clock stability and accuracy

Even though the unperturbed atomic transition is an infinitely precise and stable reference, as soon as it is coupled to a noisy environment, its energy levels start to move degrading the accuracy and stability of the reference. The stabilized local oscillator frequency can be written

$$\nu_{LO} = \nu_{at}[1 + \epsilon + y(t)], \tag{1.34}$$

where ν_{at} is the unperturbed atomic frequency, ϵ represents the clock inaccuracy caused by systematic shifts (DC Zeeman or Stark shift, collisions, black body radiation, Doppler effect) and $y(t)$ represents the clock instability sources (fluctuations of the systematics, quantum projection noise, Dick effect). Concerning the accuracy, it is in principle always possible to characterize the environment inside which the clock is working. For instance, single ion clocks can now reach the low 10^{-18} systematic uncertainty limited by the residual motion of the ion and thermal radiation [135]. On the other hand, the stability of the clock can be affected by noise on both the transition probability P_2 and the detuning Δ that are usually modeled as white frequency noise leading to a clock stability after a running time τ

$$\sigma_y(\tau) = \frac{\sigma_{\nu_{at}}}{\nu_{at}}\sqrt{\frac{T_c}{\tau}} = \frac{1}{\nu_{at}}\sqrt{\sigma_\Delta^2 + \frac{\sigma_{P_2}^2}{|dP_2/d\Delta|^2}}\sqrt{\frac{T_c}{\tau}}, \tag{1.35}$$

where T_c is the cycle time. The scaling as $1/\nu_{at}$ explains why optical clocks experience a huge interest.

While work can be done reducing all the technical sources of instability, there is a fundamental limit called standard quantum limit[10] [145] that cannot be overcome by "classical" means. Its contribution to the clock stability reads

$$\sigma_{y,QPN}(\tau) = \frac{1}{2\sqrt{N}\nu_{at}|dP_2/d\Delta|}\sqrt{\frac{T_c}{\tau}}. \tag{1.36}$$

The presence of the slope of the spectroscopy line at the denominator shows the importance of using long interrogation times. Indeed, the narrower the line, the better the stability.

[10] This feature is discussed in more details in section 1.5.1.

1.3.4 Current status of TACC

As its name suggests, TACC was initially conceived to be a compact atomic clock. By design, it is a passive microwave clock that locks the signal generated by one SYRTE's hydrogen maser on a ^{87}Rb transition. The clock performances have been carefully analyzed for thermal atoms (80 nK) and the main instability sources have been identified [69]. As displayed on table 1.1, the clock presents a stability $\sigma_y(\tau) = 5.8 \times 10^{-13}\tau^{-1/2}$ and is mainly limited by atom temperature fluctuations. This leads to fluctuations of the atomic density and magnetic potential seen by the atoms, and thus fluctuations of the detuning via the Zeeman and collisional shifts. The next major instability source is due to magnetic field fluctuations that directly lead to frequency noise and might actually also be responsible for the temperature noise. The third source is due to the local oscillator noise that disturbs the frequency stability via the Dick effect [146]. Then comes the quantum projection noise.

Relative frequency stability (10^{-13})	shot-to-shot	At 1s
Measured, without correction	2.0	7.2
Measured, after N correction	**1.5**	**5.8**
Atom temperature	1.0	3.9
Magnetic field	0.7	2.6
Local oscillator	0.7	2.7
Quantum projection noise	0.4	1.5
N correction	0.4	1.5
Atom loss	0.3	0.3
Detection	0.3	1.1
Total estimate	**1.5**	**6.0**

Table 1.1: **TACC stability budget.** adapted from [69].

While the first two terms can probably be reduced together through a better control of the magnetic fields (more stable current sources and more stable coils position) and the third one by a reduction of dead times (more efficient cooling, longer interrogation time, non-destructive measurement), the fourth one is fundamental and cannot be reduced that "easily". The next generation of this experiment will be dedicated to this purpose using cavity quantum-electrodynamics [92].

On the other hand, this good stability compared to other similar compact clocks, shows that TACC is also a metrological platform suitable for the discovery and study of more general quantum phenomena. It for instance permitted the study of the spin self-rephasing mechanism [72] that enables very long coherent times and contrast revivals for thermal ensembles. Besides, the implementation of an atom interferometry scheme using Bose-Einstein condensates has also been investigated recently [147].

Keeping in mind this atom interferometry spirit, we propose here to use this device to experimentally study the generation of spin squeezing through non-linear collisional interactions in a spinor Bose-Einstein condensate [78], and hence contribute to the ongoing development of quantum metrology. Before going into the details of spin squeezing, let's first have a look at the theoretical description of degenerate quantum gases.

1.4 Bose-Einstein condensation

Predicted in 1925 [148] and first observed in 1995 [40, 41], Bose-Einstein condensates (BEC) have become the spearhead of the study of cold atoms and quantum physics [42, 123, 149, 150]. This unusual state of matter is often compared to lasers for their similar coherence properties. Indeed, it has been shown that they possess a well defined phase that can lead to spatial interferences [37]. This combined with their very high phase-space density makes BECs very interesting for atom interferometers, at first sight [19, 38, 49]. In addition, this wave-particle duality associated with the second-order coherence of condensed ensembles also led to the recent realization of the famous Hong-Ou-Mandel [151] experiment with metastable Helium [152], reinforcing the analogy between atomic physics and quantum optics. There is however one significant difference between photons and atoms: the inter-particle interactions, that greatly modifies their spatial dynamics and coherence properties. Indeed, even though condensed ensembles usually contain less atoms than thermal clouds, their much higher density leads to enhanced interactions. Even if the impact of these interactions can be troublesome: higher atom-losses, frequency noise due mean-field shifts and so on, they can also lead to very interesting and valuable physical phenomena such as vortices [153, 154], state-dependent spatial dynamics [80, 155] and number squeezing [60–62, 78]. These beneficial effects can in principle be combined to enhance the precision of atomic interferometers [55].

In this section is reviewed the theoretical description of degenerate quantum gases, from the ideal Bose gas formalism to the interacting BEC in a cigar-shaped trap. As the density of the condensate is involved in several physical phenomena (atom loss, collisional shift), its expression is derived in the regime realized by our experiment.

1.4.1 Ideal Bose gas

Quantum mechanically a particle such as an atom in a gas, can be seen as a wave characterized by its de Broglie wavelength:

$$\lambda_T = \sqrt{\frac{2\pi\hbar^2}{mk_BT}}, \tag{1.37}$$

where $\hbar$ and k_B are the Plank and Boltzman constant respectively, m is the particle mass and T the gas temperature. At high temperatures, the De Broglie wavelength is

much smaller than the mean inter-particle spacing $n^{-1/3}$, where n is the atomic density. The system is thus governed by Boltzman statistics and can be treated classically. As illustrated on figure 1.11, as the temperature decreases, the De Broglie wavelength increases until it becomes comparable to the distance between two particles. The "classical" non-condensed atoms then start to macroscopically populate the ground state of the system, increasing the probability for them to be in the same state (bosonic attraction). The system subsequently enters a degenerate regime and the atoms start to behave as a coherent matter-wave. For a uniform three dimensional gas, the condensation occurs when [150]

$$n\lambda_T^3 \geqslant \zeta(3/2) \approx 2.612, \tag{1.38}$$

where ζ is the Riemman zeta function. This transition corresponds to a critical temperature

$$T_c = \frac{2\pi\hbar^2}{mk_B}\left(\frac{n}{\zeta(3/2)}\right)^{2/3}. \tag{1.39}$$

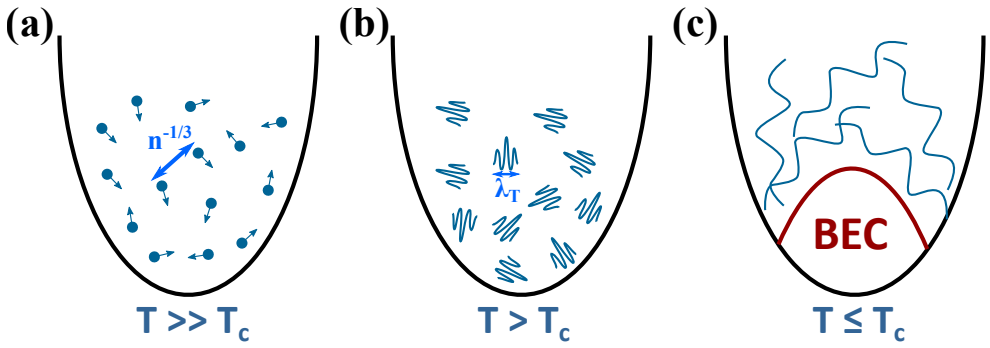

Figure 1.11: **Bose Einstein condensation.** (a) At high temperatures, the atoms behave classically. (b) When the temperature decreases, coherence properties of the atoms described by the de Broglie wavelength λ_T start to emerge. (c) When temperature becomes smaller than the critical temperature T_c defined in Eq. 1.39, the atoms enter the degenerate regime and a condensate forms in the ground state of the trap. While the temperature decreases, the condensate grows until all the atoms reach the ground state to form a pure BEC.

In the case of N non-interacting bosons trapped in a harmonic potential $V(\mathbf{r}) = \frac{m}{2}((\omega_x x)^2 + (\omega_y y)^2 + (\omega_z z)^2)$, the ground state of the system corresponds to having all the particles in the lowest single particle state [149]: $\Phi_0(\mathbf{r_1}, \mathbf{r_2}, ..., \mathbf{r_N}) = \prod_{i=1}^{N} \varphi_0(\mathbf{r_i})$ with the single particle wave function

$$\varphi_0(\mathbf{r}) = \left(\frac{m\overline{\omega}}{\pi\hbar}\right)^{(3/4)} \exp[-\frac{m}{2\hbar}(\omega_x x^2 + \omega_y y^2 + \omega_z z^2)], \tag{1.40}$$

where $\overline{\omega} = \sqrt[3]{\omega_x\omega_y\omega_z}$ is the mean trapping frequency. The density is simply $n_0(\mathbf{r}) = N|\varphi_0(\mathbf{r})|^2$ and the cloud size is only fixed by the harmonic oscillator length $a_{ho} = \sqrt{\frac{\hbar}{m\overline{\omega}}}$.

1.4.2 Gross-Pitaevskii equation

In the condensed regime, because of the high densities, inter-atomic interactions have to be taken into account in the description of the system. A spinless fluid of interacting bosons can be described by the many-body Hamiltonian [156]

$$H = \sum_i^N H_0(\mathbf{p}_i, \mathbf{r}_i) + \frac{1}{2}\sum_{i,j}^N H_{int}(\mathbf{r}_i - \mathbf{r}_j), \tag{1.41}$$

where $H_0(\mathbf{p}, \mathbf{r}) = -\frac{\hbar^2}{2m}\nabla^2 + V(\mathbf{r})$ is the free particle Hamiltonian, containing the kinetic energy and the trapping potential, and H_{int} represents the atomic interactions. There are several ways to model the atomic interactions but here we will limit ourselves to the usual contact potential corresponding to short range s-wave collisions [149],

$$H_{int}(\mathbf{r}_i - \mathbf{r}_j) = g\delta(\mathbf{r}_i - \mathbf{r}_j), \tag{1.42}$$

where $g = 4\pi\hbar^2 a_s/m$ is the interaction strength with the s-wave scattering length a_s. This potential is only valid in the case of many condensed atoms in a dilute gas where the s-wave scattering length is much smaller than the inter-particle distance. In order to find the ground state of the system, N Schrödinger equations have to be solved and this would require too much computational efforts. Instead we will use the fact that we are dealing with a quantum many-body system of identical particles to describe the ensemble with a mean field approach. To do so, we re-write the Hamiltonian using the second quantization formalism with the boson field operator $\hat{\Psi}(\mathbf{r}, t) = \sum_i \varphi_i(\mathbf{r}, t)\hat{a}_i$ where $\varphi_i(\mathbf{r}, t)$ is the single-particle wave function and $\hat{a}_i$ the corresponding annihilation operator for the mode i,

$$\begin{aligned}\hat{H} &= \int d\mathbf{r}\hat{\Psi}^\dagger(\mathbf{r}, t)H_0(\mathbf{p}, \mathbf{r})\hat{\Psi}(\mathbf{r}, t) + \frac{1}{2}\int\int d\mathbf{r}d\mathbf{r}'\hat{\Psi}^\dagger(\mathbf{r}, t)\hat{\Psi}^\dagger(\mathbf{r}', t)g\delta(\mathbf{r} - \mathbf{r}')\hat{\Psi}(\mathbf{r}', t)\hat{\Psi}(\mathbf{r}, t) \\ &= \int d\mathbf{r}\hat{\Psi}^\dagger(\mathbf{r}, t)H_0(\mathbf{p}, \mathbf{r})\hat{\Psi}(\mathbf{r}, t) + \frac{g}{2}\int d\mathbf{r}\hat{\Psi}^\dagger(\mathbf{r}, t)\hat{\Psi}^\dagger(\mathbf{r}, t)\hat{\Psi}(\mathbf{r}, t)\hat{\Psi}(\mathbf{r}, t).\end{aligned} \tag{1.43}$$

The time evolution of the field operator is given by the Heisenberg equation of motion:

$$i\hbar\frac{\partial\hat{\Psi}(\mathbf{r}, t)}{\partial t} = [\hat{\Psi}(\mathbf{r}, t), \hat{H}]. \tag{1.44}$$

That we can re-write using standard commutation relations

$$i\hbar\frac{\partial\hat{\Psi}(\mathbf{r},t)}{\partial t} = H_0(\mathbf{p},\mathbf{r})\hat{\Psi}(\mathbf{r},t) + g|\hat{\Psi}(\mathbf{r},t)|^2\hat{\Psi}(\mathbf{r},t). \tag{1.45}$$

Note that as it is, this equation still requires to treat each particle individually. Now let's use the fact that Bose-Einstein condensation occurs when a single-particle state, typically the ground state $\varphi_0(\mathbf{r},t)$, is macroscopically occupied. This means that $N_0 >> 1$, N_0 being the number of condensed atoms. In this case, $[\hat{a}_0, \hat{a}_0^\dagger] = \hat{a}_0\hat{a}_0^\dagger - \hat{a}_0^\dagger\hat{a}_0 = 1 \Rightarrow \hat{a}_0\hat{a}_0^\dagger = 1 + \hat{a}_0^\dagger\hat{a}_0 \approx N_0$. We can thus neglect the non-commutativity of the annihilation and creation operators and treat them as ordinary numbers: $\hat{a}_0 \equiv \hat{a}_0^\dagger \equiv \sqrt{N_0}$.

In 1947 Bogolioubov developed a theory for very low temperatures [157] in which the condensed and thermal parts of the field operator can be separated,

$$\hat{\Psi}(\mathbf{r},t) = \psi(\mathbf{r},t) + \delta\hat{\Psi}'(\mathbf{r},t). \tag{1.46}$$

$\psi(\mathbf{r},t)$ is a complex classical field (order parameter) which represents the condensed part of the total field operator $\Psi(\mathbf{r},t)$ and fixes the density of the condensate $n_c(\mathbf{r},t) = |\psi(\mathbf{r},t)|^2$. $\delta\hat{\Psi}'(\mathbf{r},t)$ is the field operator describing the remaining non-condensed particles whose density is then $n_{nc}(\mathbf{r},t) = \langle\Psi'^\dagger(\mathbf{r},t)\Psi'(\mathbf{r},t)\rangle$. It contains all the other weakly populated excited states and can in general be treated as a perturbation. The "mean-field" appellation lies in the fact that the total ensemble is now described as a macroscopic mean field $\psi(\mathbf{r},t) = \langle\hat{\Psi}(\mathbf{r},t)\rangle = \sqrt{N_0}\varphi(\mathbf{r},t)$ fluctuating as $\delta\hat{\Psi}'(\mathbf{r},t)$. We will moreover place ourselves in the limit of zero temperature, for which the population in the non-condensed modes is negligible. More details about the Bogoliubov theory can be found in [158]. Equation (1.45) then becomes the well known Gross-Pitaevskii equation

$$i\hbar\frac{\partial\psi(\mathbf{r},t)}{\partial t} = \left(-\frac{\hbar^2}{2m}\nabla^2 + V(\mathbf{r},t) + g|\psi(\mathbf{r},t)|^2\right)\psi(\mathbf{r},t). \tag{1.47}$$

This equation, derived by Gross [159] and Pitaevskii [160] in the late 1950's, describes the temporal and spatial evolution of the order parameter for an ensemble of quantum degenerate bosons. Here the macroscopic wave-function is normalized on the total number of atoms:

$$N = \int d\mathbf{r}|\psi(\mathbf{r},t)|^2. \tag{1.48}$$

From now on we will only consider a pure condensate, such that N is the total atom number (≡number of condensed atoms), $\varphi(\mathbf{r},t)$ is the single atom wave-function of the ground state and $\psi(\mathbf{r},t)$ is the macroscopic complex wave-function of the Bose-Einstein condensate under the mean field approach. The stationary solution of equation (1.47) gives the ground state of the system, and the substitution

$$\psi(\mathbf{r},t) = \psi(\mathbf{r})e^{-i\mu t/\hbar}, \tag{1.49}$$

allows us to derive the time-independent Gross-Pitaevskii equation

$$\left(-\frac{\hbar^2}{2m}\nabla^2 + V(\mathbf{r}) + gn(\mathbf{r})\right)\psi(\mathbf{r}) = \mu\psi(\mathbf{r}), \tag{1.50}$$

where μ is the chemical potential of the system which corresponds to the energy required to remove a particle from the atomic ensemble. The general solution of equation (1.50) can then be found by minimizing the energy functional [149]

$$E[\psi] = \int d\mathbf{r}\left[\frac{\hbar^2}{2m}|\nabla\psi(\mathbf{r})|^2 + V(\mathbf{r})|\psi(\mathbf{r})|^2 + \frac{g}{2}|\psi(\mathbf{r})|^4\right]. \tag{1.51}$$

This can be easily done by numerical integration [161]. Unfortunately, there is no general analytical expression for the wave function, however approximations can be made depending on the strength of the interactions and the geometry of the trapping potential.

1.4.3 Dimensional crossover regime for a cigar-shaped trap

The ground-state properties of a trapped BEC highly depends on the shape of the trapping potential. I will therefore focus on cigar-shaped traps which are used in our experiment. More complete studies with other trapping geometries and the inclusion of vortices can be found in [149, 150, 162–165]. In the case of elongated potentials of transverse and longitudinal angular frequencies $\omega_\perp = \sqrt{\omega_y\omega_z}$ and ω_x, the relevant parameter determining the ground state properties is defined by the ratio between the interaction energy and the kinetic energy:

$$\kappa = \frac{Na_\perp a_s}{a_x^2} = \frac{N\lambda a_s}{a_\perp}, \tag{1.52}$$

where $\lambda = \omega_x/\omega_\perp$ is the trap aspect-ratio and $a_\perp = \sqrt{\frac{\hbar}{m\omega_\perp}}$ and $a_x = \sqrt{\frac{\hbar}{m\omega_x}}$ are the transverse and longitudinal harmonic oscillator lengths. Besides, if $\omega_\perp >> \omega_x$ as it is often the case in cigar-shaped traps, then the evolution time of the transverse motion is so much faster than the one of the longitudinal motion that the two directions can be decoupled and the condensate wave-function factorized $\psi(\mathbf{r}) = \phi_\perp(r_\perp)\phi_\parallel(x)$ in cylindrical coordinates. This way, equation (1.50) becomes

$$\begin{aligned}&\left(-\frac{\hbar^2}{2m}\nabla_\perp^2\phi_\perp(r_\perp) + \frac{1}{2}m\omega_\perp^2 r_\perp^2\phi_\perp(r_\perp) + g|\phi_\parallel(x)|^2|\phi_\perp(r_\perp)|^2\phi_\perp(r_\perp) - \mu\phi_\perp(r_\perp)\right)\phi_\parallel(x)\\ &= \left(\frac{\hbar^2}{2m}\nabla_x^2\phi_\parallel(x) - \frac{1}{2}m\omega_x^2x^2\phi_\parallel(x)\right)\phi_\perp(r_\perp).\end{aligned} \tag{1.53}$$

Multiplying by $\phi^*(r_\perp)$ and integrating over $r_\perp$ lead to

$$\mu\phi_\parallel(x) = -\frac{\hbar^2}{2m}\nabla_x^2\phi_\parallel(x) + \frac{1}{2}m\omega_x^2x^2\phi_\parallel(x) + \mu_\perp(n_x)\phi_\parallel(x), \tag{1.54}$$

with $n_x = |\phi_\parallel(x)|^2$ and

$$\mu_\perp(n_x) = \int 2\pi r_\perp \phi^*(r_\perp) \left(-\frac{\hbar^2}{2m}\nabla_\perp^2 + \frac{1}{2}m\omega_\perp^2 r_\perp^2 + g n_x |\phi_\perp(r_\perp)|^2 \right) \phi_\perp(r_\perp) dr_\perp. \tag{1.55}$$

Finally re-injecting into equation (1.53) yields

$$-\frac{\hbar^2}{2m}\nabla_\perp^2\phi_\perp(r_\perp) + \frac{1}{2}m\omega_\perp^2 r_\perp^2\phi_\perp(r_\perp) + g n_x|\phi_\perp(r_\perp)|^2\phi_\perp(r_\perp) = \mu_\perp(n_x)\phi_\perp(r_\perp). \tag{1.56}$$

Through this equation, the system is treated as an axially homogeneous condensate with density per unit length $n_x(x) = |\phi_\parallel(x)|^2$ and local equilibrium chemical potential $\mu_\perp(n_x)$. Furthermore, it has been heuristically shown that this local equilibrium chemical potential reads [163]

$$\mu_\perp(n_x) = \hbar\omega_\perp\sqrt{1 + 4a_s n_x(x)}, \tag{1.57}$$

This local equilibrium chemical potential is linked to the total chemical potential (constant) via

$$\mu = \mu_\perp(n_x) + V(x) = \hbar\omega_\perp + V(L), \tag{1.58}$$

where L is defined as the half length of the condensate along the x direction such that $n(L) = n(-L) = 0$. Extracting n_x from equation (1.58) leads to

$$n_x(x) = \frac{1}{4a_s\hbar\omega_\perp}\left(V(L) - V(x)\right)\left(\frac{V(L) - V(x)}{\hbar\omega_\perp} + 2\right), \tag{1.59}$$

where $V(x) = \frac{1}{2}m\omega_x^2 x^2$ but L is unknown so far. In order to estimate it, a parameter $\alpha = 2\left(\frac{\mu}{\hbar\omega_\perp} - 1\right)$ is introduced such that

$$L = \sqrt{\frac{\hbar\omega_\perp\alpha}{m\omega_x^2}} = \frac{a_x^2}{a_\perp}\sqrt{\alpha}. \tag{1.60}$$

Injecting the parametrized half length, we end up with

$$n_x(x) = \frac{\alpha}{16a_s}\left[1 - \left(\frac{x}{L(\alpha)}\right)^2\right]\left\{\alpha\left[1 - \left(\frac{x}{L(\alpha)}\right)^2\right] + 4\right\}. \tag{1.61}$$

Now the only unknown parameter is α which can be found using the definition of the total atom number $N = \int_{-L}^{L} n_x(x)dx$. After some trivial calculations we end up with this simple equation

$$\alpha^3(\alpha + 5)^2 = (15\kappa)^2, \tag{1.62}$$

that can be easily solved numerically.

Concerning the wave-function in the transverse direction, following [166], we choose $\phi_\perp(r_\perp) = \frac{1}{\sqrt{\pi}w_\perp}\exp(-r_\perp^2/2w_\perp^2)$, where the Gaussian width $w_\perp(n_x)$ is taken as a variational parameter satisfying equation (1.56). After some arithmetic and using the expression (1.57), we end up with the width

$$w_\perp(n_x) = a_\perp(1 + 4a_s n_x(x))^{1/4}. \tag{1.63}$$

This Gaussian transverse wave-function does not describe the real state, but allows to get a simple analytical expression which produces results very close to the exact ones, as as testifies the comparison with the full numerical resolution of the 3-D Gross Pitaevski equation displayed on figure 1.13 (b).

Once we have found α, equations (1.63) and (1.60) give us the condensate width and half length. Then the whole condensate volume can be derived using cylindrical coordinates

$$\mathcal{V} = \int_{-L}^{L}\int_0^{\sqrt{2}w_\perp(n_x)}\int_0^{2\pi} r dr d\theta dx = 2\pi\int_{-L}^{L} w_\perp^2(n_x)dx. \tag{1.64}$$

And finally the mean density reads

$$< n >= \frac{N}{\mathcal{V}} \tag{1.65}$$

No approximation concerning κ has been made so far. In order the check the validity of this general model, let's compare it with the two extreme limits: the mean field 1D and the Thomas-Fermi regimes.

Mean field quasi 1D regime If $\kappa << 1$, then interactions can be treated as a perturbation and the radial ground-state is determined by the harmonic oscillator. That is considering the transverse dynamics frozen and only investigating the low frequency motions. That way equation (1.50) becomes [167]

$$\hbar\omega_\perp + \frac{1}{2}\hbar\omega_x^2 x^2 + g_{1D}N|\phi_\parallel(x)|^2 = \mu, \tag{1.66}$$

with $g_{1D} = \frac{g}{2\pi a_\perp^2}$. This corresponds to fixing the radial density per unit area to its mean value $N/2\pi a_\perp^2$ and studying the evolution of the longitudinal density per unit length $|\phi_\parallel(x)|^2$. This leads to [161]

$$\mu_{1D} = \hbar\omega_\perp\left(1 + \frac{(3\kappa)^{\frac{2}{3}}}{2}\right) \text{ and } \langle n_{1D}\rangle \approx \frac{N\sqrt{\lambda}}{4\pi a_{ho}^3(3\kappa)^{1/3}}. \tag{1.67}$$

Under this regime, equation (4.30) becomes $\alpha \approx (3\kappa)^{2/3}$ which leads to the cloud dimensions ((1.60) and (1.63))

$$L^{1D} \approx \frac{a_x}{\sqrt{\lambda}}(3\kappa)^{1/3} \text{ and } w_\perp^{1D} \approx a_\perp. \tag{1.68}$$

Injecting it into equations (1.58) and (1.64) gives the same chemical potential and mean density as expressed in (1.67).

Thomas-Fermi regime If $\kappa >> 1$ then the system if governed by large density and repulsive forces (positive scattering lengths) and it is considered as "strongly"[11] interacting:

$$\frac{E_{int}}{E_{kin}} \propto N\frac{a_s}{a_{ho}} >> 1. \tag{1.69}$$

In this case, the kinetic energy term in equation (1.50) can be neglected and the ground state of the system is only determined by the external and chemical potentials [162]:

$$n_{TF}(\mathbf{r}) = \begin{cases} \frac{\mu_{TF}-V(\mathbf{r})}{g} \text{ if } \mu > V(\mathbf{r}) \\ 0 \text{ otherwise} \end{cases} \tag{1.70}$$

The wave-function has therefore the form of an inverted parabola which is a convenient way of differentiating between condensed and non-condensed samples. Using the normalization condition (1.48) with the integration volume defined by (1.70), one finds the well known Thomas-Fermi chemical potential and cloud dimensions along the radial and longitudinal directions

$$\mu_{TF} = \frac{\hbar\omega_\perp}{2}(15\kappa)^{2/5} \ , \ R_{TF} = \sqrt{\frac{2\mu_{TF}}{m\omega_\perp^2}} \text{ and } L_{TF} = \sqrt{\frac{2\mu_{TF}}{m\omega_x^2}}. \tag{1.71}$$

Finally, using the geometric volume defined by equation (1.70), one derives the averaged volume occupied by the atoms, as well as the averaged density

$$\mathcal{V}_{TF} = \frac{4\pi}{3}\frac{a_{ho}^3}{\sqrt{\lambda}}\left(\frac{2\mu_{TF}}{\hbar\omega_\perp}\right)^{3/2} \text{ and } \langle n_{TF}\rangle = \frac{3N\sqrt{\lambda}}{4\pi a_{ho}^3(15\kappa)^{3/5}}. \tag{1.72}$$

On the other hand, under this regime, equation (4.30) becomes $\alpha \approx (15\kappa)^{1/5}$ which leads to the cloud dimensions ((1.60) and (1.63))

$$L^{TF} \approx \frac{a_x}{\sqrt{\lambda}}(15\kappa)^{1/5} \text{ and } w_\perp^{TF}(x) \approx \frac{a_\perp(15\kappa)^{1/5}}{\sqrt{2}}\sqrt{1-\left(\frac{x}{L}\right)^2}. \tag{1.73}$$

Injecting it into equations (1.58) and (1.64) gives the same chemical potential and mean density as expressed in (1.72).

Figure 1.12 compares the evolution of the effective radius[12], half axial length, the chemical potential and the averaged density as a function of the parameter κ for the cross-over model, the 1D regime and the Thomas-Fermi approximation. The model is in good agreement with the two usual extreme cases. Experimentally, our BEC usually contains between 500 and $15{\cdot}10^3$ atoms meaning that $\kappa \in [7\cdot10^{-2}, 2]$ with $\{\omega_x, \omega_\perp\} \approx 2\pi\{2.9, 83\}$ Hz. We thus are exactly in the intermediate region represented by the reddish area on figure 1.12 justifying the development of such a cross-over theory.

[11] The relation $a_s \ll n^{-1/3}$ justifying the elastic binary collision to model atomic interactions is still valid though.

[12] Here we compare the Gaussian width of the cross-over and 1D regime with the Thomas-Fermi radius $R^{TF}/\sqrt{2}$.

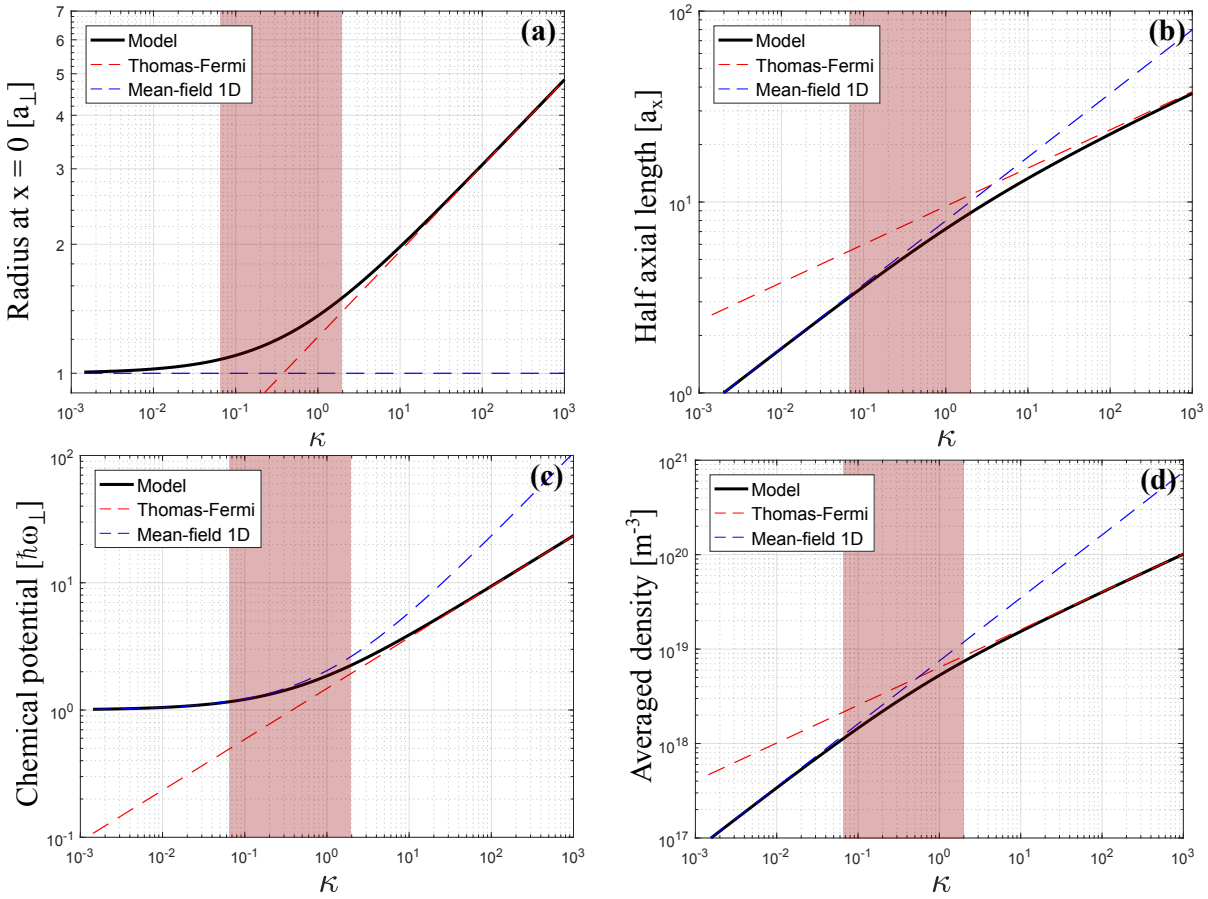

Figure 1.12: **Comparison of the model.** The central radius **(a)**, half axial length **(b)**, chemical potential **(c)** and averaged density **(d)** are plotted as a function of κ using the cross-over model detailed in the text (black line), the Thomas-Fermi approximation (red dashed line) and the mean field 1D approximation (blue dashed line). The reddish area represents the range achieved in the experiment. For the radii, we compare the Gaussian width of the cross-over and 1D regime with the Thomas-Fermi radius $R^{TF}/\sqrt{2}$.

Figure 1.13 shows the radial and longitudinal density profiles derived with the cross-over model and with the mean-field 1D and Thomas-Fermi approximations in the intermediate regime ($\kappa \approx 0.7$). The derived model is in relatively good agreement with the three dimensional numerical resolution of the Gross-Pitaevskii equations[13] (1.50) (black dots).

The precise estimation of the atomic density is of primary importance since it is involved in several physical processes that we will get to encounter in what follows (atoms lifetime and collisional shift).

[13]This numerical simulation is detailed in section 4.1.1.

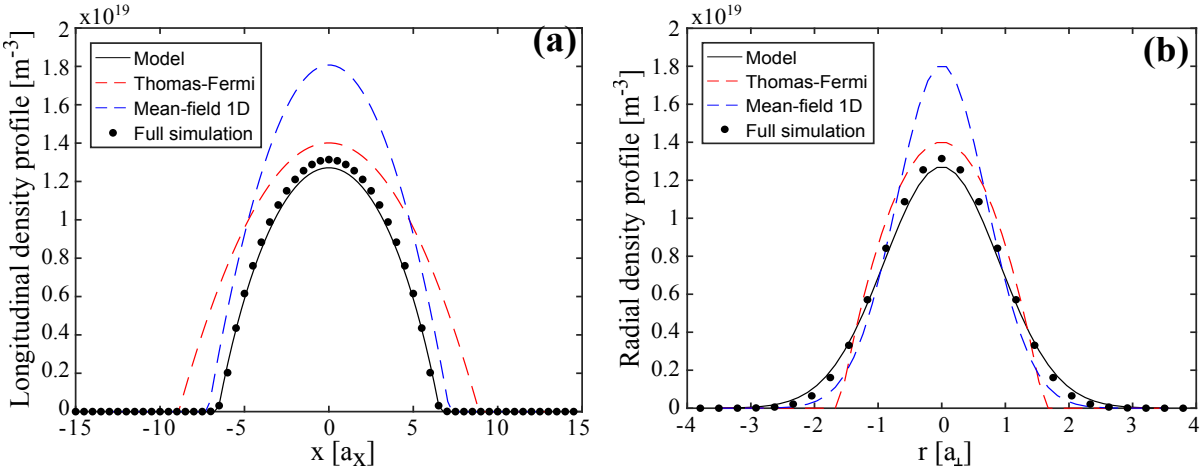

Figure 1.13: **Calculated density profiles.** Longitudinal **(a)** and radial **(b)** density profiles derived by the cross-over (black line), the mean-field 1D (blue dashed line) and Thomas-Fermi (red dashed line) model, for $\kappa \approx 0.7$. The black dots correspond to a full three dimensional numerical resolution of equation (1.50).

1.4.4 Theoretical description of a two-component BEC

Getting closer to the experimental situation, let's now introduce an internal degree of freedom and derive the evolution of a two-component BEC. Following the method used to derive equation (1.47) in the case of a bimodal BEC, one can derive the set of coupled Gross-Pitaevskii equations for the macroscopic wave functions of the two sates $\psi_{1,2}$ with additional interaction terms [150]

$$\begin{aligned} i\hbar\frac{\partial\psi_1(\mathbf{r},t)}{\partial t} &= \left[-\frac{\hbar^2}{2m}\nabla^2 + V_1(\mathbf{r},t) + g_{11}|\psi_1(\mathbf{r},t)|^2 + g_{12}|\psi_2(\mathbf{r},t)|^2\right]\psi_1(\mathbf{r},t) \\ i\hbar\frac{\partial\psi_2(\mathbf{r},t)}{\partial t} &= \left[-\frac{\hbar^2}{2m}\nabla^2 + V_2(\mathbf{r},t) + g_{22}|\psi_2(\mathbf{r},t)|^2 + g_{12}|\psi_1(\mathbf{r},t)|^2\right]\psi_2(\mathbf{r},t), \end{aligned} \tag{1.74}$$

where the interaction strength between states $|i\rangle$ and $|j\rangle$ reads $g_{ij} = \frac{4\pi\hbar^2}{m}a_{ij}$. This set of equations is the starting point of the study of various physical phenomena such as dark-bright solitons, Josephson-like oscillations, quantum state engineering [168–170] to name a few, and the state-dependent spatial dynamics will be the one of interest here.

In the case of a homogeneous gas, it can be shown that the stability of the system is subject to the following conditions [123]

$$g_{11} > 0,\ g_{22} > 0,\ \text{and}\ g_{11}g_{22} > g_{12}^2. \tag{1.75}$$

If all the above conditions are fulfilled, then any disturbance in the atomic densities will increase the energy of the system. On the other hand, if the the third condition is not

fulfilled and $g_{12} > 0$, then the ground state of the system corresponds to having the two modes spatially separated [171]. This means that if an initially pure BEC is prepared in a coherent superposition, the two components will spatially separate. Because the initial state is not stationary, the wave-function spatial overlap between the two states will oscillate at a frequency that depends on the trapping geometry and the mean-field interaction [83]. In the experimental case of a harmonically trapped spinor BEC, no analytical treatment is available so far. Several theoretical studies are nonetheless available to predict the spatial dynamics and the inhomogeneous phase evolution of the two states [172–175].

As we will see in the next section, this spatial dynamics is of particular interest as it strongly enhances a non-linear collisional interaction between the two modes of the BEC, that can eventually lead to spin squeezing and many-particle entanglement.

1.5 Spin squeezing for metrology

Once all the technical instabilities have been reduced, the precision of atomic clocks and interferometers reaches a level limited by the probabilistic nature of quantum systems, called standard quantum limit [51,145]. The most efficient way to overcome this threshold is to induce quantum correlations in the system via non-linear interactions [52], and spin-squeezed states are one specific kind of entangled states [176, 177] that can be relevant for metrological applications. The non-linearity can be produced by many different mechanisms [77], and here we will focus on spin squeezing arising from collisions in a spinor BEC [60, 61, 78, 178]. The metrological relevance of such states has already been demonstrated in an atomic clock [57] and field sensors [13, 79].

This section is therefore dedicated to the study of the spin noise distribution of an atomic ensemble in a coherent superposition, from the usual standard quantum limit to spin squeezing. The transition from one to the other will be then described in the framework of the one-axis-twisting scheme [76]. The temporal evolution of the atomic state will be briefly tackled as well as the physical mechanisms behind the elastic interaction mediated spin squeezing [78], ensued from the previously approached state-dependent spatial dynamics.

1.5.1 Standard quantum limit

After a resonant interaction pulse, the atomic state containing initially N atoms in $|1\rangle$ is converted into a so-called coherent spin state (CSS) [179]

$$|\psi\rangle_{CSS} = (c_1|1\rangle + c_2|2\rangle)^{\otimes N}\,, \tag{1.76}$$

where $|c_1|^2+|c_2|^2 = 1$ and $c_{1,2} \in [0;1]$. In the case of a resonant $\frac{\pi}{2}$-pulse, the measurement of such a state is subject to quantum projection noise [145], which is a fundamental

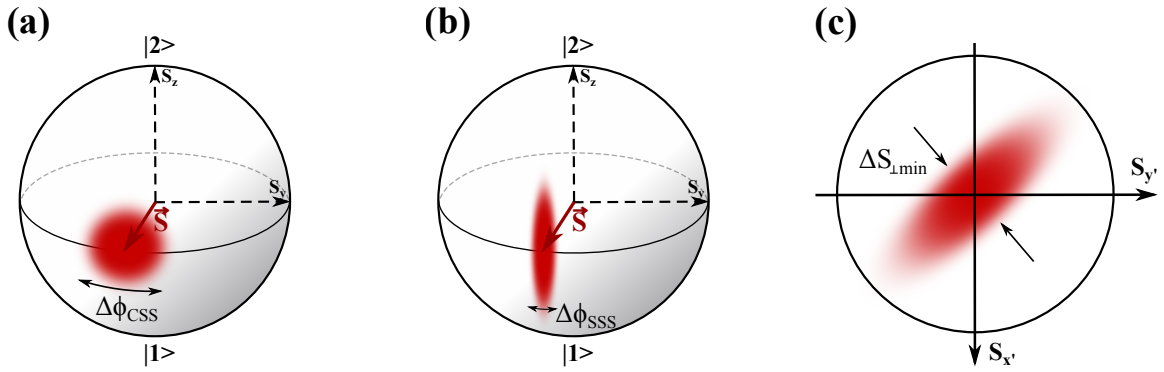

Figure 1.14: **Spin noise distribution** for a coherent spin state (CSS) **(a)** and a spin squeezed state (SSS) **(b)**. The resulting uncertainty on the phase measurement $\Delta\phi$ is indicated in both cases.

noise stemming from the probabilistic nature of quantum systems. Indeed, during the detection process, as each atom in the CSS is projected onto one of the two clock states, the outcome is subject to a statistical uncertainty, similarly to what happens in a coin-tossing game. More quantitatively, the fluctuation of the population difference $\langle S_z \rangle = 0$ follows a binomial distribution $\langle \Delta S_z^2 \rangle = \langle \Delta S_y^2 \rangle = \langle \Delta S_\perp^2 \rangle = \frac{N}{4}$. This defines the standard quantum limit as the highest precision with which the atomic phase can be measured: $\langle \Delta \phi_{CSS}^2 \rangle = \frac{\langle \Delta S_{\perp,CSS}^2 \rangle}{|\langle \mathbf{S} \rangle|^2} = \frac{1}{N}$. Note that these fluctuations must satisfy the Heisenberg uncertainty relation

$$\langle \Delta S_z^2 \rangle \langle \Delta S_y^2 \rangle \geq \frac{\langle S_x \rangle^2}{4}. \tag{1.77}$$

In the case of an arbitrary population imbalance, the z-component of the spin vector and the corresponding variance read

$$S_z = N \frac{|c_2|^2 - |c_1|^2}{2} \text{ and } \langle \Delta S_\perp^2 \rangle = N |c_2|^2 (1 - |c_2|^2). \tag{1.78}$$

The resulting phase sensitivity is therefore maximum for equal populations in the two states ($S_z = 0$) justifying the working point of atomic clocks and interferometers as stated in section 1.3. As illustrated on figure 1.14 (a), this noise can be represented on the Bloch sphere by considering that each individual spin is uniformly distributed around the mean collective spin.

1.5.2 Spin squeezing

Because of the Heisenberg uncertainty relation, the spin noise distribution of the two quadratures cannot be arbitrarily reduced while keeping the spin length constant. The idea behind spin squeezing is thus to redistribute the noise between the two quadratures. That way, as depicted on figure 1.14 (b), the fluctuations will be reduced along the phase

direction and increased along the orthogonal one. This noise reduction can be quantified with the normalized number difference variance defined as the ratio between the reduced population variance with respect to the quantum projection noise [76]

$$\begin{aligned}\mathcal{V}(S_z) &= \frac{\langle \Delta S^2_{\perp,min}\rangle}{\Delta S^2_{\perp,CSS}} \\ &= \frac{4\langle \Delta S^2_{\perp}\rangle}{N} \text{ for } \langle S_z\rangle = 0.\end{aligned} \tag{1.79}$$

Realizing $\mathcal{V}(S_z) < 1$ is referred to as number squeezing, meaning that the population difference is measured with an enhanced precision. This parameter is nonetheless not well suited for metrological applications such as atomic clocks and atom interferometry, in the sense that it does not take into account the coherence of the system. This the reason why another quantity, the squeezing parameter introduced by D. Wineland in 1992 [180], is often preferred

$$\begin{aligned}\xi^2 &= \frac{\Delta\phi^2}{\Delta\phi^2_{CSS}} \\ &= \frac{\langle \Delta S^2_{\perp,min}\rangle}{|\langle \mathbf{S}\rangle|^2}\frac{|\langle \mathbf{S}_{CSS}\rangle|^2}{\langle \Delta S^2_{\perp,CSS}\rangle} \\ &= 4\frac{\langle \Delta S^2_{\perp,min}\rangle}{C^2 N} \text{ for } \langle S_z\rangle = 0,\end{aligned} \tag{1.80}$$

where C is the contrast of the interrogation scheme. Using this notation, a coherent spin state at the standard quantum limit corresponds to $\xi^2 = 1$, while a metrologically useful spin squeezed state presents $\xi^2 < 1$.

It is moreover possible to theoretically estimate this reduced variance. Indeed, a geometrical reasoning done in [181] gives

$$\langle \Delta \hat{S}^2_{\perp,min}\rangle = \frac{1}{2}\langle(\Delta \hat{S}^2_{x'} + \Delta \hat{S}^2_{y'} - |\Delta \hat{S}^2_{-}|)\rangle, \tag{1.81}$$

with $\hat{S}_- = \hat{S}_{x'} - i\hat{S}_{y'}$ and the x'-y' plane corresponds to the plane orthogonal to the mean spin direction, as illustrated on figure 1.14 (c). The spin operators are expressed as a function of the field operators as

$$\begin{cases} \hat{S}_x = \frac{1}{2}\int d\mathbf{r}[\hat{\Psi}^\dagger_2(\mathbf{r})\hat{\Psi}^\dagger_1(\mathbf{r}) + \hat{\Psi}^\dagger_1(\mathbf{r})\hat{\Psi}^\dagger_2(\mathbf{r})] \\ \hat{S}_y = \frac{i}{2}\int d\mathbf{r}[\hat{\Psi}^\dagger_2(\mathbf{r})\hat{\Psi}^\dagger_1(\mathbf{r}) - \hat{\Psi}^\dagger_1(\mathbf{r})\hat{\Psi}^\dagger_2(\mathbf{r})] \\ \hat{S}_z = \frac{1}{2}\int d\mathbf{r}[\hat{\Psi}^\dagger_2(\mathbf{r})\hat{\Psi}^\dagger_2(\mathbf{r}) - \hat{\Psi}^\dagger_1(\mathbf{r})\hat{\Psi}^\dagger_1(\mathbf{r})]. \end{cases} \tag{1.82}$$

The derivation of equation (1.81) lies on the possibility to estimate the dynamical evolution of the field operators which is far from being a simple task and the next section is dedicated to this purpose in the case of the one-axis-twisting scheme [76].

1.5.3 One-axis-twisting Hamiltonian in a spinor BEC

There are many ways of achieving spin squeezing [77] and we will focus here on the one-axis-twisting scheme realized via elastic collisional interactions in a bimodal BEC as initially proposed in 2001 [78]. This particular way of generating spin squeezing has already been heavily studied theoretically [78, 84, 178, 182–185] and only three times experimentally[14] [60, 61, 186] for the last two decades. Here, we will simply recall a few results facilitating the understanding of our experimental study presented in chapter 5. The idea is to experimentally realize the famous non-linear one-axis-twisting Hamiltonian

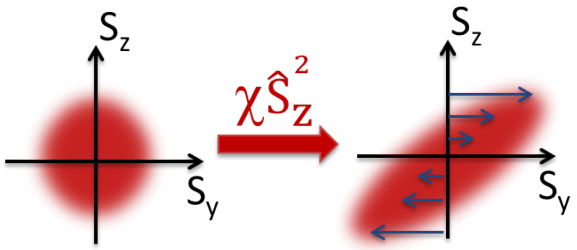

Figure 1.15: **Effect of the one axis twisting Hamiltonian.** Starting with a CSS, the one-axis-twisting Hamiltonian induces a rotation of the spins with a velocity proportional to S_z, resulting in a shearing of the spin noise distribution.

[76]

$$\hat{H} = \hbar\chi \hat{S}_z^2. \tag{1.83}$$

Intuitively, the effect of such Hamiltonian can be interpreted as follows. As the $\hat{S}_z$ operator induces a rotation of the spins around the z-axis of the Bloch sphere, the $\hat{S}_z^2$ operator will induce a rotation of the spins around the z-axis with an angular velocity proportional to S_z. As a result, in the laboratory reference frame, states with $S_z > 0$ ($S_z < 0$) will rotate faster (slower) than states on the equator. As illustrated on figure 1.15, in the reference frame of the Bloch vector located along the x-axis, this results in the expected elliptic spin noise distribution. The small axis is then smaller than the initial radius given by the quantum projection noise.

Let's first start by assuming that a strong $\frac{\pi}{2}$-pulse has quickly transferred N atoms intially in $|1\rangle$ into a coherent superposition between $|1\rangle$ and $|2\rangle$. The generalization of the Hamiltonian (1.43) to the case of a bimodal BEC leads to [181]

$$\hat{H} = \sum_{j\in[1,2]} \int d\mathbf{r} \hat{\Psi}_j{}^\dagger(\mathbf{r},t) H_0(\mathbf{p},\mathbf{r}) \hat{\Psi}_j(\mathbf{r},t) + \sum_{(i,j)\in[1,2]} \frac{g_{ij}}{2} \int d\mathbf{r} \hat{\Psi}_i{}^\dagger(\mathbf{r},t) \hat{\Psi}_j{}^\dagger(\mathbf{r},t) \hat{\Psi}_j(\mathbf{r},t) \hat{\Psi}_i(\mathbf{r},t). \tag{1.84}$$

[14] Only the first two references were successful.

As in section 1.4.2, we will use a mean field approach to describe the system. This way, $\hat{\Psi}_j(\mathbf{r},t) \approx \varphi_j(\mathbf{r},t)\hat{a}_j$ where $\hat{a}_j$ is the annihilation operator for state $|j\rangle$ and $\varphi_j(\mathbf{r})$ is the corresponding normalized single particle wave-function. Equation (1.84) hence becomes

$$\begin{aligned}\hat{H} &= \hat{\mathcal{H}}_0 + \hat{H}_{int} \\ &= \int d\mathbf{r}\varphi_1^*(\mathbf{r},t)H_0(\mathbf{p},\mathbf{r})\varphi_1(\mathbf{r},t)\hat{a}_1^\dagger\hat{a}_1 + \int d\mathbf{r}\varphi_2^*(\mathbf{r},t)H_0(\mathbf{p},\mathbf{r})\varphi_2(\mathbf{r},t)\hat{a}_2^\dagger\hat{a}_2 \\ &+ \frac{U_{11}}{2}\hat{a}_1^\dagger\hat{a}_1^\dagger\hat{a}_1\hat{a}_1 + \frac{U_{22}}{2}\hat{a}_2^\dagger\hat{a}_2^\dagger\hat{a}_2\hat{a}_2 + U_{12}\hat{a}_1^\dagger\hat{a}_2^\dagger\hat{a}_2\hat{a}_1,\end{aligned} \tag{1.85}$$

where $U_{ij}(t) = g_{ij}\int d\mathbf{r}|\varphi_i(\mathbf{r},t)|^2|\varphi_j(\mathbf{r},t)|^2$ and $\hat{\mathcal{H}}_0$ represents the kinetic energy and trapping potential of the non-interacting two-component BEC. Then using the commutation relations of the creation and annihilation operators and the change of variables $\hat{N} = \hat{a_1}^\dagger\hat{a_1} + \hat{a_2}^\dagger\hat{a_2}$ and $S_z = \frac{1}{2}(\hat{a_2}^\dagger\hat{a_2} - \hat{a_1}^\dagger\hat{a_1})$ the interaction Hamiltonian becomes

$$\begin{aligned}\hat{H}_{int} = &\frac{1}{4}(U_{11}(t) + U_{22}(t))\hat{N} + \frac{1}{8}(U_{11}(t) + U_{22}(t) + 2U_{12}(t))\hat{N}^2 \\ &+ \frac{1}{2}(U_{22}(t) - U_{11}(t))(\hat{N}-1)\hat{S}_z + \frac{1}{2}(U_{11}(t) + U_{22}(t) - 2U_{12}(t))\hat{S_z}^2.\end{aligned} \tag{1.86}$$

The first two terms proportional to $\hat{N}$ and $\hat{N}^2$, only correspond to atom-number-dependent energy shifts, identical for the two states. They will therefore translate into different overall phases for states with different total atom numbers. As there is no phase reference in the system to which these phase-shifts can be compared to, they can safely be neglected here. The third term proportional to $\hat{S}_z$ represents a rotation of the spins around the z-axis and with an angular velocity linear in N. It will therefore convert total atom number fluctuations into phase noise. The last term, proportional to $\hat{S_z}^2$ is non linear and corresponds to the one we were looking for. Note that these last two terms (proportional to $\hat{S}_z$) actually describe a frequency shift, called collisional shift, arising from elastic collisions between atoms in a coherent superposition [112, 129].

By identification with equation (1.83), we get

$$\begin{aligned}\chi &= \frac{1}{2\hbar}(U_{11}(t) + U_{22}(t) - 2U_{12}(t)) \\ &= \frac{1}{2\hbar}\int d\mathbf{r}\left(g_{11}|\varphi_1(\mathbf{r},t)|^4 + g_{22}|\varphi_2(\mathbf{r},t)|^4 - 2g_{12}|\varphi_1(\mathbf{r},t)|^2|\varphi_2(\mathbf{r},t)|^2\right).\end{aligned} \tag{1.87}$$

As the s-wave scattering length of ^{87}Rb are very close to each other ([a_{11}, a_{12}, a_{22}] $\approx$ [1.025, 1, 0.974] a_{12} [124]), if the two modes are spatially overlapping then $\varphi_1 = \varphi_2$ and $\chi \approx 0$. As the squeezing time-scale is inversely proportional χ, this means that the interaction time required to get a squeeze state is a priori very long compared to the coherence time and lifetimes of the system. This is where the state-dependent spatial dynamics tackled in section 1.4.4 becomes interesting. Indeed, right after the initial $\frac{\pi}{2}$-pulse the two modes of the condensate will start to separate, leading to a decrease of

the cross term U_{12} and a subsequent increase of the coefficient χ. Indeed, it was shown in [61, 84] that reducing the wave function spatial overlap of the two BEC components increases χ by several orders of magnitude.

In order to get the temporal evolution of the initial[15] atomic state, let's first expand it in the Fock state basis [174]

$$\begin{aligned} |\Psi(t=0)\rangle &= [c_1|1,\phi_0\rangle + c_2|2,\phi_0\rangle]^N \\ &= \sum_{N_1=0}^{N} \left(\frac{N!}{N_1!N_2!}\right)^{1/2} c_1^{N_1} c_2^{N_2} |N_1:\phi_0, N_2:\phi_0\rangle, \end{aligned} \tag{1.88}$$

where

$$|N_1:\phi_1, N_2:\phi_2\rangle = \frac{[a^\dagger_{1,|\phi_1\rangle}]^{N_1}}{\sqrt{N_1!}} \frac{[a^\dagger_{2,|\phi_2\rangle}]^{N_2}}{\sqrt{N_2!}} |0\rangle. \tag{1.89}$$

Then the temporal evolution of each Fock state simply reads [181]

$$|N_1:\phi_0, N_2:\phi_0\rangle \to e^{i\int H_{int}(t)dt/\hbar} |N_1:\phi_1(N_1,N_2;t), N_2:\phi_2(N_1,N_2;t)\rangle, \tag{1.90}$$

where $H_{int}(t)$ is given by equation (1.86) for which the operators have been replaced by their expectation values under the mean field approximation for large atom numbers. The temporal evolution of the single particle wave-function is given by the set of coupled Gross-Pitaevskii equations (1.74) with $\psi_i = \sqrt{N_i}\varphi_i$. The numerical resolution of equations (1.90) and (1.74) give access to the reduced variance of the spin given by equation (1.81).

This simple two-mode approach already gives a good intuitive understanding of the physical mechanisms behind this elastic interaction mediated spin squeezing. More details about this theoretical study with the inclusion of decoherence and particle loss can be found in [181, 187]. A different approach close to the experiment but without atomic losses is also presented in [84]. Furthermore, some orders of magnitudes close to experimental situations will be given at the beginning of chapter 5.

[15] Here the initial time is taken right after the first $\pi/2$-pulse.

Chapter 2

Experimental set-up and preliminary studies

*****

This chapter is dedicated to a brief overview of our experimental set-up. As this project has been initiated in 2006, it has already been thoroughly described in previous manuscripts [103, 113, 188, 189]. I will therefore just recap and emphasize some important points for the understanding of the work presented here. The different parts of the set-up and the temporal sequence will be reviewed. The experimental realization and characterization of a pure Bose-Einstein condensate via evaporative cooling will also be presented. The good agreement of the population lifetimes with the recently published values for the decay rates confirms the accuracy of the density estimation in the cross-over regime. In addition, a residual oscillation of the atomic cloud with a fluctuating phase will be highlighted and modeled. This study will lay the groundwork for the investigation of the impact of an in-homogeneous Rabi frequency on the squeezing measurement

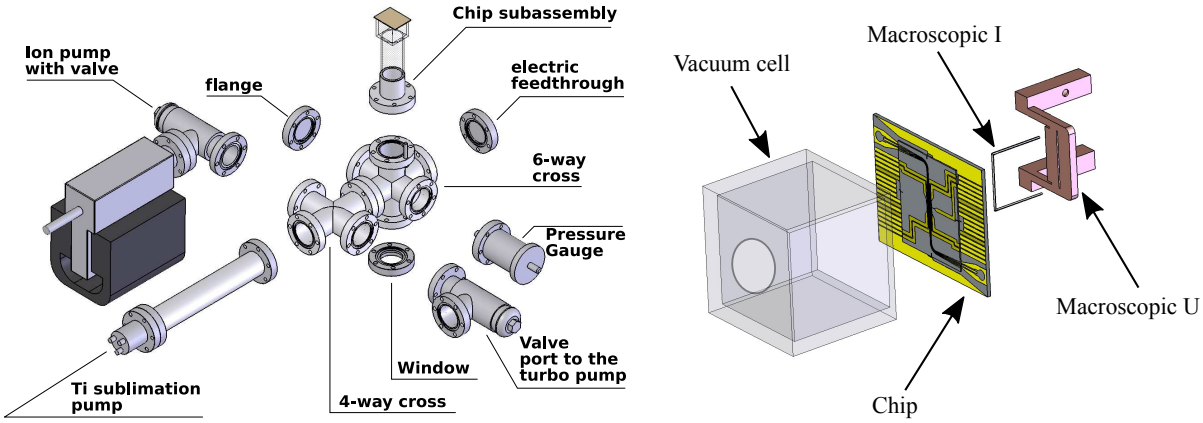

Figure 2.1: **Vacuum system and chip assembly. Left**: overview of the vacuum system. Adapted from [103]. **Right**: Overview of the chip assembly. The chip is glued on top of the Pyrex cell and replaces its upper wall. A macroscopic "I" and "U" shaped wires used to generate the MOT quadrupole field are glued on top of the chip. Adapted from [188].

2.1 Experimental set-up

The experimental set-up is composed of four main parts. Firstly, the vacuum system, made up from standard CF40 parts (Flanges, 6-way and 4-way crosses), a spectroscopy cell antireflective coated for 780 nm and an ion pump (Meca2000 PID 25). A titanium sublimation pump has also been installed and is used once in a while in order to improve the vacuum. Without atoms, the pressure given by a Bayard-Alpert pressure gauge (Leybold IE514) reads $\approx 1.4 \times 10^{-9}$ mbar. Two dispensers[1] (SAES Getters) located at the bottom of the glass cell play the role of the Rb source. With the dispenser working

[1] Only one is working at a time though.

continuously with the nominal current[2] of 4.17 A, the pressure rises up to $\approx 1.7 \times 10^{-9}$ mbar. The global assembly is illustrated on figure 2.1.

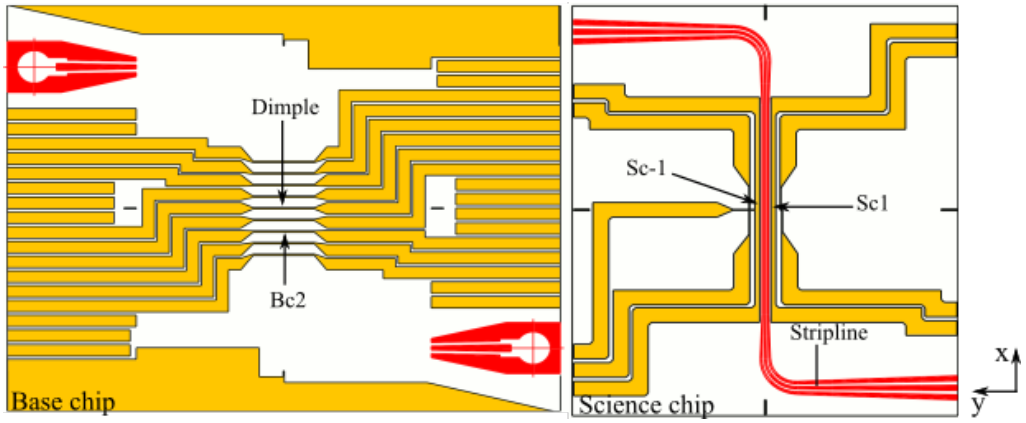

Figure 2.2: **Chip layout.** Base chip **(left)** and science chip **(right)** schematics. The wires used in the experiment are labeled. The dimple and stripline, which is actually the central wire of the coplanar waveguide, are used to generate the magnetic traps (dimple traps), Bc2 is used the compress the MOT and Sc1 (-1) is used the generate the RF field to perform the evaporative cooling (interrogation). The coplanar waveguide used to radiate the MW interrogation field is represented in red. Adapted from [103].

Secondly, the atom-chip whose schematic is shown on figure 2.2. It is actually made of two layers, the base chip and the science chip glued on top of each other. The ensemble is glued on top of the cell and replaces its top wall [190]. Its surface is coated to reflect 780 nm light and allows the implementation of a mirror-MOT [191]. It contains DC conductors driven by homemade low noise current sources [103] to trap the atoms, and a co-planar wave-guide, resonant for 6.8 GHz, used to generate the interrogation microwave field. The central wire of this wave-guide[3] is also used to generate magnetic traps. Two macroscopic wires (I and U), represented on figure 2.1 (right) and used to generate the MOT quadrupole field [192], are glued on a hollowed copper piece on top of the chip. This copper piece is also used to water-cool the ensemble. Three pairs of coils are placed around the cell to generate the required bias magnetic fields. As depicted on figure 2.3, the system is covered by a two-layer Mumetal shield to isolate the atoms from spurious external magnetic fields.
Thirdly, the optical system whose energy diagram is represented on figure 2.4. Three different 780 nm laser sources, including two external-cavity-diode-lasers (ECDL) [193], are used. The Repumper, locked by saturation absorption spectroscopy [194] on the cross over between $|F' = 1\rangle$ and $|F' = 2\rangle$, is used to pump the atoms into $|F = 2\rangle$. Part

[2]This particular current corresponds to a trade off between MOT loading and atoms lifetime in the final magnetic trap.
[3]Also referred to as "stripline".

of this beam is also used to offset lock a second ECDL, called Master, on the cross over between $|F' = 2\rangle$ and $|F' = 3\rangle$. This second laser is used to pump and detect the atoms, and inject a single diode laser (LD785-SE400), the slave. This slave is used to cool down and push the atoms. Concerning the detection system, a small camera catches the MOT fluorescence and two CCD cameras are used to perform absorption imaging along two horizontal orthogonal directions x (Andor iKon M 934-BRDD) and y (PCO Sensicam QE). More details on the detection system can be found in chapter 3 and in [188, 189].

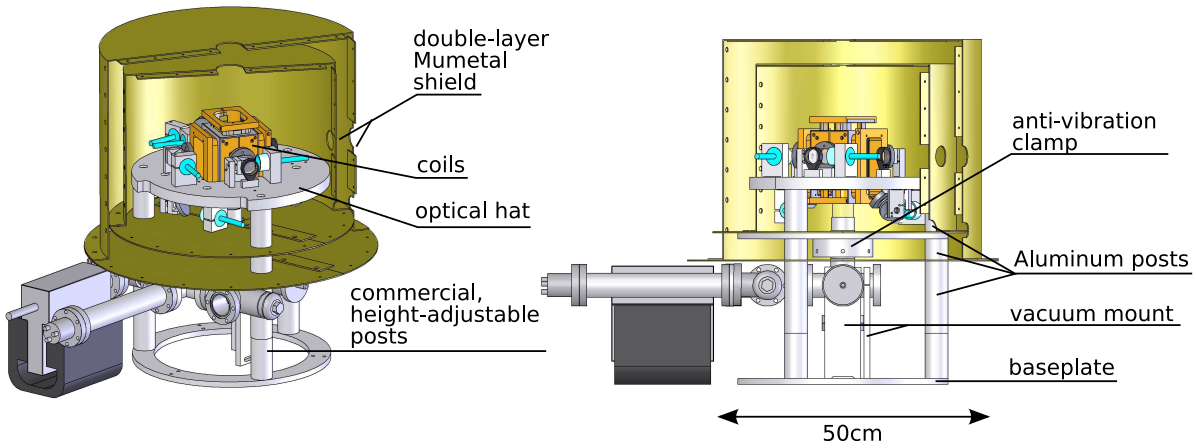

Figure 2.3: **Overview of the whole apparatus.** Three pairs of coils are placed around the cell, and a holed aluminum platform called optical hat is used to support the polarization plates and output collimators that bring the different laser beams to the atoms. The ensemble is covered by a two-layer Mumetal shield to isolate them from external magnetic fields. Taken from [103].

Fourthly, the interrogation signals. As already stated, the clock transition $|1\rangle \rightarrow |2\rangle$ is driven with a two-photon pulse requiring the combination of radio-frequency and microwave signals. The RF photon at ≈ 1.8 MHz comes from a commercial synthesizer SRS DS345, while the microwave one is generated by a homemade frequency chain [195] which converts the 100 MHz from a stable hydrogen maser distributed at SYRTE [196] into the required 6.834 GHz using a Non Linear Transmission Line (LPN 7100). The MW signal is sent to the on-chip coplanar waveguide and the RF one is sent to an adjacent wire Sc-1 represented on figure 2.2.

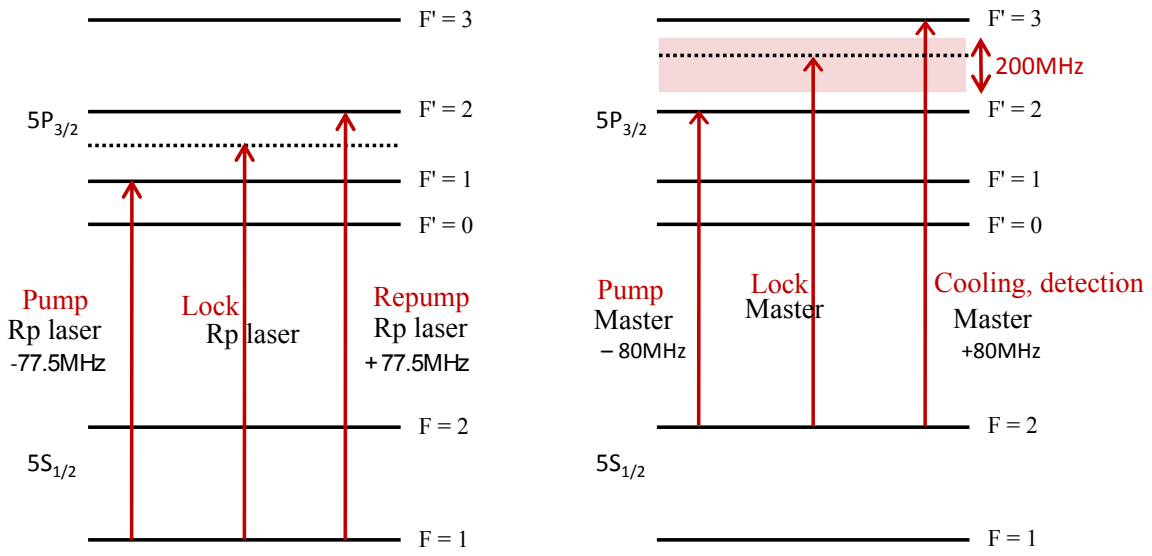

Figure 2.4: **Laser frequencies.** Energy diagrams of the Repumper and master lasers. Both of them are locked on a cross-over transition and the useful frequencies are achieved thanks to Acousto-Optic Modulators (AOM) driven at the indicated frequencies. The slave is injected by the master and works at the cooling frequency.

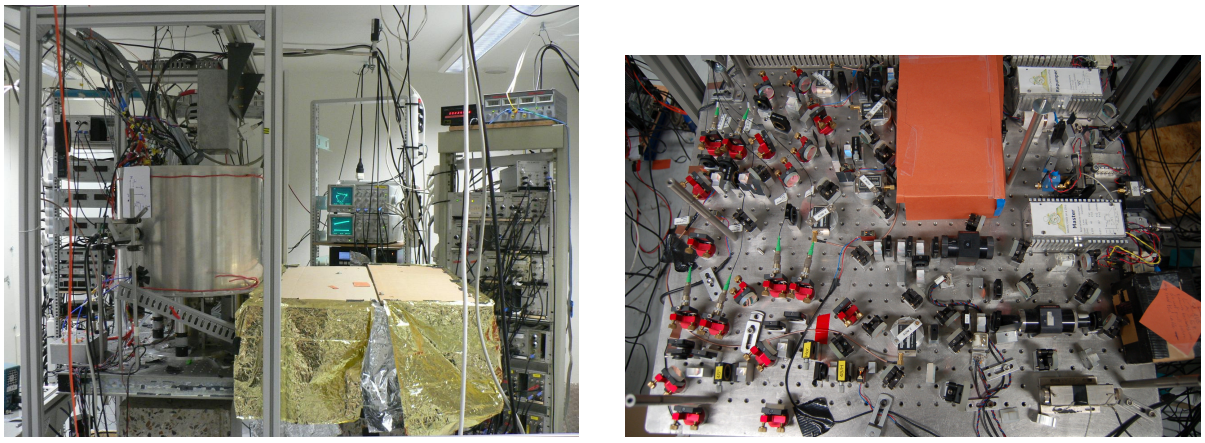

Figure 2.5: **Experimental setup. Left**: overview of the whole system. The Mumetal shield installed on the optical table is covering the cell and the chip. Next to it, the optical system is covered by a thermal blanket to isolate it from external thermal fluctuations. The current sources and lasers electronics are also visible in the back. **Right**: Uncovered optical system with the three lasers on the right. Each beam goes through a succession of isolators, mirrors, $\lambda/2$-plates, cubes and AOM before being coupled to the fibers and sent to the atoms. The saturated absorption spectroscopy is located below the orange cardboard.

2.2 Experimental sequence

A typical sequence whose temporal evolution is represented on figure 2.6 consists of the following steps.

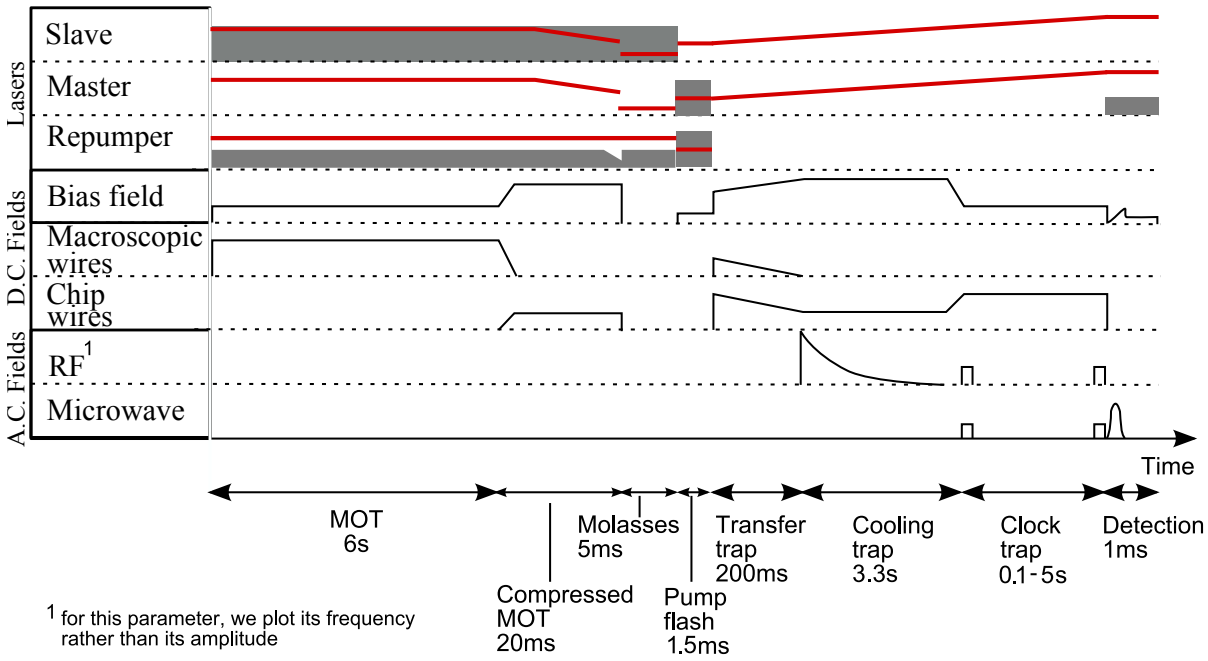

Figure 2.6: **Temporal sequence of a typical experimental cycle.** The grey areas depict amplitude changes while the red lines show relative frequency evolutions. The full cycle typically last between 11 and 15 s depending on the interrogation time and the MOT duration. adapted from [188].

- **Magneto-Optical Trap** The chip surface, used to reflect the cooling beams, is used together with the macroscopic U that creates the quadrupole field, to generate a mirror MOT that loads approximately 4×10^6 atoms in 6 s.
- **Compressed Magneto-Optical Trap** The macroscopic I's current is then ramped to compress the MOT for 20 ms and reduce its temperature to $\approx 45\mu K$.
- **Optical Molasses** To further cool down the atoms, a 4 ms optical molasses [4] is created by turning off all the magnetic fields and increasing the detuning of the cooling beams. At the end, we get a cloud containing between 3.5 and 4.10^6 atoms at $\approx 5\mu K$.
- **Optical pumping** Two very short (1.5 ms) light pulses (master pump and Rp pump) are shone to transfer the atoms into the $|1\rangle$ state. Usually we get a 90% transfer efficiency, that we estimate by performing a Stern-Gerlach measurement.

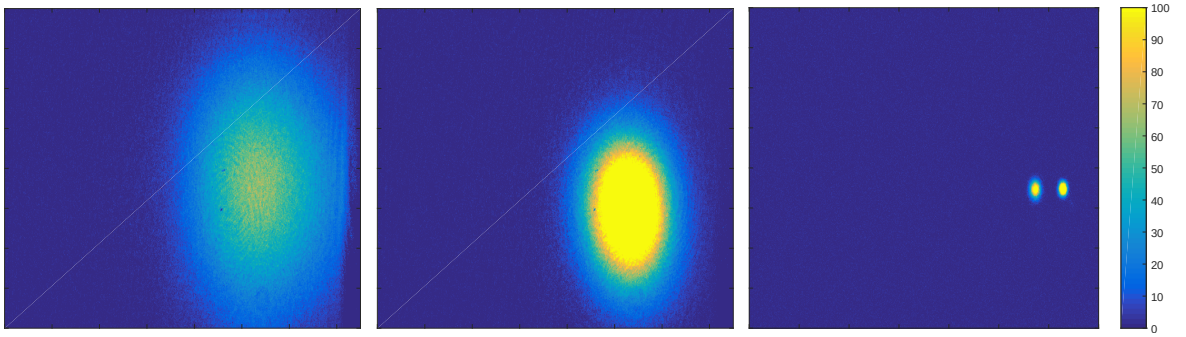

Figure 2.7: **Evolution of the atomic cloud during the sequence.** The CMOT (45 μK), molasses (5 μK) and thermal cloud (80 nK) in a coherent superposition are imaged after a 8 ms time of flight. These clouds come from a MOT containing approximately 4×10^6 atoms. The right side of the images corresponds to the chip surface. The indicated color scale represents the atom number per pixel and is identical for the three pictures.

- **First magnetic trap** A first off-chip magnetic trap is created with the macroscopic I and the central wire of the coplanar wave-guide to catch and bring the atoms closer to the chip in 5 ms. Approximately 70% of the atoms are transferred and and their temperature rises up to approximately 10μK.

- **Evaporation trap** While decreasing the macroscopic I current, the chip currents (dimple and stripline) are ramped up for 500 ms to further compress the trap $(\omega_x, \omega_y, \omega_z) = 2\pi\times$ (0.5, 1.2, 1.2) kHz. Then an RF knife is used to progressively remove the hottest atoms in the trap and perform the evaporative cooling [197]. After 3.3 s, depending on the final RF frequency we get between 6.10^4 atoms at 80 nK, just above the condensation threshold, and 10^4 fully condensed atoms.

- **Interrogation trap** Finally, the atom are slowly (700 ms) transferred into the final interrogation trap $(\omega_x, \omega_y, \omega_z) = 2\pi\times$ (2.9, 92, 74) Hz located 350 μm below the chip surface. This trap is very elongated along the x-axis and this is why we talk about a cigar-shaped trap. The slow ramp is implemented to avoid the excitation of atomic motional modes inside the trap and especially along the longitudinal direction [113]. Unless specified otherwise, every interrogation sequence takes place in this trap.

- **Detection** After the interrogation, the two atomic states are imaged on a CCD camera located along the slow axis of the trap (y-axis). The next chapter is dedicated to the implementation and calibration of our dual state detection system.

2.3 Experimental characterization of our BEC

As stated previously, an evaporation stage is dedicated to the cooling of the cloud and can lead to Bose-Einstein condensation [104,197]. The idea is to tightly confine the atoms and couple the hottest ones with an adjacent non trapping state through a RF field. This actually corresponds to lowering the extremities of the magnetic trap and let the hottest atoms escape. The tight confinement allows a rapid thermalization of the remaining atoms via elastic collisions, decreasing the overall temperature of the ensemble. By cleverly scanning the RF frequency, the phase space density will increase, eventually leading to Bose-Einstein condensation. The competition between elastic and inelastic collisions imposes strong constraints on the trapping confinement and the cooling duration.
In this section is detailed the characterization of our Bose-Einstein condensates, starting with the estimation of the condensed fraction followed by the measurement of the atoms lifetime in the interrogation trap.

2.3.1 Condensed fraction measurements

In the case of an interacting trapped Bose gas, the condensed fraction reads [149]:

$$\frac{N_c}{N_c + N_{th}} = 1 - (\frac{T}{T_c})^3 - \frac{\zeta(2)}{\zeta(3)} \frac{\mu}{k_B T_c} (\frac{T}{T_c})^2 [1 - (\frac{T}{T_c})^3]^{2/5}, \tag{2.1}$$

where N_c is the condensed atom number, N_{th} is the non-condensed atom number, T is the cloud temperature and T_c is the critical temperature of Bose-Einstein condensation (2.5). The second term accounts for interactions whose contribution becomes significant at low temperatures ($T < T_c$). Via equation (2.1), one can characterize the efficiency of the evaporation and check the purity of the BEC.
The analysis is performed at the end of the evaporation trap $(\omega_x, \omega_y, \omega_z) = 2\pi\times$ (0.5, 1.2, 1.2) kHz with a 10 ms time of flight. The temperature is scanned via the final frequency of the RF evaporation ramp ($f_{ev} \in [2.2, 1.94]$ MHz). Moreover, the cloud is imaged along the strong axis of the trap.

Fitting procedure: The simplest way to determine the condensed fraction is to fit the cloud density profile with a bimodal distribution. Indeed, the shape of thermal part of the cloud is Gaussian, whereas the BEC density profile can be well fitted with a parabola in this direction and under the Thomas-Fermi approximation

$$OD_{Gauss}(y, z) = OD_{peakG} \exp[-\frac{1}{2}(\frac{y - y_0}{\sigma_y})^2 - \frac{1}{2}(\frac{z - z_0}{\sigma_z})^2], \tag{2.2}$$

$$OD_{para}(y, z) = OD_{peakP} \max\{[1 - (\frac{y - y_0}{R_y})^2 - (\frac{z - z_0}{R_z})^2], 0\}, \tag{2.3}$$

σ_i being the spatial extension of the thermal phase and R_i being the Thomas-Fermi radius along the i-direction. According to the study performed in section 1.4.3, in the evaporation trap, the tight confinement makes the Thomas-Fermi approximation valid ($\kappa \approx 400$).

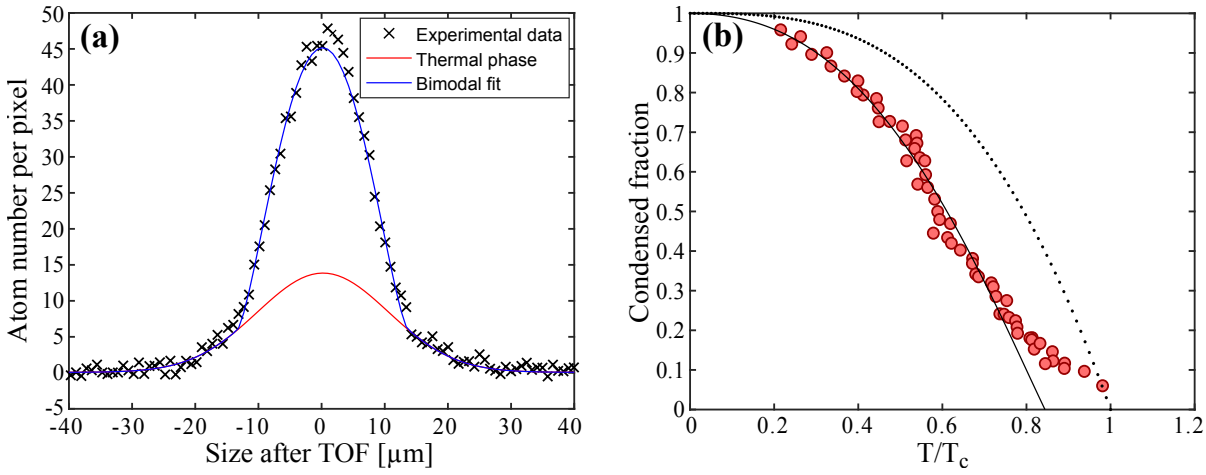

Figure 2.8: **Condensed fraction measurement. (a)** Cross section of the atomic cloud slightly below the critical temperature, where the two phases are well distinguishable. The experimental points (black crosses) are well fitted with a bimodal function (blue line) obtained according to the protocol detailed in the text. The red line represents the thermal phase used to estimate the temperature of the atomic ensemble. **(b)** The condensed fraction is plotted as a function of the normalised temperature for atoms just after the evaporation trap with a 10 ms time of flight. The red dots are experimental data, the black line is a fit with equation (2.1) for a gas with interactions in the Thomas-Fermi limit and the dotted line is for a gas without interactions.

However, when the condensate phase becomes larger than the thermal one, the fit has some trouble with the small Gaussian wings which leads to a Gaussian profile converging on the condensate. This can be somehow circumvented by applying the following procedure inspired from [198]:

- The first step is to determine the size of the condensate i.e. the Thomas-Fermi radii. To do so, we start by fitting the whole cloud with the parabolic function (Eq. (2.3)). This will give a good first estimation of the Thomas-Fermi radii and the position of the center of the cloud. Then we use these parameters as initial guess for the fit using the bimodal distribution which is the sum of Eq. (2.2) and (2.3).

- The second step is to remove the condensed part from the whole cloud using the previous fitted parameters. Now the remaining part corresponds to the pure ther-

mal phase which can be fitted with the Gaussian (Eq. (2.2)). The spatial extension of this cloud (σ_i) will be used to estimate the temperature of the cloud.

- The third step consists in subtracting the thermal fraction and the background from the initial cloud. The remaining cloud is now a pure BEC which can be fitted with Eq. (2.3).

Figure 2.8 (a) shows the atomic distribution slightly below the critical temperature. At this temperature, the condensed parabolic phase and the thermal Gaussian wings are clearly visible.

Temperature estimation: Now that we have access to the condensed fraction, we need to estimate the ensemble temperature. After time of flight expansion, the temperature of the cloud along the i-axis can be expressed as [149]:

$$k_B T = \frac{m\sigma_i^2}{\frac{1}{\omega_i^2} + T_{tof}^2}, \tag{2.4}$$

where σ_i is the cloud diameter and the time of flight $T_{tof} = 10$ ms. Furthermore, the critical temperature below which the condensation theoretically occurs reads [149]

$$T_c = \frac{\hbar\overline{\omega}}{k_B}\left(\frac{N}{\xi(3)}\right)^{1/3} \approx 0.94\frac{\hbar\overline{\omega}}{k_B}N^{1/3}, \tag{2.5}$$

and $\overline{\omega}/(2\pi) = (\omega_x\omega_y\omega_z)/(2\pi)$ is the geometrical mean of the trap frequencies. The condensed fraction is displayed as a function of the normalized temperature T/T_c on figure 2.8 (b). When the condensed fraction exceeds 90%, the thermal wings become too small to be detected by the fitting procedure and the temperature cannot be accurately estimated anymore. The global evolution is however well reproduced by equation (2.1) with a chemical potential $\mu = 6.5$ kHz, which is consistent with equation 1.71 (≈ 7.6 kHz).

In order to ensure its purity, the final evaporation frequency is set such that a small part of the BEC is cut by the RF knife. After optimization, a quasi-pure BEC containing a maximum of 1.5×10^4 atoms can be obtained.

2.3.2 BEC lifetimes

In section 1.2.3, we emphasized the possibility for one atom to leave the trap because of inelastic collisions. We will now compare the theoretical prediction with the experimental data. We recall that the population loss for the two states $|1\rangle$ and $|2\rangle$ can be described

by the following rate equations:

$$\begin{aligned} \frac{1}{N_1}\frac{dN_1}{dt} &= -\gamma_{bck} - \gamma_{12} n_2 \\ \frac{1}{N_2}\frac{dN_2}{dt} &= -\gamma_{bck} - \gamma_{22} n_2 - \gamma_{12} n_1. \end{aligned} \tag{2.6}$$

Because of the relatively low densities ($< 10^{19}$ m^{-3}), we can safely neglect the effect of three-body recombination [125].
Experimentally, we prepare a BEC in $|1\rangle$, $|2\rangle$ or in a coherent superposition, and we measure the remaining populations in the interrogation trap, after different trapping times. The results are displayed on figure 2.9, where the points are the experimental data and the lines correspond to the theoretical predictions obtained with (2.6) and the published values for the decay rates $\gamma_{22} = 8.1(3)\times10^{-14}$ cm^3/s and $\gamma_{12} = 1.51(18)\times10^{-14}$ cm^3/s [124]. A linear fit on the cyan curve gives the decay rate due to collision with the background gas $\gamma_{bck} = 0.20 \pm 0.01$ similar to the previously measured value in [113]. The rather good agreement between the two shows the good accuracy of the density estimation using the cross-over formalism developed in section 1.4.3.

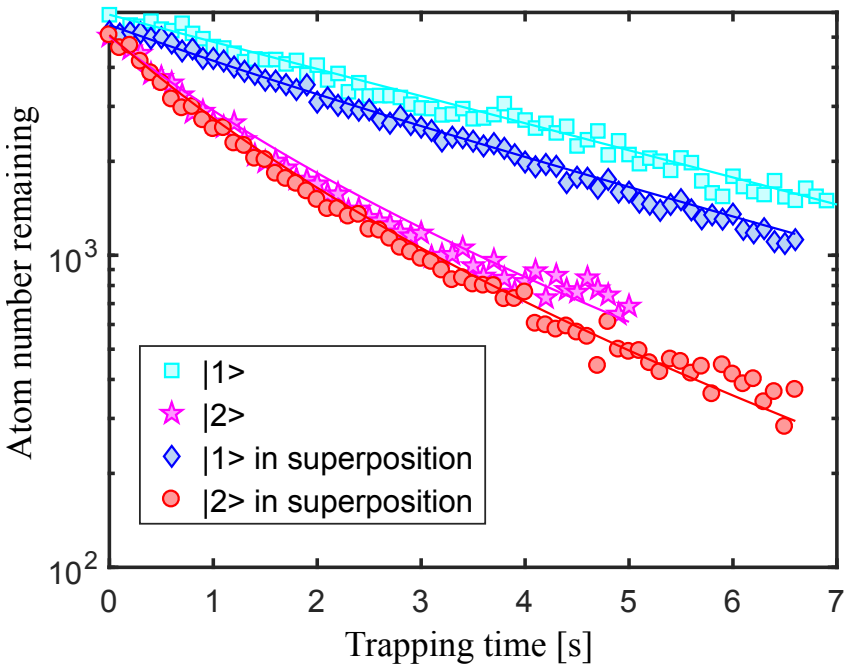

Figure 2.9: **Lifetime of our trapped BEC.** Atom number remaining in the interrogation trap as a function of the trapping time. The plain lines are derived using the experimental initial atom numbers and the rate equations (2.6). The density is derived in the cross over regime presented in section 1.4.3.

2.4 Study of the cloud position inside the trap

This section is dedicated to the study of the atomic center of mass motion of our BEC inside the interrogation trap $(\omega_x, \omega_y, \omega_z) = 2\pi\times$ (2.9, 92, 74) Hz and along the vertical direction. Indeed, the position of the cloud clearly fluctuates from shot-to-shot and this could impact the squeezing measurement, as we will see on section 5.4.3. More precisely, figure 2.10 (a) shows the evolution of the cloud's center of mass when the trapping duration is scanned. The sinusoidal fit gives a 74 Hz oscillation which corresponds to the trapping frequency along the vertical direction, and a 8 μm peak-to-peak amplitude after a 23 ms time of flight. We checked that this oscillation and the shot-to-shot fluctuations are identical for the two clock states. The fluctuation of the distance between the two cloud's centers of mass is on the order of 2 μm, which corresponds to the error in the estimation of the center of mass with a Gaussian or parabolic fit. Furthermore, as the two states are imaged simultaneously using a detection method[4] that transfers $|1\rangle$ into $|2,0\rangle$, the two clock states have different magnetic moments during time of flight. This hence rules out random kicks at the trap release and magnetic noise during time of flight as possible explanations for this position noise.

Let's therefore first assume that the observed position fluctuations happen inside the trap[5] and try to model the data. Inside the trap, the velocity and position of the center of mass can be described by

$$v_0(t_{trap}) = V_0 \sin(2\pi\nu_z t_{trap} + \phi), \tag{2.7}$$

$$z_0(t_{trap}) = -A_0 \cos(2\pi\nu_z t_{trap} + \phi) + Z_0, \tag{2.8}$$

where t_{trap} is the trapping time, V_0 is the amplitude of the center of mass velocity, $A_0 = \frac{V_0}{2\pi\nu_z}$ is the oscillation amplitude, Z_0 is the mean position of the center of mass inside the trap, $\nu_z \approx 74$ Hz is the vertical trapping frequency and ϕ is the phase of the oscillation. The free parameters V_0 and ϕ can be adjusted to match the experimental data. Then, integrating the Newton's laws of motion, the position after time of flight reads

$$z(t_{tof}; t_{trap}) = z_0(t_{trap}) + v_0(t_{trap}) t_{tof} - \frac{g}{2} t_{tof}^2, \tag{2.9}$$

where t_{tof} is the time of flight and g is the nominal gravitational acceleration taken equal to 9.81 $m.s^{-2}$. Figure 2.10 (b) shows the temporal evolution of the cloud's position in the trap and during a 23 ms time of flight, for different trapping times. This simulation can be used to reproduce the oscillation and the noise after time of flight and reverse time to deduce what happened inside the trap.

Figure 2.10 (c) shows the numerical reconstruction of the oscillation of the cloud after time of flight (blue) and inside the trap (red) using $V_0 = 550$ μm/s and $\sigma(\phi) \approx \frac{\pi}{2}$. Both

[4] This method is detailed in section 3.4

[5] This will be experimentally verified in section 5.4.3

the noise and the oscillation match the experimental data displayed on figure 2.10 (a). It therefore looks like the observed shot-to-shot noise is actually due to a fluctuation of the phase of the oscillation which corresponds to a fluctuation of the cloud position at the time when the oscillation begins. The 4 μm oscillation amplitude and 8.5 μm shot to shot noise after 23 ms time of flight actually correspond to 0.38 μm and 0.77 μm inside the trap. Moreover, the $\frac{\pi}{2}$ phase shift between the blue and red curves indicates that the position after time of flight is mainly determined by the velocity inside the trap.

In order to check this assertion, the evolution of the shot to shot noise and the oscillation amplitude have been plotted as a function of the time of flight on figure 2.10 (d). Concerning the noise, the small offset compared to its value at 23 ms and the linear behavior confirm that the observed position fluctuations after time of flight are due to velocity fluctuations inside the trap. The red linear fit gives $\sigma(v_0) \approx 360\mu$m/s. The simulation represented by the plain lines is in agreement with the experimental data and the expected evolution of the noise, considering that position and velocity fluctuations are uncorrelated $\sigma(z) = \sqrt{\sigma(z_0)^2 + \sigma(v_0)^2 t_{tof}^2}$. More quantitatively, the simulation gives $\sigma(z_0) = 0.77$ μm and $\sigma(v_0) = 367$ μm/s.

Concerning the mean oscillation, velocity and position are directly correlated such that $A(t_{tof}) = A_0 + V_0 t_{tof}$, leading to $A_0 = 0.38$ μm and $V_0 = 174$ μm/s. The fact that this measured V_0 is smaller than the programmed one (550 μm/s) is due to the phase noise that reduces the average oscillation amplitude.

Condition	**Amplitude** [μ**m**]	σ(**z**) [μ**m**]	$\mathbf{V_0}$ [μ**m/s**]	$\sigma(\mathbf{V_0})$ [μ**m/s**]
After 23ms tof	4	8.5	-	-
In trap	0.38	0.77	550	360

Table 2.1: **Cloud position parameters.**

The numerical values of the trajectory parameters are summarized in Table 2.1. Experimentally, we identified the oscillation and the noise to appear during the transfer between the evaporation and the interrogation trap as it was already pointed out in [113]. Considering that the evaporation and interrogation traps have different vertical positions, the mean oscillation may be explained by a non perfectly adiabatic transfer. The origin of the shot to shot noise remains unexplained though. A possible explanation could be magnetic noise in a specific frequency range that is amplified by a parametric heating like phenomenon. We also noticed that the position of the MOT has an effect on the phase of the oscillation in the interrogation trap, but not on the amplitude. Consequently, a fluctuation of the MOT position could somehow lead to a fluctuation of the phase of the oscillation in the final trap, but it seems a bit strange that this initial position memory is conserved over the whole sequence.

This experimental study and numerical simulation will be used in section 5.4.3 to investigate the effect of this position noise on the squeezing measurement.

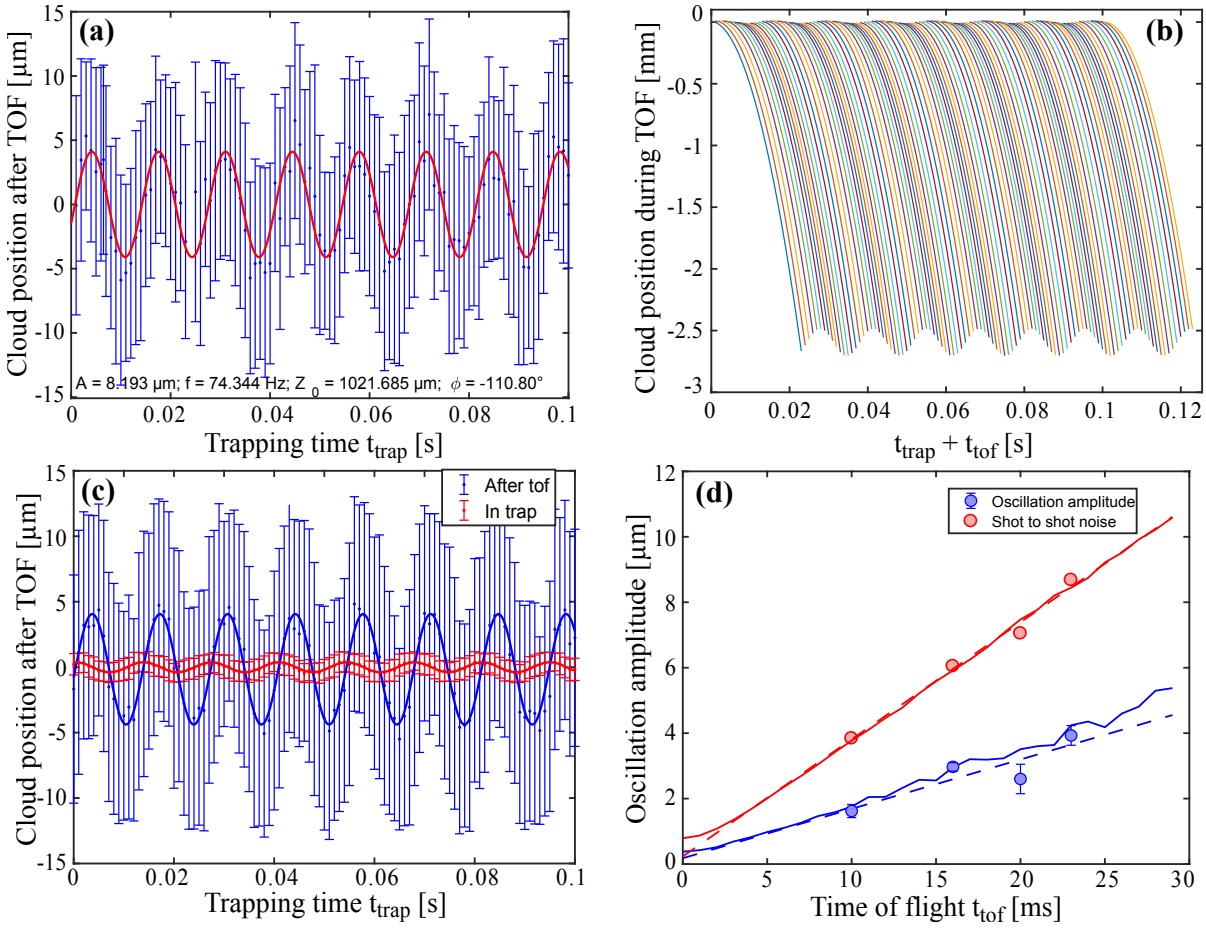

Figure 2.10: **Center of mass oscillation.** **(a)** The trapping time of the interrogation trap is scanned and the BEC is imaged after a 23 ms time of flight. Each point corresponds to the position averaged over 30 shots and their corresponding error bars to its standard deviation. the red line corresponds to a sinusoidal fit: $z(t) = B + \frac{A}{2}\sin(2\pi\nu_z t + \phi)$. A mean oscillation is clearly visible, despite a significant shot to shot noise ($\sigma(z) \approx 8.5\mu$m). **(b)** To illustrate the simulation, the center of mass trajectories inside the trap are plotted and during a 23 ms time of flight. Each color corresponds to a different trapping time and the in-trap oscillation has been increased for clarity. **(c)** In trap (red) and after 23 ms time of flight (blue) center of mass oscillation after offset subtraction obtained with the simulation explained in text with $V_0 = 550$ μm/s and $\sigma(\phi) \approx \frac{\pi}{2}$. Plain lines are sinusoidal fits that give after tof (in trap) $A = 4.1\mu$m (0.38μm) and $\sigma(z) = 8.5\mu$m (0.8μm). **(d)** The same procedure is applied for different times of flight and the evolution of the oscillation amplitude (blue points) and standard deviation of the center of mass (red circles) are plotted. The dashed lines are linear fit and the plain lines correspond to the numerical model explained in the text.

Chapter 3

Detection system

*****

In the domain of cold atoms, physicists develop increasingly sophisticated methods to manipulate atomic states and study complex quantum systems. However at the end of the day, our only way to observe and interpret the atoms' response to these manipulations is to detect them, destructively or not. The characterization and calibration of the detection system is therefore a crucial step in the development of every cold atom experiment. And this is even more true in the context of atomic clocks and spin-squeezing-based quantum metrology since its realization is directly related to our knowledge of the populations in the two clock states.
Keeping that in mind, our detection system must satisfy the following requirements;

- Imaging a wide range of densities: from dilute thermal clouds ($\sim 10^{11}$ at.cm^{-3}) to BEC ($\sim 10^{13}$ at.cm^{-3}.
- Low detection noise in order to get a shot-noise limited detection system and observe the effect of spin squeezing.
- High fidelity of the atom number estimation.
- Dual state detection within a single experimental cycle.
- Fast dynamic acquisition (< 1 s).

In this chapter we present our detection system, starting with the basics of time of flight absorption imaging and atom number estimation. Then the accuracy of this estimation is analyzed in the context of dense samples. The effective absorption cross-section of the atoms due to non perfect polarization of the detection light is also estimated. The main noise sources are subsequently characterized and reduced using appropriate detection parameters and a post-processing algorithm whose purpose is to minimize the effect of optical interference and diffraction fringes. In addition, an alternative more stable dual-state detection method, enabling the simultaneous imaging of the two clock states with a single light pulse, is presented. The proper functioning of the whole detection is finally analyzed by comparing the behavior of the population difference fluctuations with the standard quantum limit.

3.1 Time of flight absorption imaging

In order to fulfill all the requirements listed above, a time of flight absorption imaging technique [100, 199] has been chosen. The absorption gives access to the spatial distribution of the atomic cloud and thus enables the direct monitoring of the state-dependent spatial dynamics investigated in this manuscript. It moreover provides a good spatial resolution and high signal to noise ratio in spite of the limited optical accesses and low numerical apertures due to the presence of the atom chip. In this section, the basic principle of the imaging technique is reviewed, as well as the estimation of the atom number

from the acquired pictures. The experimental realization of a double state detection scheme historically implemented on TACC is also presented.

3.1.1 Detection principle and atom number estimation

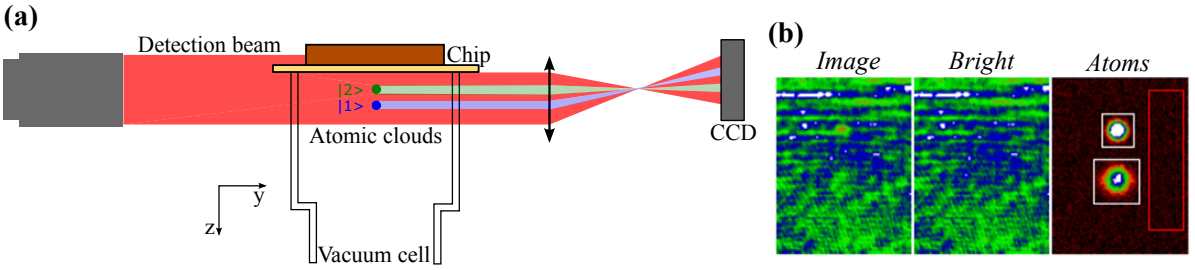

Figure 3.1: **Absorption detection scheme and typical images.** **(a)** Drawing of the imaging set-up for the two state detection whose principle is explained on the text. Adapted from [188]. **(b)** Acquired images with atoms (*Image*), without atoms (*Bright*) and the reconstructed column density (*Atoms*). The two white rectangles define the areas inside which the atom numbers are estimated and the red one is used to correct for intensity fluctuations between *Image* and *Bright*

Following the interrogation, the standard single state detection starts by turning off the trapping magnetic fields such that the atoms begin to fall under the action of gravity. After 8 to 25 ms time of flight a light beam, resonant with the $|F = 2\rangle \rightarrow |F' = 3\rangle$ cycling transition, is shone on the atoms. Because of the multiple absorption-emission cycles and the fact that spontaneous emission is isotropic, the light intensity in the direction of propagation y is reduced making a shadow on the CCD camera, as depicted on figure 3.1. This attenuation is proportional to the atomic density n_{at} according to the Beer-Lambert law

$$dI = -n_{at}\sigma(I)Idy, \tag{3.1}$$

where σ is the absorption cross section. In the case of an arbitrary intensity I and detuning δ, it can be expressed as [110]

$$\sigma(I) = \frac{\sigma_0}{1 + \frac{I}{I_{sat}} + (\frac{\delta}{\Gamma/2})^2}. \tag{3.2}$$

where Γ is the natural linewidth of the transition, $I_{sat} = \hbar\omega\Gamma/2\sigma_0$ is the saturation intensity and $\sigma_0 = 3\lambda^2/2\pi$ is the natural cross section of the transition for a $\sigma^{\pm}$ polarized light. Estimating the atomic density from equation (3.1) requires two images: one with atoms called *Image* and one without atoms called *Bright*. The two-dimensional atomic column density then reads [200]:

$$n(x,z) = \int_{-\infty}^{+\infty} n(x,y,z)dy = \int_{I_{bright}}^{I_{image}} \frac{1 + \frac{I}{I_{sat}} + (\frac{\delta}{\Gamma/2})^2}{I\sigma_0} dI \tag{3.3}$$

$$= \frac{1 + (\frac{\delta}{\Gamma/2})^2}{\sigma_0} \ln(\frac{I_{bright}}{I_{image}}) + \frac{1}{\sigma_0 I_{sat}}(I_{bright} - I_{image}) \tag{3.4}$$

The first term corresponds to the low intensity limit ($\frac{I}{I_{sat}} < 0.1$) for which the spontaneous emission occurs much faster than the absorption. The number of diffused photons per atom is then proportional to the intensity. The second term corresponds to saturated case for which the atoms populate the excited state and diffuse photons with a constant rate $\Gamma/2$.

However, as we do not directly measure the light intensity, we have to link it to the number of photo-electrons acquired by the CCD camera. Let's start with the number of incoming photons seen by the atoms $N_{ph} = IA\tau/\hbar\omega$, where A is the pixel area in the object plane and τ the pulse duration. As there are some optics (cell walls, lens) between the atoms and the CCD camera, the received intensity is reduced by a factor T representing the overall optical transmission. Then the photons hitting the CCD are converted into photo-electrons with an efficiency η. These photo-electrons are subsequently counted in the analog-digital conversion stage with a conversion gain g. This gives the number of photo-electrons per pixel (i,j) that we call counts

$$N_{counts}(i,j) = Tg\eta \frac{IA\tau}{\hbar\omega}. \tag{3.5}$$

The normalized incoming detection intensity then reads:

$$I/I_{sat} = \frac{2\sigma_0}{Ag\eta T\Gamma\tau} N^*_{bright}. \tag{3.6}$$

According to equation (3.4) and at resonance, the number of atoms per pixel can be expressed as a function of the number of counts:

$$N(i,j) = \underbrace{\frac{A}{\alpha\sigma_0} \ln(\frac{N^*_{bright}(i,j)}{N'_{image}(i,j)})}_{N_L} + \underbrace{\frac{2}{g\eta\tau T\Gamma}(N^*_{bright}(i,j) - N'_{image}(i,j))}_{N_H}. \tag{3.7}$$

where $\alpha \leq 1$ accounts for non perfect polarization of the imaging light, and section 3.2.1 is dedicated to its origin and calibration.

In order to take into account the dark counts of the camera and the ambient stray light, two additional images (*Darkimage* and *Darkbright*) are taken without the detection light and under the same conditions as the two first images. These two background frames are then removed from the original pictures: $N'_k = N_k - N_{k,dark}$. Furthermore, as the light intensity can fluctuate between the two successive pictures *Image* and *Bright*, a

region of the CCD without atoms is used to estimate this fluctuation. The *Bright* frame is renormalized by a factor r derived as the ratio of the mean intensities of the two frames integrated over the renomalization area A_r, delimited by the red rectangle on figure 3.1 (b),

$$N^*_{bright} = \frac{\sum_{A_r} N'_{image}}{\sum_{A_r} N'_{bright}} N'_{bright} \equiv r(A_r) N'_{bright}. \tag{3.8}$$

The detected atom number is then: $N_{det} = \sum_i \sum_j N(i,j)$, where the sum is made inside the two analysis areas represented by the white rectangles on figure 3.1 (b). As it appears on equation (3.7), working at low intensities bears the advantage of measuring the atom number without having to calibrate the camera as it only depends on the absorption cross section and the pixel size. On the other hand, at high intensities the atom number is directly given by the number of missing photons and does not depend on the cross section which is not trivial to evaluate.

3.1.2 Standard double state imaging

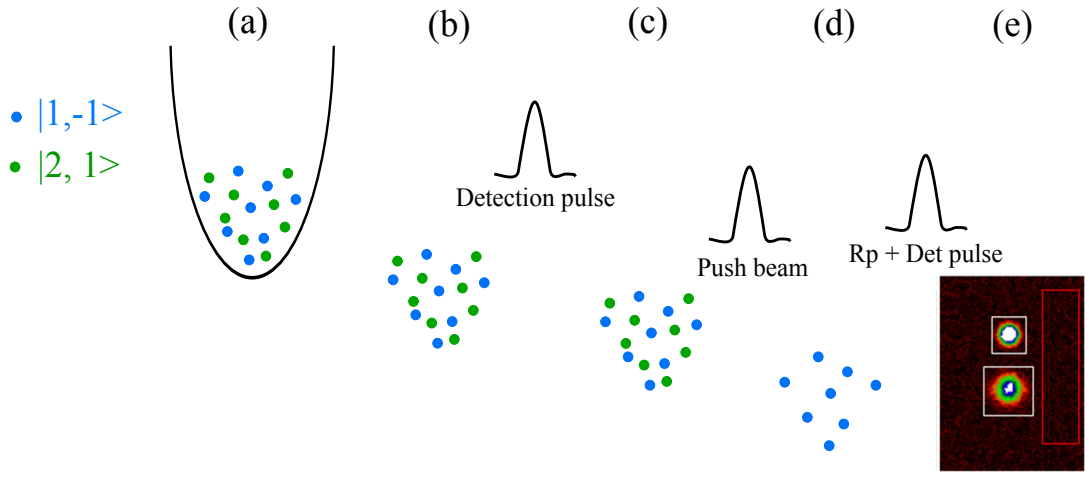

Figure 3.2: **Schematic of the double detection technique. (a)** Atoms in clock states $|1\rangle$ (blue) and $|2\rangle$ (green). **(b)** The trap is released and the two states fall together under the action of gravity. **(c)** The detection pulse, resonant with $|F = 2\rangle$, is applied to detect atoms in $|2\rangle$. **(d)** The cooling light is used to push the detected atoms away. **(e)** The repumper and detection light are sent to transfer the atoms initially in $|1\rangle$ to $|F = 2\rangle$ and detect them.

As we want to investigate number squeezing, we need a way to estimate the atom number in each clock state within the same experimental sequence. As depicted on figure 3.2, the method is threefold. First, after turning the trapping fields off, a detection pulse

is shone to the atoms in order to detect the population in $|2\rangle$. Second, a part of the cooling light is sent to remove the previously detected atoms in $|2\rangle$. And third, a repumper pulse is sent together with the detection light to transfer the remaining atoms from $|1\rangle$ into F=2 and detect them.

Technically, because of the required short time delay between the acquisition of the two pictures, a frame transfer technique has to be used. It consists in blocking one half of the CCD camera with a razor blade, while the other half is illuminated by the detection pulses. The photo-electrons accumulated during the first detection phase are transferred and stored into this dark area of the CCD. The second detection pulse can then fill again the emptied pixels. After the acquisition of the two pictures, all the filled pixels can finally be read out to give the *Image* and *Bright* pictures.

3.2 Detection calibration and accuracy

In order to correctly estimate the number of atoms by applying equation (3.7), one needs to thoroughly calibrate all the involved parameters. The camera's characteristics have already been carefully calibrated by former Ph.D. students and all the calibration methods and optimizations are detailed in [189]. For convenience sake, the main detection characteristics are recalled in table 3.1.

Names	**Symbols**	**Values**	**uncertainties**	**Units**
Linewidth	Γ	$2\pi\times6.0667$	-	MHz
Cross section	σ_0	0.2907	-	μm^2
Gain	g	0.859	±0.008	-
Efficiency	η	0.972	±0.032	-
Pixel size (in the imaging plane)	ps	5.2	±0.12	μm
Magnification	-	2.51	-	-
Optical transmission	T	0.86	±0.025	-
Pulse length	τ	20	±0.5	μs
Effective cross section parameter	α	0.76	±0.025	-

Table 3.1: **Detection parameters.** The linewidth and natural cross section have been derived from [110], the other parameters come from [189] except the effective cross section parameter which is measured in section 3.2.1.

These values were quickly checked and the effective cross section parameter α did not coincide with the previously measured value of 1 [189]. The following section is thus dedicated to its estimation. On the other hand, as we will work with quite dense samples (BEC), we need to make sure that the time of flight is sufficiently long so that the optical density is low enough to correctly detect all the atoms and estimate the populations.

3.2.1 Calibration of the effective cross section

Assuming that the camera's parameters have been well calibrated, the atom number should not depend on the incoming light intensity, provided that it is higher than the saturation intensity. However as depicted on figure 3.3 (a), the detected atom number increases with I/I_{sat}.
This feature is characteristic of a non perfectly controlled polarization. One way of understanding this effective cross section is the following: if the polarization of the imaging light is not perfect (σ^+ in our case), then the probability for one atom to be excited in the desired state ($F = 2 \rightarrow F' = 3$) becomes lower than one. This means that increasing the detection light intensity increases the number of atoms transferred via the right channel, like in a repumping process. And this is the reason why we observe a positive slope for $I > I_{sat}$ on figure 3.3 (a). In order to take into account this effective cross section, we introduced a calibration parameter $0 < \alpha < 1$ in equation (3.7)

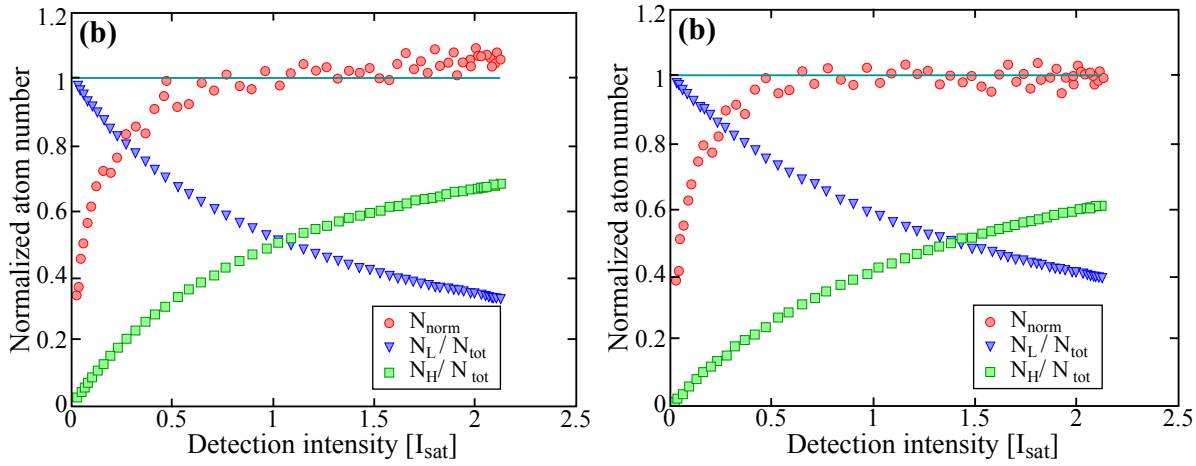

Figure 3.3: **Calibration of an effective cross section.** A thermal cloud of approximately 6×10^4 atoms is produced and detected after 20 ms time of flight, alternatively with $I = I_{sat}$ and a variable intensity. Then the atom number is normalize over the one measured at the saturation intensity in order to get rid of preparation fluctuations. Initially, the cross section is taken equal to σ_0 ($\alpha = 1$) **(a)**, then the least mean square minimization described in the text is applied and the data are corrected with the α coefficient **(b)**.

As explained in [201], the protocol to determine α is the following. First one needs to produce and detect a series of atomic clouds with a fixed number of atoms for different detection intensities. Every other shot has to be realized with $I = I_{sat}$ in order to keep track of the prepared atom number. The shots with the scanned intensity give the atom numbers N_H and N_L (defined in equation (3.7)) while the ones with the fixed intensity give N_H^{ref} and N_L^{ref}. Then two parameters have to be derived:

$$\zeta(\alpha) = \frac{N_H + \frac{1}{\alpha}N_L}{N_H^{ref} + \frac{1}{\alpha}N_L^{ref}} \text{ and } \chi^2(\alpha) = \frac{1}{N_{err}^2}\sum_i (1 - \xi_i(\alpha))^2, \tag{3.9}$$

where i refers to a single shot, $N_{err}^2 = \frac{\sigma^2(N^{ref})}{<N^{ref}>^2}$ estimates the error made on the atom number due to preparation fluctuations. Finally, α is chosen to minimize the quantity χ^2 (least mean square minimization).

After repeating this procedure many times and under different conditions (atom numbers, temperatures, pulse lengths) we got

$$\boxed{\alpha = 0.76 \pm 0.025} \tag{3.10}$$

The calibrated evolution of the detected atom number as a function of the detection intensity is displayed in figure 3.3 (b).

3.2.2 Imaging very small and dense clouds

Working with Bose-Einstein condensates implies being able to efficiently image very dense atomic ensembles which is not straightforward. For instance, as depicted on figure 3.4, at short times of flight the BEC is dense enough to diffract the imaging light around itself and the resulting fringes will obviously skew the atom number estimation. This puts a strong constraint on the minimum relevant time of flight.

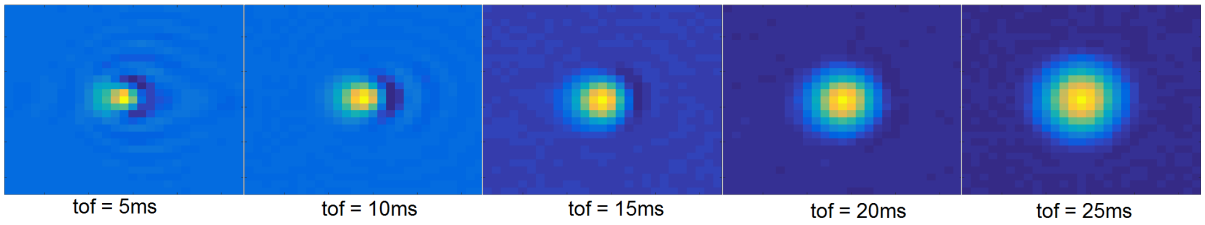

Figure 3.4: **Optical diffraction around our BEC.** Very dense atomic cloud (optical density ≈ 2 and N $\approx 10^4$ atoms) imaged after different indicated times of flight. Each of the displayed pictures corresponds to an average of 20 shots taken at $I = I_{sat}$. For short TOF, the cloud is so small and dense that the imaging light is diffracted around it. As the cloud expands while increasing the time of flight, the fringes disappear.

More quantitatively, figure 3.5 depicts the measured atom number as a function of TOF. When the atomic density is too high, the number of atoms is not properly estimated by equation (3.7). This is probably due to multiple emission and re-absorption of the same photon by several atoms in the cloud, which is not taken into account by the Beer-Lambert law. Then, as soon as the optical density is sufficiently low so that all the atoms in the cloud are excited by the imaging light, the atom number reaches a plateau which corresponds to the correct atom number. This restricts our minimum relevant time of flight to 20 ms. Note that this high density issue is due to the fact that the cloud is imaged along its strong axes (y, z).

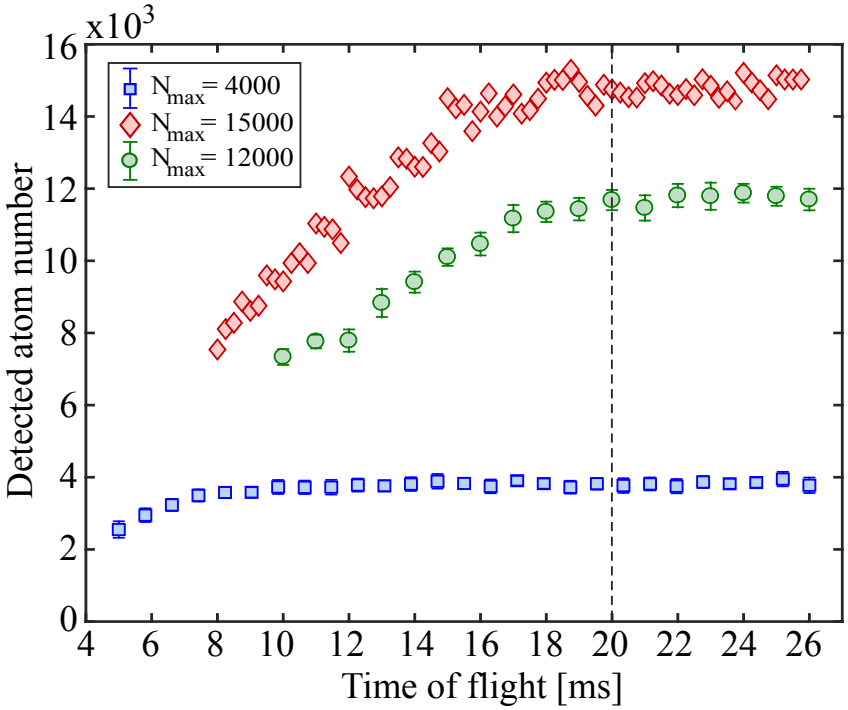

Figure 3.5: **Optimisation of the time of flight.** Mean detected atom number plotted as a function of the TOF. The dashed line represents the time from which the optical density is low enough to detect all the atoms.

3.3 Towards a shot noise limited detection system

Now that we can detect and estimate the population of the two clock states, let's analyze the stability of our detection system. Several sources of noise such as photon shot noise, inhomogeneous illumination (optical fringes), residual stray light, dark current and so on, can indeed deteriorate the quality of the acquired image and skew the atom number estimation. Thanks to the low working temperature of our CCD camera (-60°), dark currents can safely be neglected [189]. Moreover, as background pictures are acquired and removed from the principal images (*Image* and *Bright*) and as the atoms and the CCD camera are well isolated from external lights, the contribution of the residual stray light can also be neglected. Remains the inevitable photon shot noise that will be studied at the beginning of this section, and the impact of optical fringes that actually have a dramatic effect on the atom number stability. A numerical post-processing method that greatly reduces the effect of this noise will be presented and its efficiency will be challenged at the end of this part.

3.3.1 Theoretical estimation of the Photon Shot Noise

This fundamental noise source stems from the probabilistic nature of the photoelectric conversion. It can be shown that for a given incoming laser beam, a statistical probability of the number of emitting photo-electrons gives rise to a fundamental detection noise following the standard Poisson distribution [202] and translate into number of counts according to

$$\sigma^2(N_{e^-}) = \langle N_{e^-} \rangle \Longrightarrow \sigma^2(N_{counts}) = g\langle N_{counts} \rangle. \tag{3.11}$$

Let's now derive the influence of this noise on the detected atom number. From equation (3.7) and converting the fluctuations in photoelectrons into fluctuations in number of counts via equation (3.11), one can derive the impact of the photon shot noise (PSN) on the detected atom number per pixel when the system is only limited by PSN [201]:

$$\sigma^2(N)_{PSN} = gH^2 \left(\langle N'_{image} \rangle + \langle r \rangle^2 \langle N'_{bright} \rangle + \frac{\langle N'_{bright} \rangle^2 \sigma^2(r)}{g} \right) \tag{3.12}$$

$$+ gL^2 \left(\frac{1}{\langle N'_{image} \rangle} + \frac{1}{\langle N'_{bright} \rangle} + \frac{\sigma^2(r)}{g\langle r \rangle^2} \right) \tag{3.13}$$

$$+ 2gHL \left(1 + \langle r \rangle + \frac{\langle N'_{bright} \rangle}{g\langle r \rangle} \sigma^2(r) \right) \tag{3.14}$$

with $L = \frac{A}{\sigma_0}$ and $H = \frac{2}{g\eta\tau T\Gamma}$. Here we assumed that all the random processes are uncorrelated.
We can see that the formula takes into account the fluctuations of the renormalisation factor defined by equation (3.8), let's now see how significant it is. If the detection is limited by the photon shot noise, then

$$\frac{\delta r}{r} = \frac{\sum_{i,j} \delta N_{image}(i,j)}{\sum_{i,j} < N_{image}(i,j) >} - \frac{\sum_{i,j} \delta N_{bright}(i,j)}{\sum_{i,j} < N_{bright}(i,j) >}, \tag{3.15}$$

leading to:

$$\sigma^2(r) = g\langle r \rangle^2 \left(\frac{1}{\sum_{i,j} \langle N_{image}(i,j) \rangle} + \frac{1}{\sum_{i,j} \langle N_{bright}(i,j) \rangle} \right). \tag{3.16}$$

Experimentally $\langle r \rangle \approx 1$, $g = 86\%$, each pixel has approximately 3.10^4 counts ($I \approx I_{sat}$) and the renormalization area contains 10^5 pixels which gives $\sigma^2(r) \approx 5.7 \times 10^{-10}$. The contribution of the renormalisation factor fluctuations to the photon shot noise is then:

$$\sigma^2(N)_r = H^2 \langle N_{bright} \rangle^2 \sigma^2(r) + L^2 \frac{\sigma^2(r)}{\langle r \rangle^2} + 2HL \langle N_{bright} \rangle \frac{\sigma^2(r)}{\langle r \rangle} \tag{3.17}$$

$$\approx 3.1 \times 10^{-4} \text{ atoms/pixel}. \tag{3.18}$$

In order to check this result experimentally, we acquired 100 images with the same parameters and averaged the calculated r. we found $\sigma^2(r) \approx 1.2 \times 10^{-6}$ leading to $\sigma^2(N)_r \approx 6 \times 10^{-2}$ atoms/pixel, which is almost 200 times higher! This shows that the experimental fluctuations of r are not dominated by the photon shot noise. We will nonetheless identify and get rid of this additional noise source in the next part.

For the time being, let's neglect the fluctuations of r and derive the expression of the atom number per pixel fluctuations due to photon shot noise:

$$\boxed{\sigma(N)^2_{PSN} = gH^2(\langle N'_{image}\rangle + r^2\langle N'_{bright}\rangle) + gL^2(\frac{1}{\langle N'_{image}\rangle} + \frac{1}{\langle N'_{bright}\rangle}) + 2gHL(1+r)} \tag{3.19}$$

By misuse of language, in the following PSN will refer to equation (3.19).

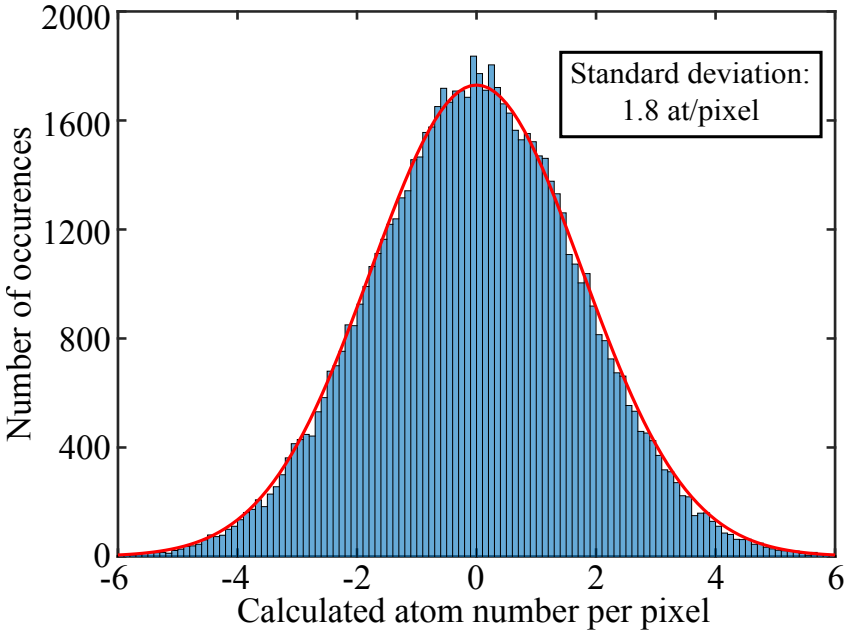

Figure 3.6: **Experimental estimation of the photon shot noise.** Histogram of the fictitious atom number per pixel over an area of 75500 pixels at $I = I_{sat}$, and without any visible optical fringes. The red curve is not an adjustment but directly the expected photon shot noise derived from equation (3.19).

One way to experimentally estimate this noise is to acquire many shots without "real" atoms (the dispenser is off) and derive the statistics of the calculated fictitious atom numbers. Even though we do not trap atoms, because of the PSN, the system still measures something. This is because the number of photons will not be exactly the same for the *Image* and *Bright* frames used to derive the fictitious atom number. Figure 3.6 shows the histogram of the calculated atom number per pixel which is in good agreement with the theoretical prediction (3.19).

3.3.2 Numerical fringe reconstruction

The second most important noise source is due to diffraction fringes created by any object in the beam path between the out-coupler of the fiber and the CCD camera. As we normalize each image by its corresponding *Bright* frame, this spatial modulation should disappear at first order. Nonetheless, any slight modification of the fringe pattern in between these two images will create artificial differences in the *Bright* and *Image* frames and skew our populations estimation. The first things that come to mind to get rid of this effect are isolating the camera and optical mounts from any vibrations and minimizing the time in between the two images. However as depicted on figure 3.7 (a), despite these efforts the final images are still affected by moving fringes.

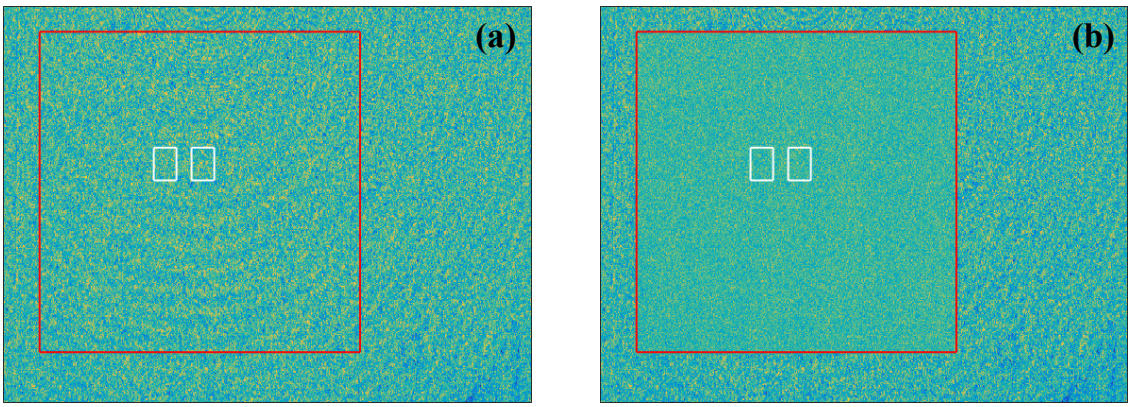

Figure 3.7: **Typical image degraded by moving fringes before and after correction.** Single shot atom number per pixel image without **(a)** and with **(b)** the numerical fringes reconstruction. The red rectangle (125×10^3 pixels) corresponds to the renormalisation area in which the fringe pattern is reconstructed and the two white ones correspond to the analysis areas (900 pixels) at the atoms position.

Another solution consists in removing those fringes numerically. The idea of this bright frame reconstruction algorithm [203] is to reconstruct the fringe pattern from a set of raw *Bright* frames previously stored. Each of these raw *Bright* frames is weighted and their contributions are summed in order to retrieve the experimental *Image* frame's background as accurately as possible. At the end of the process, the *Bright* frames basis is updated replacing the oldest frame by the new one.

More precisely, as it is illustrated on figure 3.8, the fringes will be reconstructed inside the previous renormalisation area which should now contain the analysis areas at the positions of the atoms. These analysis areas will be masked and the fringes will be reconstructed around it. This means the fringes present inside these zones will not be taken into account by the algorithm and therefore this process lies on the fact that there is no small unexpected pattern around the atoms. Then the reconstructed *Bright* frames will be used in the atom number derivation (3.7).

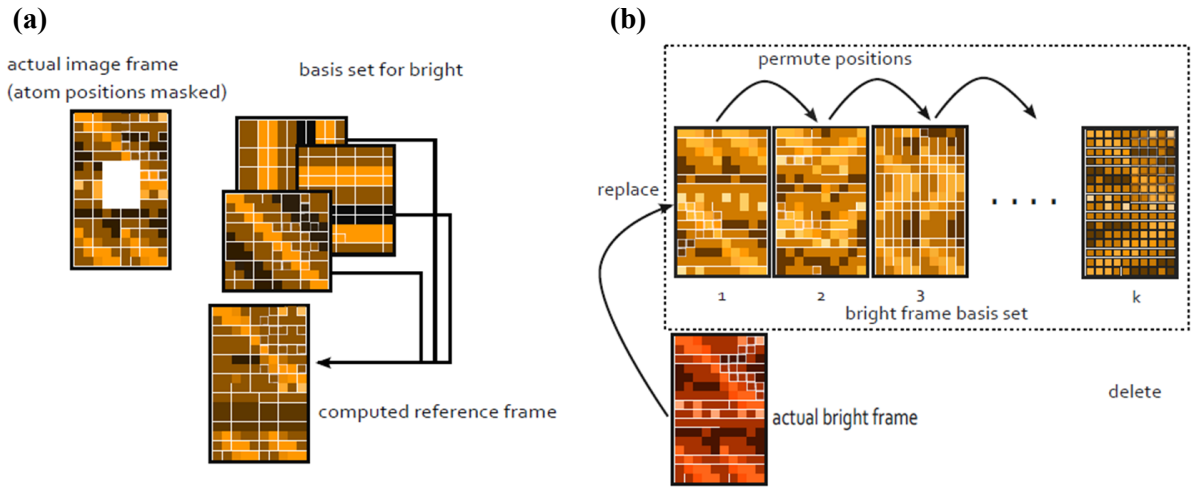

Figure 3.8: **Principle of the numerical fringe reconstruction algorithm. (a)** The actual *Image* frame without atoms is reconstructed using a linear combination of *Bright* frames previously stored. This reconstructed frame is then used as the current *Bright* frame to derive the atom number using equation (3.7). **(b)** The old *Bright* frame is subsequently stored inside the basis in place of the oldest one in order to keep the basis updated. Adapted from [189].

Note that another advantage of using the bright frame reconstruction algorithm is that it does not require the renormalisation factor (3.8) anymore. Indeed, as the *Bright* frame has been directly reconstructed from the *Image* frames, they should present the same background intensity. On top of that, as the reconstructed *Bright* picture is noise free, even in the absence of fringes the photon shot noise can be reduced by a factor up to $\sqrt{2}$.

3.3.3 Experimental study of the fringes reconstruction efficiency

If we want to perfectly reconstruct the fringe pattern, the basis would need to have as many frames as pixels. However, we also want to treat the images dynamically inside each experimental cycle and therefore we need to find a trade off between noise reduction efficiency and computational time. We found an optimum of 100 pictures which allows us to efficiently reduce the detection noise below the photon shot noise in less than 1 s. Indeed, figure 3.9 shows the inter-pixel noise reduction induced by the bright fringe reconstruction, which almost reaches the maximum noise reduction of $\sqrt{2}$ [203]. Moreover, figure 3.10 (a) shows that the correction always reduces the detection noise, no matter the detection intensity.

The efficiency of this method is however subject to some conditions. Indeed, as it is

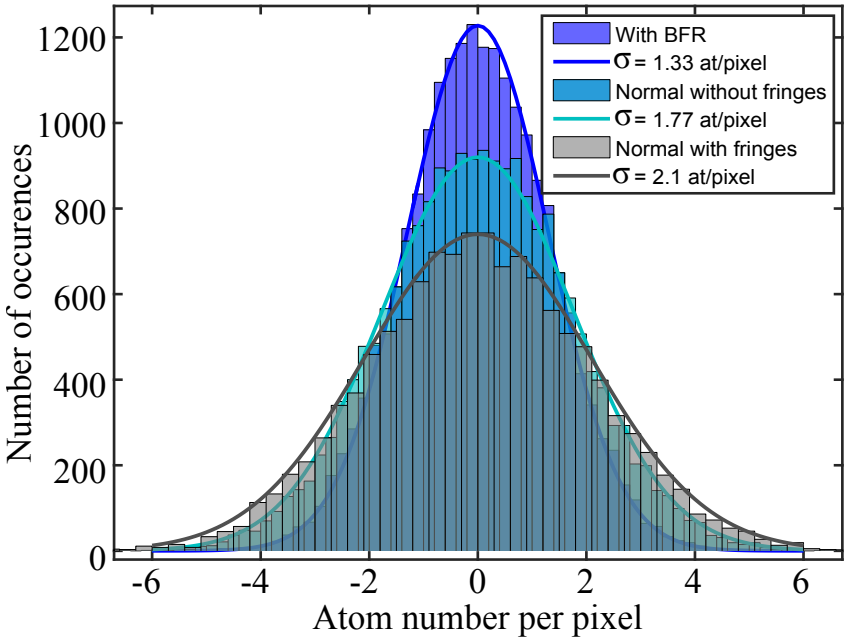

Figure 3.9: **Detection noise estimation in three different cases.** Histograms of the calculated atom numbers per pixel over the same area as figure 3.6 at $I = I_{sat}$ and without atoms, without fringes (clear blue), with fringes (grey) and using the fringe reconstruction algorithm (dark blue). The standard deviation of the data without fringes was directly derived from eq. (3.19) showing that the detection is limited by photon shot noise in the absence of fringes. On the other hand, a Gaussian adjustment is applied in the first and last cases giving a standard deviation of $2.1 > \sigma_{PSN}$ for the degraded data and $\sigma_{PSN}/\sqrt{2} < 1.33 < \sigma_{PSN}$ after correction.

shown on figure 3.10 (b), the noise is effectively reduced only if the analysis rectangle is small enough so that the fringes pattern inside is the same as the one around. Moreover, we need to let "enough" space between the white and red rectangles in order to have enough fringes to reconstruct. As stated before, the fringes inside the analysis areas are not taken into account by the algorithm, the size of these areas thus matters. The larger they are, the less precise the reconstruction will be.

Another way to check the fidelity of the reconstruction is to measure the resulting renormalisation factor. Averaging over 100 shots under the same conditions as (3.18), we find $\langle \delta r^2 \rangle \approx 5.8 \pm 0.1 \times 10^{-10}$ which corresponds to the theoretical expectation for photon shot noise limited detection.

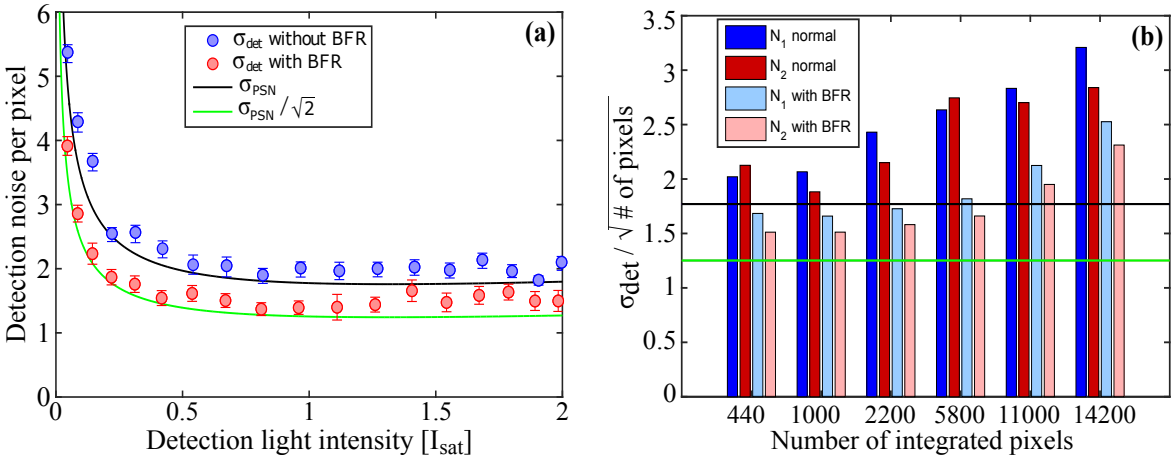

Figure 3.10: **Efficiency of the fringe reconstruction algorithm versus intensity and analysed area.** **(a)** Series of 200 images (10^3 pixels) have been acquired and analysed for different imaging intensities, without any fringe reconstruction (blue dots) and applying the fringe reconstruction algorithm (red dots). **(b)** A set of 50 images taken at $I = I_{sat}$ has been treated using different analyzed area sizes with (light colors) and without (heavy colors) the reconstruction algorithm. On both graphs, the black line corresponds to the theoretical photon shot noise calculated from (3.19) and the green line corresponds to the maximum noise reduction of $\sqrt{2}$ triggered by the numerical fringe reconstruction as explained in the text.

3.4 Implementation of the Adiabatic Rapid Passage

This second double state detection scheme was initially investigated on TACC in order to minimize state-dependent detection efficiency due to the repumping step and reduce technical noise arising from frequency fluctuations of the imaging laser between the detection of the two states. This detection method allows the simultaneous detection of the two clock states with only one detection pulse, which should reduce the noise due to laser frequency and power fluctuations during the detection. This method, very similar to the one described in [82], has already been investigated on our set-up by former Ph.D. students [113, 189], but the available microwave power was limiting the efficiency of the transfer which could not reach 100 %. Its brief description, experimental implementation including the addition of a high power amplifier, and calibration are presented in this section.

3.4.1 Limitations of the standard double detection

The standard double detection scheme whose principle is depicted on figure 3.2, has several drawbacks. First of all, as the two states are detected with different light pulses,

the measured transition probability is sensitive to power and frequency fluctuations of the detection laser. This effect will be highlighted later on figure 3.15. Second of all, as it has already been pointed out in [113], this detection method can present a lower detection efficiency for state $|1\rangle$. Indeed, in average one atom needs to scatter several rempumping photons before reaching the imaging transition and as the repumping beam is sent together with the detection beam, no detection photon is scattered by this atom during the repumping process. Because the incoming light power is reduced at the center of the cloud, the denser the atomic ensemble, the more dramatic this effect. Such state-dependent detection efficiency is illustrated on figure 3.11 (a) in the framework of Rabi oscillations. Another yet minor drawback is the need to push away the atoms detected with the first detection pulse so that they are not counted twice. Besides, from a more technical point of view, it is worth recalling that this methods requires a camera with frame transfer, that would no longer be necessary using the ARP and the numerical fringe reconstruction algorithm.

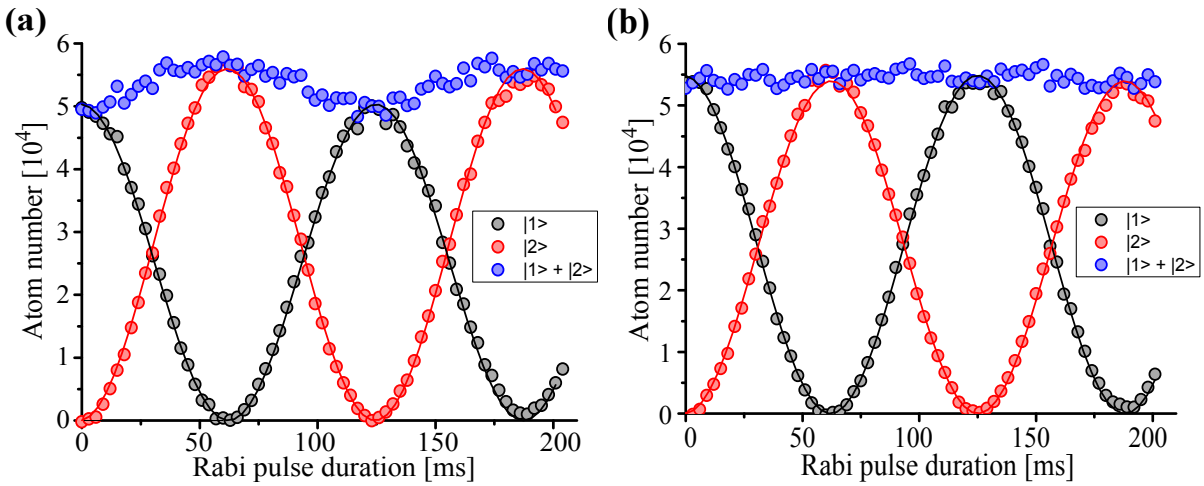

Figure 3.11: **Comparison of the two detection schemes in term of state detectivity.** Rabi oscillations between the two clock states $|1\rangle$ (black) and $|2\rangle$ (red) detected with the two presented detection methods. In the case of the SDD **(a)**, the oscillation of the total atom number (blue) testifies of a state-dependent detection efficiency. The sinusoidal fits give a detection efficiency of $|1\rangle$ lower than the one of $|2\rangle$ by a factor 0.89. On the other hand, for the ARP **(b)** the total atom number (blue) remains constant and the fits give the same detection efficiency for the two states.

3.4.2 Principle

As depicted on figure 3.12, the idea is to first transfer all the atoms initially in $|1\rangle$ into a non-trapping state in $F = 2$, namely $|2, 0\rangle$. Then the transferred cloud starts to fall under the action gravity during approximately 1 ms. Next the atoms initially in $|2\rangle$ are released from the trap by turning off the trapping fields and start to fall as well. Finally the imaging light is sent to detect both states simultaneously.

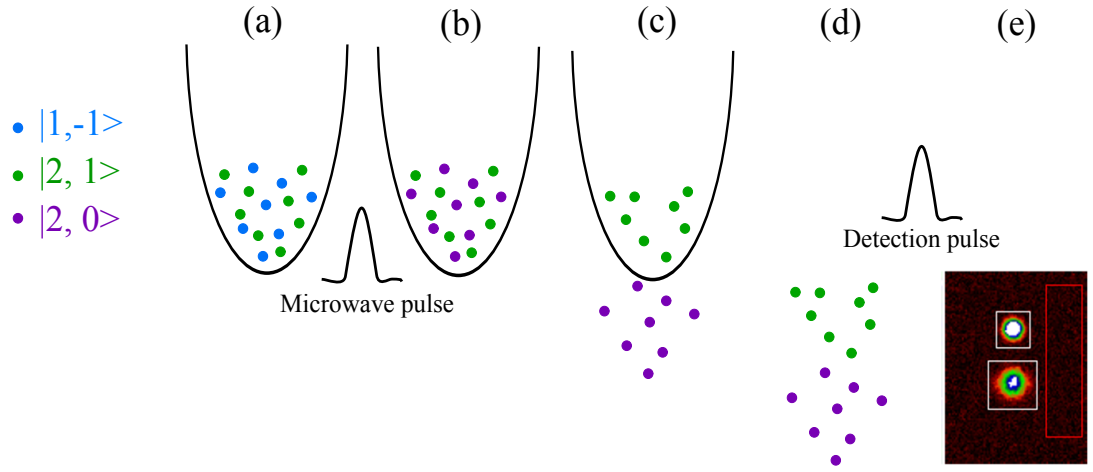

Figure 3.12: **Schematic of the ARP technique. (a)** Atoms in clock states $|1\rangle$ (blue) and $|2\rangle$ (green). **(b)** A 1.5 ms microwave pulse transfers all the atoms from $|1\rangle$ to $|F = 2, m_F = 0\rangle$ (purple). **(c)** The atoms initially in $|1\rangle$ fall under the action gravity during 1 ms. **(d)** The trapping fields are turned off and the atoms in $|2\rangle$ begin to fall as well. **(e)** After some time of flight, the two states are imaged simultaneously with the same detection pulse.

Because of the microwave field inhomogeneity (cf sections 2.4 and 5.4.3 and [74]) and the high dependency of this transition on the magnetic field, reaching a 100% transfer efficiency is not trivial. A powerful solution consist in implementing an adiabatic rapid passage (ARP) technique [204,205]. The idea is to slowly sweep the MW frequency across resonance in order to keep the atoms in the same dressed state which will adiabatically evolve from $|1\rangle$ to $|2, 0\rangle$. The adiabaticity is ensured by the condition

$$\frac{d\delta}{dt} << \Omega^2, \tag{3.20}$$

where Ω and δ denote the corresponding Rabi frequency and the detuning.

Another difficulty is that the transfer has to be fast and adiabatic at the same time. The transfer velocity constraint has two origins: first, as the transferred atoms are not trapped, they will start to fall as soon as they reach $|2, 0\rangle$. Therefore, if the transfer is too slow, the cloud will be elongated or even fragmented. Second, as we want to study

and control the evolution of the spin distribution, we want to make the transfer on a shorter time-scale than the spin dynamics (10-100 ms). This timing constraint combined with condition (3.20) imply a strong limit on the minimum required Rabi frequency.

On the other hand, this double state detection method bears the advantage of using only one imaging pulse and therefore the resulting measured transition probability is insensitive to frequency and power fluctuations of the imaging light. Moreover if the ARP is well implemented, meaning that state $|1\rangle$ is perfectly transferred into $|2,0\rangle$, the two states are detected with the same maximum efficiency. Let's note that because the atoms are in $|2,0\rangle$, they still need to be pumped to $|2,2\rangle$ by the first detection photons in order to be detected.

3.4.3 Experimental realization

As the transition $|1,-1\rangle \rightarrow |2,0\rangle$ does not have the same magnetic moment, it is very sensitive to magnetic field fluctuations. A frequency ramp is thus required in order to have a 100% efficiency. Instead of directly ramping the MW frequency, we ramp the Zeeman magnetic field (bias field along the x-axis) which is easier to implement experimentally. The adiabaticity is ensured by a Blackman pulse shape for the microwave power and a half-Blackman ramp for B_x (figure 3.13), which also minimizes off-resonance excitations [206].

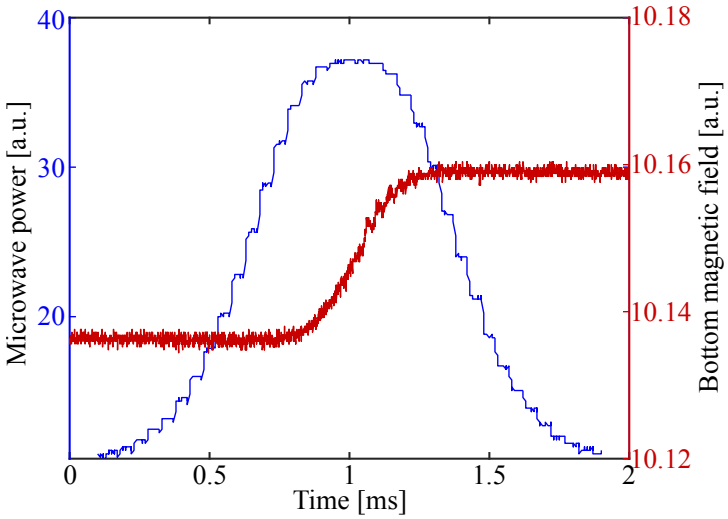

Figure 3.13: **Blackman shapes used for the microwave pulse and the Zeeman field ramp.** Temporal profiles of the microwave power after amplification (+20.4 dB) and bottom magnetic field sweep used for achieving adiabatic rapid passage. The time steps visible on the amplitude curve are due to the 50 μs timing resolution of the experiment control.

The strong microwave field is generated by our second homebuilt microwave chain

(the first one is used to generate the clock microwave photon). A 40 dB microwave amplifier (GaAs FET Linear Power Amplifier KUPA 7000A) is then used to amplify the signal in order to get a sufficiently high Rabi frequency. It is subsequently combined with the MW interrogation signal and sent to the on-chip coplanar waveguide. The Blackman shapes, represented on figure 3.13 have the following expressions, where τ is the pulse duration:

$$V_{chainA} = V_{min} + (V_{max} - V_{min})[\frac{21}{50} - \frac{1}{2}\cos(2\pi\frac{t}{\tau}) + \frac{2}{25}\cos(4\pi\frac{t}{\tau}))] \tag{3.21}$$

$$B_x = B_{center} + \frac{B_{span}}{2} - B_{span}[\frac{t}{\tau} - \frac{25}{42\pi}\sin(2\pi\frac{t}{\tau}) + \frac{1}{21\pi}\sin(4\pi\frac{t}{\tau}))] \tag{3.22}$$

With $V_{min} = 0.4V, V_{max} = 0.82V, B_{center} = 3.055G, B_{span} = 0.1G$ and $\tau = 1.5ms$. The voltage numbers are sent to a voltage-controlled attenuator located at the output of the chain.

3.4.4 Efficiency of the ARP

To quickly test this imaging technique, all the atoms start in $|1,-1\rangle$ and the strong MW pulse transfers then into $|2,0\rangle$. Then both the detection and repumper beams are sent to detect them as if there were no ARP. This way the atoms transferred in $|2,0\rangle$ and the remaining ones in $|1,-1\rangle$ can be spatially discriminated. For 6000 atoms, a transfer of $99.45\% \pm 0.94\%$ can be achieved, whose uncertainty is related to the detection noise.

For completeness, we took 50 images of the two sates (after a resonant $\frac{\pi}{2}$-pulse) using standard double state detection, and 50 images of only state $|1\rangle$ (without interrogation pulse) with the ARP. Then the two sets of 50 images are averaged and the first one (two clouds) is fitted with a parabolic function in order to get the average position and dimensions of the clouds. The second set of averaged images is subsequently fitted with the same parabolic function but keeping the dimensions, positions and background fixed[1], only the amplitude is kept as a free parameter. As it appears clearly on figure 3.14, the fitted empty area gives an amplitude at the center of the cloud of -0.03 ± 0.15 atom/pixel, which is consistent with 0 and confirms that the transfer is perfect within the detection noise. We check that the transfer has the same efficiency for our maximum atom number ($N_{BEC} \approx 15 \times 10^3$).

3.5 Calibration using the standard quantum limit

In order to complete the characterization of our detection system, we will now check the accuracy of our atom number estimation by comparing the measured atomic noise

[1] As the fit tries to minimize the difference between the sum of all the pixel of the fitting function and the actual image, the program tends to increase the background to compensate the low amplitude.

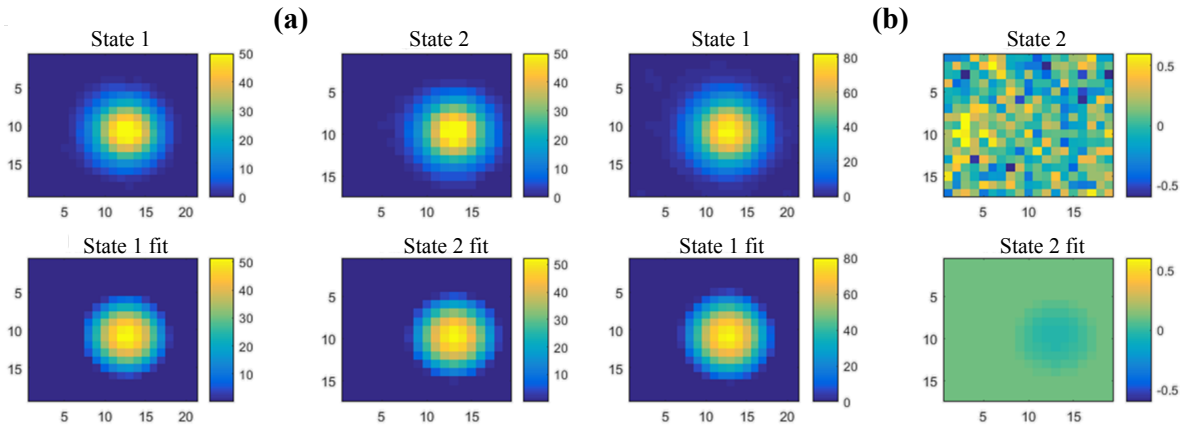

Figure 3.14: **Characterization on the ARP efficiency. (a)** 4000 atoms are prepared in a coherent superposition and imaged with the standard double state detection method 50 times. The 50 images are averaged (upper images), and the averaged clouds are fitted with a parabola (lower images). **(b)** 4000 atoms are prepared in $|1\rangle$ and imaged with the ARP method + repumper 50 times. The "state 1" images correspond to the atoms detected with the ARP and the "state 2" images correspond to the remaining one detected after being re-pumped.

of a coherent superposition with the quantum projection noise. Being fundamental, the standard quantum limit appears like a trustful quantity to calibrate the detection system [60, 61]. Others absolute atom number calibration techniques can also be found in [83].

3.5.1 Experimental investigation of the atomic noise

In order to evaluate the performances of our system in terms of atomic noise and check the calibration of our detection, we used the following procedure. We prepare the atoms in a coherent superposition by applying a resonant $\pi/2$ pulse and detect the populations in the two states N_1 and N_2 directly after the pulse. Then we compute the transition probability P_2 and the population difference S_z:

$$P_2 = \frac{N_2}{N_1 + N_2} \text{ and } S_z = \frac{N_2 - N_1}{2}. \tag{3.23}$$

These two quantities are of particular interest because they offer two different representations of the same physical feature: the atomic noise of a coherent superposition. The standard statistical tool to study the transition probability fluctuations is the standard deviation,

$$\sigma(P_2) = \sqrt{\frac{\sigma_{det}^2(N_1, N_2)}{\overline{N}^2} + \frac{\sigma_{qpn}^2}{\overline{N}} + \sigma_{tech,P_2}^2}, \tag{3.24}$$

while the variance is preferred to study the population difference fluctuations because it scales quadratically with the total atom number $N = N_1 + N_2$,

$$\sigma^2(S_z) = \sigma_{det}^2(N_1, N_2) + \sigma_{qpn}^2 \overline{N} + \sigma_{tech,S_z}^2 \overline{N}^2. \tag{3.25}$$

In equations (3.24) and (3.25), the first term represents the impact of the single state detection noises $\sigma_{det,i}$ on P_2 or S_z (with $i = 1$ and 2 for states $|1\rangle$ and $|2\rangle$) and it can be easily shown that

$$\sigma_{det}^2(N_1, N_2) = \frac{\overline{N_1}^2 \sigma_{det,2}^2 + \overline{N_2}^2 \sigma_{det,1}^2}{\overline{N}^2}. \tag{3.26}$$

In the case of an equal superposition and if the two analysis areas are roughly the same (same number of pixels and same incoming intensity), then $\sigma_{det}^2(N_1, N_2) \approx \frac{\sigma_{det}^2}{2}$. The second term is the quantum projection noise which has already been defined in section 1.5.1. In the case of a coherent spin state and after a $\frac{\pi}{2}$-pulse, we should have $\sigma_{qpn} = 0.5$. The last term represents technical noise due to preparation noise like Rabi frequency fluctuations or detection efficiency fluctuations between the two states because of imaging laser power and frequency instabilities [189]. Note that the later is suppressed with the ARP imaging technique.

3.5.2 Comparison between the different detection techniques

In this section, the two detection methods presented above are compared using the measured atomic noise of a coherent superposition described by equation (3.24). In order to emphasize the difference between the two techniques, the frequency noise of the detection laser has been voluntarily degraded. For this purpose, thermal atoms (≈ 80 nK) are first prepared in a coherent superposition with a 70 ms $\pi/2$ pulse. The two states are then detected using either the standard double detection or the adiabatic rapid passage after a 10 ms time of flight. The atom number is controlled with the MOT loading time.

As depicted on figure 3.15 the technical noise of the SDD method is significantly degraded by the frequency noise of the detection laser while the ARP is unaffected. Moreover, the difference in detection noise is explained by the different "waiting" time between detection of the two states. More specifically, the time required to push the detected atoms makes the time of flight slightly higher for state $|1\rangle$, and thus the cloud bigger in the case of the standard double detection. As the number of integrated pixels is higher, the detection noise increases.

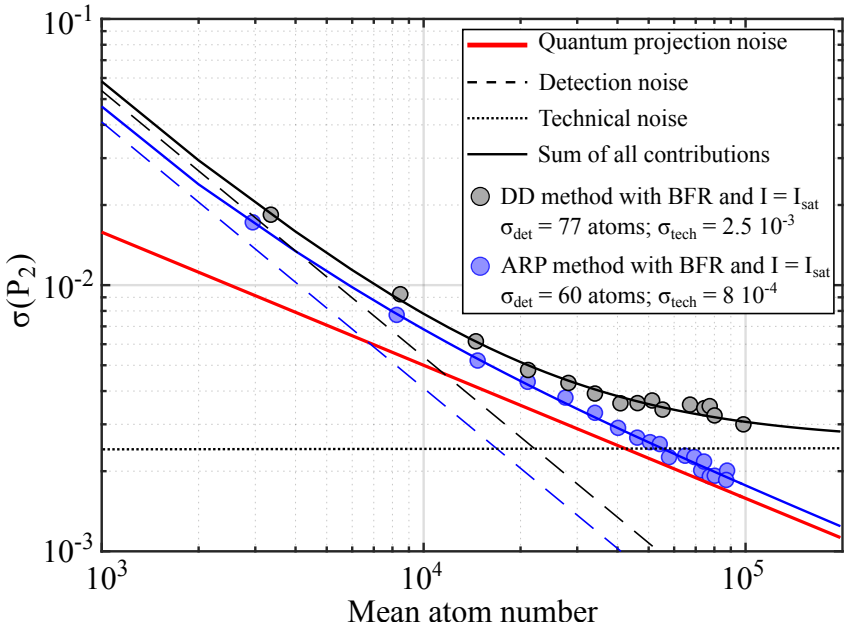

Figure 3.15: **Comparison between SDD and ARP.** The standard deviation of the transition probability P_2 is plotted as a function of the total detected atom number using the double detection method (black points) or the adiabatic rapid passage (blue points). Each point is an average of 300 shots. The black and blue lines corresponds to a fit using equation (3.24) where σ_{qpn} is fixed to 0.5 and σ_{det} and σ_{tech} are taken as free parameters. The red line represents the quantum projection noise for a 50% transition probability. The contribution of the detection noise for the two detection methods is indicated with the dashed lines.

3.5.3 Optimum solution to investigate squeezing

Concerning the squeezing measurement, the good calibration of the atom number is primordial. For this purpose, we will use the ARP imaging technique with the bright frame reconstruction algorithm described in section 3.3.2.

Figure 3.16 shows the evolution of the atomic noise of a coherent superposition probed via the transition probability (a) and the population difference (b) as a function of the detected total atom number. The evolution of $\sigma(P_2)$ shows the contribution of the detection noise (blue line) with respect to the standard quantum limit (red line). More precisely, it indicates that our detection system is dominated by shot noise from 3000 atoms. Besides, the evolution of $\sigma(S_z)^2$ is used to calibrate the atom number. According to equation (3.25), this noise should scale linearly with the measured atom number with a rising slope of 0.25. The fit giving a negligible quadratic part and a slope of 0.248 ± 0.008 testifies of the good calibration of our detection system. On the other hand, the detection noise of approximately 33 atoms is, as expected, a bit below photon shot noise:

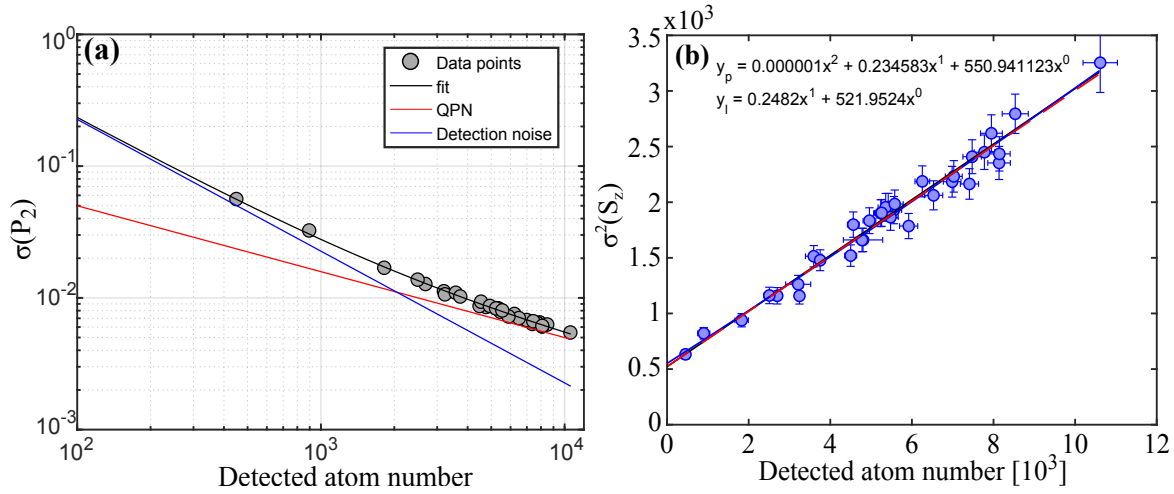

Figure 3.16: **Atomic noise on P_2 and S_z versus atom number. (a)** Noise on P_2 as a function of the total atom number. The black stars are experimental data, the black line is a fit with equation (3.24), the blue line represents the detection noise and the red line represents the quantum projection noise. **(b)** Variance of the population difference S_z as a function of the total atom number. The red dashed line represents a linear fit which yields to a slope of 0.248±0.008 and a detection noise of 32.4 ± 1.4 atoms, whereas the blue dashed line represents a quadratic fit with a linear part of 0.23±0.03 and a quadratic part of $(1.3\pm2.7)\times10^{-6}$.

$\frac{\sigma_{PSN}}{\sqrt{2}} < \sigma_{det} < \sigma_{PSN}$, with $\sigma_{PSN} = 39$ atoms for a integrated area containing 380 pixels. All the fitted parameters are regrouped in table 3.2.

Fitted quantity	σ_{det}	σ_{qpn}	σ_{tech}
P_2 (eq. (3.24))	32.7 ± 1	0.495 ± 0.07	$(0.6 \pm 1.2)\ .10^{-3}$
S_z (eq. (3.25))	33.2 ± 2	0.48 ± 0.03	$(1.1 \pm 2)\ .10^{-3}$
S_z (linear)	32.3 ± 1	0.498 ± 0.008	-

Table 3.2: Table regrouping the the fits on P_2 and S_z for the three free parameters σ_{det}, σ_{qpn} and σ_{techn}.

Chapter 4

State-dependent spatial dynamics in a bimodal BEC

*****

First observed in 1998 [80], the phase evolution of a two-component Bose-Einstein condensates has been experimentally investigated several times since then [81, 82, 155]. As already stated before, we would like to get use of the spontaneous spatial dynamics to investigate the generation of spin squeezing arising from collisions in a Bose-Einstein condensate. Prior to the study of the spin noise distribution, a good understanding of the separation and its impact on the coherence of the system is necessary.

This chapter is hence dedicated to the experimental study of an interacting bimodal BEC. Keeping in mind the quantum metrological context in which this experiment has been designed, the coherence properties as well as the spatial dynamics of such a system are of particular interest here. Firstly, a theoretical model is introduced to explain the experimental data and provide some intuitive hints about the involved physical phenomena. Secondly, a direct evidence of the spontaneous spatial dynamics is presented. A Ramsey interferometric scheme is also introduced to study the coherence of the interacting system. Thirdly, three different parameters (sensitivity function, contrast and relative frequency) extracted from the interferometric measurement are analyzed. Each of these three parameters provides valuable information on the atomic ensemble (coherence, mean-field dephasing, spatial dynamics). Fourthly, different parameters such as trapping frequencies or atom numbers are investigated in order to optimize the state-dependent spatial dynamics in terms of contrast and time scale.

4.1 Theoretical considerations

The complete theoretical study of a two-component Bose-Einstein condensate in a harmonic trap is not trivial and many recent publications are dedicated to this topic [166, 171, 174, 175, 207, 208], with a particular focus on the impact of atom losses on the coherence of the system in [173].

In this section, we introduce a numerical model initiated in [113], that we use to reproduce the experimental data. It consists in solving the coupled Gross-Pitaevskii equations in three dimensions and in the presence of losses, and it is very similar to the ones developed in [83, 168, 209]. Some predictions concerning the spatial dynamics and its impact on the atomic coherence are then inferred using our experimental conditions.

4.1.1 Numerical model

As no full analytical treatment of the interacting bimodal BEC in a harmonic trap is available, a numerical simulation was developed to model the spatial and temporal evolution of the two modes wave-functions, and its working principle is the following. To the set of coupled Gross-Pitaevkii equations (1.74) developed in section 1.4.4, we add the contribution of atomic losses and the coupling to an interrogation field of Rabi frequency Ω and zero detuning, leading to [209]

$$
\begin{aligned}
i\hbar\frac{\partial\psi_1(\mathbf{r},t)}{\partial t} &= \left[-\frac{\hbar^2}{2m}\nabla^2 + U_1(\mathbf{r},t) + g_{11}|\psi_1(\mathbf{r},t)|^2 + g_{12}|\psi_2(\mathbf{r},t)|^2 - i\hbar K_1(\mathbf{r},t)\right]\psi_1(\mathbf{r},t) \\
&\quad + \frac{\hbar\Omega}{2}\psi_2(\mathbf{r},t) \\
i\hbar\frac{\partial\psi_2(\mathbf{r},t)}{\partial t} &= \left[-\frac{\hbar^2}{2m}\nabla^2 + U_2(\mathbf{r},t) + g_{22}|\psi_2(\mathbf{r},t)|^2 + g_{12}|\psi_1(\mathbf{r},t)|^2 - i\hbar K_2(\mathbf{r},t)\right]\psi_2(\mathbf{r},t) \\
&\quad + \frac{\hbar\Omega}{2}\psi_1(\mathbf{r},t),
\end{aligned}
\tag{4.1}
$$

where the interaction strength between states $|i\rangle$ and $|j\rangle$ reads $g_{ij} = \frac{4\pi\hbar^2}{m}a_{ij}$. We also added the loss terms $K_1(\mathbf{r},t) = \gamma_{bck} + \frac{1}{2}\gamma_{12}|\psi_2|^2$ and $K_2(\mathbf{r},t) = \gamma_{bck} + \frac{1}{2}\gamma_{12}|\psi_1|^2 + \frac{1}{2}\gamma_{22}|\psi_2|^2$ already defined in section 1.2.3 accounting for atom loss.

For convenience, let's rewrite the system in a more compact form

$$
i\hbar\frac{d}{dt}\begin{pmatrix}\psi_1(\mathbf{r},t)\\ \psi_2(\mathbf{r},t)\end{pmatrix} = \begin{pmatrix}H_{kin}+H_1 & \frac{\hbar\Omega}{2}\\ \frac{\hbar\Omega}{2} & H_{kin}+H_2\end{pmatrix}\begin{pmatrix}\psi_1(\mathbf{r},t)\\ \psi_2(\mathbf{r},t)\end{pmatrix}, \tag{4.2}
$$

where

$$
\begin{aligned}
H_{kin} &= -\frac{\hbar^2}{2m}\nabla^2 \\
H_i &= U_i(\mathbf{r},t) + g_{ii}|\psi_i(\mathbf{r},t)|^2 + g_{ij}|\psi_j(\mathbf{r},t)|^2 - i\hbar K_i(\mathbf{r},t)
\end{aligned}
\quad , \tag{4.3}
$$

and $j = 2$ if $i = 1$ and conversely.

The numerical resolution of such set of coupled equations is done in two steps. First the ground state of the system is found,without any coupling between internal states ($\Omega = 0$), using an imaginary time propagation (or direct relaxation) method [210, 211]. It simply consists in redefining the time as imaginary : $t \rightarrow$ -iτ, and derive the time evolution of the wave-functions by applying the propagator

$$
\psi(\mathbf{r}, t+dt) = e^{-i\hat{H}dt}\psi(\mathbf{r},t). \tag{4.4}
$$

To illustrate the method, let's consider a linear Hamiltonian $\hat{H}$. By expanding the wave function in the basis of the eingenstates of the Hamiltonian $\psi(\mathbf{r},t) = \sum c_k|\phi_k\rangle$ with $\hat{H}|\phi_k\rangle = E_k|\phi_k\rangle$, equation (4.4) becomes $\psi(\mathbf{r},t+dt) = \sum c_k e^{-E_k d\tau}|\phi_k\rangle$. The contribution of the eigenstates thus decreases exponentially with their energy meaning that the sum converges towards the least energy state, namely the ground state.

Following this, concerning the "mean field + trapping potential" part of the Hamiltonian, the propagator (4.4) becomes

$$
\begin{pmatrix}\psi_1(\mathbf{r},t+dt)\\ \psi_2(\mathbf{r},t+dt)\end{pmatrix}_{MF} = \underbrace{\begin{pmatrix}e^{-iH_1dt} & 0\\ 0 & e^{-iH_2dt}\end{pmatrix}}_{\mathcal{L}(dt)}\begin{pmatrix}\psi_1(\mathbf{r},t)\\ \psi_2(\mathbf{r},t)\end{pmatrix}. \tag{4.5}
$$

The contribution of the kinetic energy term H^{kin} is solved in momentum space using a discrete Fourier transform [212]. In that space, the propagation of the kinetic energy is simply given by

$$\begin{pmatrix}\psi_1(\mathbf{r},t+dt)\\ \psi_2(\mathbf{r},t+dt)\end{pmatrix}_{Kin} = \underbrace{\begin{pmatrix}e^{-i\tilde{H}_{kin}dt} & 0\\ 0 & e^{-i\tilde{H}_{kin}dt}\end{pmatrix}}_{\mathcal{K}(dt)}\begin{pmatrix}\psi_1(\mathbf{r},t)\\ \psi_2(\mathbf{r},t)\end{pmatrix}, \tag{4.6}$$

where

$$\tilde{H}_{kin} = \frac{\hbar^2}{2m}\|\mathbf{k}\|^2. \tag{4.7}$$

Indeed, it can be shown that $FFT(H_{kin}\psi(\mathbf{r},t)) = \frac{\hbar^2}{2m}\|\mathbf{k}\|^2 FFT(\psi(\mathbf{r},t))$, where $\|\mathbf{k}\|^2 = k_x^2 + k_y^2 + k_z^2$ is the norm of the momentum $\mathbf{k}$ and FFT represents the fast Fourier transform algorithm [209, 213]. For each imaginary time-step, the global propagation of the wave-functions is then given by (split-step method)

$$\begin{pmatrix}\psi_1(\mathbf{r},t+dt)\\ \psi_2(\mathbf{r},t+dt)\end{pmatrix}_{GS} = \mathcal{L}\left(\frac{dt}{2}\right).FFT^{-1}.\mathcal{K}\left(dt\right).FFT.\mathcal{L}\left(\frac{dt}{2}\right).\begin{pmatrix}\psi_1(\mathbf{r},t)\\ \psi_2(\mathbf{r},t)\end{pmatrix}, \tag{4.8}$$

where $FFT.H.U \equiv FFT(H.U)$ and idem for FFT^{-1}.

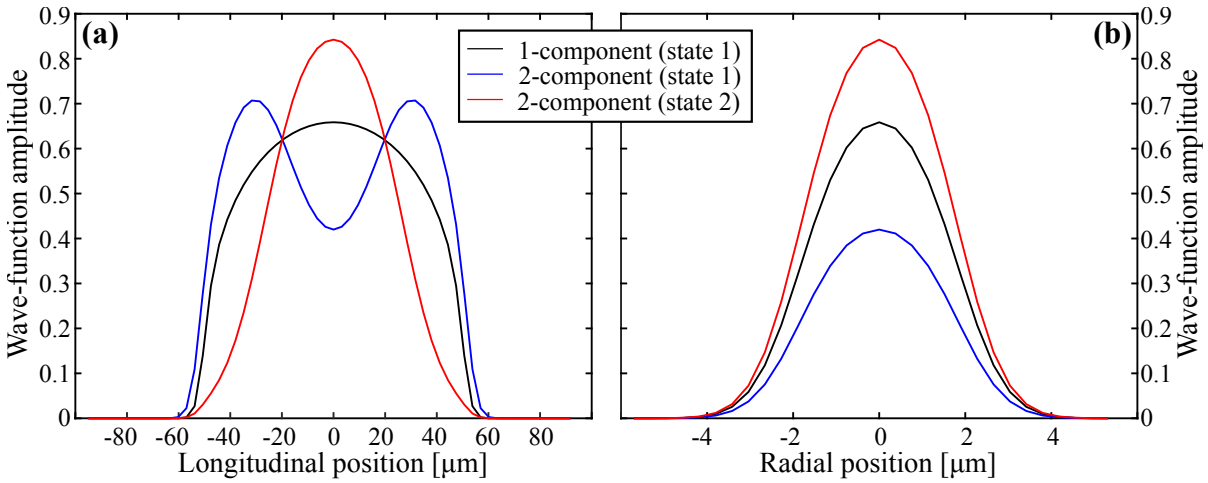

Figure 4.1: **BEC ground states.** Longitudinal **(a)** and radial **(b)** ground state profiles of the one-component (black line) and two-component (blue and red lines) BEC. The total atom number is 12×10^3.

As the global evolution is not unitary, the wave-functions have to be normalized at each time-step. Using this method, the ground-states of the one-component and two-component BEC can be obtained, as illustrates figure 4.1. Note that, this model was also used to derive the ground state of a single component BEC on figure 1.13 in section 1.4.3, to check the validity of the atomic density estimation in the cross-over regime.

Second, once the ground state has been found, its time evolution is derived using the same propagators (4.5) and (4.6) but with a real time ($t \in \mathbb{R}$). The evolution of the internal states is done separately through the propagator [214]

$$\begin{pmatrix}\psi_1(\mathbf{r},t+dt)\\ \psi_2(\mathbf{r},t+dt)\end{pmatrix}_{Int} = \underbrace{\begin{pmatrix}\cos(\frac{\Omega}{2}dt) & -i\sin(\frac{\Omega}{2}dt)\\ -i\sin(\frac{\Omega}{2}dt) & \cos(\frac{\Omega}{2}dt)\end{pmatrix}}_{\mathcal{I}(dt)} \begin{pmatrix}\psi_1(\mathbf{r},t)\\ \psi_2(\mathbf{r},t)\end{pmatrix}. \tag{4.9}$$

The total propagation of the wave-function during a time-step dt is finally given by

$$\begin{pmatrix}\psi_1(\mathbf{r},t+dt)\\ \psi_2(\mathbf{r},t+dt)\end{pmatrix} = \mathcal{I}\left(\frac{dt}{2}\right).\mathcal{L}\left(\frac{dt}{2}\right).FFT^{-1}.\mathcal{K}\left(dt\right).FFT.\mathcal{L}\left(\frac{dt}{2}\right).\mathcal{I}\left(\frac{dt}{2}\right).\begin{pmatrix}\psi_1(\mathbf{r},t)\\ \psi_2(\mathbf{r},t)\end{pmatrix} \tag{4.10}$$

More precisely, the resolution is performed in three dimensions and the trapping potentials are harmonic ($\{\omega_x,\omega_y,\omega_z\} = 2\pi \times \{2.9, 92, 74\}$ Hz) and identical for the two states. Moreover, the loss terms and the s-wave scattering lengths are taken from [124].

4.1.2 Theoretical predictions

Before starting the experiment, let's have a look at some theoretical predictions using the previously described numerical model with our cigare-shaped trap. On figure 4.1 is displayed the ground state of a single-component and two-component BEC. Because of elastic interactions, the ground state of the dual-component BEC is deformed compared to the one-component situation. Namely, state $|1\rangle$ is localized toward the borders of the trap resulting in the double peaked distribution, while state $|2\rangle$ gets more confined at the center. The shape of the radial component is however barely affected, only the relative amplitudes change. This shows that the dynamics is mainly one dimensional, which is consistent with our trapping geometry ($\omega_x << \sqrt{\omega_y\omega_z}$). In the following, we will therefore focus on the axial dynamics.

Let's now see how the atomic system will evolve after the application of a resonant $\frac{\pi}{2}$-pulse. Figure 4.2, shows the temporal evolution of the two longitudinal wave-functions. The first 70 ms correspond to the application of a resonant $\frac{\pi}{2}$-pulse that coherently prepares the two-component BEC. Then state $|1\rangle$ goes toward the borders of the trap while state $|2\rangle$ gets denser at the center. The two states briefly recombine before state $|2\rangle$ also split and becomes localized at the periphery of the trap. This dual oscillation is repeated in a pseudo-periodic manner.

This demixing effect can be interpreted as follows. Because the two-component's ground state interaction energy differs from the single component's one, the system after the $\frac{\pi}{2}$-pulse is no longer in its least energy state. To minimize its energy, the atomic ensemble converts its newly increased interaction energy into kinetic energy, leading to phase separation. As the two states separate, the moving atoms experience a growing trapping potential until it compensates their initial kinetic energy. The atoms will then

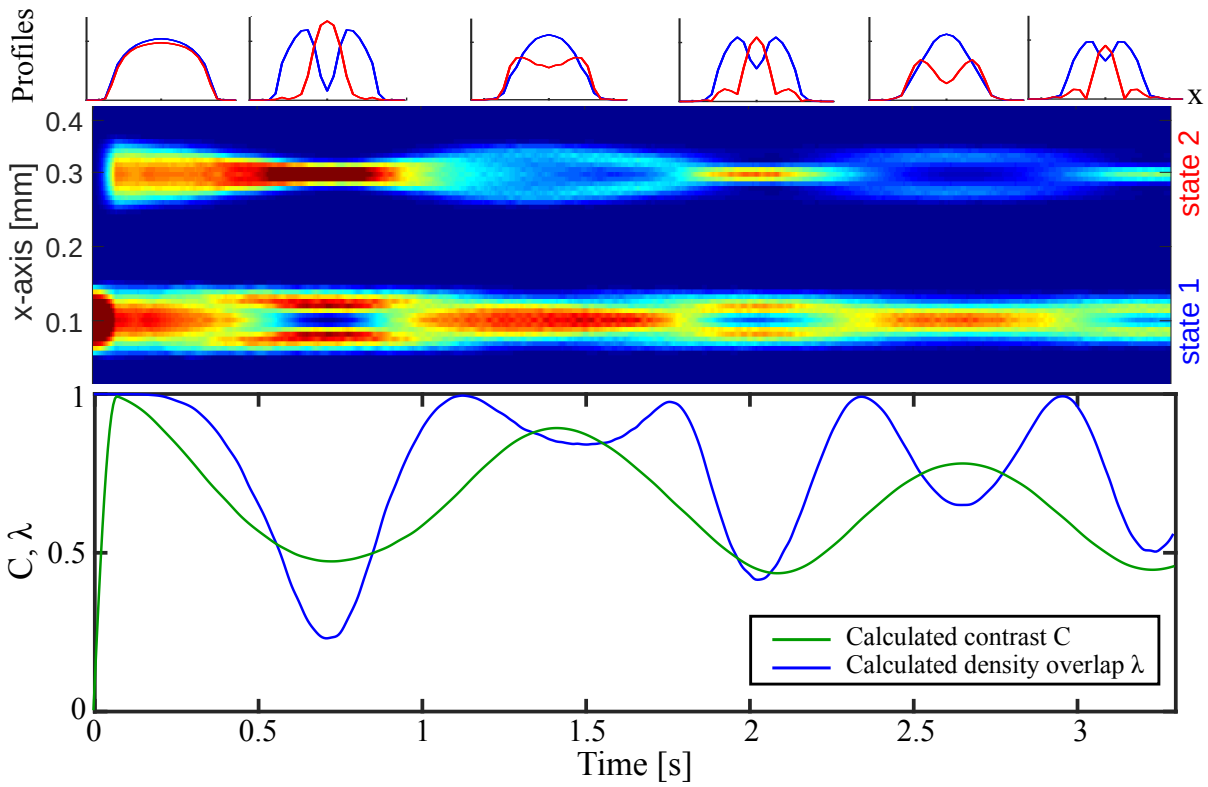

Figure 4.2: **Numerical simulation of the temporal evolution of the bimodal BEC.** The longitudinal wave-functions of the two states are represented as a function of the trapping time. Some cross-section profiles are also displayed ($|1\rangle$ in blue and $|2\rangle$ in red), as well as the calculated density overlap and contrast derived with eq. (4.12) and (4.11) respectively. The first 70ms correspond to the $\pi/2$-pulse.

recombine at the center and the system will undergo a quasi-periodic oscillation. The fact that state $|2\rangle$ also separate when state $|1\rangle$ comes back at the center of the trap is due to atom loss. The dynamics is characterized by two quantities: the density overlap λ that quantifies the spatial dynamics, and the contrast C that quantifies the phase coherence of the ensemble. In the case of a standard Ramsey interferometer ($\frac{\pi}{2} - T_R - \frac{\pi}{2}$), the contrast reads [174]:

$$C = \frac{2|\int d^3r \hat{\psi}_1^\dagger \hat{\psi}_2|}{\int d^3r \hat{\psi}_1^\dagger \hat{\psi}_1 + \int d^3r \hat{\psi}_2^\dagger \hat{\psi}_2}, \tag{4.11}$$

where $\hat{\psi}_i$ is the field operator of state $|i\rangle$, whose spatial and temporal dependency have been omitted for the sake of clarity. The relative phase and the spatial overlap of the the two condensates is included in the crossed term. On the other hand, the density overlap

is given by [61]

$$\lambda = \frac{\int d^3r |\hat{\psi}_1|^2 |\hat{\psi}_2|^2}{\sqrt{\int d^3r |\hat{\psi}_1|^4 \int d^3r |\hat{\psi}_2|^4}}. \tag{4.12}$$

4.2 Experimental investigation of the demixing

In this part we propose another direct observation of such state-dependent dynamics in a very elongated magnetic trap. In order to investigate this physical process in more details, a Ramsey interferometry protocol will be implemented, giving access to the coherence and the frequency evolution of the interacting atomic system.

4.2.1 Direct observation

A BEC of approximately 10^4 atoms is initially prepared in the ground state $|1\rangle$ of a cigar-shaped trap ($\{\omega_x, \omega_y, \omega_z\} = 2\pi \times \{2.9, 92, 74\}$ Hz), and a resonant $\frac{\pi}{2}$-pulse is subsequently applied in order to place it in a coherent superposition. The two states are then imaged after different trapping times. The spatial dynamics, displayed on figure 4.3, is only observed in the x direction corresponding to the weakest confinement.

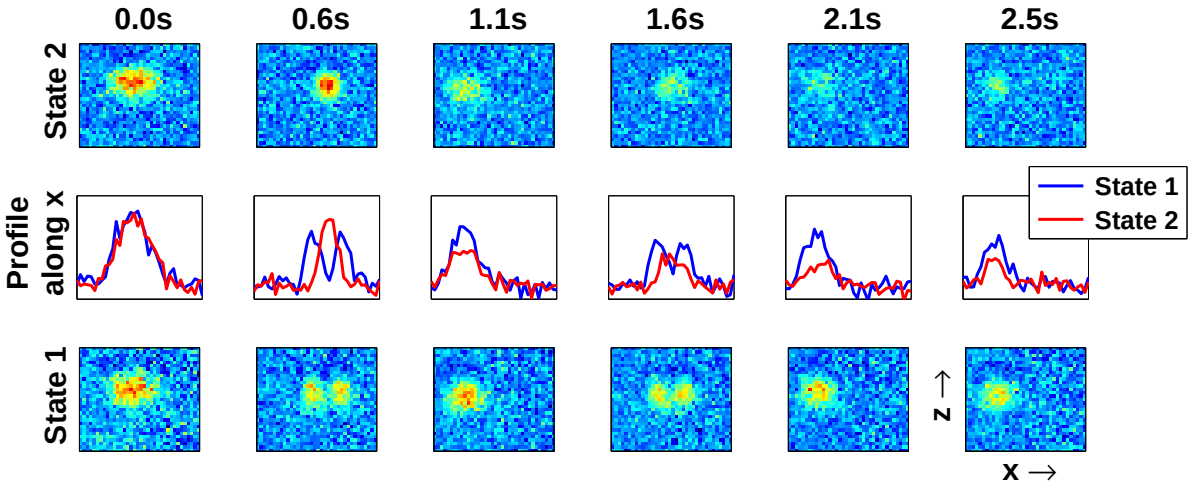

Figure 4.3: **Typical cloud profiles integrated along y after a 30 ms time of flight.** In this experiment a BEC of 10^4 atoms is produced in its ground state. A resonant $\frac{\pi}{2}$-pulse prepares them in an equal superposition of the two states and the cloud dynamics is monitored in time. The trapping time is indicated. Adapted from [113].

First the two states are spatially superimposed. Then, because $a_{11} > a_{22}$, state $|1\rangle$ starts to move toward the border of the trap while state $|2\rangle$ gets denser at the center. A maximum separation of approximately 50μm after time of flight between the two peaks

of state $|1\rangle$ is achieved after 600 ms. Next the atoms in $|1\rangle$ go back to the center of the trap until they superimpose again with the atoms in $|2\rangle$ after $T_R \approx 1.1$ s. The horizontal oscillation of the center of mass is due to non perfect transfer from the evaporation trap to the interrogation trap; even though the transferring ramp is 1 s long, the cloud is still a bit excited which induces this oscillations along the weak axis.
One striking difference with the theoretical prediction shown on figure 4.2, is that experimentally, state $|2\rangle$ only undergoes a breathing-type oscillation but does not separate spatially as state $|1\rangle$. The understanding of this discrepancy is still under investigation.

The limited spatial resolution of the experimental data does not allow us to perform a precise and quantitative analysis. Nonetheless, as it can be directly linked to the wave-function spatial overlap between the two states, the contrast of a Ramsey interferometer becomes an appealing tool to study this demixing effect. It will moreover provide valuable information on the evolution of the coherence and the frequency shifts of this interacting system.

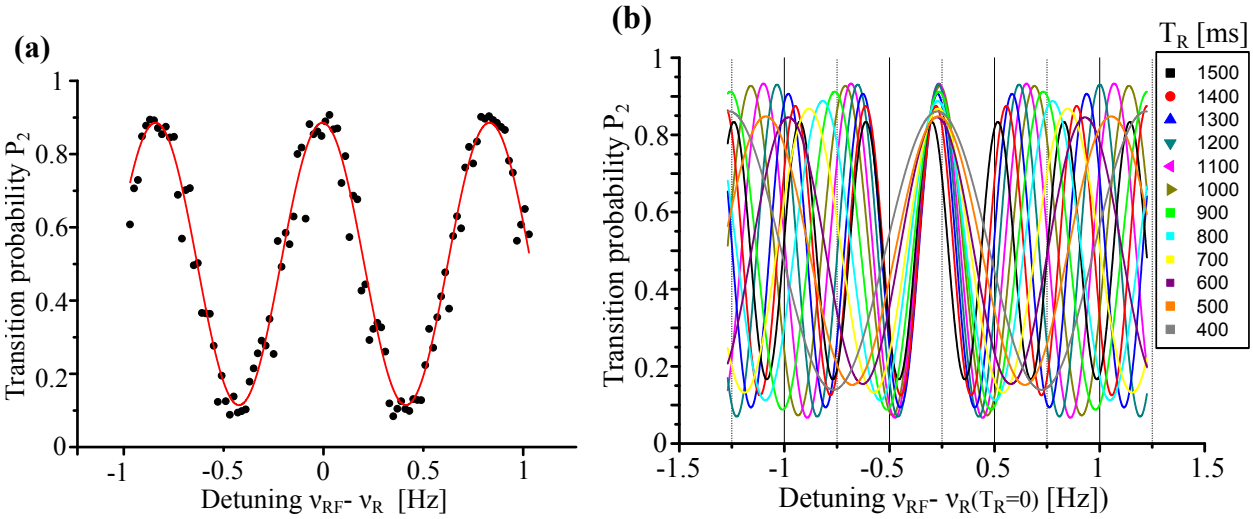

Figure 4.4: **Ramsey spectra of** 12.10^3 **condensed atoms initially.** **(a)** Ramsey spectrum for $T_R = 1.2$ s, obtained by scanning the local oscillator frequency. The black dots are experimental data, while the red line represents the a fit with eq. (4.13). **(b)** Fits of Ramsey spectra obtained for different Ramsey times (colored lines).

4.2.2 Quantitative study using Ramsey interferometry

As the transition probability between two internal states depends on their spatial overlap and drops to zero when the two states are completely separated, driving the atomic transition enables the monitoring of the overlap. The idea is therefore to use the experimental apparatus as a Ramsey interferometer in order to get valuable insights concerning the observed spatial dynamics (wave-function spatial overlap, coherence, frequency shift). To

do so, we prepare 12.10^3 condensed atoms in a cigar-shaped trap with trapping frequencies $\{\omega_x, \omega_y, \omega_z\} = 2\pi \times \{2.9, 92, 74\}$ Hz and perform the interrogation with two 70 ms $\frac{\pi}{2}$-pulses, separated by a free evolution time T_R. The Ramsey spectroscopy is performed by scanning the RF frequency of the two-photon drive, the MW frequency being fixed at approximately 6.8 GHz. After the interrogation, the two states are simultaneously imaged using the adiabatic rapid passage after 23 ms time of flight and the transition probability is derived from the measured atom numbers in the two states N_1 and N_2. The fringes, displayed on figure 4.4 (a), are then obtained by plotting P_2 versus the RF frequency ν_{RF}. In order to probe the states dynamics, such spectroscopy is performed for different free evolution times. Each of the acquired spectra is fitted with the standard Ramsey transition probability

$$P_2 = \frac{1}{2}(1 + C\cos(2\pi(\nu_{RF} - \nu_R)T_R^{eff})), \tag{4.13}$$

with three free parameters: the contrast of the interferometer C, the frequency of the central fringe ν_R (the "R" stands for Ramsey) and an effective interrogation time between the two interrogations pulses T_R^{eff} defined in the next section. Several of these fits are displayed on figure 4.4 (b).

Each of these three parameters is of particular interest and will be thoroughly analyzed in the next three sections. One can however directly notice the significant contrast and Ramsey frequency dependencies with T_R. Besides it is worth keeping in mind that during the interrogation, the system undergoes state-dependent spatial dynamics and asymmetric losses.

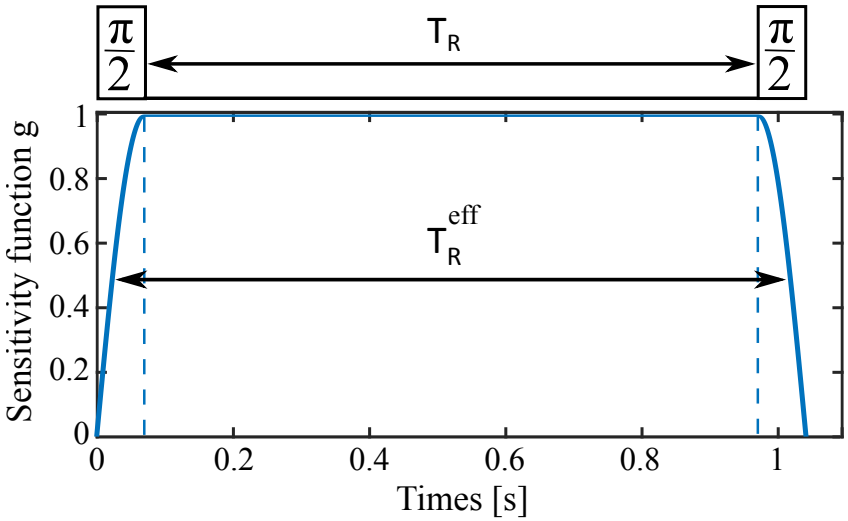

Figure 4.5: **Ramsey interrogation and sensitivity function.** The sensitivity function derived from equation (4.15) is displayed below the time sequence of the Ramsey interrogation to illustrate the effective interrogation time due to finite pulses duration.

4.3 Effective Ramsey time and sensitivity function

As illustrated on figure 4.5, because of the finite duration of the interrogation pulses, the period during which the atoms are sensitive to phase variations is longer than the chosen free evolution time, defined as the time between the end of the first $\frac{\pi}{2}$-pulse and the beginning of the second one.

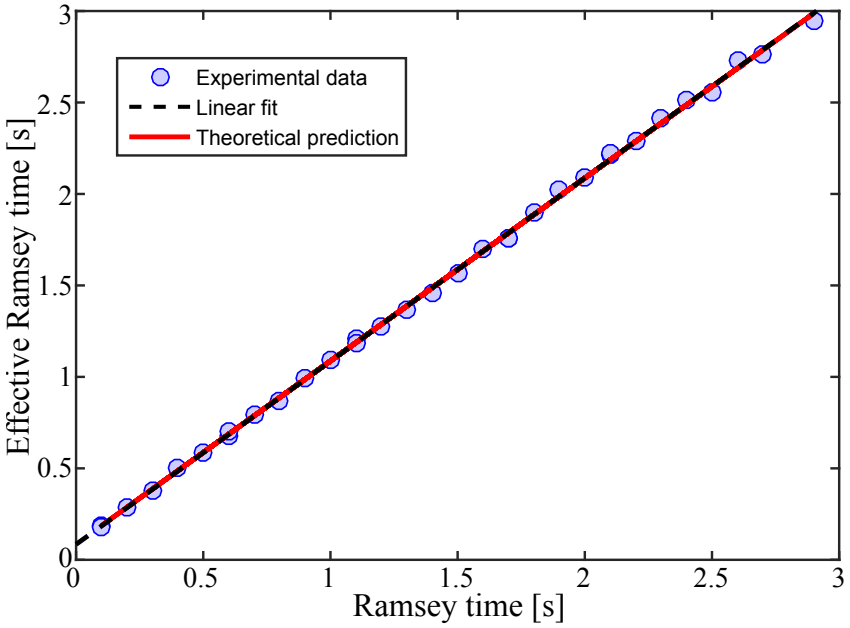

Figure 4.6: **Effective Ramsey time measurement.** Measured Ramsey time extracted from the fit (4.13) (circles) and expected effective Ramsey time derived from equation (4.14) (solid red line) as a function of the chosen Ramsey times T_R. The line corresponds to $T_R^{eff} = T_R + 0.089$ s. The dashed line represents a linear fit $T_R^{eff} = a \cdot T_R + b$ with $a = 1.001 \pm 0.004$ and $b = 0.085 \pm 0.007$ s, in good agreement with the theoretical prediction.

This leads to an effective Ramsey time that can be predicted using the sensitivity function of the interferometer $g(t)$ [215].

$$T_R^{eff} = \int_0^{2\tau+T_R} g(t)dt, \tag{4.14}$$

where τ is the pulses duration, and in the case of square pulses

$$g(t) = \begin{cases} \sin(\frac{\pi(t+\tau+T_R)}{2\tau}) \text{ for } 0 < t < \tau \\ 1 \text{ for } \tau < t < \tau + T_R \\ \sin(\frac{\pi(-t+2\tau+T_R)}{2\tau}) \text{ for } \tau + T_R < t < 2\tau + T_R. \end{cases} \tag{4.15}$$

On figure 4.6 is displayed the effective Ramsey time given by the fit (4.13) (blue circles) and the one derived from equation (4.14) (red line). The experimental data are in good agreement with the theoretical prediction.

This measurement will be particularly useful to compare the temporal evolution of experimental parameters with our numerical simulation of the states dynamics.

4.4 Coherence of the Ramsey interferometer

The contrast of a clock or an interferometer reflects the spatial overlap and phase coherence of the atomic ensemble. Experimentally it corresponds to the visibility of the interference fringes

$$C = \frac{P_{2,max} - P_{2,min}}{P_{2,max} + P_{2,min}} = 2P_{2,max} - 1, \tag{4.16}$$

if the fringes are symmetric around $P_2 = 0.5$ ($\Delta << \Omega_R$). Theoretically, it is derived with equation (4.11).

It is clear that $C = 1$ for two superimposed components with the same density profiles and uniform phase. However, as we will see in this section, the spatial dynamics, atom losses and other dephasing mechanisms modulate and deteriorate the coherence of the system. After listing the different involved decoherence sources present in the experiment, we will study the evolution of the interferometer's contrast during the sequence and compare the experimental data with the numerical model. We will also see that the the "usual" estimation of the contrast by fitting the standard Ramsey oscillations is no longer accurate in the presence of asymmetric losses. An experimental protocol and a post-processing method used to circumvent this issue will be presented.

4.4.1 Decoherence sources

Before focusing on the experimental contrast evolution, let's first have a look at the different main decoherence sources involved in our system.

- **Inhomogeneous dephasing.** Position-dependent fluctuations of the atomic frequency (magnetic noise) or Rabi frequency (MW inhomogeneity and fluctuation of the atoms position), inhomogeneous collisional shifts and so on, can lead to an inhomogeneous dephasing between the individual spins and eventually reduce the coherence and the contrast of the system. Basically, any inhomogeneous frequency shift will translate into phase noise and limit the coherence of the ensemble. The resulting contrast loss is usually characterized by an exponential decay of the temporal Ramsey fringes with a decoherence rate noted γ_d.
- **Atom losses.** When a trapped particle is lost, a part of the internal energy is converted into kinetic energy which can heat the system through secondary collisions and thus reduce the coherence of the ensemble.

- **Two body losses.** When two atoms in $|2\rangle$ collide, spin flip can occur. The consequence is that one atom will end up in $|2,0\rangle$ and will be lost, and the other in $|2,2\rangle$ which is a trapped state. If this atom remains trapped, the resulting atomic ensemble will become a statistical mixture leading to a contrast loss. Using a Stern and Gerlach protocol, we checked that no atom populates the $|2,2\rangle$ state during the Ramsey sequence, even for the highest initial atom number (1.5×10^4 atoms).This means that the kinetic energy resulting from the collision is high enough for the atom to escape from the trap.

  Besides, from what I understood, there is still an open question concerning the impact of such losses on the coherence of the remaining atoms. One hypothesis would be to say: as the atoms are in a coherent superposition, such collisions also build up to an incoherent population in $|1\rangle$ arising from the projection of the initial coherent spin state $\left(\frac{|1\rangle+|2\rangle}{\sqrt{2}}\right)^{\otimes N}$. As we have no way of estimating or getting rid of this incoherent population in $|1\rangle$, the contrast is hence reduced. On the other hand, one could argue that if the atoms are independent, these losses should not provide any information concerning the other atoms. In the same way that one roll of dice is not affected by the previous one, and the probability to get a given number is always 1/6. Let's keep that uncertainty in mind for now.

- **Reduced wave-function overlap**. Because of the crossed term in equation (4.11), a reduced wave-function overlap will lead to a contrast reduction. This overlap is characterized by the density overlap λ defined in equation (4.12).

- **Interaction with non-condensed atoms**. If the condensate is not pure (non-perfect evaporation or heating due to collisions) interactions between the condensed and non-condensed parts can impact the coherence of the system. In addition, the application of an interrogation pulse always induces the creation of quasi-particles that do not populate the ground-state and whose effect can therefore only be studied using a multimode model [183, 216]. As we do not have such model at our disposal, let's just keep in mind that thermal effects can disturb the coherence and the dynamics of the system, for later interpretation of the experimental data.

4.4.2 Contrast evolution

Experimentally, the amplitude of the oscillation of P_2 displayed on figure 4.4 gives acces to the contrast of the Ramsey interferometer through equation (4.13). The fitted contrast is represented by the red circles on figure 4.7, as a function of the effective Ramsey time. The first point with $T_R \approx 0$ s corresponds to the efficiency of a π-pulse. As the pulses are not infinitely short compared to the spatial dynamics, the phase separation starts during the first pulse, leading to a reduced overlap and hence a contrast reduction. Then the contrast decreases rapidly, reflecting the inhomogeneous growth of the relative

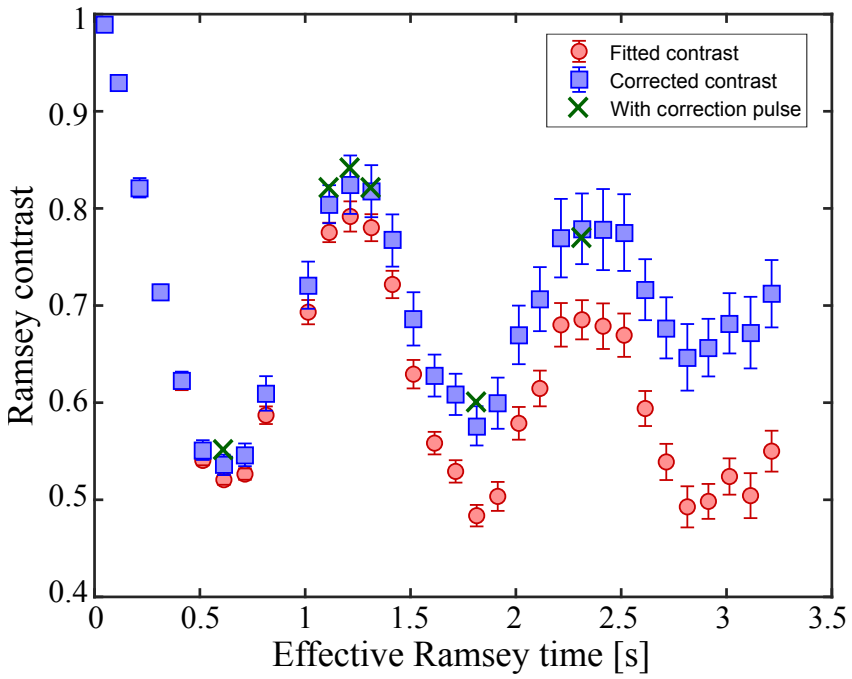

Figure 4.7: **Contrast of the Ramsey interferometer as a function of T_R.** The red circles directly come from the fits represented on figure 4.4 and obtained with equation (4.13). The green crosses are obtained by adding a correction pulse that places the Bloch vector back on the equator at the end of T_R (cf 4.9 (a)). The blue squares represent the numerically corrected contrast, whose calculation is explained below and on figure 4.9 (b).

phase between the two states, until it reaches a local minimum for a Ramsey time which coincides with the largest spatial separation observed on figure 4.3. This minimum is therefore directly related to the spatial separation of the two states. The second part of the oscillation corresponds to a spontaneous contrast revival due to the reduction of the phase separation. When the two wave-functions overlap again, the contrast reaches a maximum of $78 \pm 2\%$ for a revival time $T_{rev} = 1.2$ s. Another full oscillation with a reduced visibility is visible.

This contrast estimation, though, is not accurate in the presence of asymmetric losses. It is actually an underestimation of the real coherence of the system and the next section is dedicated to the study of the impact of asymmetric losses on the contrast measurement.

4.4.3 Asymmetric losses and contrast estimation

As presented in section 2.3.2, our system presents important asymmetric losses that significantly reduce the measured contrast. As illustrated on figure 4.8, because the loss rate of state $|2\rangle$ is higher than the one of state $|1\rangle$, during the free evolution time the

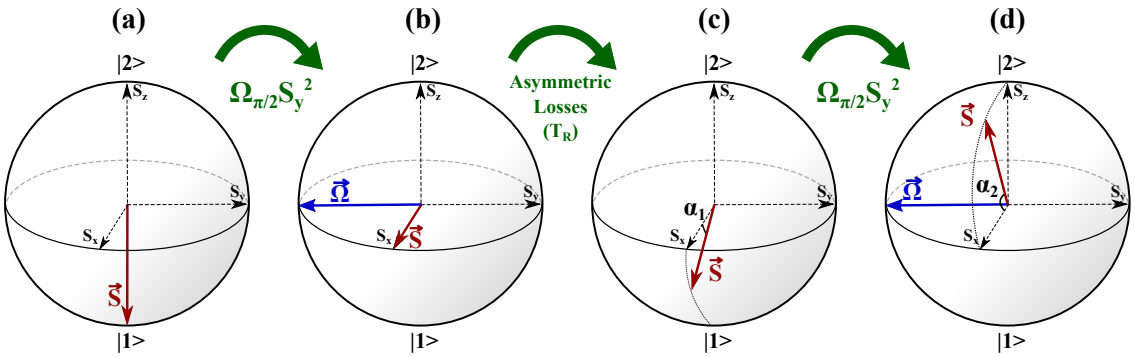

Figure 4.8: **Illustration of the contrast underestimation due to asymmetric losses on the Bloch sphere.** First, all the atoms, represented by their collective spin in red, are prepared in $|1\rangle$ **(a)**. Second, a first resonant $\frac{\pi}{2}$-pulse puts the spins on the equator **(b)**. Third, the asymmetric losses make the collective spin go down below the equator during the free evolution time **(c)**. Finally a second $\frac{\pi}{2}$-pulse is applied to close the interferometer **(d)**. However, because the collective spin was making an angle α_1 below the equator at the beginning of the pulse, it will not reach the north pole even though the pulse is perfect and the ensemble is coherent. At the end of the interferometer, the collective spin makes an angle $0 < \alpha_2 < 90°$ with the equator plane of the Bloch sphere.

collective spin slowly goes down below the equator of the Bloch sphere, such that even if there is no dephasing, the second $\frac{\pi}{2}$-pulse will not enable the collective spin to reach the north pole of the Bloch sphere. The maximum value of P_2, and therefore the contrast C, would thus be higher if the collective spin would have been on the equator before the second interrogation pulse. As a result, because of asymmetric losses, the contrast of the "standard" Ramsey fringes does not give an accurate estimation of the coherence of the system.

In order to circumvent this, we modified the standard Ramsey sequence by adding a correction pulse at the end of the free evolution time and just before the second interrogation pulse (cf. figure 4.9 (a)). This additional pulse has the same Rabi frequency and frequency as the other pulses, but its duration and phase are set such that the Bloch vector ends up on the equator of the Bloch sphere. Typically, its duration is found by increasing the second pulse length of the standard Ramsey sequence, at resonance, until P_2 reaches a maximum. And its phase is set such that the Rabi vector of this pulse is always orthogonal to the Bloch vector, even when the local oscillator frequency is scanned. This is achieved by setting $\varphi_{corr} = 2\pi\nu_{RF}T_R$ $[2\pi]$ using a phase modulation function of a commercial MW synthesizer (Keysight-Agilent E8267D). By scanning the RF frequency we acquire and fit Ramsey spectra for different Ramsey times and extract the experimentally corrected contrast represented by the green crosses on figure 4.7. This method thus enables a better measurement sensitivity (higher contrast) than the standard Ramsey sequence in the presence of significant asymmetric losses.

In addition, as these losses are well understood (cf figure 2.9) we should be able to derive the angle between the collective spin vector and the equator of the Bloch sphere and numerically compute the true contrast from a measurement without correction pulse. The principle of this post-processing correction, illustrated on figure 4.9 (b), is the following.

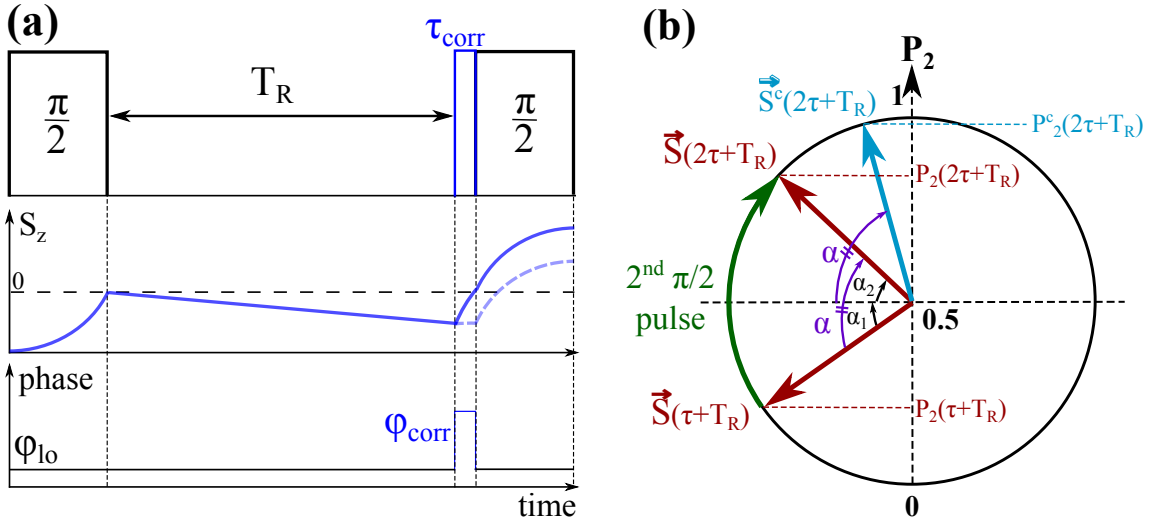

Figure 4.9: **Scheme illustrating the corrected contrast estimation. (a)** Modified Ramsey interferometric scheme. An additional correction pulse is added after the free evolution time in order to place the Bloch vector on the equator of the Bloch sphere. Its phase has to be modulated the keep the Rabi vector of this pulse orthogonal to the Bloch vector. The temporal evolution of the population difference with (plain line) and without (dashed line) correction is indicated for $\varphi_{corr} \approx \varphi_{lo}$. **(b)** This scheme represents the plane defined by the collective spin just before the second interrogation pulse and orthogonal to the equator of the Bloch sphere.

First we need to compute the angle α_1 between the equator and the Bloch vector $\overrightarrow{S}(\tau + T_R)$ just before the second $\pi/2$-pulse, τ being the pulse duration. If we know the averaged initial atom number and the loss rates, then we can derive $P_2(\tau + T_R)$ which is directly related to α_1 via equation (4.17). Then we extract $P_2(2\tau + T_R)$ from the top of the central fringe of the Ramsey spectra (figure 4.4), which is linked to α_2 via equation (4.17).

$$\alpha_1 = \sin^{-1}\left(\frac{1/2 - P_2(\tau + T_R)}{C/2}\right) \text{ and } \alpha_2 = \sin^{-1}\left(\frac{P_2(2\tau + T_R) - 1/2}{C/2}\right). \qquad (4.17)$$

The corrected transition probability, which corresponds to the transition probability given by the second interrogation pulse if the collective spin vector would have remained on the equator of the Bloch sphere, then reads

$$P_2^c(2\tau + T_R) = \frac{1}{2}[1 + C\,\sin(\alpha)], \tag{4.18}$$

where $\alpha = \alpha_1 + \alpha_2$ is the angle by which the second interrogation pulse has rotated the collective spin vector (cf figure 4.9 (b)). Now if we assume that the fringes are symmetric around $P_2 = 0.5$ which is legitimate in the case of smal detunings ($\Delta << \Omega_R$), then

$$C = 2P_2^c(2\tau + T_R) - 1 = C\,\sin(\alpha). \tag{4.19}$$

We finally end up with one non-linear equation to solve:

$$\sin^{-1}\left(\frac{1 - 2P_2(\tau + T_R)}{C}\right) + \sin^{-1}\left(\frac{2P_2(2\tau + T_R) - 1}{C}\right) = \frac{\pi}{2}. \tag{4.20}$$

In the Bloch sphere representation considered on figure 4.9, solving this equation amounts to finding the maximum transition probability given by a perfect $\frac{\pi}{2}$-pulse (i.e. $\alpha = \frac{\pi}{2}$) which actually corresponds to the normalized spin length $|\overrightarrow{S}| = \frac{CN/2}{N/2}$. This numerically corrected contrast is represented by the blue crosses on figure 4.7 and is in perfect agreement with the contrast measured with the correction pulse (blue squares). The higher errorbars are due to the uncertainty of the atom number required to derive $P_2(\tau + T_R)$ used in (4.20). From now on, the term "corrected contrast" will be used to refer to the contrast that has been numerically post-corrected as described above.

4.4.4 Comparison with our numerical model

In order to verify the validity of this contrast measurement, we used the numerical model presented in section 4.1.1 to reproduce the experimental data. In the case of the standard Ramsey sequence, the contrast is given by equation (4.11). With the correction pulse, it can be shown that the contrast theoretically reads

$$\begin{aligned} C_{corr} &= \frac{N_1 + N_2}{2\sqrt{N_1 N_2}} C \\ &= \frac{C}{2\sqrt{P_2(\tau + T_R)(1 - P_2(\tau + T_R))}}, \end{aligned} \tag{4.21}$$

where N_1 and N_2 are the atom numbers at the end of the interrogation time T_R (before the correction pulse). This actually corresponds to the Q parameter in [84].

On figure 4.10 are displayed the fitted and post-corrected experimental contrasts and the calculated C and C_{corr} derived with equation (4.11) and (4.21) respectively, resulting from our numerical simulation. With only background losses ($\gamma_{bck} = 0.2\ \mathrm{s}^{-1}$). The contrast revival is as expected very good and the frequency of the oscillation is slightly smaller than for the experimental points. With two-body and three-body losses, the amplitude of the oscillation reduces but also its period.

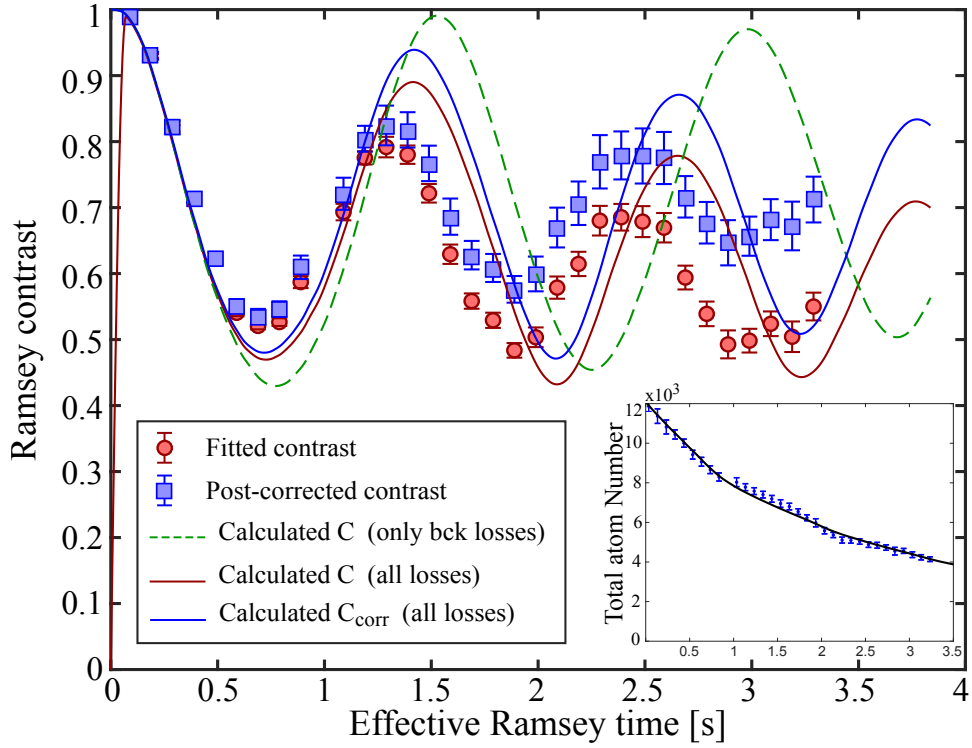

Figure 4.10: **Numerical simulation of the contrast evolution.** The fitted (red circles) and post-corrected (blue squares) contrasts are plotted as a function of the effective Ramsey time. Our numerical model is used with the experimental parameters detailed at the beginning of section 4.2.2 without losses (green dashed line) and with the many-body losses highlighted on figure 2.9 (red and blue lines for C and C_{corr} respectively). The fast initial contrast growth corresponds to the first $\frac{\pi}{2}$-pulse of 70 ms. The inset shows the evolution of the experimental (points) and calculated, without free parameter, (line) total atom number.

It however looks like the dynamics' amplitude is overestimated by the calculation (larger oscillation). More specifically the damping of the oscillation is much slower on the calculated curve than on the experimental points. Indeed, experimental phase noise and decoherence sources could explain why the measured contrast revivals are smaller than the calculated ones, but it cannot explain why the measured contrast minima are higher. Moreover, the oscillation frequency is also a bit understimated by the calculation. By looking at the difference between the contrast C_{corr} with and without many body losses, one could think that the model underestimates the loss coefficients, or misses an additional loss channel. The inset nonetheless shows that the total atom number decay is well reproduced by the model.

Another possibility could be that, maybe because of the important elastic and inelastic collisions, a part of the remaining trapped atoms have been somehow excited

and entered higher thermal modes that do not participate to the mean field dynamics anymore, or at least in a different manner. It could also be possible that these higher thermal modes act on the condensed one as a friction force that damps the spatial dynamics. Theoretical works concerning the excitation of thermal modes in a spinor BEC and their effect on its coherence properties and dynamics are currently under investigation.

4.4.5 Summary of the contrast study

To sum-up this study of the Ramsey contrast, several points are worth emphasizing:

- We observed the spatial dynamics of our spinor BEC and showed that the contrast of a Ramsey interferometer is a good quantitative witness of the phase and spatial dynamics.
- The detrimental effect of asymmetric losses on the contrast can be partially circumvented by applying a correction pulse before closing the interferometer. This method is in good agreement with a numerical post-correction procedure lying on geometrical considerations.
- The numerical simulation based on the Gross Pataevskii equations under the mean field approximation reproduces the observed dynamics with two main differences. The simulation predicts a splitting of state $|2\rangle$ after the first revival time, which is not observed experimentally. And an additional damping term seems to be missing in the model to accurately depict the measured contrast evolution.
- A better knowledge of the inelastic processes involved in a trapped spinor BEC, and their effect on its coherence properties are necessary to understand the observed behavior.

4.5 Study of the Ramsey frequency under asymmetric losses

Besides the contrast, the central frequency of the Ramsey fringes also provides several valuable information concerning the atomic system. Indeed, as we will see, it gives access to the atomic frequency that depends on the mean field interactions, the atomic densities and the wave-function spatial overlap via the collisional shift [112]. In this section, we will first investigate the relation between Ramsey frequency and atomic frequency and see that the latter can be probed during the interferometric sequence. Its evolution will then be explained by analyzing the different involved frequency shifts such as the AC and DC Zeeman shifts and the collisional shift. Finally, we will try to understand the effect of the state-dependent spatial dynamics on the mean field frequency shift.

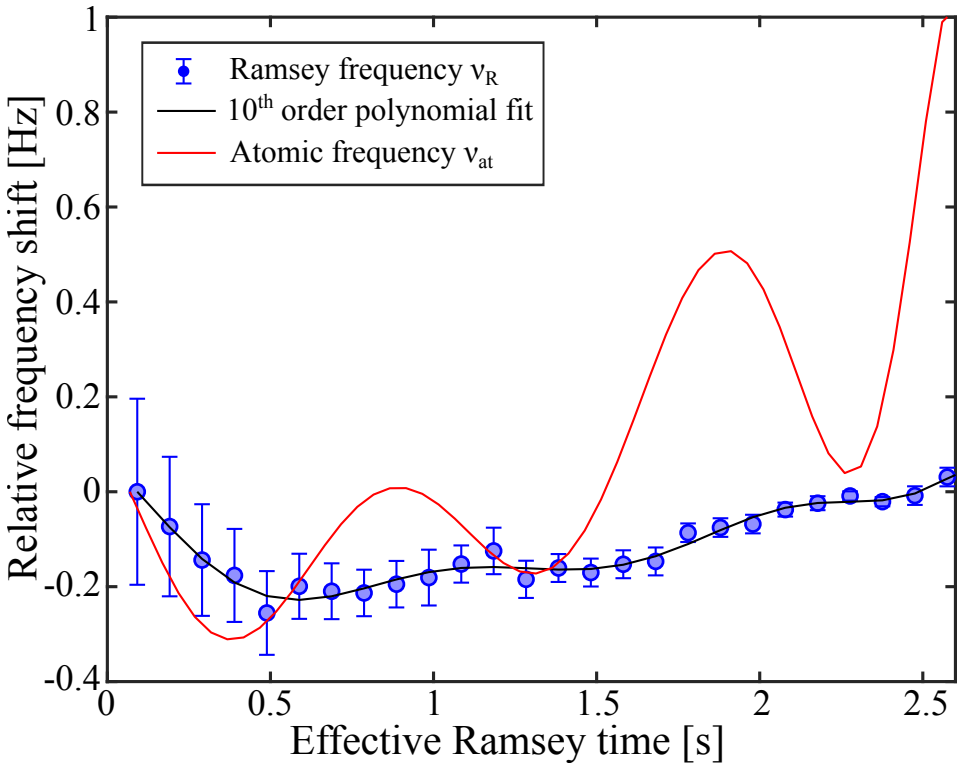

Figure 4.11: **Frequency evolution as a function of the effective Ramsey time.** The Ramsey frequency ν_R (blue points) directly comes from the fit of the Ramsey spectra with equation (4.13). Its behaviour is then fitted with a high order polynomial (black line) used to derive the atomic frequency ν_{at} (red line) thanks to equation (4.23).The decreasing errorbars coincide with the narrowing of the Ramsey fringes when T_R increases.

4.5.1 Ramsey frequency versus atomic frequency

As displayed on figure 4.11, the Ramsey frequency ν_R, defined as the central frequency of the Ramsey fringes fitted with equation (4.13), changes significantly when T_R is scanned. The full understanding of this behavior is not trivial and it will be detailed in the following.

If the atomic frequency changes during the free evolution time, then the Ramsey frequency does not correspond to the atomic frequency but to its average over T_R. If we assume that the pulse duration is much smaller than the other time scales of the system, the Ramsey frequency ν_R reads:

$$\nu_R = \frac{1}{T_R}\int_0^{T_R} \nu_{at}(t)dt. \tag{4.22}$$

This equation can be inverted in order to access the atomic frequency at different T_R

$$\nu_{at}(T_R) = \frac{d}{dT_R}(T_R\nu_R(T_R)). \tag{4.23}$$

As the accurate calculation of equation (4.23) requires a much higher temporal sampling than the one used in the experiment, a 10^{th} order polynomial fit is used to reproduce the evolution of ν_R and derive ν_{at} with a sufficiently high precision. Figure 4.11 and equation (4.23) thus enable us to follow the evolution of the atomic frequency over the free evolution time. These two frequencies (ν_R and ν_{at}) are displayed on figure 4.11. Physically, the atomic frequency changes can have different origins that we will investigate in the following.

4.5.2 AC Zeeman shift

As the two clock states are coupled by a two-photon excitation, the clock is sensitive to a two-photon light shift. Indeed, because the two interrogation pulses dress the states, the transition frequency during the pulses is different from the one during the free evolution time. The detailed derivation of this shift including the coupling to all the other Zeeman states has been performed for our experiment in [103].

In principle, if the polarization of the RF and MW fields are perfectly linear, only the MW photon induces a light shift mainly because of the coupling with the intermediate state $|2,0\rangle$. However, as shown on figure 4.12 (a), Increasing the RF power does induce a frequency shift testifying of the ellipticity of the RF field polarization with respect to the quantization field. This ellipticity has already been highlighted in [113] and most likely comes from the inductive coupling in the neighboring wires on the chip. This is nonetheless not too dramatic since the RF and MW photons dress the energy levels in opposite directions. We can thus minimize this frequency shift by adapting the power imbalance between these two fields, conserving the two-photon Rabi frequency:

$\Omega_R = \frac{\Omega_{rf}\Omega_{mw}}{4\Delta}$ where Δ is the detuning between the MW photon and the intermediate state (cf. figure 1.5). The frequency shift can be written [189]

$$\Delta\nu_{AC}(T_R) = \frac{\Delta AC}{1 + \frac{\pi T_R}{2\tau_\pi}}, \tag{4.24}$$

where ΔAC is the total AC Zeeman shift and τ_π the duration of a π-pulse.

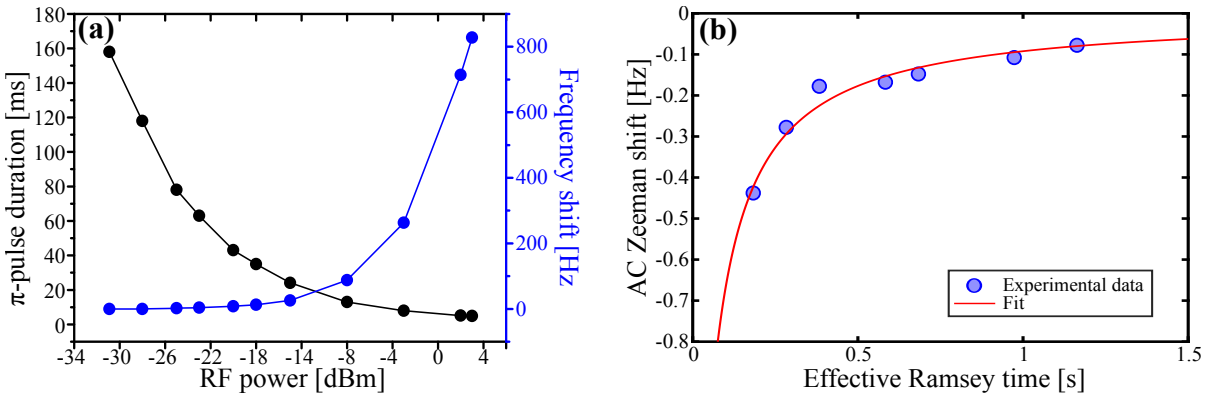

Figure 4.12: **Characterization of the AC Zeeman shift.** Measurement performed in the clock trap, with a thermal ensemble (no demixing) of $\approx 5 \times 10^4$ atoms. **(a)** Relative frequency shift induced by the RF field as a function of its power. The presence of this frequency dependency shows that the polarization of the RF field is not perfectly linear. The duration of the corresponding π-pulses is also indicated for a MW power of 6.5 dBm. **(b)** Relative frequency shift as function of the effective Ramsey time before optimisation. The blue points correspond to the frequency of the central fringe of Ramsey spectra and the red line is a numerical fit using equation (4.24). The fit gives $\Delta AC = -1.13 \pm 0.2$ Hz.

There are two ways of measuring this shift. Either by measuring the Ramsey frequency for different Ramsey times and use equation (4.24) to estimate ΔAC as illustrated on figure 4.12 (b). Or by fixing the Ramsey time and measuring the frequency of the central fringe by successively letting the MW ($\rightarrow \nu_R^{mw}$) and RF ($\rightarrow \nu_R^{rf}$) fields "on" during the free evolution time, and comparing the two frequency differences with respect to the Ramsey frequency[1] ($\rightarrow \nu_R$). Then the AC Zeeman shift is simply the sum of the two shifts induced by the interrogation fields: $\Delta AC = (\nu_R^{rf} - \nu_R) + (\nu_R^{mw} - \nu_R)$. This shift is measured and minimized ($\Delta AC \lesssim 50$ mHz) regularly and every time the Rabi frequency is changed. This effect can therefore not explain the shifts observed on figure 4.11.

[1] with no field on during the free evolution time.

4.5.3 Inhomogeneous DC Zeeman shift

The second possible reason for the observed frequency shift is the inhomogeneous Zeeman shift. Indeed, during the free evolution time, the atoms in state $|1\rangle$ go to the borders of the trap and therefore experience a increasing frequency shift due to the growing trapping potential

$$\nu_{12}^{Zeeman} = \nu_{min} + \beta(B(\mathbf{r}) - B_m)^2, \tag{4.25}$$

with $\nu_{min} = 6834678113,59$ Hz, $\beta = 431.3596$ Hz.G^{-2} and $B_m = 3.228917$ G is the so called magic field [111, 112]. Let's now rewrite the position-dependent magnetic field as a function of the separation between the two states $B(\mathbf{r}) = B_0 + \Delta B(\mathbf{r})$, B_0 being the field at the trap bottom. The induced position-dependent frequency shift along the longitudinal axis of the trap reads

$$\Delta\nu_{12}^{Zeeman} = 2\beta\Delta B(x)(B_0 - B_m) + \beta\Delta B(x)^2, \tag{4.26}$$

where $\Delta B(x) = B^{sep} - B^{unif} = \frac{m\omega_x^2}{2\mu_B g_F m_F}\Delta x^2$ and Δx the separation between the two states. Assuming that state $|2\rangle$ stays at the center ($x = 0$), the Zeeman shift due to the spatial separation is

$$\Delta\nu_{12}^{Zeeman} = \beta(B_0 - B_m)\frac{m\omega_x^2}{\mu_B g_F m_F}\Delta x^2 + \beta\frac{m^2\omega_x^4}{\mu_B^2 g_F^2 m_F^2}\Delta x^4 \tag{4.27}$$

$$= (9.66 \times 10^{-6})\left(\frac{B_0 - B_m}{1\text{G}}\right)\left(\frac{\Delta x}{1\mu\text{m}}\right)^2 + (2.16 \times 10^{-13})\left(\frac{\Delta x}{1\mu\text{m}}\right)^4. \tag{4.28}$$

In our case, figure 4.13 (b) shows that the bottom field has to be chosen 38 mG below the magic field in order to minimize the clock sensitivity to magnetic field fluctuations, which is surprisingly very close to the one that minimizes the clock instability for a thermal ensemble of atoms [196]. Besides, as the separation is smaller than 100 μm (cf. figure 4.1), figure 4.13 (a) shows that this position-dependent shift is very small and cannot explain the evolution of the atomic frequency. It will thus be neglected in the following.

4.5.4 Collisional shift

The third possible origin for the observed frequency shift is the collisional shift. Indeed, mean-field interactions shift the resonance according to [112]

$$\nu_{coll} = \frac{\hbar}{m}n[\alpha_{22}a_{22} - \alpha_{11}a_{11} + (2\alpha_{12}a_{12} - \alpha_{22}a_{22} - \alpha_{11}a_{11})\frac{n_1 - n_2}{n}], \tag{4.29}$$

where $n = n_1 + n_2$, n_i is the atomic density of state $|i\rangle$ and α_{ij} is the two-particle correlation at zero separation, defined as $\alpha_{i,j} = g_{i,j}^{(2)}(0)$, where [129]

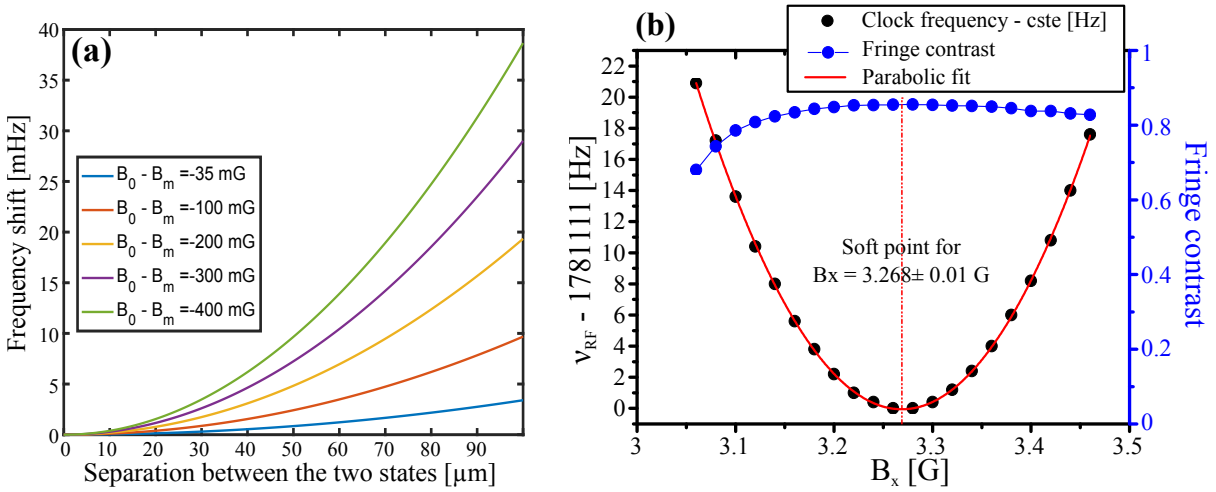

Figure 4.13: **Position-dependent Zeeman shift.** (a) Frequency shift $\Delta\nu_{12}^{Zeeman}$ induced by the trapping potential for different bottom fields. **(b)** Evolution of the Ramsey frequency and fitted contrast when scanning the quantization magnetic field. The dots are experimental data and the red line is a parabolic fit. A soft spot at which magnetic field fluctuations are greatly reduced is found 38 mG below the magic field.

$$g_{i,j}^{(2)}(r_1, r_2) = \frac{< \hat{\Psi}_i^\dagger(r_1)\hat{\Psi}_j^\dagger(r_2)\hat{\Psi}_i(r_2)\hat{\Psi}_j(r_1) >}{< \hat{\Psi}_i^\dagger(r_1)\hat{\Psi}_i(r_1) >< \hat{\Psi}_j^\dagger(r_2)\hat{\Psi}_j(r_2) >}, \tag{4.30}$$

assuming that α_{ij} only depends on the distance between the colliding particles $r = r_1 - r_2$. When T_R is scanned the wave-functions of the two states are distorted, which modifies the interstate two-particle correlation at zero separation α_{12}. In the case of overlapping condensed atoms, $\alpha_{ii} = 1$ and $\alpha_{12} = 1$ [112, 217]. Moreover, in our case, asymmetric losses make n and $n_2 - n_1$ vary during T_R and the spatial dynamics discussed previously should make α_{12} oscillate below 1.

First let's assume that there is no demixing, such that $\alpha_{12} = 1$. As this shift depends on the total number of atoms, we can use it to check the atom number stability during the sequence. We thus compute ν_{coll} in two ways. On one hand using the mean atom number measured at each T_R and our knowledge on the evolution of $S_z(T_R)$. And on the other hand by taking the initial mean atom number measured at the first T_R and using our knowledge on the atomic density and losses to derive the temporal evolution of ν_{coll}. These two evolutions are displayed on figure 4.14 (a) in black dashed line and green dots respectively.

Then we plot (solid blue line) the average of $\nu_{coll}(\alpha_{12} = 1)$ over the corresponding Ramsey time to compare it with the experimental Ramsey frequency. The difference between these two curves is due to the spatial separation and the modulation of α_{12}. To emphasize this additional shift, we plot in cyan squares $\nu_{demixing} = \nu_{at} - \nu_{coll}(\alpha_{12} = 1)$ which corresponds to the difference between the atomic frequency and the collisional

shift without demixing. This oscillation of $\nu_{demixing}$ can be explained by an oscillation of α_{12} via the wave-function spatial overlap. It therefore seems possible to extract α_{12} for a non-perfect superposition ($n_2 \neq n_1$)

$$\begin{aligned} \alpha_{12} &\equiv \frac{m}{2\hbar a_{12}(n_1 - n_2)}(\nu_{coll}(\alpha_{12}) - \nu_{coll}(\alpha_{12} = 1)) + 1 \\ &= \frac{m}{2\hbar a_{12}(n_1 - n_2)}(\nu_{atomic} - \nu_{collshift}) + 1. \end{aligned} \tag{4.31}$$

The temporal evolution of α_{12} is displayed on figure 4.14 (b).

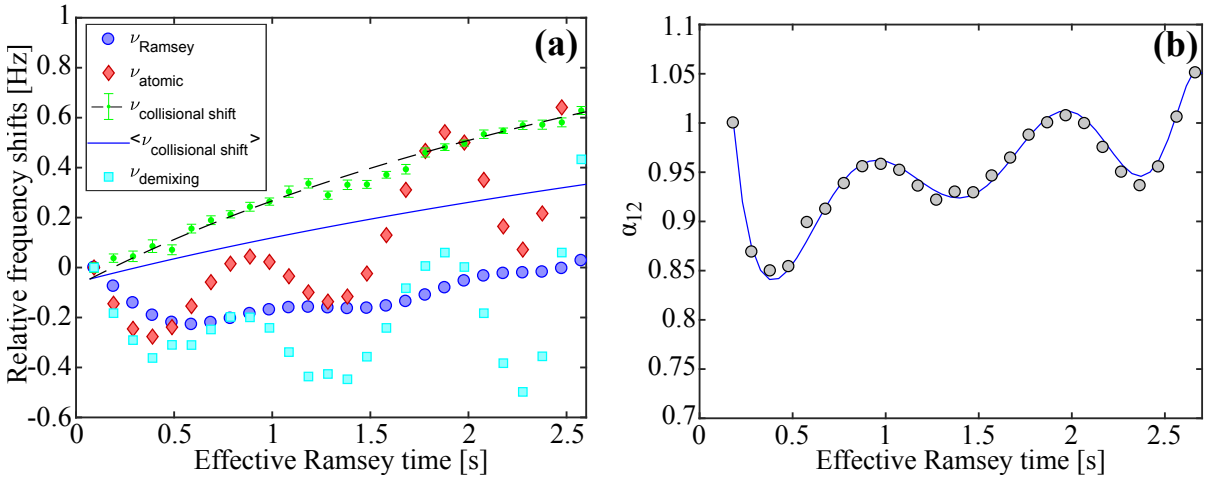

Figure 4.14: **Frequency shifts during the demixing sequence. (a)** Temporal evolution of the frequency shifts during the Ramsey sequence for 1.2×10^3 atoms initially. The blue circles represent ν_R already displayed on figure 4.4, the red diamonds ν_{at} calculated from equation (4.23), the green dots show the expected collisional shift calculated from equation (4.29) without demixing ($\alpha_{12} = 1$) and the cyan squares show the difference between red and green to exhibit the frequency change originated from the state-dependent spatial dynamics through α_{12}. The dashed curve represents the same quantity as the green dots but derived with the initial atom number and the measured lifetimes in order to check the stability of the initial atom number. The blue line is the averaged of the dashed one over the Ramsey time. **(b)** Temporal evolution of α_{12} derived with equation (4.31). The blue line is a fit of the experimental data (black circles).

4.6 Demixing under different experimental conditions

Let's recall at this point that the objective is to use this state-dependent spatial dynamics in order to generate spin squeezing through the non-linear elastic interactions, enhanced when the two modes are separated. This implies that we are looking for a large spatial separation at half the revival time, and a high contrast revival. To minimize the contrast deterioration due to atom loss, the dynamics also needs to be fast.
In the following, we will see how the demixing evolves when scanning the trapping frequencies, initial atom number and the first pulse duration.

4.6.1 Influence of the trapping frequencies

Technically the main parameters controlling the dynamics are the density and the longitudinal frequency [83]. Table 4.1 regroups the parameters used to generate five different traps as well as their respective trapping frequencies and spatial positions, derived from the magnetic field simulation used in [92]. Each of these traps has been realized experimentally and optimized every time (pulses calibration and reduction of the AC Zeeman shift). Ramsey spectra were acquired and equation (4.13) was used to extract the corrected contrast (cf. section 4.4.3).

Colour	$\mathbf{I}_s$ [A]	$\mathbf{I}_d$ [A]	$\mathbf{B}_x$[G]	$\mathbf{B}_y$ [G]	**Frequencies [Hz]**	**Position [mm]**
●	1	0.01	3.055	6	$\{2.9; 92; 74\}$	$\{-0.05; 0.002; 0.35\}$
●	1	0.015	3.091	6.5	$\{3.6; 108; 92\}$	$\{-0.03; 0.002; 0.32\}$
●	1	0.02	3.128	7	$\{4.4; 128; 113\}$	$\{-0.02; 0.001; 0.29\}$
●	1.95	0.08	3.31	13	$\{8.7; 128; 115\}$	$\{-0.05; 0.001; 0.29\}$
●	1.95	0.01	3.01	13	$\{3.6; 236; 228\}$	$\{-0.08; 0.001; 0.29\}$

Table 4.1: **Trapping parameters.** Stripline (I_s) and dimple (I_d) currents, bias fields along x and y, and resulting trapping frequencies and trap position with respect to the chip. The corresponding colors of figure 4.15 are also indicated. The previously used clock trap is represented in black.

The most straightforward feature to compare them is the Ramsey contrast. On figure 4.15 is displayed the time evolution of the corrected contrast for the five traps cited above. As expected, the tighter the longitudinal axis of the trap, the faster the dynamics but also the smaller the spatial separation characterized by a higher contrast at half the revival time. Furthermore, as the only significant difference between the blue and cyan curves is the longitudinal trapping frequency, we can use them to highlight the effect of a reduced wave-function overlap at the revival time. Indeed they correspond to the same

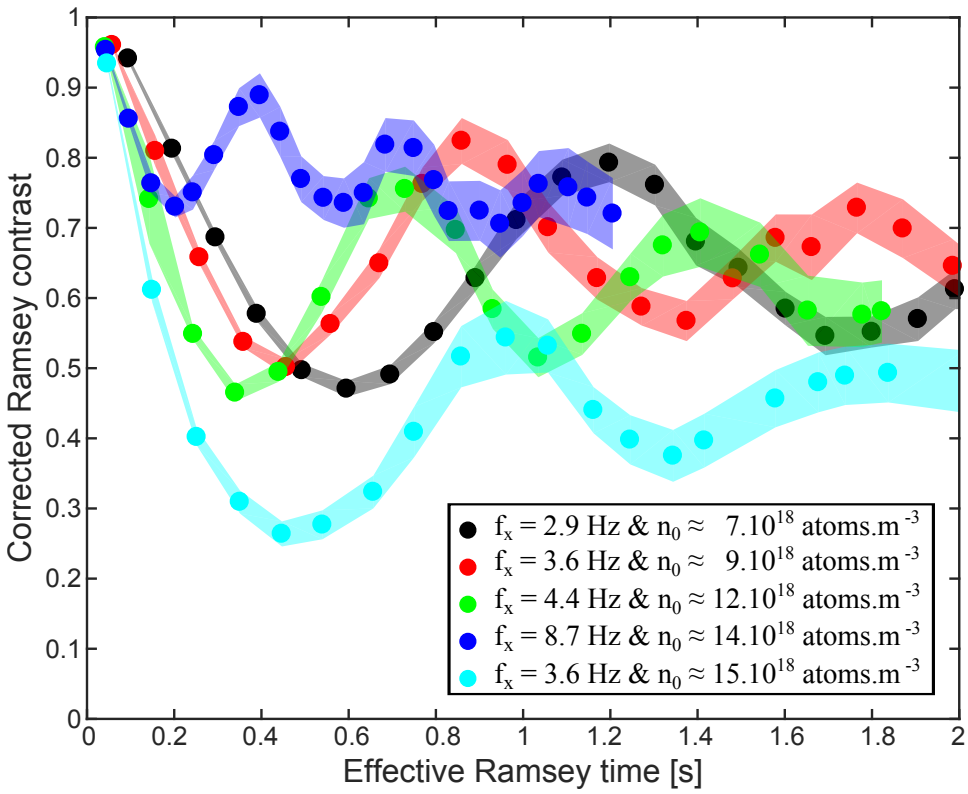

Figure 4.15: **Time evolution of the Ramsey contrast for different trapping geometries.** For each color, Ramsey spectra are acquired, the fitted contrast is corrected the method described in section 4.4.3 and the effective Ramsey time is explained in section 4.3. Each curve corresponds to a trap defined in table 4.1 and labeled by its color. The longitudinal trapping frequencies and initial densities are indicated.

atomic density and have therefore the same atomic losses. Similarly, the red and cyan curves have the same longitudinal trapping frequency but different densities. This shows that for this density range, the revival time is mostly determined by the longitudinal trapping frequency while the spatial separation is controlled by both the axial trapping frequency and the atomic density.

Unfortunately, there is no perfect configuration for which the separation is fast and large with a high contrast revival. In order to study the influence of other parameters, we chose the "green" trap which appears like a trade-off between good contrast revival, large separation and short revival time.

4.6.2 Influence of the atom number

Let's now fix the trapping frequency and study the influence of the atom number on the spatial dynamics. As the contrast of the interferometer is directly related to the spin

length that intervenes in the squeezing parameter ξ^2, these contrast results will be used in the squeezing section to derive the Wineland squeezing parameter (1.80).

Clock trap

First, in the clock trap (black), we reiterated the experimental protocol described in section 4.2.2 with different initial atom numbers. The different estimated contrasts measured at $T_R/2$ and T_R are regrouped on figure 4.16. This measurement enables another verification of the contrast estimation. Indeed, the numerically corrected contrast is always in agreement with the one obtained with the correction pulse. Moreover, the higher the initial atom number, the bigger the discrepancy between the raw and corrected contrasts because of the increasing asymmetric losses.

An additional[2] fixed decay rate $\gamma_d = 0.05\ \mathrm{s}^{-1}$ has been added to match the first points and guide the eye. This decoherence rate finds its justification in the presence of experimental phase noise that has not been considered in the simulation. As we will see in section 5.4, this noise mostly comes from fluctuations of density-dependent frequency shift (collisional) because of atom number instabilities. It is quite clear that the measured contrast decreases faster than the calculated one with γ_d and this shows that the decoherence rate increases with the atom number, which is compatible with the observed phase noise.

On the other hand, the faster decrease of the contrast probed at half the revival time (at maximal separation), shows that increasing the initial density enhance the spatial separation. Indeed intuitively, increasing the initial populations should increase the initial interaction energy and therefore the momentum "kick" transferred to the atoms after the first $\frac{\pi}{2}$-pulse leading to a larger and faster spatial separation. This is true up to a certain atom number, around 8000 atoms, from which the separation increases more slowly and the contrast revival decreases more rapidly. This could mean that there is an atomic density from which the inelastic collisions become more significant than the elastic ones, destroying the phase coherence of the BEC.

Green trap

Now for completeness, and to deepen our understanding of this interacting system, complete Ramsey spectra were acquired in the "green" trap ($\{4.4; 128; 113\}$ Hz) for different initial atom numbers. On figure 4.17 are displayed the fitted and corrected contrasts as well as the frequency, obtained thanks to the previously detailed methods, as a function of the effective Ramsey time. Again, when the initial density increases, the first contrast minimum decreases more than its first revival, testifying of an increasing spatial separation. A similar effect is visible on the frequency curves. Unfortunately, higher initial densities also means higher two-body loss rates which are responsible for the reduced contrast revival.

[2]On top of the decoherence induced by atom losses.

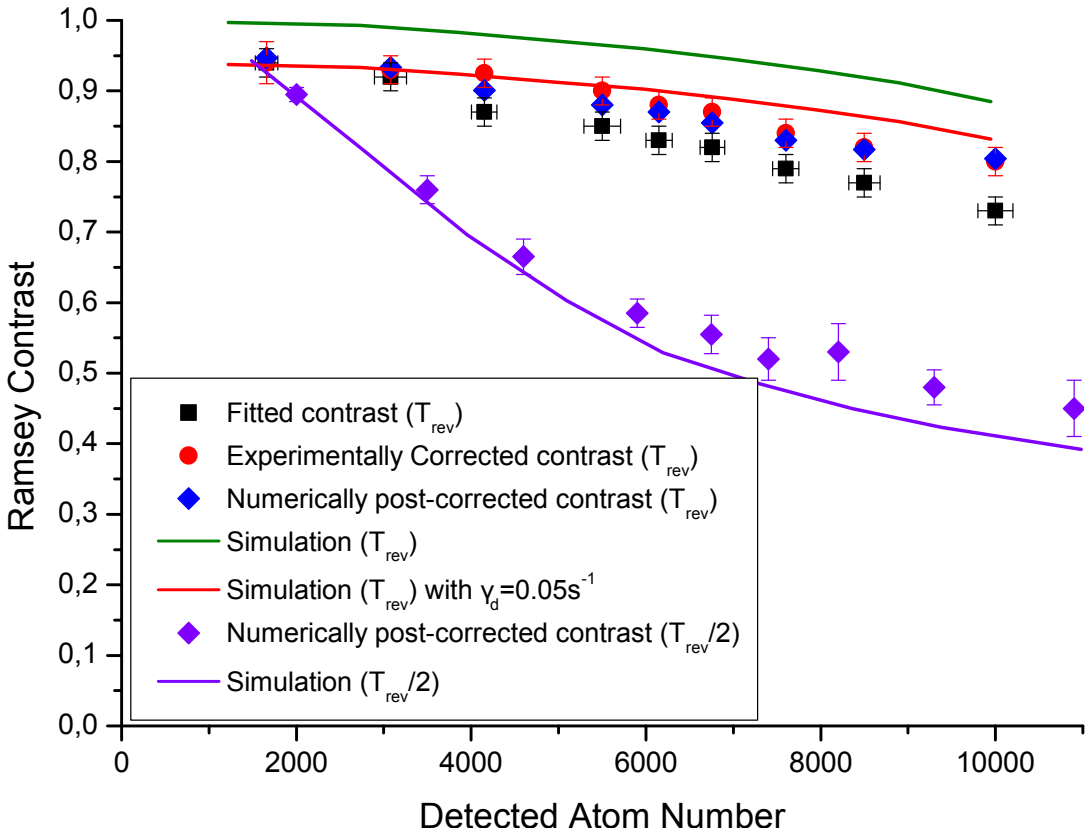

Figure 4.16: **Evolution of different estimations of the Ramsey contrast with atom number.** In the clock trap, several contrast evolution curves similar to figure 4.7 have been acquired for different initial atom numbers. Different contrasts are plotted as a function of the detected atom number at the revival time: the "raw" fitted contrast (black squares), the fitted contrast obtained with a correction pulse (red circles), the contrast that has been post corrected with the protocol described in section 4.4.3 (blue diamonds). The solid lines correspond to the result of the numerical resolution of the coupled Gross Pitaevskii-equations without additional decoherence rate (green) and with $\gamma_d = 0.05\text{s}^{-1}$ (red). The contrast at half the revival time is also indicated (violet) to emphasize the increase of the spatial separation with the initial atom number.

One noticeable feature is that the calculated curves reproduce well the contrast evolution for low atom numbers. We used the first evolution with 4000 atoms to adjust the decoherence rate to $\gamma_d = 0.1\ \text{s}^{-1}$. Note that it is higher than the one used in the clock trap, and this confirms that decoherence is related to the atomic density. When the initial atom number increases, the calculated frequency of the oscillation decreases while the experimental one remains constant. The damping of the oscillation is also much more pronounced experimentally. This means that the damping and the frequency of the oscillation are increased by something that depends on the initial density and is

not taken into account in our Gross Pitaevskii simulation. Again, it could be thermal excitations induced by the inelastic collisions that increase with the density.

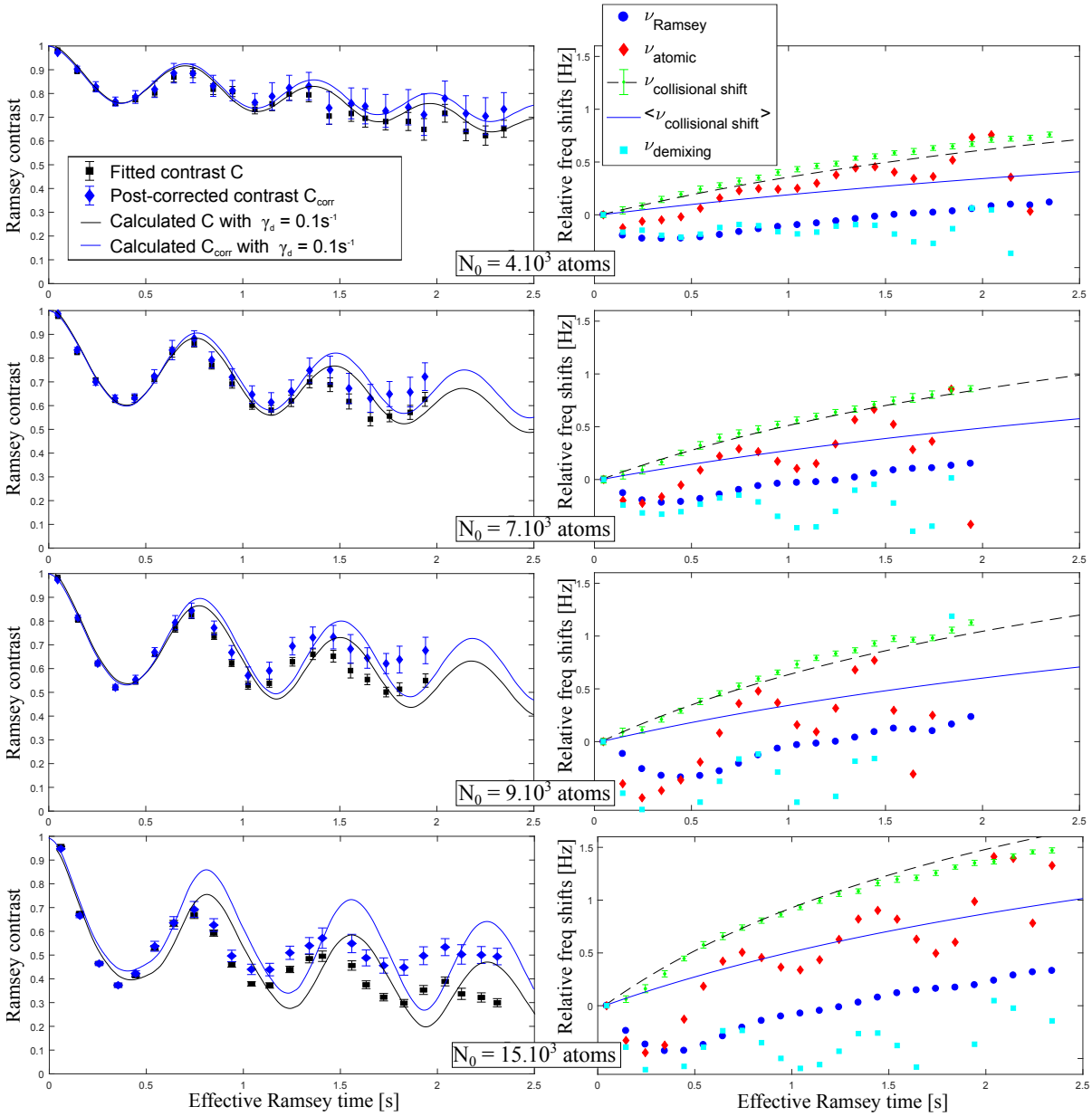

Figure 4.17: **Contrast and frequency time evolution in the "green" trap for different initial atom numbers.** Ramsey spectra for different Ramsey times have been acquired for several indicated initial atom numbers loaded in the "green" trap. The contrast (left) and frequency (right) evolutions are plotted for the indicated initial atom numbers. The legend is the same as on figure 4.14.

4.6.3 Influence of the pulse duration

The effect of the Rabi frequency of the $\frac{\pi}{2}$-pulses has also been studied in order to check if it has an impact on the contrast estimation. Indeed, so far we used rather long pulses (70 ms) implying that the dynamics starts during the first pulse and goes on during the second one. This could thus limit the resolution of the contrast estimation. However, reducing the pulses duration down to 6 ms did not significantly modified the contrast curves. The only effect was an increase of the noise on the measured transition probability that will be explained in section 5.4.3.

We also investigated the effect of the population ratio after the first pulse by varying the first pulse duration while keeping the Rabi frequency constant. The idea was the following: by imbalancing the populations at the beginning of the sequence, we could for instance get equal populations at the end of the free evolution time and get an higher contrast. Yet the maximum separation and contrast revival was found to be for equal initial populations.

4.7 Conclusion

In this chapter we studied the state-dependent spatial dynamics occurring in a spinor BEC. We used the contrast on a Ramsey interferometer to quantitatively study the resulting phase evolution and quantified the impact of asymmetric losses on the contrast estimation. The study of the Ramsey frequency highlighted the spatial dynamics through a modification of the collisional shift. This study will be particularly useful to understand the dynamics of the spins during the squeezing sequence in the next chapter. The study of the influence of the trapping frequencies and atom number showed that the dynamics can be easily controlled.

On the other hand, even though our numerical model reproduces well the experimental data for a small number of atoms, there is a damping effect that increases with the atomic density that has not been taken into account. Our best guess so far is the interaction between the condensed phase and higher order thermal modes, but this needs to be further investigated.

For the purpose of using this spatial dynamics to generate spin squeezing, we want a large and fast separation with a high contrast revival. Unfortunately, because of two-body losses, such perfect situation does not seem easy to achieve. We will therefore focus on the clock trap for which the ratio between contrast revival and separation looks fine.

Chapter 5

Spin squeezing in a dual component BEC

*****

In this chapter, we present our results concerning the generation of spin squeezing arising from the spontaneous state-dependent spatial dynamics studied in the previous chapter. The principle of this method is recalled and recent theoretical studies are used to estimate the achievable amount of squeezing that we can hope for. Then the experimental sequence, implemented to probe the spin noise distribution by performing the state tomography, is presented. We will found that because of the significant asymmetric losses present in our system, a counter-intuitive protocol has to be applied in order to efficiently probe the spin noise distribution. The state tomography measurement will be subsequently presented and an atom number correlation will be studied and used to post-correct the raw data. Finally, the stability budget of the resulting atomic clock will be drawn up in order to estimate the technical noise sources limiting our measured amount of squeezing.

5.1 Theoretical considerations

5.1.1 Proposal

As already introduced in section 1.5.3, the spin dynamics in this system can be well described by the "one-axis-twisting" Hamiltonian which takes the form [76]:

$$\hat{H}/\hbar = \delta \hat{S}_z + \Omega \hat{S}_\varphi + \chi \hat{S}_z^2, \tag{5.1}$$

where the first term describes spin rotations along the equator of the Bloch sphere at a detuning δ between the local oscillator and the atomic resonance. The second term describes spin rotations around an axis $S_{\phi_{lo}} = \cos(\phi_{lo})S_x$ - $\sin(\phi_{lo})S_y$ due to the coupling with a driving field with Rabi frequency Ω and phase ϕ_{lo}. The third term, due to elastic collisional interactions in the two-mode BEC, is responsible for the shearing of the spin noise distribution. We also showed in section 1.5.3 that the non-linear coefficient χ reads

$$\chi = \frac{1}{2\hbar} \int d\mathbf{r} \left(g_{11} |\varphi_1(\mathbf{r},t)|^4 + g_{22} |\varphi_2(\mathbf{r},t)|^4 - 2g_{12} |\varphi_1(\mathbf{r},t)|^2 |\varphi_2(\mathbf{r},t)|^2 \right). \tag{5.2}$$

We recall that the idea is to use the spontaneous state-dependent spatial dynamics studied in the previous chapter to reduce the crossed term in equation (5.2) and enhance the non linear interaction eventually leading to spin squeezing through the non-linear Hamiltonian (5.1) [78].

5.1.2 Theoretical predictions and state of the art

The resolution of this interaction-mediated spin squeezing is quite complex and will not be tackled here. It has nonetheless already been thoroughly investigated using different approaches (two-modes stationary, multimode, analytical) in [84, 178, 182, 183, 187, 218].

It results from these theoretical studies several points that are worth mentioning here. First of all, two parameters are used to quantify the squeezing: the first one is the squeezing parameter ξ^2 [180], that takes into account the coherence of the ensemble described by the contrast of the clock or interferometer and the noise reduction induced by the non-linear dynamics, and the second one is the time t_{best} at which the squeezing reaches its maximum.

Without decoherence the maximum achievable squeezing is not limited and increases with the atom number: $\xi^2 \propto N^{-2/3}$. While one-body losses barely affect it, two-body and three-body losses significantly limit the maximum achievable squeezing. More precisely, the analytic formulas derived in [178] show that for two spatially separated symmetric condensates in states $|1\rangle$ and $|2\rangle$, and in the limit of small losses, the best squeezing for 10^4 atoms in our clock trap ($\{\omega_x, \omega_y, \omega_z\} = 2\pi \times \{2.9, 92, 74\}$ Hz) is $\xi^2(t_{best}) = -17.2$ dB reached at $t_{best} = 23$ ms (the loss rates have been taken from [124]). For comparison, in an optimized trap and for $N \to \infty$, $\xi^2(t_{best}) \to -17.5$ dB for $t_{best} = 1.8$ ms.

Similar results were derived in the case of two actively separated and recombined condensates using state-dependent microwave potentials [61, 187]. In particular, using loss rates from [81, 125], 1250 atoms and a cigar-shaped trap ($\{\omega_x, \omega_\perp\} = 2\pi \times \{115, 500\}$ rad.s^{-1}), they found $\xi^2 \approx -13$ dB with $T_{rev} \approx 13$ ms. Experimental instabilities however limited the measured squeezing to $\xi^2 = -2.5$ dB initially [61] and $\xi^2 = -4.3$ dB after some technical improvement [13].

On the other hand, a different group studied the obtainable squeezing relying exclusively on the spontaneous spatial dynamics [84], but also neglecting atom losses. Using a multimode analysis and a spin echo-type sequence ($\frac{\pi}{2} - T_{rev} - \pi - T_{rev} - \frac{\pi}{2}$), they show that the tighter the trap, the better and faster the dynamics and the better the squeezing. Using a spherical trap ($\omega_r = 2\pi \times 500$ rad.s^{-1}) and 1.5×10^5 atoms, they derive a maximum squeezing $\xi^2 \approx -10$ dB, with $T_{rev} \approx 13$ ms. They also show that using a cigar-shaped trap increases the non-linear interaction but also increases the revival time and decreases the overlap leading to a smaller squeezing. Namely for $\{\omega_x, \omega_\perp\} = 2\pi \times \{100, 500\}$ rad.s^{-1} they derive $\xi^2 \approx -7$ dB with $T_{rev} \approx 56$ ms. This shows that much denser atomic samples are required in order to get spin squeezing from the spontaneous spatial separation of the dual-component BEC.

Considering our much smaller trapping frequencies and achievable atom numbers, our long revival times, and the presence of considerable atom losses, we should expect a significantly smaller amount of squeezing. Unfortunately, Alice Sinatra performed some simulations using our experimental parameters, which showed that the final squeezing value is too much dependent on the s-wave scattering lengths to allow accurate predictions.

5.2 Experimental implementation

In this section, we will develop a protocol to perform the tomography of the potentially squeezed atomic state. After presenting the principle, we will emphasize the issues arising from the presence of significant asymmetric losses. A systematic calibration protocol used to perform the state tomography will then be implemented. Unless specified otherwise, all the experimental data are obtained in the clock trap $\{\omega_x, \omega_y, \omega_z\} = 2\pi \times \{2.9, 92, 74\}$ Hz, with 9000 atoms initially. The dynamics in this trap has already been studied in chapter 4. The free evolution time is set to correspond to the first revival time $T_R = T_{rev} = 1.2$ s, for which the contrast reaches 90%, and the Rabi frequency is $\Omega_R = 2\pi \times 3.6$ Hz leading to 70 ms $\frac{\pi}{2}$-pulses.

5.2.1 Experimental sequence

The experimental sequence, illustrated on figure 5.1, is very similar to a standard clock sequence with Ramsey interrogation.

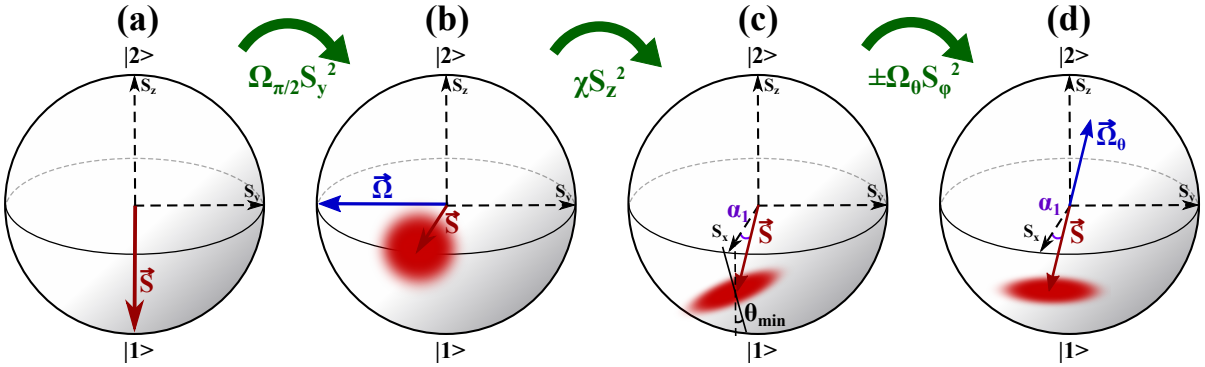

Figure 5.1: **Schematic of the experimental sequence.** The collective spin starts on the south pole (a). Then a first $\pi/2$ pulse of Rabi vector Ω places the condensate in a coherent superposition (b). Next the state dependent spatial dynamics occurs during the free evolution time T_R, leading to the shearing of the spin noise distribution ($\rightarrow \theta$) and the asymmetric losses induce a rotation of the spins around the y axis ($\rightarrow \alpha_1$) (c). Then a second pulse of variable duration, whose Rabi vector is aligned with the Bloch vector, is applied in order to rotate the spin distribution along itself (d). The later is subsequently probed probed by measuring the atom numbers N_1 and N_2 after a 23 ms time of flight.

After preparing a BEC of N atoms in $|1\rangle$, we apply a first near resonant $\pi/2$ pulse which prepares the atoms in a coherent superposition between the two clock states. Its precise frequency is determined in section 5.2.3. Then the atoms evolve freely during T_R which corresponds to one demixing-remixing period. During this free evolution time,

the non-linear elastic interactions shear the spin noise distribution which becomes elliptic and makes an angle θ_{min} with respect to S_x. At the same time, asymmetric losses make the spins rotate around S_y by an angle α_1. When the two states recombine, the collective spin therefore ends up below the equator of the Bloch sphere. A particular combination of detuning and phase-shift has to be found in order to align the Rabi vector $\overrightarrow{\Omega_\theta}$ with the Bloch vector $\overrightarrow{S}$ and rotate the spin noise distribution about its mean with a second interrogation pulse of variable duration and perform the tomography of the squeezed state. Section 5.2.3 is dedicated to this calibration. Finally, for each rotation angle θ the spin noise distribution is probed by detecting the two states simultaneously using the adiabatic rapid passage detection scheme (cf. 3.4) after a 23 ms time of flight.

We use a standard Rabi flopping measurement, that consists in applying a single resonant interrogation pulse and scanning its duration, to calibrate the rotation angle with the pulse duration τ (cf figure 5.2 (a)) yielding

$$\theta[^\circ] = \frac{180}{\tau_\pi}\tau[s]. \tag{5.3}$$

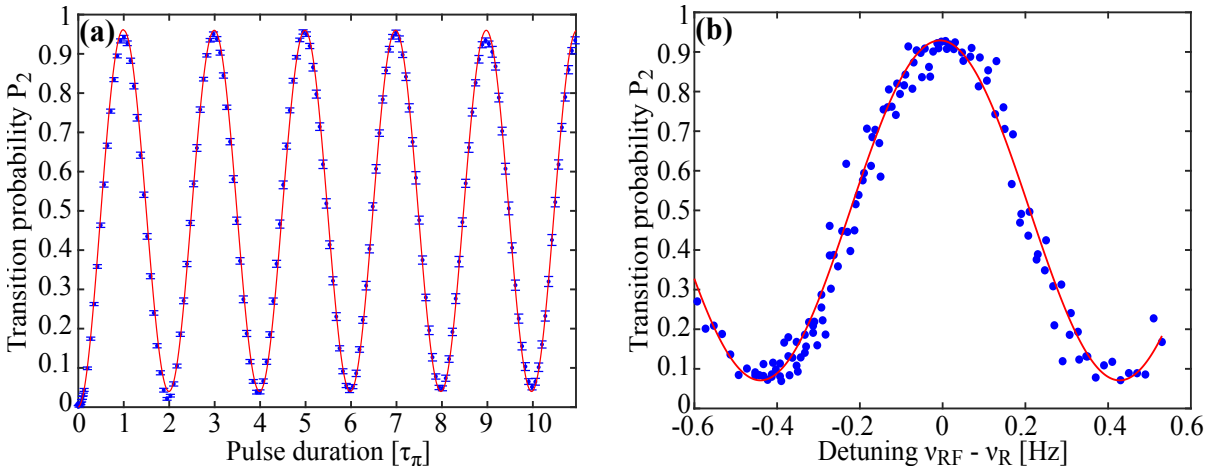

Figure 5.2: **Rabi oscillations and Ramsey central fringe** performed on a pure BEC of 9,000 atoms initially. **(a)** Rabi flopping measurement with $\Omega_R = 2\pi \times 3.6$ rad.s^{-1} ($\tau_\pi = 140$ ms) used to calibrate the rotation angle θ. The reduced contrast is due to the spontaneous spatial dynamics studied in the previous chapter that occurs during the interrogation pulse. **(b)** Ramsey central fringe obtained by scanning the RF frequency ν_{RF} of the standard Ramsey sequence ($\theta = \pi/2$) with $T_R = 1.2$ s. The fit in red gives a resonant frequency $\nu_R = 1781112.221 \pm 0.004$ Hz and a contrast of $85 \pm 2\%$, which corresponds to a corrected contrast of $90 \pm 3\%$.

5.2.2 Spin trajectories and asymmetric losses

In the previous chapter, we added a correction pulse in order to place the Bloch vector back on the equator of the Bloch sphere and counteract the geometrical effect of asymmetric losses (cf. section 4.4.3). However, this technique was implemented at the end of my Ph.D. and we hence used a different method to perform the tomography of the state. Instead of placing the Bloch vector on the equator, we applied a calibrated detuning and local oscillator phase-shift in order to place the Rabi vector of the second Ramsey pulse out of the equator plane and align it with the spin vector. In this section we will therefore analyze the different collective spin trajectories on the Bloch sphere relative to the asymmetric losses and the induced detunings.

To illustrate the mechanisms, let's first start with the simplest and naive approach to probe the spin noise distribution. The idea is to set the local oscillator frequency to the Ramsey frequency ν_R measured on figure 5.2 (b) and scan the second pulse duration, and thus the rotation angle θ, with a $\pm 90°$ local oscillator phase-shift ϕ_{lo} between the two interrogation pulses.

Figure 5.3 shows such a measurement. As the local oscillator frequency corresponds to the Ramsey frequency, the total phase accumulated by the atoms during the Ramsey time ϕ should be close to zero. This phase reads

$$\phi = 2\pi \int_{\tau}^{\tau+T_R} (\nu_{RF} - \nu_{at}(t))dt = 2\pi(\nu_{RF} - < \nu_{at} >)T_R, \tag{5.4}$$

where $< \nu_{at} >$ is the mean atomic frequency over T_R and corresponds the Ramsey frequency ν_R.

The collective spin should therefore come back along $\overrightarrow{S}_x$ after T_R. Moreover, because of the asymmetric losses, we expect to observe an oscillation of P_2 around its value before the second pulse $P_2(\tau + T_R)$, symmetric for $\phi_{lo} = \pm 90°$. The experimental data, however, shows a marked asymmetry (blue and red points respectively). This observed asymmetry can actually be explained with a non-zero detuning between the local oscillator and the atomic transition at the time of the second pulse ($\nu_{RF} - \nu_{at}(\tau + T_R) \neq 0$). Indeed, as the Ramsey frequency is the average of the atomic frequency over the free evolution time, and because the atomic frequency changes during T_R (cf section 4.5), the local oscillator frequency does not match the atomic frequency at the end of the free evolution time. This places the Rabi vector around which the spins rotate, out of the equator plane[1] making the rotation axis different for $\phi_{lo} = \pm 90°$. This is illustrated on the two Bloch spheres on figure 5.3. This detuning ($\nu_{RF} - \nu_{at}(\tau + T_R) \neq 0$) can be deduced from the value of the transition probability when the second pulse is a π-pulse ($\theta = 180°$), and the scheme on figure 5.4 (a):

$$\delta = -\frac{\Omega_R}{2\pi} \tan(\beta) \tag{5.5}$$

[1] According to equation (1.27).

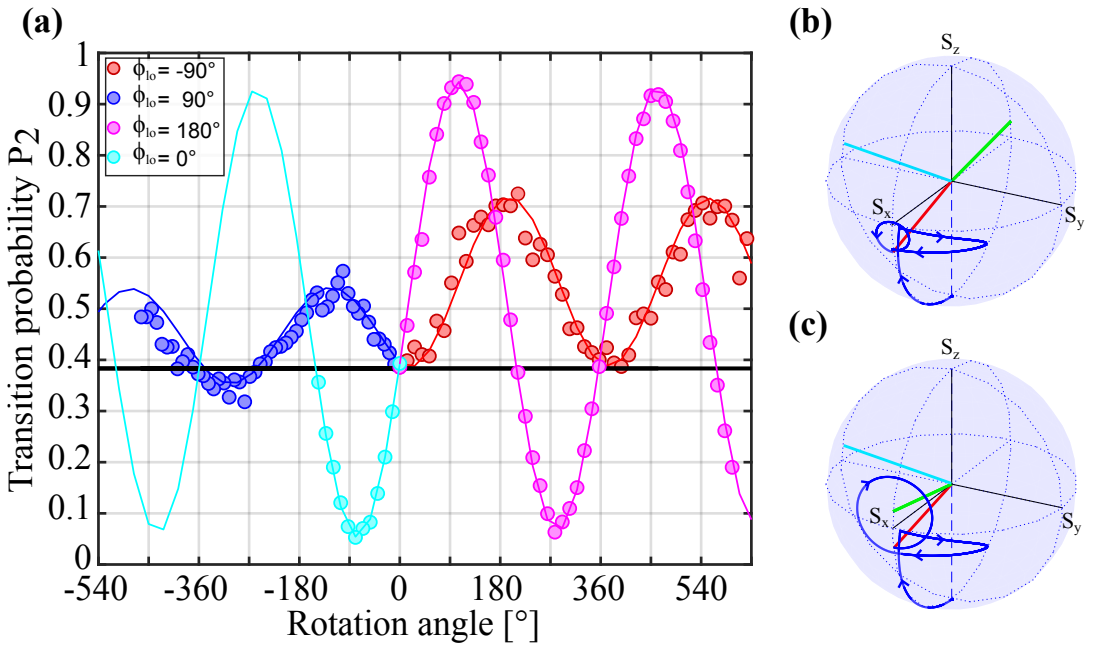

Figure 5.3: **Evolution of P_2 in a squeezing sequence. (a)** The squeezing sequence illustrated on figure 5.1 is applied to 9000 condensed atoms with $\nu_{RF} = \nu_R$ and for four different local-oscillator phase-shifts. The lines come from a numerical simulation detailed in section 1.2.3 with a detuning with respect to the atomic frequency after T_R, $\delta = 0.4$ Hz given by eq. (5.5). The non symmetric oscillation of P_2 for $\phi_{lo} = \pm 90°$ is striking. The data for $\phi_{lo} = 0°$ and $\phi_{lo} = 180°$ are shown as references, and the black line indicates $P_2(\tau + T_R)$. Spin trajectories during the sequence for $\phi_{lo} = +90°$ **(b)** and $\phi_{lo} = -90°$ **(c)** and $\theta = 360°$ are represented (blue line). The Rabi vector during the first (cyan vector) and second (green vector) pulse and the Bloch vector at the end of the sequence are indicated.

with

$$\beta = \frac{1}{2}\left(\alpha_1 - \sin^{-1}\left(2\frac{P_2(3\tau_{\pi/2} + T_R) - 1}{C}\right)\right) \tag{5.6}$$

Taking the values of figure 5.3 for P_2, we get $\delta \approx 0.4$ Hz. This calculated detuning can now be used to model our data using the numerical resolution of the Bloch equations (with losses) with the squeezing sequence (fig. 5.1). Without any adjustable parameter, other than the adjunction of a decoherence term ($\gamma_d = 0.05\ \mathrm{s}^{-1}$) that models the contrast reduction due to the spatial dynamics, the simulation yielding to the plain lines on figure 5.3 confirms the previous reasoning.
On the other hand, for $\phi_{lo} = 0°$ (cyan) and $\phi_{lo} = 180°$ (magenta) the expected Rabi like oscillation is observed with a reduced contrast consistent with the discussion of section 4.4.

Let's now use this study to implement an experimental protocol to systematically

align the Bloch and Rabi vectors in order to perform the tomography of our so far hypothetical squeezed state.

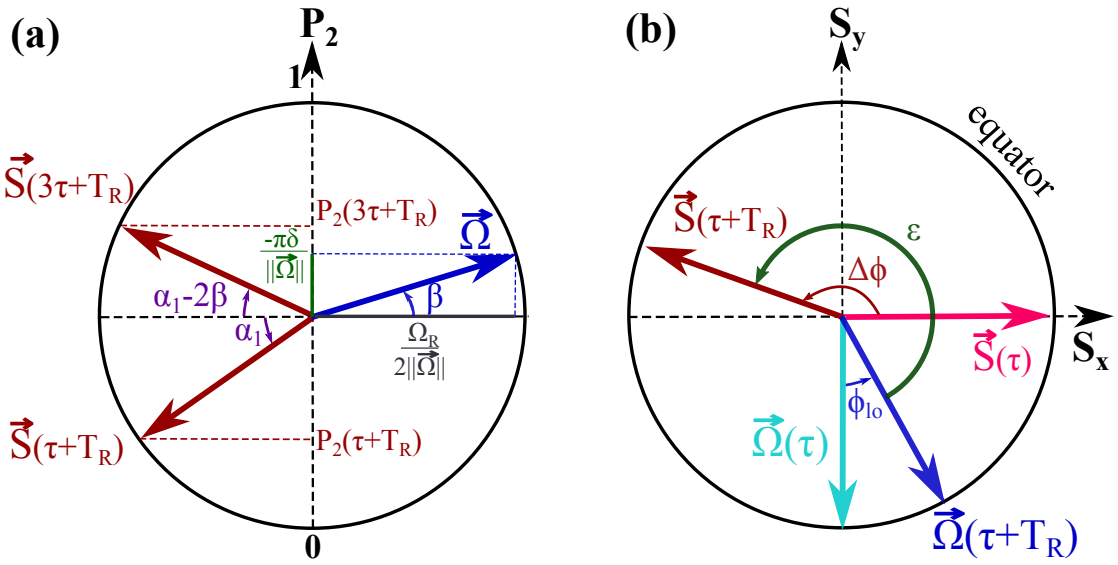

Figure 5.4: **Illustration of spin rotations on the Bloch sphere.** **(a)** Bloch **S** and Rabi **Ω** vectors in a plane orthogonal the equator of the Bloch sphere illustrating equations (5.5) and (1.27). **(b)** Bloch **S** and Rabi **Ω** vectors before (τ) and after ($\tau + T_R$) the free evolution time in the equator plane of the Bloch sphere. ϕ_{lo} is the local oscillator phase-shift, ϕ is the accumulated atomic phase (5.4) and ϵ is the angle between the Bloch and Rabi vector that we want to set to 0° or 180°.

5.2.3 Systematic calibration protocol

As stated before, we want to align the Rabi vector $\overrightarrow{\Omega}$ with the spin vector $\overrightarrow{S}$ so that the second pulse only rotates the spin distribution around itself (meaning that the final transition probability does not depend on the second pulse duration). The protocol used to find the corresponding interrogation frequency and phase-shift ϕ_{lo} is threefold:

1°) Find the detuning. First record the value of the transition probability right before the second pulse of the Ramsey sequence $P_2(\tau + T_R)$. From this value, one can derive the detuning so that the Rabi vector $\overrightarrow{\Omega}$ has the same z-component as $\overrightarrow{S}$. Using the previous reasoning for $\beta = \pm\alpha_1$ and assuming that the atomic frequency is constant over the second pulse duration, the detuning between the atomic frequency at the end

of the free evolution time $\nu_{at}(\tau + T_R)$ and the local oscillator reads

$$\begin{aligned}\delta &= \nu_{RF} - \nu_{at}(\tau + T_R) \\ &= \pm\frac{\Omega_R}{2\pi}\frac{[2P_2(\tau + T_R) - 1]}{\sqrt{C^2 - [2P_2(\tau + T_R) - 1]^2}}.\end{aligned} \tag{5.7}$$

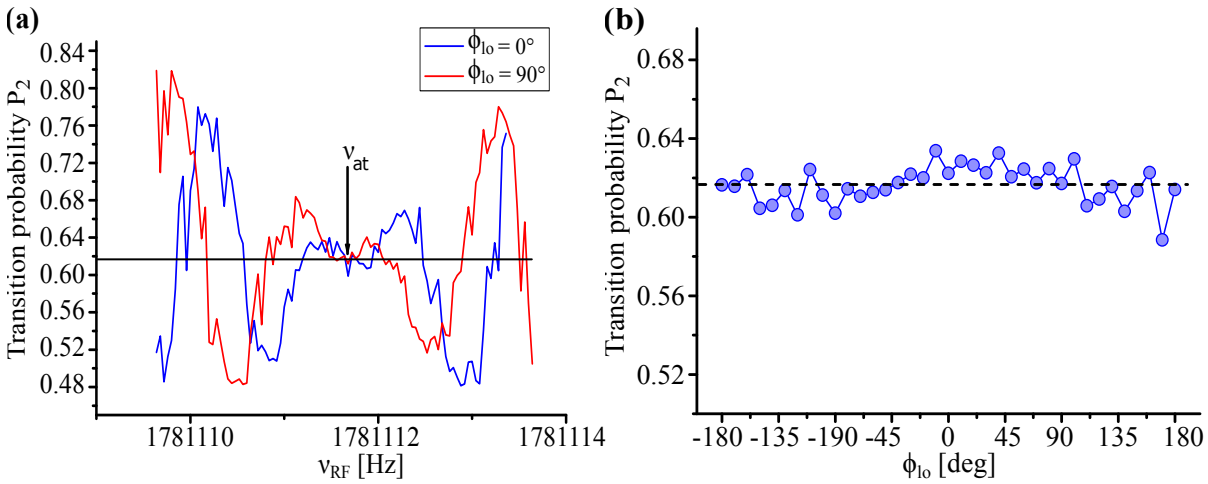

Figure 5.5: **Estimation of the atomic frequency before the second pulse. (a)** The interrogation frequency is scanned for the two indicated phase-shifts between the two interrogation pulses while the duration of the second pulse is set to be a π-pulse. The atomic frequency before the second pulse is indicated and corresponds to the one for which the transition probability does not depend on the phase. **(b)** The phase-shift is scanned when the local oscillator frequency matches the atomic frequency. The almost constant transition probability validates the evaluation of ν_{at}.

2°) Find the atomic frequency before the second pulse. As this detuning is derived with respect to the atomic frequency before the second pulse which differs from the measured Ramsey frequency because of the collisional shift (cf section 4.5), one needs to estimate ν_{at} at that time. Experimentally, this frequency corresponds to the one for which the final transition probability is equal to 1 - $P_2(\tau + T_R)$ and does not depend on the phase-shift ϕ_{lo} when the second interrogation pulse is a $\pi-$pulse. Indeed, the resonant[2] $\pi-$pulse just symmetrizes the spin vector with respect to the equator of the Bloch sphere. Figure 5.5 shows the experimental estimation of ν_{at} for $P_2(\tau + T_R) \approx 0.39$. We find $\nu_R - \nu_{at} \approx 0.4$ Hz which also roughly correspond to the detuning that we can extract from figure 4.14.

[2]in this case $\delta = 0$ and the Rabi vector $\overrightarrow{\Omega}$ lies on the equator of the Bloch sphere.

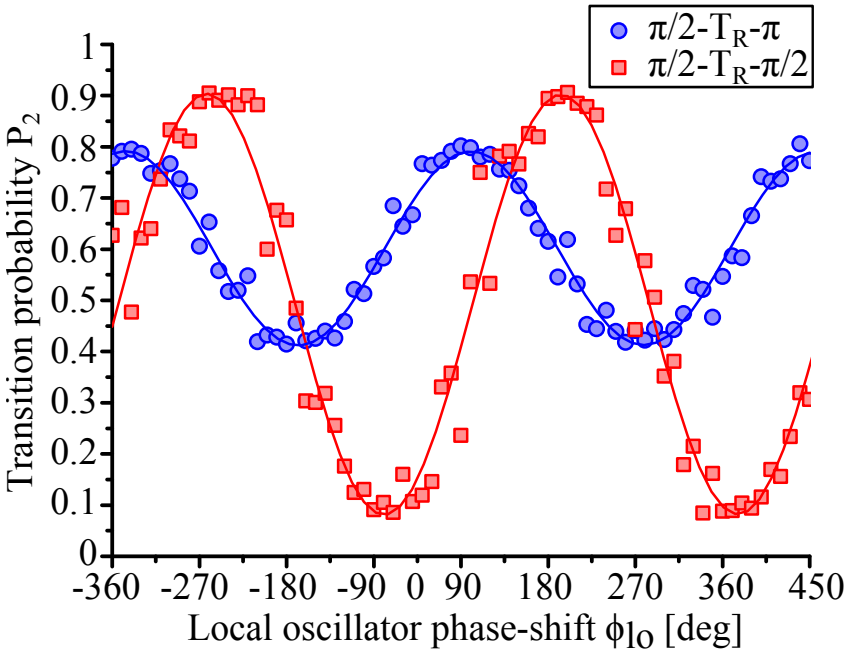

Figure 5.6: **Determination of the local oscillator phase-shift.** The detuning is set so that the Rabi vector has the same z-component as the Bloch vector (δ). The local oscillator phase-shift is scanned for two different second pulse durations: τ_π (blue) and $\tau_{\pi/2}$ (red). The local oscillator phase-shift required to align the two vectors corresponds to the one for which P_2 does not depend on the second pulse duration and equates $P_2(\tau + T_R) \approx 0.39$ here.

3°) Find the appropriate local oscillator phase-shift ϕ_{lo}. Let's first set the interrogation frequency [3] to $\nu_{RF} = \nu_{squeez} = \nu_{at} \pm \delta$ using figure 5.5 and equation (5.7). Now the Rabi vector has the right z-component. As shown on figure 5.6, by scanning ϕ_{lo} with different second pulse durations, we will identify the right phase-shift for which $P_2(2\tau_{\pi/2} + T_R, \phi_{lo}) = P_2(\tau_{\pi/2} + T_R)$.

This phase-shift can also be determined theoretically using equations (5.7) and (5.4). Using figure 5.4 (b), one can derive the local oscillator phase-shift to apply in order to get $\epsilon = 0$ or π.

$$\phi_{lo} = \frac{\pi}{2} - \epsilon + \Delta\phi \tag{5.8}$$

$$= \frac{\pi}{2} - \epsilon + 2\pi[\nu_{at}(\tau + T_R) - \nu_R + \delta]T_R. \tag{5.9}$$

Figure 5.6 gives $\phi_{lo} \approx 160°$ which is consistent with $\phi_{lo} \approx 163°$ calculated with equation 5.9 and $\nu_R - \nu_{at}(\tau + T_R) = 0.4$ Hz and $\delta = 0.81$ derived with equation 5.7.

[3] The frequency is identical for both pulses, and because the detuning to the resonant frequency is much smaller than the Rabi linewidth, the transition probability after the first pulse is not affected.

These three steps allows a systematic alignment of the Bloch and Rabi vectors and have to be applied before each state tomography measurement. Let's now have a look at the squeezing measurement itself.

5.3 Spin squeezing measurement

The measurement sequence is illustrated on figure 5.1. In the following, a pure BEC containing 9000 atoms is prepared in $|1\rangle$. A first $\frac{\pi}{2}$-pulse (70 ms) places it in a coherent superposition. During a free evolution time (1.2 s), the state-dependent spatial dynamics discussed in the previous chapter will spatially separate the two states, leading to an increase of the non linear interaction (5.2) and subsequently to spin squeezing. A second interrogation pulse of duration θ is then applied with the frequency and phase-shift previously calibrated in section 5.2.3 to rotate the spin noise distribution around itself. The two states are then imaged using the adiabatic rapid passage imaging technique and the population in each states $N_{1,2}$ is estimated. Typically, approximately 300 shots are acquired for each rotation angle.
Before describing our data analysis and presenting the state tomography, we propose to study the influence of a fluctuating atom number on the population difference measured at the end of the sequence.

5.3.1 Influence of a total atom number fluctuation

For each rotation angle, we measure a correlation between the population difference and the detected total atom number (5.7 (b)). This section hence is dedicated to the understanding of this correlation, justifying the post-correction applied during the data analysis.

Atomic losses

Despite our efforts concerning the stabilization of the experiment, there is still a $\approx 3\%$ relative fluctuation of the initial atom number. As depicted of figure 5.7 (a), because the losses present in our system are asymmetric, this preparation noise will directly affect the measured population difference at the end of the sequence

$$S_z(T_R) = \frac{N_2(\frac{N_0}{2}, T_R) - N_1(\frac{N_0}{2}, T_R)}{2}, \tag{5.10}$$

where N_0 is the initial atom number. Theoretically, by deriving the population difference after the sequence with a fluctuating initial atom number, it is possible to estimate the sensitivity of S_z with respect to this noise. On figure 5.7 (b) is displayed the slope $\left[\frac{dS_z}{dN}\right]_{loss}$ (blue line) and $\overline{N}\left[\frac{dS_z^n}{dN}\right]_{loss}$ (red line), N being the final atom number and $S_z^n = \frac{S_z}{N}$ the normalized population difference, as a function of the initial atom number. Note that

this initial atom number is not known experimentally. Our knowledge of the final atom number and population decay only enables us to estimate the expected average initial population.

Experimentally, by plotting a similar curve as the one displayed on figure 5.9 (b) without second pulse ($\theta = 0°$) and for different initial atom numbers, we can extract the slopes and compare them with the previous calculation. As expected, the larger the initial atom number, the larger the asymmetry and the larger the impact on the final population difference. The reduced sensitivity of S_s^n with respect to the initial atom number appears clearly.

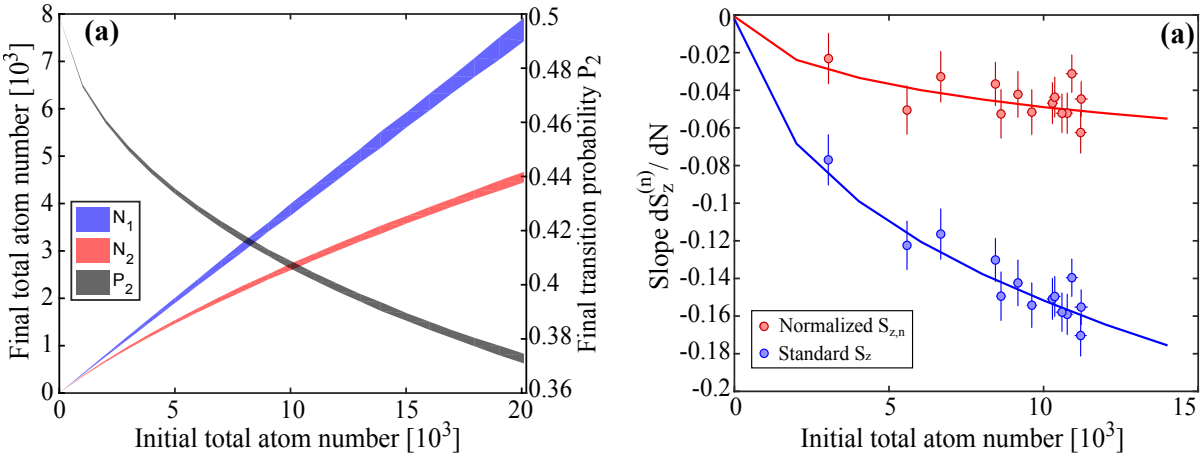

Figure 5.7: **Effect of initial atom number fluctuations on the final population difference. (a)** Population in the two states as a function of the initial atom number in a sequence $\frac{\pi}{2} - T_R$. The decrease of the transition probability due to the asymmetric losses is also indicated. The uncertainty (standard deviation) is represented by the increasing width of the curves. **(b)** Sensitivity of the detected population difference with respect to fluctuations of the detected atom number induced by initial atom number fluctuations, as a function of the initial averaged atom number. The blue line corresponds to $\left[\frac{dS_z}{dN}\right]_{loss}$ and the red one to the normalized population difference $\overline{N}\left[\frac{dS_z^n}{dN}\right]_{loss}$. The dots represent experimental data.

Collisional shift

Without second interrogation pulse, the measurement is not sensitive to the phase that the atoms have accumulated during the free evolution time. However, as soon as a second pulse is applied the interferometer's sensitivity to this atomic phase increases and reaches its maximum for a second $\pi/2$-pulse. Indeed, using equation (1.20) under the condition of small detunings ($\Delta << \Omega_R$), we can derive the expression of the normalized population difference as a function of the second pulse duration and detuning

$$S_z^n(\theta) \approx \frac{C}{2}\cos(\overline{\phi})\sin(\theta), \tag{5.11}$$

where $\overline{\phi} = 2\pi \int_0^{T_R}(\nu_{lo} - \nu_{at}(t))dt + \phi_{lo}$ is the overall accumulated phase during the free evolution time. Any frequency noise will therefore impact S_s^n via the accumulated phase $\overline{\phi}$.

At this point, the largest atom number dependency is the collisional shift whose expression is recalled in the case of a pure BEC (cf. section 4.5.4)

$$\nu_{coll} = \frac{\hbar}{m} n[a_{22} - a_{11} - (2\alpha_{12}a_{12} - a_{22} - a_{11})\frac{n_2 - n_1}{n}], \tag{5.12}$$

As a result, if the initial atom number fluctuates, then the density n fluctuates and because of the asymmetric losses $n_2 - n_1$ fluctuates as well. The overall collisional shift will therefore fluctuate during the sequence. The resulting sensitivity to final atom number fluctuations induced by initial atom number fluctuations reads

$$\left[\frac{dS_z^n}{dN}\right]_{coll} = \frac{dS_z^n}{d\phi} \times \frac{d\phi}{dN} \tag{5.13}$$

$$= -\frac{C}{2}\sin(\overline{\phi})\sin(\theta) \times \frac{d}{dN}\left(2\pi \int_0^{T_R} \nu_{at}(t)dt\right) \tag{5.14}$$

$$= -\pi T_R C \sin(\overline{\phi})\sin(\theta)\frac{d\langle\nu_{at}\rangle_{T_R}}{dN}, \tag{5.15}$$

where C is the interferometer contrast, ϕ is the accumulated phase close to $\frac{\pi}{2}$ and $\frac{d\langle\nu_{at}\rangle}{dN}$ is the linear dependency of the Ramsey frequency[4] with respect to the final atom number. Moreover, in the squeezing sequence, the detuning is set so that the two vectors ($\mathbf{S}$ and $\mathbf{\Omega}$) are aligned, meaning that the overall accumulated phase is $k\frac{\pi}{2}$ where k is an odd integer. This enables a maximum sensitivity to phase fluctuations and this is the reason why atomic clocks also work in that configuration.

In principle, one could derive equation (5.12) for different initial atom numbers and find out its dependency with respect to the final atom number $\frac{d\langle\nu_{coll}\rangle_{T_R}}{dN}$. However, as we saw in section 4.5, the spatial dynamics impacts the evolution of the atomic frequency in a non-trivial way via the parameter α_{12}, and prevents us from accurately predicting the collisional shift. We thus used the measurement performed in section 4.6.2, where we acquired Ramsey spectra for different initial atom numbers, to fit the evolution of the Ramsey frequency with the detected atom number. The corresponding derivative $\frac{d\nu_R}{dN}$ is displayed on figure 5.8 (a) (black line). This slope has also been determined using the clock measurements detailed in the next section 5.4 (blue points). Using this measurement, we can now derive the impact of an atom number fluctuation on the

[4]Indeed, we saw in section 4.5 that the Ramsey frequency corresponds to the atomic frequency averaged over T_R.

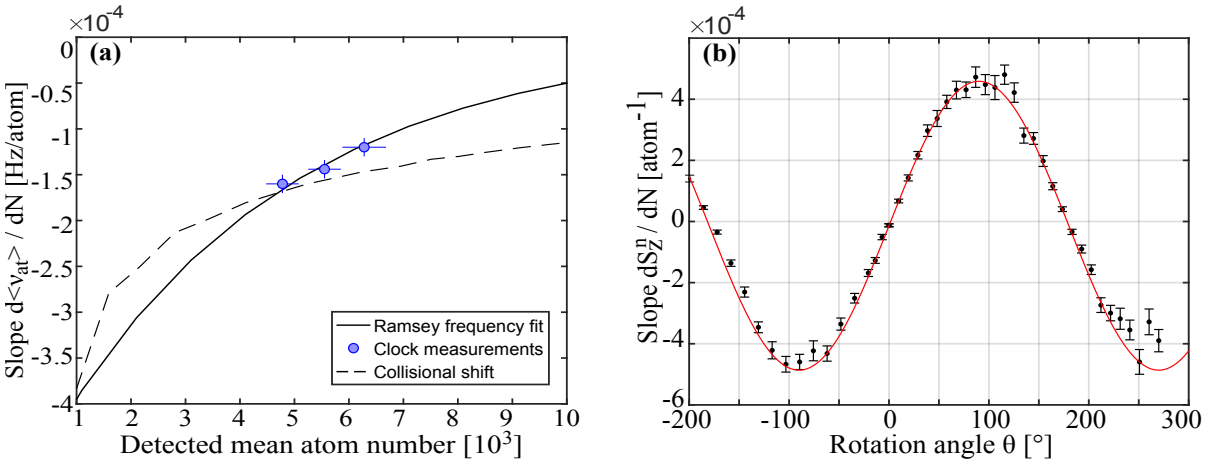

Figure 5.8: **Influence of the collisional shift on the final population difference. (a)** Dependency of the Ramsey frequency with respect to the detected atom number after the squeezing sequence with $T_R = 1.2$ s. The black line is obtained by calculating the slope $\frac{d<\nu_R>_{T_R}}{dN}$ with the measurement performed in section 4.6.2. The blue points correspond to clock measurements whose principle is explained in section 5.4.1. The evolution of the collisional shift derived with eq. (5.12) and $\alpha_{12} = 1$, is also indicated (dashed line) **(b)** Sum of the two contributions during the squeezing sequence. The slope at $\theta = 0°$ is determined by the losses $\left[\frac{dS_z^n}{dN}\right]_{loss}$ while the oscillation is governed by the collisional shift $\left[\frac{dS_z^n}{dN}\right]_{coll}$. The slope vanishes for $\theta \approx 2.5°$.

measured population difference during the squeezing sequence by calculating equation (5.15). The total calculated slope $\left[\frac{dS_z}{dN}\right]_{loss} + \left[\frac{dS_z}{dN}\right]_{coll}$ is displayed on figure 5.8 (b) (red line).

Experimentally, for each θ we can extract the slope $\frac{dS_z^n}{dN}(\theta)$ as it is done on figure 5.9 (b). The experimental slope is in good agreement with the calculated one. An interesting feature is that this slope vanishes for a non zero rotation angle $\theta \approx 2.5°$.

Post-processing the data for this correlation

As for each shot, we know the final atom number and its averaged correlation with the population difference, it is possible to correct the data accordingly. This means removing the measured slope $\frac{dS_z}{dN}(\theta)$ from the raw data for each rotation angle θ.

5.3.2 Data analysis

In order to link the measured atom numbers to the squeezing parameter and the spin noise distribution, the following data analysis is performed for each rotation angle θ. The notation $\overline{X}$ corresponds to the average of the fluctuating quantity X, and the errorbars correspond to one standard deviation.

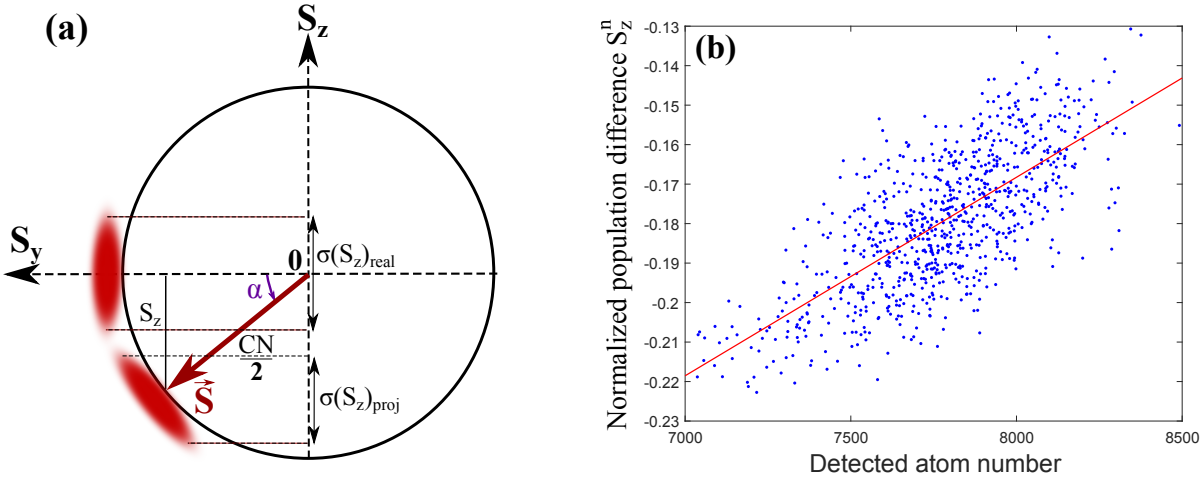

Figure 5.9: **(a)** scheme representing the underestimation of the spin noise due to non-zero mean population difference. C is the contrast of the Ramsey interferometer and α is the angle the the Bloch vector makes with respect to the equator after the free evolution time and because of the asymmetric losses. **(b)** Atom number correlation for $\theta \approx 10°$.

- Runs whose total atom numbers $N = N_1 + N_2$ differ from their mean $\overline{N}$ by more than 3 standard deviations are discarded. These outliers can be due to problems during the image acquisition or the laser locks, and in practice this concerns about 1% of the data.

- The normalized population difference $S_z^n = \frac{N_2 - N_1}{2N}$ and the angle between the collective spin and the equator of the Bloch sphere $\alpha = \text{asin}(\frac{S_z^n}{C/2})$ are derived (cf. figure 5.9 (a)), where C is the contrast of the Ramsey interferometer calculated in the previous chapter 4.4. The population difference is normalized in order to reduce its dependency to total atom number fluctuations.

- The correlation between population difference and total atom number is estimated by fitting the distribution S_z^n vs N (cf. figure 5.9 (b)). As explained in the previous section, since we can measure this correlation for each shot, we can legitimately correct the data accordingly. Namely,

$$S_{z,corr}^n(i) = S_z^n(i) - s_p \times (N(i) - \overline{N}), \tag{5.16}$$

  where $s_p = \frac{dS_z^n}{dN}$ is the slope measured on figure 5.9 (b) and i represents one of the 300 shots at a given rotation angle.

- The variance of the normalized population difference times the mean atom number $\overline{N}\sigma^2(S_{z,corr}^n)$ is derived. At this point, we also check that the Allan variance of $S_{z,corr}^n$ integrates as white frequency noise in order to be sure that there is no drift that could worsen the results.

- The detection noise estimated in section 3.5 is removed from the data:

$$\Delta S_z^2 = \overline{N}^2 \sigma^2(S^n_{z,corr}) - \sigma^2_{det}(S_z) \tag{5.17}$$

- Finally, the fact that the collective spin ends up below the equator of the Bloch sphere leads to an underestimation of the spin noise by a factor $\cos(\overline{\alpha})^2$ (figure 5.9 (a)) which has to be taken into account. ΔS_z^2 is then normalized by the quantum projection noise $N/4$, leading to the final normalized variance and squeezing parameter [180]

$$\mathcal{V}^2 = \frac{4\Delta S_z^2}{\overline{N}\cos(\overline{\alpha})^2} \text{ and } \xi^2 = \frac{4\Delta S_z^2}{\overline{N}C^2\cos(\overline{\alpha})^2}. \tag{5.18}$$

5.3.3 Spin tomography

As the long cycle time (≈13 s) prevents us from acquiring the whole tomography in a single run[5], the complete acquisition has been stretched out over several days. Before every measurement run, the atom number is stabilized around the target value and the whole calibration protocol described in section 5.2.3 is applied to find the correct detuning and phase-shift. Figure 5.10 shows the stability of the transition probability and total atom number, ensuring a similar environment in which the full tomography has been performed. The error bars on figure 5.10 (a) already show the ellipticity of the spin noise distribution.

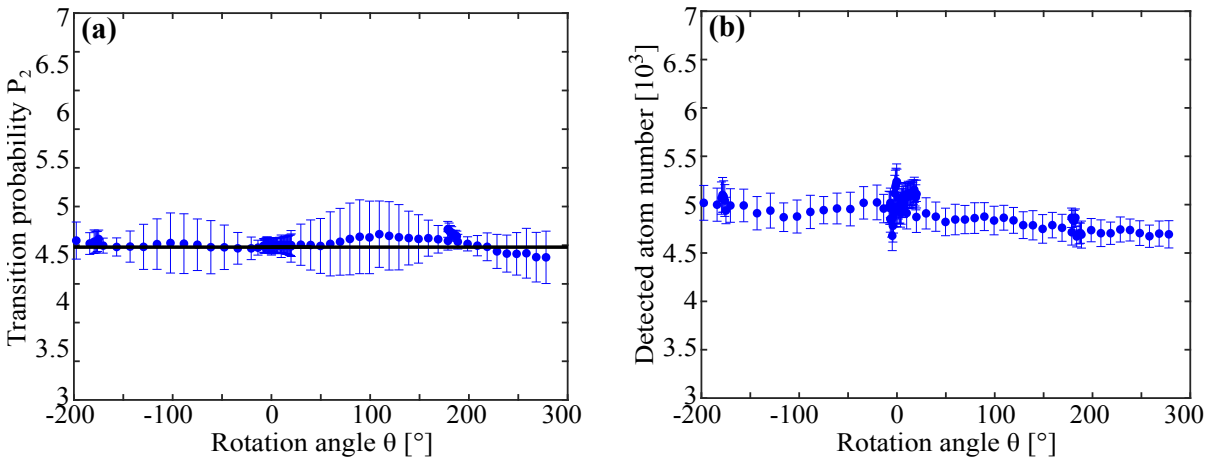

Figure 5.10: **Stability of the P_2 and N during the tomography.** Measured transition probability **(a)** and total atom number **(b)** as a function of the rotation angle θ.

Figure 5.11 shows the evolution of $10\log(\xi^2)$ so that 0 dB corresponds to the standard quantum limit. For $\theta_{min} = 2.5°$, we measure a minimum noise of $\xi^2 = -1.3 \pm 0.4$ dB

[5]Mostly because of a drift in the atom number.

($\mathcal{V}^2 = -2.2 \pm 0.3$ dB) for a 90% contrast testifying of metrologically useful spin squeezing. On the other hand, for $\theta \approx 90°$, the long axis of the ellipse is probed and corresponds to $\xi^2 \approx 16$ dB. Note that this configuration ($\theta \approx 90°$) corresponds to a usual clock measurement. We will use that feature to study the involved phase noises in the next section (5.4). We will also see that the fact that the other noise minima at $\theta \approx \pm 180°$ are higher than for $\theta = 2.5°$ can be explained by an increased phase noise.

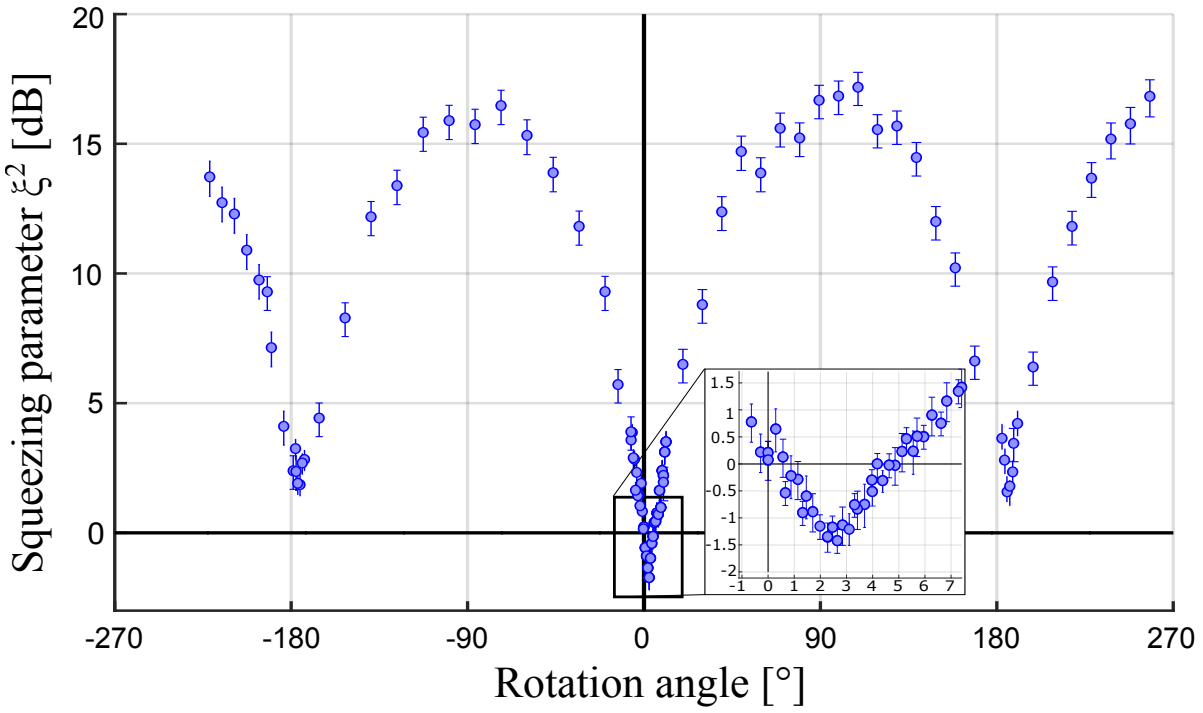

Figure 5.11: **Spin noise tomography.** $10\log(\xi^2)$ is plotted as a function of the rotation angle θ. A minimum spin noise $\xi^2 = -1.3 \pm 0.4$ dB is observed for $\theta_{min} = 2.5°$.

One noticeable feature is that the minimum noise is measured for a rotation angle $\theta_{min} \approx 2.5°$ which corresponds to the one for which the slope displayed on figure 5.8 vanishes, meaning that the final population difference is, to first order, insensitive to initial atom number fluctuations. As we will see in the next section, this is not so surprising, since the major instability source is related to atom number fluctuations.

5.4 Technical noise analysis

As discussed in section 5.1.2, theoretically, a much higher squeezing could in principle be achieved even in the presence of losses. The possible limitations are threefold: a low non-linear interaction, a non-perfect spatial overlap at the revival time that reduces

the contrast, and possible phase noises that induce noise on the measured population difference and also reduce the contrast.
Concerning the interactions, even if it is possible that our spatial separation is not large enough, our measured squeezing parameter is most likely limited by the large asymmetric losses that quickly deteriorate the squeezing [178, 181]. Once again, losses are a major limitation in our system. The exact estimation of this reduction is nonetheless not trivial to estimate in our case because of the too high sensitivity with respect to the s-wave scattering lengths [219].
The reduced contrast at the revival time is in great part due to asymmetric losses (cf. figure 4.10) and only explains the difference between $\mathcal{V}^2 = -2.2$ dB and $\xi^2 = -1.3$ dB. The presence of thermal excitations could also affect the coherence of the ensemble [183]. However the impact of thermal effects on a spinor BEC is still an on-going research topic [220].

Finally, a significant phase noise could also explain why we do not measure a better squeezing. As what we call squeezing corresponds to a reduction of the quantum projection noise, it is possible that this reduction is masked by another dominant noise. Indeed, we can rewrite the squeezing parameter as a function of possible technical noises σ_s

$$\begin{aligned}(\xi^2)_{min} &= \frac{\sigma^2(S_z) - \sigma^2_{det}}{\sigma^2_{QPN}} = \zeta^2 + \frac{\sum_s \sigma_s^2}{\sigma^2_{QPN}} \\ &= -1.3 \text{ dB} \approx 0.73,\end{aligned} \tag{5.19}$$

where ζ corresponds to the noise reduction coefficient coming from the squeezing, the last term corresponds to all the other noise sources contributing to the population difference fluctuations, and $\sigma^2_{QPN} = \frac{\overline{CN}}{4}\cos^2(\overline{\alpha})$.

5.4.1 Clock measurement

To investigate this path, we will perform a clock measurement that has nothing to do with the squeezing experiment but provides a reliable estimate of the experimental instabilities. We will then try to explain the stability at one shot by calculating the contribution of all the identified noise sources. In parallel, we will derive the contribution of these noise sources to the squeezing measurement detailed previously. Once we have identified enough instabilities to explain the short term stability of the clock, we will know that we have found the most dominant instabilities, and we will be able to say by how much it limits our squeezing parameter.

For that purpose, we ran our system almost as a standard clock ($\frac{\pi}{2} - T_R - \frac{\pi}{2}$) for 9000 atoms initially and with 70 ms $\frac{\pi}{2}$-pulses and $T_R = 1.2$ s. The only difference is that we made the first pulse longer so that the spin vector ends up on the equator of the Bloch

sphere after the interrogation time[6]. This way, we can run the clock in the linear regime (that is to say at half fringe), and convert the fluctuations of the transition probability into frequency. To follow the central frequency, we successively take one shot on each side of the fringe, and every twenty shots the local oscillator frequency is corrected in order to keep the Bloch vector on the equator ($P_2 = 0.5$) and follow the clock frequency. This step corresponds to the feedback loop represented on figure 1.7.
The Allan deviation of the measured frequency is displayed on figure 5.12. The "corrected data" (red points) corresponds to the raw data (blue points) corrected for atom number fluctuations, as explained in section 5.3.1. The stability at one shot of the corrected data reads $\sigma_y(T_c) = 2.6 \times 10^{-12}$, while for the raw data $\sigma_y(T_c) = 3.7 \times 10^{-12}$.

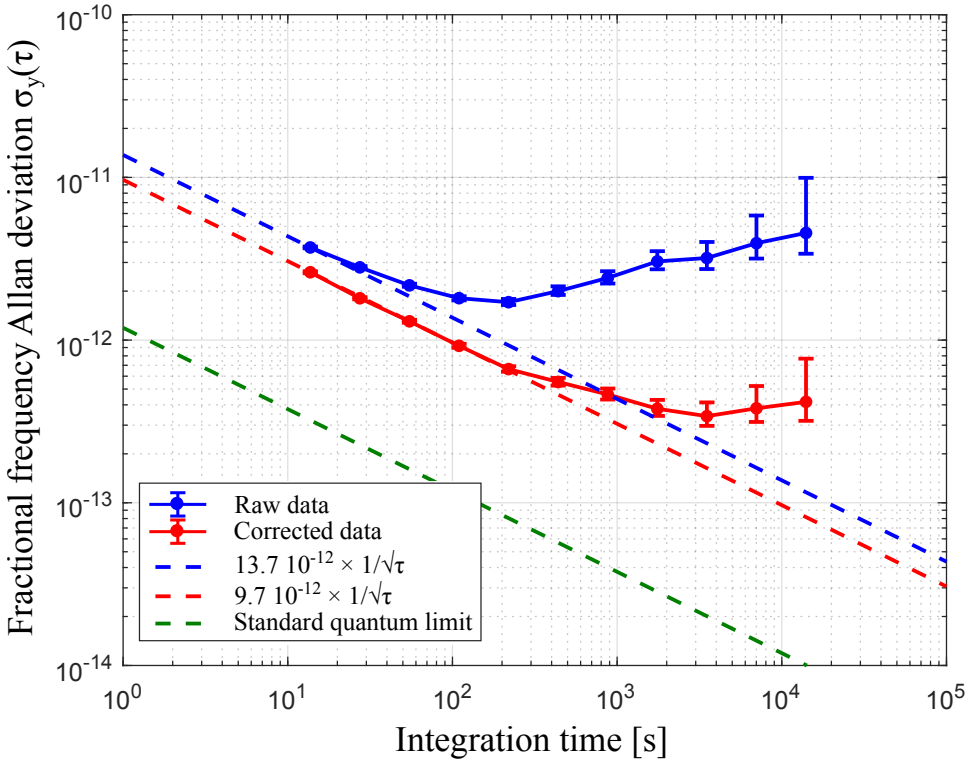

Figure 5.12: **BEC clock stability.** The Allan deviation of the clock frequency is displayed with (red points) and without (blue points) atom number correction. The errorbars correspond to three sigma. The standard quantum limit corresponding to the detected atom number is indicated as a reference in green.

We will now try to explain this stability at one shot by investigating all the relevant sources of instability involved in the experiment and estimate their impact on the measured squeezing. The link between clock stability and frequency or population noise is

[6]This difference will be taken into account in the estimation of the technical noise involved in the squeezing measurement.

given by equation (1.35) in section 1.3.3. Moreover, by differentiating equation (5.11) we can convert the frequency noise identified by the clock measurement on fluctuations of S_z according to

$$\sigma_s = \overline{N}\pi T_R C \sin(\overline{\phi})\sin(\theta)\sigma_\nu. \tag{5.20}$$

The goal of this part is thus to estimate the second term of equation (5.19).

5.4.2 Atomic losses as a statistical process

We already saw that the instability due to fluctuations of the initial atom number can be well measured and corrected (section 5.3.1). However, this correction is not perfect and is subject to an uncertainty related to the detection noise. Moreover, because inelastic collisions are a statistical process and because we can only access the final atom number, the clock frequency is subject to an additional uncertainty that we cannot correct.

Instability due to the atom number correction process

Because of a fluctuation of the detected atom numbers due to imperfect detection, the atom number correction (5.16) induces an instability on the clock measurement [69]

$$\sigma_{y,corr} = \sqrt{2}\left|\frac{d\langle\nu_{at}\rangle}{dN}\right|\frac{\sigma_{det}}{\nu_{at}} \approx 1\times 10^{-12} \tag{5.21}$$

and the squeezing measurement

$$\sigma_{corr} = \sqrt{2}\overline{N}\left|\frac{dS_z^n}{dN}\right|\sigma_{det} \tag{5.22}$$

This fluctuation is nonetheless negligible at the squeezing angle, since the corrected slope vanishes (cf figure 5.8 (b)).

Symmetric losses

We already saw that the collisional shift significantly depends on the initial atom number that we can only access on average using our knowledge on the density and atomic lifetimes. More specifically, for each shot we only measure the final populations and we therefore do not precisely know when and how many atoms have been lost during the sequence. For instance if one atom is lost at the beginning of the Ramsey time it will not contribute to the collisional shift, whereas if it is lost right before the second interrogation pulse it was partly responsible for this frequency shift but will not be detected. This effect has already been studied in our set-up for a thermal ensemble with a density-independent loss rate [69]. As we deal here with condensed samples, we have to take into account the effect of density-dependent losses. To first approximation, the

same reasoning can however be applied using the averaged loss rates

$$\begin{aligned} K_1 &\approx \gamma_{bck} + \frac{1}{2}\gamma_{12}\langle n_2(t)\rangle \\ K_2 &\approx \gamma_{bck} + \frac{1}{2}\gamma_{12}\langle n_1(t)\rangle + \frac{1}{2}\gamma_{22}\langle n_2(t)\rangle, \end{aligned} \tag{5.23}$$

where $\langle\rangle$ represents the temporal average over the interrogation time. The number of trapped atoms in state $|i\rangle$ at a time t then reads $N_i(t) = N(T_R)e^{K_i(T_R-t)}$. Our uncertainty concerning this number can be expressed as [69]

$$\sigma_{N_i}(t) = \sqrt{N(T_R)(e^{K_i(T_R-t)} - 1)e^{K_i(T_R-t)}}. \tag{5.24}$$

By integrating $\sigma_{N_i}(t)$ over the Ramsey time, we get the contribution of these unavoidable frequency noise

$$\begin{aligned} \sigma_{y,sym}(1 \text{ shot}) &= \frac{1}{\nu_{at}}\frac{d\nu_R}{dN}\langle N_1 + N_2\rangle \frac{\sqrt{\langle\sigma_{N_1}\rangle^2 + \langle\sigma_{N_2}\rangle^2}}{N_1 + N_2} \\ &\approx 1.58 \times 10^{-12}. \end{aligned} \tag{5.25}$$

This noise source therefore plays a significant role in the stability budget. Furthermore, we can convert this noise into phase noise, and estimate its impact on the detected population difference using (5.11) with $C = 90\%$ and $\overline{N} = 5000$. This leads to

$$\begin{aligned} \left(\frac{\sigma_s^2}{\sigma_{QPN}^2}\right)_{sym\,loss} &= 11 \text{ for } \theta = 90° \\ \left(\frac{\sigma_s^2}{\sigma_{QPN}^2}\right)_{sym\,loss} &= 0.03 \text{ for } \theta = 2.5°. \end{aligned} \tag{5.26}$$

Asymmetric losses

As the losses are asymmetric, the population difference also fluctuates during the free evolution time. This means that there is an additional instability coming from the asymmetric part of the collisional shift. This time only the asymmetric part of the losses (γ_{22}) plays a role, meaning that the uncertainty concerning the population difference during the Ramsey time reads

$$\sigma_{N_{2,asym}} = \sqrt{N(T_R)(e^{\frac{1}{2}\gamma_{22}\langle n_2(t)\rangle(T_R-t)} - 1)e^{\frac{1}{2}\gamma_{22}\langle n_2(t)\rangle(T_R-t)}}. \tag{5.27}$$

From equation (5.12), this impact the one shot clock stability with

$$\begin{aligned} \sigma_{y,asym}(1 \text{ shot}) &= \frac{\hbar}{m\nu_{at}}(2a_{12}\langle\alpha_{12}\rangle - a_{11} - a_{22})\langle\sigma_{n_2}\rangle \\ &\approx 1.63 \times 10^{-12}. \end{aligned} \tag{5.28}$$

Here the density has been calculated with the model developed in section 1.4.3 and $\langle\alpha_{12}\rangle \approx 0.91$ derived from figure 4.14 (b). This frequency noise also affect the squeezing measurement up to

$$\begin{aligned}\left(\frac{\sigma_s^2}{\sigma_{QPN}^2}\right)_{asym\,loss} &= 23 \text{ for } \theta = 90^\circ \\ \left(\frac{\sigma_s^2}{\sigma_{QPN}^2}\right)_{asym\,loss} &= 0.06 \text{ for } \theta = 2.5^\circ.\end{aligned} \tag{5.29}$$

We can already see that most all the noise observed for $\theta = 90^\circ$ (16.5 dB) on figure 5.11 is explained by phase noise due to these *symmetric* and *asymmetric* losses (15 dB).

5.4.3 Impact of a noisy Rabi frequency on the squeezing measurement

In section 2.4, we realized that the atomic cloud is oscillating inside the trap. On the other hand, it has already been pointed out that because the microwave interrogation field is radiated from the on-chip coplanar waveguide, its amplitude presents a strong spatial dependency, especially along the vertical direction [74, 113, 196]. The space-dependent Rabi frequency then reads

$$\Omega_R(z) = \Omega_{R0}\exp\left(-\frac{z}{l_z}\right), \tag{5.30}$$

where $l_z \approx 41\mu$m [74]. Here the origin of the z-axis has been taken at the trap bottom such that Ω_{R0} corresponds to the Rabi frequency at the trap bottom. The combination of these two features implies a fluctuation of the Rabi frequency seen by the atoms and hence a noise on the measured population difference. Let's first verify that the measured position noise and oscillation (figure 2.10) happen inside the trap. We will then re-estimate the microwave inhomogeneity and measure its impact on the squeezing measurement.

Effect of the mean oscillation and estimation of the MW inhomogeneity

In order to experimentally check that the oscillation happens inside the trap and measure the microwave inhomogeneity, we scanned the trapping time before applying a single short $\frac{\pi}{2}$-pulse (6 ms). This way, the atomic cloud should receive the interrogation pulse at different positions inside the trap. The resulting mean transition probability as well as the position of the clouds after time of flight are plotted on figure 5.13 (a). The oscillation of P_2[7] with a $\frac{\pi}{2}$ phase-shift with respect to the position[8] confirms that the atoms oscillate inside the trap. Here the transition probability at resonance reads

[7] Peak to peak amplitude $\approx 1.5\%$.
[8] Also observed on figure 2.10 (c).

$$P_2(t_{trap}, \tau_{\pi/2}) = \sin^2\left(< \Omega_R(t) > \frac{\tau_\pi}{4}\right), \tag{5.31}$$

where

$$< \Omega_R(t) >= \frac{2\Omega_{R0}}{\tau_\pi} \int_0^{\tau_\pi/2} \mathrm{e}^{-\frac{z_0(t_{trap};t)}{l_z}} dt, \tag{5.32}$$

is the Rabi frequency averaged over the pulse duration and $\mathrm{z}_0(t_{trap}; t) = A_0 \cos(\omega_z(t_{trap} + t) + \phi)$ is the position of the atoms' center of mass inside the trap.

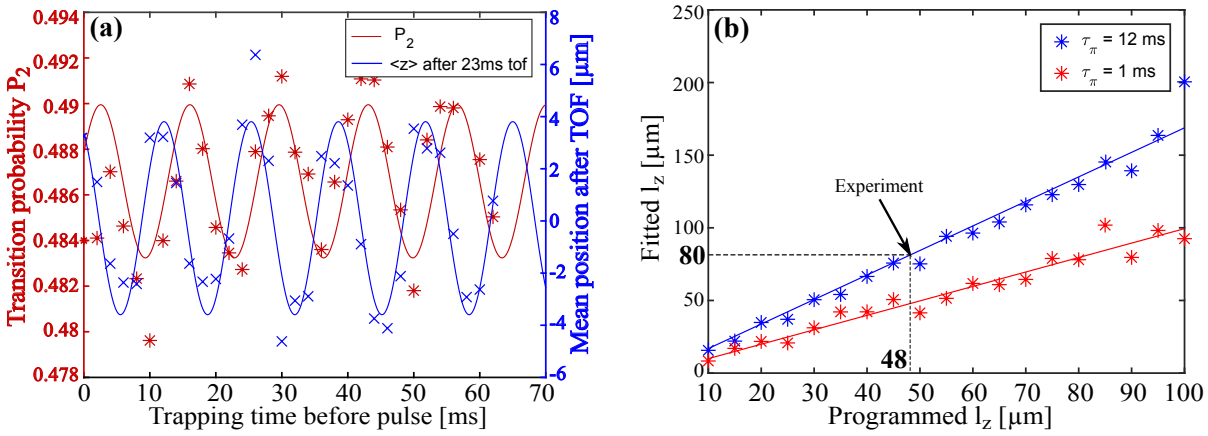

Figure 5.13: **Estimation of the microwave inhomogeneity. (a)** The trapping time before the application of a single $\pi/2$-pulse is scanned, and the transition probability P_2 and position of the center of mass $\langle z \rangle$ are recorded. The oscillation of P_2 is fitted with equation (5.31) where $< \Omega_R(t) >$ has been roughly approximated to $\Omega_R(\tau_\pi/2)$. As explained in the text, this led to an overestimated $l_z = 80 \pm 2\mu$m. **(b)** We used the simulation to numerically scan l_z in equation (5.30) and estimated it from the fit of P_2 as a function of the trapping time before the application of a $\frac{\pi}{2}$-pulse. This calculation has been realized for a high Rabi frequency ($\tau_\pi = 1ms << \frac{1}{\nu_z}$ (blue) to test the method and for the experimental Rabi frequency (red).

The simulation performed in section 2.4 gives access to $\mathrm{z}_0(t_{trap})$ from the cloud position after time of flight thanks to (2.9), and fitting the measured P_2 as a function of the trapping time with equation (5.31) will estimate the microwave inhomogeneity l_z. The only problem is that the integral of equation (5.31) cannot be easily solved analytically unless the pulse duration is small compared to the oscillation period. The averaged Rabi frequency is then almost constant over the pulse duration and $\int_0^{\tau_\pi/2} \Omega_R(t)dt \approx \Omega_R(\tau_{\pi/2})$. Experimentally, we could only achieve $\tau_{\pi/2} = 6$ ms which is comparable to the oscillation period ($\frac{1}{\nu_z} \approx 13.5$ ms). We can however assume that $< \Omega_R(t) > \approx \Omega_R(\tau_{\pi/2})$, fit the oscillation of P_2 with equation (5.31) and numerically calibrate the error on l_z. Indeed, doing so corresponds to under-sampling the cloud position which leads to an overestimation of $< \Omega_R(t) >$ and l_z.

The idea is to numerically apply this experimental sequence ($t_{trap} - \frac{\pi}{2}$) for different values of l_z and record the one extracted from the fit. This has been done for a short π-pulse of 1 ms, for which the approximation is valid, and for the experimental one of 12 ms (figure 5.13 (b)). As expected, the red line as a unitary slope whereas the blue one as a slope of 1.7, leading to a microwave inhomogeneity $l_z = 48 \pm 5$ μm, in good agreement with the anterior estimation [74]. Note that here we used the TACC platform as a MW field sensor. Let's now have a look at the impact of the shot to shot position noise on the coupling to the atoms.

Effect of the shot-to-shot noise and impact on the transition probability

In order to check that the noise in position also happens inside the trap, we acquired Rabi oscillations with 50 shots per pulse duration for two different Rabi frequencies. That way, we can check wether or not the position noise has an effect on the measured transition probability. The simulation with the previously found parameters is then used to reproduce the experimental evolution of the noise on the transition probability, as shown on figure 5.14. To compare the numerical data with the experimental one, we successively added different noise sources:
First, the quantum projection noise and the detection noise (black curve) derived as

$$\sigma(P_2)_{QPN} = \sqrt{\frac{P_2(1-P_2)}{N_1+N_2}} \text{ and } \sigma(P_2)_{det} = \sigma_{det}\frac{\sqrt{N_1^2+N_2^2}}{(N_1+N_2)^2}, \tag{5.33}$$

where $\sigma_{det} = 32$ atoms is the detection noise calculated in section 3.5 and $N_{1,2}$ are the experimental populations of the two states.
Second, the contribution of the position noise and microwave inhomogeneity estimated previously (green curve). In order to have a more intuitive picture, using equation (1.30) in the case of small detunings ($\Delta << \Omega_R$), one can write the noise of P_2 due to Rabi frequency fluctuations as a function of the pulse duration

$$\sigma(P_2) \approx \tau\sigma(\Omega_R)\sin\left(\frac{<\Omega_R>\tau}{2}\right)\cos\left(\frac{<\Omega_R>\tau}{2}\right), \tag{5.34}$$

where τ is the pulse duration. We also showed in section 2.4 that the in-trap shot-to-shot position noise is $\sigma_z = 0.77$ μm, which leads to a relative shot-to-shot fluctuation of the Rabi frequency

$$\frac{\sigma_{\Omega_R}}{<\Omega_R>} = \frac{\sigma_z}{l_z} \approx 1.6\%. \tag{5.35}$$

Third the shot to shot MW power fluctuation and the noise due to atom number fluctuation as studied in section 5.3.1 (red curve). Indeed, by integrating the power spectral density over the range $[10^{-2}; 10^5]$ Hz measured with a MW power-meter (Agilent N1913A), we estimated the relative fluctuations of the RF and MW powers right before entering the chip wires

$$\frac{\sigma(\Omega_{RF})}{\Omega_{RF}} = 1 \times 10^{-5} \text{ and } \frac{\sigma(\Omega_{MW})}{\Omega_{MW}} = 1.3 \times 10^{-4}. \tag{5.36}$$

This leads to a shot-to-shot fluctuation of Ω_{R0}.

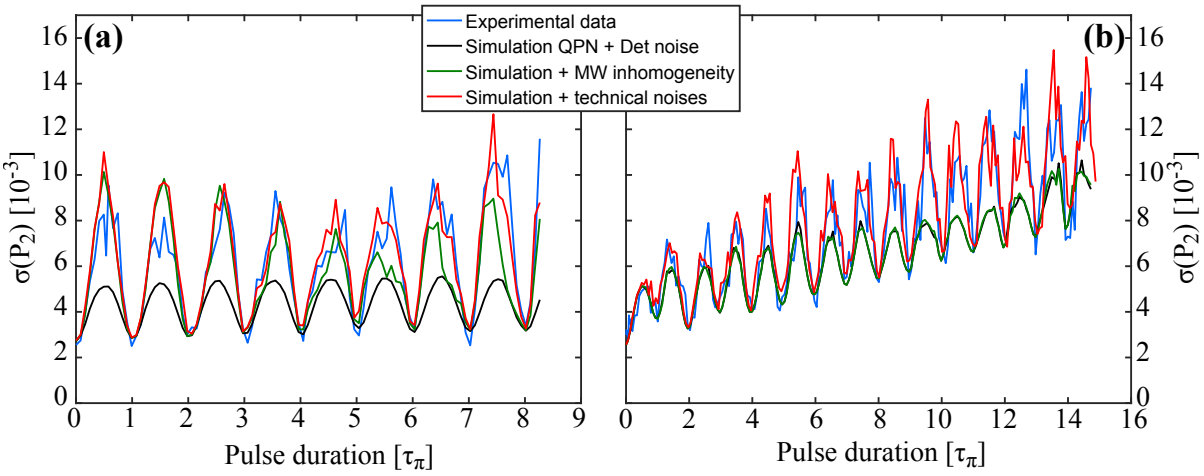

Figure 5.14: **Study of the atomic noise in a Rabi sequence.** Rabi oscillations are acquired for $\Omega_R = 2\pi \times 41.3$ Hz **(a)** and $\Omega_R = 2\pi \times 3.6$ Hz **(b)** with a BEC of 1.1×10^4 atoms initially. 50 shots are taken for each pulse duration and the shot to shot fluctuations (standard deviation) of P_2 are derived (blue line). The simulation described in the text is used to reproduce the experimental data. The quantum projection noise and detection noise are calculated from the experimental atom numbers and detection parameters (black line), then the microwave inhomogeneity $l_z = 48\mu$m and the position noise are taken into account (green line), and the shot to shot fluctuations of the MW power $\frac{\sigma(\Omega_R)}{\Omega_R} = 1.3 \times 10^{-4}$ and atom number are added to the previous noises (red line). The offset of about $3 \cdot 10^{-3}$ is due to detection noise.

It appears clearly on figure 5.14 (a) that for a high Rabi frequency, the noise on the transition probability is dominated by Rabi frequency fluctuations due to position noise and microwave inhomogeneity. The position noise hence also takes place inside the trap. This is by the way the main reason why we use rather long interrogation pulses for a given pulse area $\Omega\tau$. Using equation (5.34), we quickly see that Rabi fluctuations due to position noise have to be averaged over the pulse duration in order to match the experimental data. This means that the position noise is not due to random momentum kicks inside the trap but probably more to a one-off kick during the transfer between two traps. Equation (5.35) is then an upper bound of the Rabi frequency noise seen by the atoms, and this limit is only reached in the case of very short pulses ($\tau << 2\pi/\omega_z$).

On the other hand, for a low Rabi frequency, the dominant noise source is the atom number fluctuations due to atomic losses. Indeed, in that case the position noise is averaged out over the pulse duration and quickly becomes smaller than the quantum projection noise. Note that the atomic noise is at the standard quantum limit for a single $\pi/2$-pulse but not for several $\pi/2$-pulses (this is in agreement with the calibration of the detection system made in section 3.5). The slow increase of the quantum projection

noise contribution (black curve) is due to the atom number decreases because of atom losses as it appears on equation (5.33).

Now that we convinced ourselves that the position fluctuations also take place inside the trap, let's analyze their effect on the squeezing measurement.

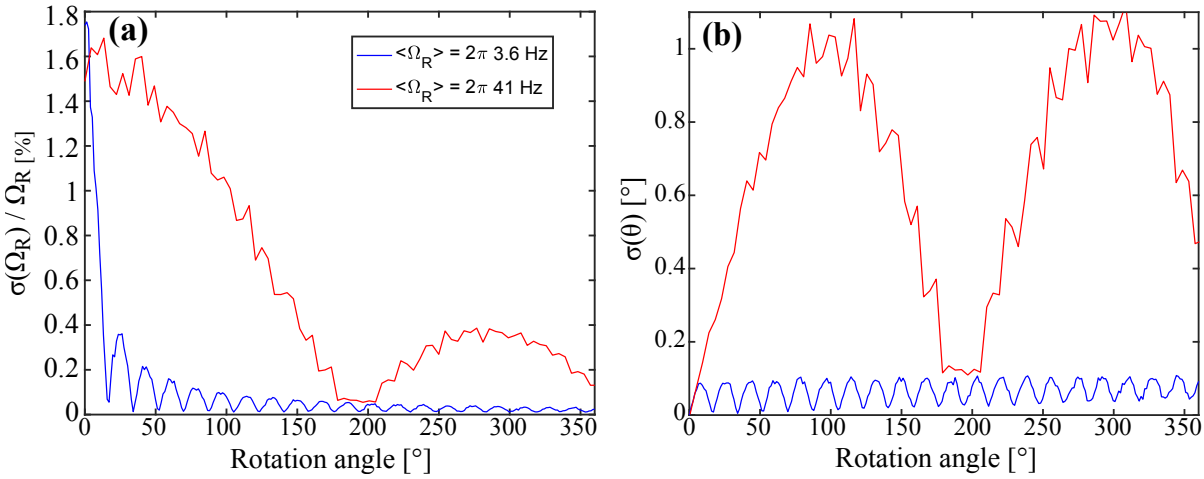

Figure 5.15: **Rabi frequency relative fluctuations.** Numerical calculation of the relative Rabi frequency noise during the second pulse of the squeezing sequence **(a)**, and the resulting uncertainty on the rotation angle **(b)**, for $\tau_\pi = 140$ ms (blue) and $\tau_\pi = 12$ ms (red). The minima occur every multiple of the oscillation period.

Impact on the rotation angle calibration

According to equation (5.3) $\theta \propto \tau\Omega_R$ which directly leads to

$$\sigma(\theta) = \tau\sigma(\Omega_R). \tag{5.37}$$

We saw that the Rabi frequency has two independent fluctuation origins: the combinaison of position noise and MW inhomogeneity that averages out over the pulse duration, and shot-to-shot fluctuation of the MW power (5.36). The averaging of the Rabi frequency fluctuations due to position noise occurs on a timescale on the order of $1/\nu_z$ which is the oscillation period. As displayed on figure 5.15 (a), the relative averaging of the Rabi frequency noise occurs much faster (in term of rotation angle) for a low Rabi frequency than for a high one. This means that its contribution to the overall noise is reduced as we already saw on figure 5.14. The error on the rotation angle is then very small ($< 0.1°$). Even in the case of the high Rabi frequency, the error on the rotation angle is below 1° and around 0.1° for $\theta = \theta_{squeezing}$ (cf figure 5.15 (b)).

Impact on the squeezing measurement

Using the same reasoning for the squeezing sequence ($\frac{\pi}{2} - T_R - \theta$), we estimate that

for $\theta = 90°$, $\sigma^2(S_z) \approx 16$ atoms and for $\theta = 2.5°$, $\sigma^2(S_z) \approx 8$ atoms. This yields

$$\left(\frac{\sigma_s^2}{\sigma_{QPN}^2}\right)_{\Omega_R} \begin{array}{l} \approx 1.3 \times 10^{-2} \text{ for } \theta = 90° \\ \approx 7 \times 10^{-3} \text{ for } \theta = 2.5°. \end{array} \tag{5.38}$$

To sum up, thanks to the long interrogation pulses, the impact of the microwave inhomogeneity is negligible.

5.4.4 Other phase noise sources

Local oscillator noise

As the transition frequency is only probed during the Ramsey time, which is only a fraction of the full experimental cycle, the local oscillator noise is sampled at a frequency $1/T_c$. This sampling leads to aliasing which can transmit high frequency noise towards the low frequency domain and degrades the clock stability. This is called the Dick effect [146]. The impact on the clock stability has already been studied in [69], and adapting the method to our current experimental parameters, we found

$$\sigma_{y,Dick}(1 \text{ shot}) = 1.2 \times 10^{-13} \text{ at 1 shot.} \tag{5.39}$$

Quantum projection noise

The quantum projection already discussed previously, induces unavoidable fluctuations of the measured transition probability that impacts the clock stability as

$$\sigma_{y,QPN}(1 \text{ shot}) = \frac{1}{\nu_{at}\sqrt{N}|\frac{dP_2}{d\nu}|} = 3.25 \times 10^{-13} \text{ at 1 shot.} \tag{5.40}$$

Detection noise

Similarly to the quantum projection noise, an imperfect detection will induce noise on the measured atom numbers and therefore on the transition probability. Its impact on the clock stability reads

$$\sigma_{y,det}(1 \text{ shot}) = \frac{\sigma_{det}}{\nu_{at}\sqrt{2N}|\frac{dP_2}{d\nu}|} = 1.95 \times 10^{-13} \text{ at 1 shot.} \tag{5.41}$$

Relative frequency stability	shot-to-shot (10^{-12})	$\frac{\sigma_s^2}{\sigma_{QPN}^2}(90°)$	$\frac{\sigma_s^2}{\sigma_{QPN}^2}(2.5°)$
Measured, without correction	3.7	145	0.73
Measured, after N correction	**2.6**	**45**	**0.73**
Asymmetric losses	1.63	23	0.06
Symmetric losses	1.58	11	0.03
N correction	1.0	9	0
Local oscillator	0.1	0.15	4×10^{-4}
Quantum projection noise	0.3	-	-
Detection noise	0.2	-	-
Total estimate	**2.5**	**43**	**0.09**

Table 5.1: **Stability budget of the BEC clock and impact on the squeezing measurement.** List of the dominant instability sources and their impact on the shot-to-clock clock stability and squeezing measurement for $\theta \approx 90°$ and $\theta = 2.5°$. The highest contributions come from density fluctuations due to atom losses. The detection noise had already been removed from the squeezing data.

5.4.5 Stability budget and squeezing limits

The previously derived instability sources are listed in table 5.1. The impact of the studied noise sources on the clock stability at one shot, the squeezing measurement at $\theta \approx 90°$ (long axis) and $\theta = 2.5°$ (small axis) are indicated.

The good agreement between the measured clock stability and noise estimation enables us to evaluate the contribution of technical noise in the measured squeezing parameter $\frac{\sigma_s^2}{\sigma_{QPN}^2}(2.5°) = 0.09$. This means that without this overall phase noise, we could have gotten at least $\xi^2 \approx -2$ dB. Moreover, we now understand why the minimum noise is measured for a rotation angle $\theta = 2.5°$ which corresponds to the ones for which the atom number dependency is reduced (cf. figure 5.8 (b)). This means that the amount of achievable squeezing is probably higher at a bigger rotation angle, but the noise reduction is compensated by the atom-number-related noise.

5.5 To go a bit further

5.5.1 Attempt to get a better squeezing

Let's now get use of the previous chapter and discuss a bit about the possible ways to improve our squeezing parameter. As the main limitation comes from atom losses, a possibility would be to reduce the interrogation time by compressing the trap for instance (cf. figure 4.15). However, if we want the spatial separation to be as large as

before, we would need to significantly increase the density which would also increase the losses and the noise associated to them. As a matter of fact, we performed the same spin tomography measurement in a tighter trap $\{\omega_x;\omega_y;\omega_z\} = 2\pi \times \{4.4; 128; 113\}$ (green points on figure 4.15). It turns out that both the shot-to-shot clock stability[9] ($\sigma_y(T_c) = 2.6 \times 10^{-12}$) and the squeezing parameter ($\xi^2 = -1.1 \pm 0.5$ dB) were slightly worse than what we obtained previously.

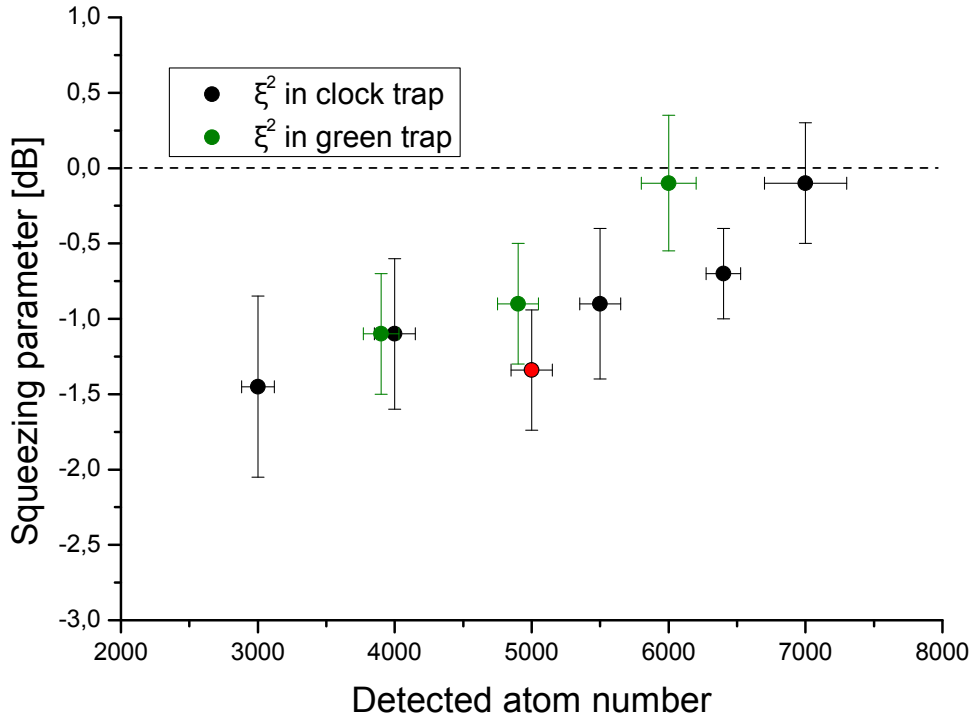

Figure 5.16: **Squeezing parameter versus atom number.** The black points are measured in the clock trap ($\{2.9; 92; 74\}$ Hz), the red point corresponds to the measurement displayed on figure 5.11, and the green ones to the so-called green trap ($\{4.4; 128; 113\}$ Hz).

We also briefly performed the same measurement with different initial atom number, scanned by cutting more or less deeply in the condensate at the end of the evaporation, and the results concerning the resulting squeezing parameter are displayed on figure 5.16. The relatively large errorbars prevent us from drawing any definitive conclusions, even though it seems that reducing the initial atom number improves the squeezing. Actually the number squeezing $\mathcal{V}^2$ is always roughly the same around -2 dB and it is only the reduced contrast (cf. figure 4.16) that deteriorate the squeezing parameter. This is also the reason why the green points are slightly worse than the black ones.

[9] With atom number correction.

5.5.2 Implementation in an inteferometric sequence

In the context of quantum metrology, the generation of a squeezed spin state only represents the first step. Next, the interactions have to be turned off and the interferometric sequence can start with the squeezed state as input.

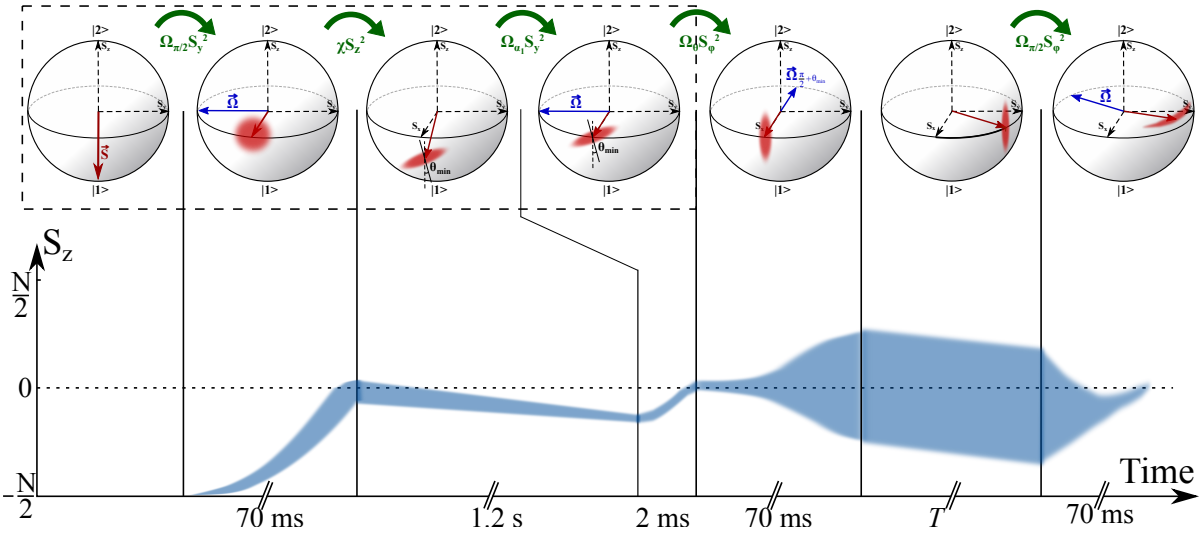

Figure 5.17: **Ramsey interferometry below the standard quantum limit.** The previously described procedure is used to generate a squeezed spin state, which is then placed back on the equator of the Bloch sphere using the correction pulse detailed in section 4.4.3. Next, a $\frac{\pi}{2} + \theta_{min}$-pulse rotates the spin noise distribution until its small axis is aligned with the phase quadrature. After a free evolution time T, another $\frac{\pi}{2}$-pulse converts the accumulated phase into populations that can be probed with a precision better than the SQL. The evolution of the population difference is also indicated.

The first four steps correspond to the state preparation described previously, with the difference that the squeezed state has now to be placed back on the equator of the Bloch sphere. This can be achieved by using a correction pulse, similar to the one described in section 4.4.3. Then the interferometer starts by aligning the small axis of the spin noise distribution with the phase quadrature. This consists in a $\frac{\pi}{2} + \theta_{min}$ rotation, and as the Bloch vector is now on the equator, this pulse just needs a $\frac{\pi}{2}$ phase-shift compared to the previous one. Finally, after a free evolution time T, a last pulse converts the phase accumulated by the atoms into populations that will be probed during the detection with a precision better than the standard quantum limit. As in a standard clock sequence, the Rabi vector of this last pulse should be aligned with the Bloch vector. To do so, one could either use another fast correction pulse to put the Bloch vector back on the equator, or use the protocol described in section 5.2.3.

This protocol can only work if the non-linear interaction responsible for the squeezing can be frozen during the free evolution time T. In our case, this interaction is not

controlled by the user, we therefore cannot easily turn it off. However, it should be possible to minimize it by further reducing the trapping confinement or by performing the measurement in free fall for instance.

5.5.3 Perspectives

The investigation of more compressed traps, such as the blue one on figure 4.15, with smaller atom numbers could be interesting. Indeed, we have to wait for the two states to recombined to perform the tomography of the state, but the optimum squeezing is supposed to occur on a faster time scale [219]. Therefore, the faster the dynamics, the higher the contrast and the better the squeezing, assuming that the non-linearity is still strong enough to significantly squeeze the state.

MW dressing On the other hand, we saw that asymmetric losses are responsible for most of our troubles: phase noise, contrast reduction and complexity of the sequence. It would thus be interesting to reduce the two-body loss rate of state $|2\rangle$. As these collisions ($|2,1\rangle + |2,1\rangle \longrightarrow |2,0\rangle + |2,2\rangle$) are energetically favorable because the energy difference between these two pairs of states ($|2,1\rangle \leftrightarrow |2,2\rangle$ and $|2,0\rangle \leftrightarrow |2,1\rangle$) are similar. Therefore, by shifting upward the energy of state $|2,2\rangle$, one could in principle reduce these losses.

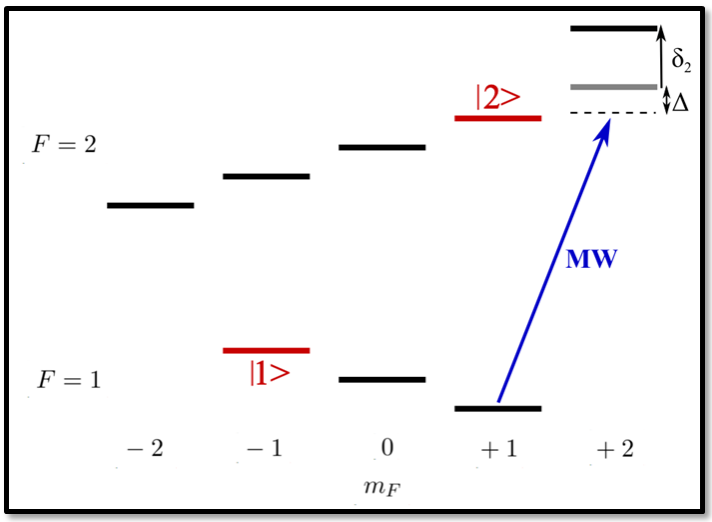

Figure 5.18: **Principle of microwave dressing of state $|2,2\rangle$.** Energy diagram with an additional microwave drive with detuning Δ with respect to $|2,2\rangle$. This microwave dressing induces a frequency shift δ_2 proportional to the corresponding microwave power.

And such shifting could be realized using a one-photon dressing with a σ-polarized microwave field. Of course, one would need to carefully check that this additional coupling does not introduce to much noise on the clock transition. It would anyway be very

interesting to observe a reduction of these losses and experimentally study their impact on spin squeezing.

Gravitational sag Another path would be to induce a small asymmetry between the trapping potential of the two states at the beginning of the sequence, in order to help the dynamics to start. It was indeed shown in Philipp Treutlein's group that this greatly enhance and hasten the spatial separation [13]. In our case, this asymmetry could come from the dependency of the quadratic Zeeman effect with respect to gravity. Indeed this leads to a displacement of the center of the trapping potentials for the two clock states. This displacement depends on the difference between the field at the trap bottom and the magic field [114], and can be estimated to be on the order of $\Delta z = 56\text{nm/G} \times (B - B_m)$ [83]. Therefore, by scanning the magnetic field at the trap bottom, one could displace the position of the two states and study its influence on the spatial dynamics.

Conclusion

*****

In this thesis, we have reported the first observation of spontaneous spin squeezing generated by the state-dependent spatial dynamics of a spinor Bose-Einstein condensate. Although the experiment was initially designed as a clock using thermal ensemble, we have used the stability and versatility provided by the TACC platform to experimentally study the coherence properties and spatial dynamics of a dual-component BEC. This high stability enabled us to measure a reduced spin noise compared to the standard quantum limit by $\mathcal{V}^2 = -2.2$ dB, that provides a metrologically useful spin squeezing $\xi^2 = -1.3$ dB with a 90% contrast after a 1.2 s interrogation time and for 5000 atoms. This shows once again the extremely stable and coherent environment provided by the atom-chip technology. We also showed that the squeezing is mainly limited by phase noise arising from the statistical nature of atom losses, and more specifically asymmetric losses. Not only these losses degrade the stability of the system, but they also greatly increase the complexity of the spin manipulations. It is however not quite clear yet how the squeezing parameter scales with the atomic density in the presence of losses. If the non-linear interaction χ scales differently than the two-body losses, then there is a chance to get a better squeezing by tuning the trapping frequencies and atom number.

Some work has also been carried out to improve the detection system with the robust implementation of the Adiabatic Rapid Passage technique and optimization of the fringe removal algorithm. This led to a shot-noise limited detection with a good accuracy of the derived atom number. Several technical difficulties had nonetheless to be faced, especially concerning the short lifetime of our laser sources, that we had to replace in average every year (each of the three lasers). At some point, we were building ECDL's like in a line production to compensate their sudden death. To find an explanation, ground loops and current noises were investigated several times, without much success though. Eventually, we decided to replace the thousands of old laser diodes brought on

E-bay several years ago by a few more expensive, yet more reliable, ones. It has been almost a year now, and the lasers are still working...

Study of an interacting dual-component BEC

The thorough characterization of the dynamics of the BEC in terms of contrast and relative frequency evolution, provided us a good experimental understanding of the system and enabled us to accurately manipulate the atomic spins. However, our attempt to model and understand the physical phenomena behind the observed dynamics was not really a success. We concluded that the simple description given by the Gross-Pitaevskii equations under the mean field approximation is not appropriate to describe our system. In that sense, the inclusion of thermal excitations in the BEC, and their coupling to the condensed part could provide a part of the solution [220]. This could also be investigated experimentally by looking at the contrast evolution of the Ramsey interferometer, varying the final evaporation frequency. Additionally, a better understanding of the impact of inelastic collisions and asymmetric losses on the coherence and fundamental structure of the condensate would be of prime interest in such a system and in the more general context of BEC based quantum metrology. Even if the work carried out here was restricted to the case of cigar-shaped traps, it was pointed out in [84] that the spatial separation could be more efficient in a spherical trap. In particular the contrast revival should be higher and obtained at a shorter time. It could therefore also be interesting to extent this study to other trapping geometries.

Towards atomic interferometers beyond the standard quantum limit

The novelty of the work developed in this manuscript lies in the relative simplicity of the sequence leading to spin squeezing. This means that atom interferometers using internal states labeling could in principle directly benefit from the high phase-space density of BEC's combined with an enhanced phase sensitivity. To do so, a preliminary sequence consisting only in applying a resonant $\frac{\pi}{2}$-pulse, waiting for the two states to recombine and rotating the spin noise distribution to place the axis with a reduced noise along the phase quadrature, would have to be implemented prior to the usual interferometric scheme. However, as opposed to the squeezing obtained with a Feshbach resonance [60] or a state-dependent potential [61], here the squeezing dynamics is not controlled by the user. The dynamics has therefore to be frozen, either by using a free fall interferometry technique, or by further reducing the trapping confinement in order to sufficiently decrease the density and the resulting mean field interaction.
Let's also mention that the spatial dynamics is only required here to enhance the very small initial non-linear collisional interaction between the two components of ^{87}Rb, because of the similar s-wave scattering lengths. Other atomic species, such as Na for instance, can be relatively easily condensed and possess possible clock states with different scattering lengths. That way, spontaneous spin squeezing could directly be observed, without the inconveniences of spatial dynamics.

On the way to an Entanglement Enhanced Trapped Atom Clock on a Chip

Still in the context of quantum metrology, the versatility of the atom chip has been pushed one step further with the recent inclusion of a pair of fibered fabry-Perot cavities [221] (cf. figure 5.19). The cavity machining, chip fabrication, assembly and alignment and characterization of the cavities are thoroughly detailed and explained in Konstantin Ott's thesis [92].

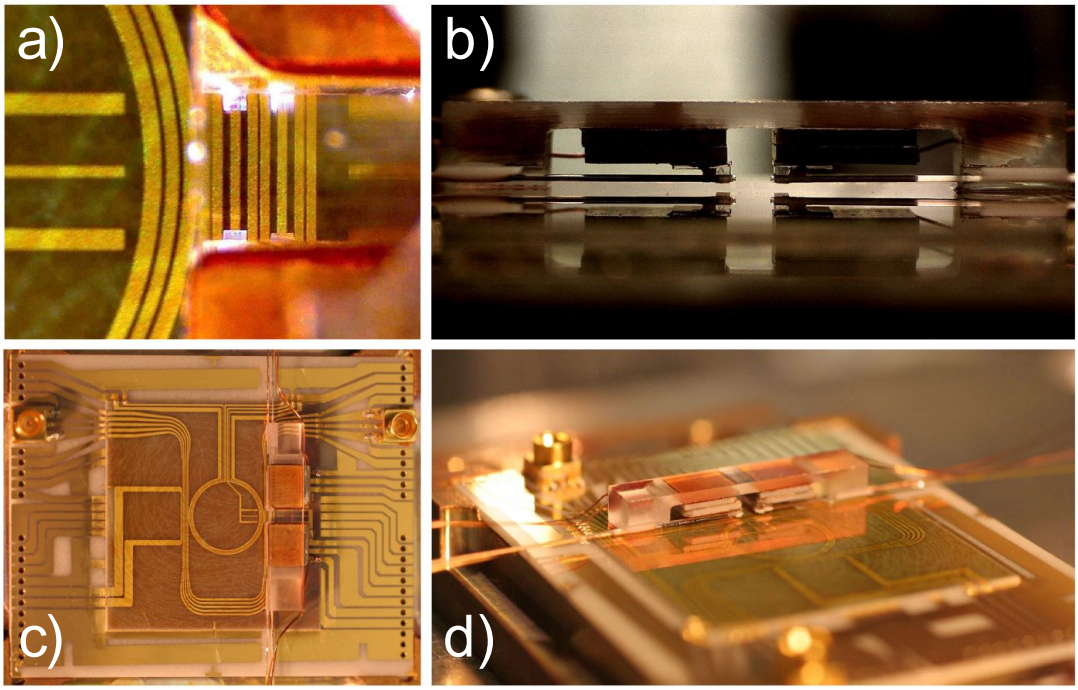

Figure 5.19: **New atom chip and cavities assembly.** Cavity mount glued to chip. a) shows the two resonators above the science chip wires. The view is slightly blurred by the quartz bridge. b) side view on the bridge where the reflection in the mirror coating is visible. c) top view of whole ensemble d) perspective view of the ensemble. Taken from [92].

The idea is to study interesting quantum effects arising from the coupling between the atoms and the light inside the cavity, in a metrological environment. The global system is very similar to the previous one, with the addition of a 2D-MOT and the fiber-cavities. The 2D-MOT with differential pumping should increase the MOT loading rate while keeping a good vacuum in the main chamber. As shown on figure 5.19, the two cavities, resonant for 780 nm and 1560 nm light, are glued on the same piezoelectric elements such that they consist in one macroscopic object. The idea is to use one of them for locking the ensemble on a 1560 nm stabilized laser, and place the atoms in the other one, called *Science cavity*. This way the locking light will not be coupled to the atoms, preventing unwanted lightshifts. This however assumes that the differential fluctuations

of the length of the two resonators are smaller that their linewidth.
The science cavity will have several applications. The first one is to generate spin squeezing with a protocol similar to the one described in [57, 59]. In a nutshell, the atomic transitions are dressed by the light inside the cavity, and the cavity resonance is shifted by the population difference of the atomic ensemble. By fixing a probe laser at half the cavity linewidth, it is possible to induce correlations spin population and atomic phase, similarly to the one-axis-twisting Hamiltonian that we studied in this manuscript. Indeed, the induced lightshift is positive is $S_z > 0$ and negative if $S_z < 0$. In this sense, our good understanding of spin rotations and manipulations to perform the tomography of the atomic state will be directly applicable. This time, the squeezing is obtained with thermal ensembles, meaning that it can directly be applied to improve our clock performance below the standard quantum limit, as it has been done in [57]. On the other hand, by probing the light transmitted through the cavity, one can perform a quantum non-demolition (QND) measurement and improve the clock performances by reducing the dead times and the Dick effect [222]. Several weak measurement schemes are available and could be realized with this new set-up [59, 223, 224].

The old set-up has been dismantled about 6 months ago, to leave room for a new improved set-up with the new chip and the 2D-MOT. We kept the old optical table and added a new one for the 2d-MOT and cavities optics. After several baking stages, the optical cavities present the same characteristics as before, which is very reassuring. We however had quite some troubles with the vacuum that went down to $10-10$ mbar after bake-out but rose up to 10^{-9} mbar after a few weeks and keep rising very slowly. This is not yet perfectly understood and the current Ph.D student on the experiment, Mengzi Huang, will probably discuss it in more details in his manuscript. Now the whole system has been mounted and is operational. The first 3D-MOT was observed recently and optimization steps are currently on-going to reproduce the old experimental sequence. In parallel, we are first working on locking one cavity using a Pound-Drever-Hall [225] lock based on a FPGA based Red-Pitaya platform, whose efficiency has been proven very recently in the Syrte's Strontium clock [226]. We hope to quickly be able to load the atoms in the science cavity and start investigating its beneficial effects on the clock stability.

Bibliography

*****

[1] Theodore H Maiman. Stimulated optical radiation in ruby. *Nature*, 187(4736):493–494, 1960. (vi).

[2] William D Phillips. Nobel lecture: Laser cooling and trapping of neutral atoms. *Reviews of Modern Physics*, 70(3):721, 1998. (vi).

[3] Claude Cohen-Tannoudji and William D Phillips. New mechanisms for laser cooling. *Phys. Today*, 43(10):33–40, 1990. (vi).

[4] Steven Chu, Leo Hollberg, John E Bjorkholm, Alex Cable, and Arthur Ashkin. Three-dimensional viscous confinement and cooling of atoms by resonance radiation pressure. *Physical Review Letters*, 55(1):48, 1985. (vi, 41).

[5] John F Clauser. Ultra-high sensitivity accelerometers and gyroscopes using neutral atom matter-wave interferometry. *Physica B+ C*, 151(1-2):262–272, 1988. (vi).

[6] Matthieu Dupont-Nivet. *Vers un accéléromètre atomique sur puce*. PhD thesis, Université Paris-Saclay, 2016. (vi, viii).

[7] Alexander Kuna, Jan Cermak, Ludvík Sojdr, Patrice Salzenstein, and Frederic Lefebvre. Lowest flicker-frequency floor measured on bva oscillators. *IEEE transactions on ultrasonics, ferroelectrics, and frequency control*, 57(3), 2010. (vii).

[8] Marco Schioppo, Roger C Brown, William F McGrew, N Hinkley, Robert J Fasano, K Beloy, TH Yoon, Gianmaria Milani, D Nicolodi, JA Sherman, et al. Ultrastable optical clock with two cold-atom ensembles. *Nature Photonics*, 11(1):48–52, 2017. (vii).

[9] TL Nicholson, SL Campbell, RB Hutson, GE Marti, BJ Bloom, RL McNally, Wei Zhang, MD Barrett, MS Safronova, GF Strouse, et al. Systematic evaluation of an atomic clock at 2 [times] 10-18 total uncertainty. *Nature Communications*, 6, 2015. (vii).

[10] Andrew D Ludlow, Martin M Boyd, Jun Ye, Ekkehard Peik, and Piet O Schmidt. Optical atomic clocks. *Reviews of Modern Physics*, 87(2):637, 2015. (vii, 14).

[11] Chin-Wen Chou, DB Hume, Till Rosenband, and DJ Wineland. Optical clocks and relativity. *Science*, 329(5999):1630–1633, 2010. (vii, 14).

[12] A Hees, J Guéna, M Abgrall, S Bize, and P Wolf. Searching for an oscillating massive scalar field as a dark matter candidate using atomic hyperfine frequency comparisons. *Physical Review Letters*, 117(6):061301, 2016. (vii, 14).

[13] Caspar F Ockeloen, Roman Schmied, Max F Riedel, and Philipp Treutlein. Quantum metrology with a scanning probe atom interferometer. *Physical Review Letters*, 111(14):143001, 2013. (vii, ix, 30, 105, 134).

[14] Adrien Facon, Eva-Katharina Dietsche, Dorian Grosso, Serge Haroche, Jean-Michel Raimond, Michel Brune, and Sébastien Gleyzes. A sensitive electrometer based on a Rydberg atom in a Schrodinger-cat state. *Nature*, 535(7611):262–269, 2016. (vii, viii).

[15] I Baumgart, J-M Cai, A Retzker, MB Plenio, and Ch Wunderlich. Ultrasensitive magnetometer using a single atom. *Physical Review Letters*, 116(24):240801, 2016. (vii).

[16] Pascal Böhi, Max F Riedel, Theodor W Hänsch, and Philipp Treutlein. Imaging of microwave fields using ultracold atoms. *Applied Physics letters*, 97(5):051101, 2010. (vii, 9).

[17] Christian Hirt, Sten Claessens, Thomas Fecher, Michael Kuhn, Roland Pail, and Moritz Rexer. New ultrahigh-resolution picture of earth's gravity field. *Geophysical research letters*, 40(16):4279–4283, 2013. (vii).

[18] Ch J Bordé. Atomic interferometry with internal state labelling. *Physics letters A*, 140(1-2):10–12, 1989. (vii).

[19] Paul R Berman and Vasili Kharchenko. Atom interferometry, 1997. (vii, vii, 20).

[20] Mark Kasevich and Steven Chu. Atomic interferometry using stimulated raman transitions. *Physical Review Letters*, 67(2):181, 1991. (vii).

[21] M De Angelis, Andrea Bertoldi, L Cacciapuoti, A Giorgini, G Lamporesi, M Prevedelli, G Saccorotti, F Sorrentino, and GM Tino. Precision gravimetry with atomic sensors. *Measurement Science and Technology*, 20(2):022001, 2008. (vii).

[22] Holger Müller, Sheng-wey Chiow, Sven Herrmann, Steven Chu, and Keng-Yeow Chung. Atom-interferometry tests of the isotropy of post-newtonian gravity. *Physical Review Letters*, 100(3):031101, 2008. (vii).

[23] Susannah M Dickerson, Jason M Hogan, Alex Sugarbaker, David MS Johnson, and Mark A Kasevich. Multiaxis inertial sensing with long-time point source atom interferometry. *Physical Review Letters*, 111(8):083001, 2013. (vii).

[24] Pierre Gillot, Olivier Francis, Arnaud Landragin, F Pereira Dos Santos, and Sébastien Merlet. Stability comparison of two absolute gravimeters: optical versus atomic interferometers. *Metrologia*, 51(5):L15, 2014. (vii).

[25] Achim Peters, Keng Yeow Chung, and Steven Chu. Measurement of gravitational acceleration by dropping atoms. *Nature*, 400(6747):849, 1999. (vii).

[26] Quentin Bodart, Sébastien Merlet, Nicola Malossi, F Pereira Dos Santos, Philippe Bouyer, and Arnaud Landragin. A cold atom pyramidal gravimeter with a single laser beam. *Applied Physics Letters*, 96(13):134101, 2010. (vii).

[27] Jürgen Neumeyer. Superconducting gravimetry. In *Sciences of Geodesy-I*, pages 339–413. Springer, 2010. (vii).

[28] Evert Jan Post. Sagnac effect. *Reviews of Modern Physics*, 39(2):475, 1967. (vii).

[29] F Riehle, Th Kisters, A Witte, J Helmcke, and Ch J Bordé. Optical ramsey spectroscopy in a rotating frame: Sagnac effect in a matter-wave interferometer. *Physical Review Letters*, 67(2):177, 1991. (vii).

[30] DS Durfee, YK Shaham, and MA Kasevich. Long-term stability of an area-reversible atom-interferometer sagnac gyroscope. *Physical Review Letters*, 97(24):240801, 2006. (vii).

[31] JK Stockton, K Takase, and MA Kasevich. Absolute geodetic rotation measurement using atom interferometry. *Physical Review Letters*, 107(13):133001, 2011. (vii).

[32] P Berg, S Abend, G Tackmann, C Schubert, E Giese, WP Schleich, FA Narducci, W Ertmer, and EM Rasel. Composite-light-pulse technique for high-precision atom interferometry. *Physical Review Letters*, 114(6):063002, 2015. (vii).

[33] I Dutta, D Savoie, B Fang, B Venon, CL Garrido Alzar, R Geiger, and A Landragin. Continuous cold-atom inertial sensor with 1 nrad/sec rotation stability. *Physical Review Letters*, 116(18):183003, 2016. (vii, viii).

[34] TL Gustavson, A Landragin, and MA Kasevich. Rotation sensing with a dual atom-interferometer sagnac gyroscope. *Classical and Quantum Gravity*, 17(12):2385, 2000. (vii).

[35] Hervé C Lefèvre. The fiber-optic gyroscope, a century after sagnac's experiment: The ultimate rotation-sensing technology? *Comptes Rendus Physique*, 15(10):851–858, 2014. (vii).

[36] CW Francis Everitt, DB DeBra, BW Parkinson, JP Turneaure, JW Conklin, MI Heifetz, GM Keiser, AS Silbergleit, T Holmes, J Kolodziejczak, et al. Gravity probe b: final results of a space experiment to test general relativity. *Physical Review Letters*, 106(22):221101, 2011. (vii).

[37] MR Andrews, CG Townsend, H-J Miesner, DS Durfee, DM Kurn, and W Ketterle. Observation of interference between two Bose condensates. *Science*, 275(5300):637–641, 1997. (vii, 20).

[38] Alexander D Cronin, Jörg Schmiedmayer, and David E Pritchard. Optics and interferometry with atoms and molecules. *Reviews of Modern Physics*, 81(3):1051, 2009. (vii, 20).

[39] DS Hall, MR Matthews, CE Wieman, and Eric A Cornell. Measurements of relative phase in two-component Bose–Einstein condensates. *Physical Review Letters*, 81(8):1543, 1998. (vii).

[40] M. H. Anderson, J. R. Ensher, M. R. Matthews, C. E. Wieman, and E. A. Cornell. Observation of Bose–Einstein condensation in a dilute atomic vapor. *Science*, 269:5221, 1995. (vii, 20).

[41] K. B. Davis, M. O. Mewes, M. R. Andrews, N. J. van Druten, D. S. Durfee, D. M. Kurn, and W. Ketterle. Bose–Einstein condensation in a gas of sodium atoms. *Phy. Rev. Lett.*, 75:3969, 1995. (vii, 20).

[42] James R Anglin and Wolfgang Ketterle. Bose–Einstein condensation of atomic gases. *Nature*, 416(6877):211–218, 2002. (vii, 20).

[43] József Fortágh and Claus Zimmermann. Magnetic microtraps for ultracold atoms. *Reviews of Modern Physics*, 79(1):235, 2007. (vii, 2, 2).

[44] Jakob Reichel and Vladan Vuletic. *Atom chips*. John Wiley & Sons, 2011. (vii, 2, 2).

[45] Tarik Berrada, Sandrine van Frank, Robert Bücker, Thorsten Schumm, J-F Schaff, and Jörg Schmiedmayer. Integrated mach–zehnder interferometer for bose–einstein condensates. *Nature Communications*, 4, 2013. (vii).

[46] Ying-Ju Wang, Dana Z Anderson, Victor M Bright, Eric A Cornell, Quentin Diot, Tetsuo Kishimoto, Mara Prentiss, RA Saravanan, Stephen R Segal, and Saijun Wu. Atom michelson interferometer on a chip using a Bose–Einstein condensate. *Physical Review Letters*, 94(9):090405, 2005. (vii).

[47] Y Shin, M Saba, TA Pasquini, W Ketterle, DE Pritchard, and AE Leanhardt. Atom interferometry with Bose–Einstein condensates in a double-well potential. *Physical Review Letters*, 92(5):050405, 2004. (vii).

[48] H Müntinga, H Ahlers, M Krutzik, A Wenzlawski, S Arnold, D Becker, K Bongs, H Dittus, H Duncker, N Gaaloul, et al. Interferometry with Bose–Einstein condensates in microgravity. *Physical Review Letters*, 110(9):093602, 2013. (vii).

[49] T Schumm, S Hofferberth, L Mauritz Andersson, S Wildermuth, S Groth, I Bar-Joseph, J Schmiedmayer, and P Krüger. Matter-wave interferometry in a double well on an atom chip. *Nature Physics*, 1(1):57–62, 2005. (vii, 20).

[50] Vladimir B Braginskii and Yurii I Vorontsov. Quantum-mechanical limitations in macroscopic experiments and modern experimental technique. *Soviet Physics Uspekhi*, 17(5):644, 1975. (viii).

[51] Giorgio Santarelli, Ph Laurent, Pierre Lemonde, André Clairon, Anthony G Mann, S Chang, Andre N Luiten, and Christophe Salomon. Quantum projection noise in an atomic fountain: A high stability cesium frequency standard. *Physical Review Letters*, 82(23):4619, 1999. (viii, 30).

[52] Vittorio Giovannetti, Seth Lloyd, and Lorenzo Maccone. Quantum-enhanced measurements: beating the standard quantum limit. *Science*, 306(5700):1330–1336, 2004. (viii, 30).

[53] Vittorio Giovannetti, Seth Lloyd, and Lorenzo Maccone. Advances in quantum metrology. *Nature Photonics*, 5(4):222–229, 2011. (viii).

[54] Julian Grond, Ulrich Hohenester, Igor Mazets, and Jörg Schmiedmayer. Atom interferometry with trapped Bose–Einstein condensates: impact of atom–atom interactions. *New Journal of Physics*, 12(6):065036, 2010. (viii).

[55] Julian Grond, Ulrich Hohenester, Jörg Schmiedmayer, and Augusto Smerzi. Mach-zehnder interferometry with interacting trapped Bose–Einstein condensates. *Physical Review A*, 84(2):023619, 2011. (viii, 20).

[56] MJ Holland and K Burnett. Interferometric detection of optical phase shifts at the heisenberg limit. *Physical Review Letters*, 71(9):1355, 1993. (viii).

[57] Ian D Leroux, Monika H Schleier-Smith, and Vladan Vuletić. Orientation-dependent entanglement lifetime in a squeezed atomic clock. *Physical Review Letters*, 104(25):250801, 2010. (viii, 30, 138, 138).

[58] Anne Louchet-Chauvet, Jürgen Appel, Jelmer J Renema, Daniel Oblak, Niels Kjaergaard, and Eugene S Polzik. Entanglement-assisted atomic clock beyond the projection noise limit. *New Journal of Physics*, 12(6):065032, 2010. (viii).

[59] Onur Hosten, Nils J Engelsen, Rajiv Krishnakumar, and Mark A Kasevich. Measurement noise 100 times lower than the quantum-projection limit using entangled atoms. *Nature*, 529(7587):505, 2016. (viii, 138, 138).

[60] C. Gross, T. Zibold, E. Nicklas, J. Esteve, and M. K. Oberthaler. Nonlinear atom interferometer surpasses classical precision limit. *Nature*, 464:1165–1169, 2010. (viii, viii, ix, 20, 30, 33, 69, 136).

[61] M. F. Riedel, P. Bohi, Y. Li, T. W. Hansch, A. Sinatra, and P. Treutlein. Atom-chip-based generation of entanglement for quantum metrology. *Nature*, 464:1170–1173, 2010. (viii, viii, ix, 20, 30, 33, 35, 69, 79, 105, 105, 136).

[62] G-B Jo, Yongil Shin, S Will, TA Pasquini, Michele Saba, Wolfgang Ketterle, David E Pritchard, Mukund Vengalattore, and M Prentiss. Long phase coherence time and number squeezing of two Bose–Einstein condensates on an atom chip. *Physical Review Letters*, 98(3):030407, 2007. (viii, 20).

[63] C Gross, H Strobel, E Nicklas, T Zibold, N Bar-Gill, G Kurizki, and MK Oberthaler. Atomic homodyne detection of continuous variable entangled twin-atom states. *Nature*, 480:219–223, 2011. (viii).

[64] Chad Orzel, AK Tuchman, ML Fenselau, M Yasuda, and MA Kasevich. Squeezed states in a Bose-einstein condensate. *Science*, 291(5512):2386–2389, 2001. (viii).

[65] Jerome Esteve, J-B Trebbia, Thorsten Schumm, Alain Aspect, Christoph I Westbrook, and Isabelle Bouchoule. Observations of density fluctuations in an elongated Bose gas: Ideal gas and quasicondensate regimes. *Physical Review Letters*, 96(13):130403, 2006. (viii).

[66] Christian Gross. Spin squeezing, entanglement and quantum metrology with Bose–einstein condensates. *Journal of Physics B: Atomic, Molecular and Optical Physics*, 45(10):103001, 2012. (viii).

[67] Jonathan P Dowling and Gerard J Milburn. Quantum technology: the second quantum revolution. *Philosophical Transactions of the Royal Society of London A: Mathematical, Physical and Engineering Sciences*, 361(1809):1655–1674, 2003. (viii).

[68] European Commission. The european cloud initiative. https://ec.europa.eu/digital-single-market/en/news/european-commission-will-launch-eu1-billion-quantum-technologies-flagship, 2016. (viii).

[69] Ramon Szmuk, Vincent Dugrain, Wilfried Maineult, Jakob Reichel, and Peter Rosenbusch. Stability of a trapped-atom clock on a chip. *Physical Review A*, 92(1):012106, 2015. (viii, 7, 14, 19, 19, 122, 122, 123, 129).

[70] Claire Lhuillier and Franck Laloë. Transport properties in a spin polarized gas, i. *Journal de Physique*, 43(2):197–224, 1982. (ix).

[71] Jean-Noël Fuchs, DM Gangardt, and Franck Laloë. Internal state conversion in ultracold gases. *Physical Review Letters*, 88(23):230404, 2002. (ix).

[72] Christian Deutsch, Fernando Ramirez-Martinez, Clement Lacroûte, Friedemann Reinhard, Tobias Schneider, Jean-Noël Fuchs, Frédéric Piéchon, Franck Laloë, Jakob Reichel, and Peter Rosenbusch. Spin self-rephasing and very long coherence times in a trapped atomic ensemble. *Physical Review Letters*, 105(2):020401, 2010. (ix, 19).

[73] G Kleine Büning, J Will, W Ertmer, E Rasel, Jan Arlt, C Klempt, F Ramirez-Martinez, F Piéchon, and P Rosenbusch. Extended coherence time on the clock transition of optically trapped rubidium. *Physical Review Letters*, 106(24):240801, 2011. (ix).

[74] Wilfried Maineult, Christian Deutsch, Kurt Gibble, Jakob Reichel, and Peter Rosenbusch. Spin waves and collisional frequency shifts of a trapped-atom clock. *Physical Review Letters*, 109(2):020407, 2012. (ix, 66, 124, 124, 126).

[75] Kurt Gibble. Decoherence and collisional frequency shifts of trapped bosons and fermions. *Physical Review Letters*, 103(11):113202, 2009. (ix).

[76] M. Kitagawa M. Ueda. Squeezed spin states. *Phys. Rev. A*, 47:5138–5143, 1993. (ix, 30, 32, 32, 33, 104).

[77] Jian Ma, Xiaoguang Wang, CP Sun, and Franco Nori. Quantum spin squeezing. *Physics Reports*, 509(2):89–165, 2011. (ix, 30, 33).

[78] A Sørensen, L-M Duan, JI Cirac, and Peter Zoller. Many-particle entanglement with Bose–Einstein condensates. *Nature*, 409(6816):63–66, 2001. (ix, 20, 20, 30, 30, 33, 33, 104).

[79] Wolfgang Müssel, H Strobel, D Linnemann, DB Hume, and MK Oberthaler. Scalable spin squeezing for quantum-enhanced magnetometry with Bose–Einstein condensates. *Physical Review Letters*, 113(10):103004, 2014. (ix, 30).

[80] D. S. Hall, M. R. Matthews, J. R. Ensher, C. E. Wieman, and E. A. Cornell. Dynamics of component separation in a binary mixture of Bose–Einstein condensates. *Phys. Rev. Lett.*, 81:1539, 1998. (ix, 20, 74).

[81] K. M. Mertes, J. W. Merrill, R. Carretero-Gonzalez, D. J. Frantzeskakis, P. G. Kevrekidis, and D. S. Hall. Nonequilibrium dynamics and superfluid ring excitations in binary Bose–Einstein condensates. *Phys. Rev. Lett.*, 99:190402, 2007. (ix, 74, 105).

[82] R. P. Anderson, C. Ticknor, A. I. Sidorov, and B. V. Hall. Spatially inhomogeneous phase evolution of a two-component Bose–Einstein condensate. *Phys. Rev. A*, 80:023603, 2009. (ix, 64, 74).

[83] Mikhail Egorov. *Coherence and collective oscillations of a two-component Bose–Einstein condensate*. PhD thesis, Swinbourne University of Technology, 2012. (ix, 30, 69, 74, 97, 134).

[84] S. A. Haine, J. Lau, R. P. Anderson, and M. T. Johnsson. Self-induced spatial dynamics to enhance spin squeezing via one-axis-twisting in a two-component Bose–Einstein condensate. *Phys. Rev. A*, 90:023613, 2014. (ix, 33, 35, 35, 88, 104, 105, 136).

[85] David E Pritchard. Cooling neutral atoms in a magnetic trap for precision spectroscopy. *Physical Review Letters*, 51(15):1336, 1983. (2, 4).

[86] Alan L Migdall, John V Prodan, William D Phillips, Thomas H Bergeman, and Harold J Metcalf. First observation of magnetically trapped neutral atoms. *Physical Review Letters*, 54(24):2596, 1985. (2, 4, 4).

[87] Philipp Treutlein. *Coherent manipulation of ultracold atoms on atom chips*. PhD thesis, Universität München, 2008. (2, 6).

[88] Mark Keil, Omer Amit, Shuyu Zhou, David Groswasser, Yonathan Japha, and Ron Folman. Fifteen years of cold matter on the atom chip: promise, realizations, and prospects. *Journal of Modern Optics*, 63(18):1840–1885, 2016. (2).

[89] Jakob Reichel, W Hänsel, P Hommelhoff, and TW Hänsch. Applications of integrated magnetic microtraps. *Applied Physics B: Lasers and Optics*, 72(1):81–89, 2001. (2, 5).

[90] Ron Folman, Peter Kruger, Jörg Schmiedmayer, Johannes Denschlag, and Carsten Henkel. Microscopic atom optics: from wires to an atom chip. *arXiv preprint arXiv:0805.2613*, 2008. (2).

[91] Shengwang Du, Matthew B Squires, Yutaka Imai, Leslie Czaia, RA Saravanan, Victor Bright, Jakob Reichel, TW Hänsch, and Dana Z Anderson. Atom-chip Bose–Einstein condensation in a portable vacuum cell. *Physical Review A*, 70(5):053606, 2004. (2).

[92] Konstantin Ott. *Towards a squeezing-enhanced atomic clock on a chip*. PhD thesis, Université Pierre et Marie Curie-Paris VI, 2016. (2, 6, 19, 97, 137, 137).

[93] Carlos L Garrido Alzar, Wenhua Yan, and Arnaud Landragin. Towards high sensitivity rotation sensing using an atom chip. In *Quantum Information and Measurement*, pages JT2A–10. Optical Society of America, 2012. (2).

[94] Thomas Fernholz, Robin Stevenson, Michael R Hush, Igor V Lesanovsky, Thomas Bishop, Fabio Gentile, Sindhu Jammi, Tadas Pyragius, Mark G Bason, Hèctor Mas, et al. Towards rotation sensing with a single atomic clock. In *SPIE Photonics Europe*, pages 990007–990007. International Society for Optics and Photonics, 2016. (2).

[95] Landry Huet. *Gravimétrie atomique sur puce et applications embarquées*. PhD thesis, Université Paris-Est, 2013. (2).

[96] S Abend, M Gebbe, M Gersemann, H Ahlers, H Müntinga, E Giese, N Gaaloul, C Schubert, C Lämmerzahl, W Ertmer, et al. Atom-chip fountain gravimeter. *Physical Review Letters*, 117(20):203003, 2016. (2).

[97] William H Wing. On neutral particle trapping in quasistatic electromagnetic fields. *Progress in Quantum Electronics*, 8(3-4):181–199, 1984. (3).

[98] Ettore Majorana. Atomi orientati in campo magnetico variabile. *Il Nuovo Cimento (1924-1942)*, 9(2):43–50, 1932. (3).

[99] DM Brink and CV Sukumar. Majorana spin-flip transitions in a magnetic trap. *Physical Review A*, 74(3):035401, 2006. (3).

[100] W Ketterle, DS Durfee, DM Stamper-Kurn, et al. Making, probing and understanding Bose–Einstein condensates. *arXiv preprint cond-mat/9904034*, 5, 1999. (3, 51).

[101] Jean Dalibard. Atomes ultra–froids, 2008. (4).

[102] Wolfgang Hänsel. *Magnetische mikrofallen fuer rubidiumatome*. PhD thesis, lmu, 2000. (4).

[103] Friedemann Reinhard. *Design and Construction of an Atomic Clock on an Atom Chip*. PhD thesis, UPMC, 2009. (4, 6, 7, 9, 37, 37, 38, 38, 39, 92).

[104] Wolfgang Petrich, Michael H Anderson, Jason R Ensher, and Eric A Cornell. Stable, tightly confining magnetic trap for evaporative cooling of neutral atoms. *Physical Review Letters*, 74(17):3352, 1995. (4, 43).

[105] Yu V Gott, MS Ioffe, and VG Telkovskii. Some new results on confinement in magnetic traps. Technical report, Academy of Sciences, Moscow, 1962. (4).

[106] John David Jackson and Ronald F Fox. Classical electrodynamics. *American Journal of Physics*, 67(9):841–842, 1999. (4).

[107] Ken Binmore and Joan Davies. *Calculus: concepts and methods*. Cambridge University Press, 2002. (5).

[108] David E. Brown. *The Hessian matrix: Eigenvalues, concavity, and curvature*. Lecture notes at BYU–Idaho Dept. of Mathematics, 2014. (5).

[109] Gregory Breit and II Rabi. Measurement of nuclear spin. *Physical Review*, 38(11):2082, 1931. (6).

[110] Daniel A Steck. Rubidium 87 d line data, 2001. (6, 7, 8, 52, 55).

[111] HJ Lewandowski, DM Harber, DL Whitaker, and Eric A Cornell. Observation of anomalous spin-state segregation in a trapped ultracold vapor. *Physical Review Letters*, 88(7):070403, 2002. (7, 7, 94).

[112] D. M. Harber et al. Effect of cold atoms on spin coherence and resonance shifts in a magnetically trapped ultracold gas. *Phys. Rev. A*, 66:053616, 2002. (7, 7, 34, 91, 94, 94).

[113] Vincent Dugrain. *Metrology with trappes atoms on a chip using non-degenerate and degenerate quantum gases*. PhD thesis, Universite Pierre et Marie Curie, 2010. (7, 9, 37, 42, 46, 48, 64, 65, 74, 79, 92, 124).

[114] P Rosenbusch. Magnetically trapped atoms for compact atomic clocks. *Applied Physics B: Lasers and Optics*, 95(2):227–235, 2009. (7, 7, 134).

[115] Gilbert Grynberg, Alain Aspect, and Claude Fabre. *Introduction to quantum optics: from the semi-classical approach to quantized light*. Cambridge university press, 2010. (8, 8).

[116] François Bardou. *Lévy statistics and laser cooling: how rare events bring atoms to rest*. Cambridge University Press, 2002. (8).

[117] A Clairon, C Salomon, S Guellati, and WD Phillips. Ramsey resonance in a zacharias fountain. *EPL (Europhysics Letters)*, 16(2):165, 1991. (8).

[118] Serge Haroche and Jean-Michel Raimond. *Exploring the quantum: atoms, cavities, and photons*. Oxford university press, 2006. (8).

[119] John F Clauser, Michael A Horne, Abner Shimony, and Richard A Holt. Proposed experiment to test local hidden-variable theories. *Physical Review Letters*, 23(15):880, 1969. (8).

[120] Thomas R Gentile, Barbara J Hughey, Daniel Kleppner, and Theodore W Ducas. Experimental study of one-and two-photon rabi oscillations. *Physical Review A*, 40(9):5103, 1989. (8).

[121] Karl Blum. *Density matrix theory and applications*, volume 64. Springer Science & Business Media, 2012. (9).

[122] Heinz-Peter Breuer and Francesco Petruccione. *The theory of open quantum systems*. Oxford University Press on Demand, 2002. (9).

[123] C. J. Pethick and H. Smith. *Bose–Einstein Condensation in Dilute Gases*. Cambridge University Press, cambridge university press edition, 2008. (10, 11, 20, 29).

[124] M Egorov, B Opanchuk, P Drummond, BV Hall, P Hannaford, and AI Sidorov. Measurement of s-wave scattering lengths in a two-component Bose–Einstein condensate. *Physical Review A*, 87(5):053614, 2013. (11, 11, 34, 46, 77, 105).

[125] EA Burt, RW Ghrist, CJ Myatt, MJ Holland, EA Cornell, and CE Wieman. Coherence, correlations, and collisions: What one learns about Bose–Einstein condensates from their decay. *Physical Review Letters*, 79(3):337, 1997. (11, 12, 46, 105).

[126] Howard Carmichael. *An open systems approach to quantum optics: lectures presented at the Université Libre de Bruxelles, October 28 to November 4, 1991*, volume 18. Springer Science & Business Media, 2009. (11).

[127] Bogdan Opanchuk and Peter D Drummond. Functional wigner representation of quantum dynamics of Bose–Einstein condensate. *Journal of Mathematical Physics*, 54(4):042107, 2013. (11).

[128] Valentin Ivannikov. Ensemble master equation for a trapped-atom clock with one- and two-body losses. *Physical Review A*, 89(2):023615, 2014. (11).

[129] W. Ketterle and H. J. Miesner. Coherence properties of Bose–Einstein condensates and atom lasers. *Phys. Rev. A*, 56:3291, 1997. (12, 34, 94).

[130] Felix Bloch. Nuclear induction. *Physical Review*, 70(7-8):460, 1946. (12).

[131] Richard P Feynman, Frank L Vernon Jr, and Robert W Hellwarth. Geometrical representation of the schrödinger equation for solving maser problems. *Journal of Applied Physics*, 28(1):49–52, 1957. (12).

[132] William Markowitz, R Glenn Hall, L Essen, and JVL Parry. Frequency of cesium in terms of ephemeris time. *Physical Review Letters*, 1(3):105, 1958. (13).

[133] R Wynands and S Weyers. Atomic fountain clocks. *Metrologia*, 42(3):S64, 2005. (14).

[134] Jocelyne Guéna, Michel Abgrall, Daniele Rovera, Philippe Laurent, Baptiste Chupin, Michel Lours, Giorgio Santarelli, Peter Rosenbusch, Michael E Tobar, Ruoxin Li, et al. Progress in atomic fountains at lne-syrte. *IEEE transactions on ultrasonics, ferroelectrics, and frequency control*, 59(3):391–409, 2012. (14).

[135] N Huntemann, C Sanner, B Lipphardt, Chr Tamm, and E Peik. Single-ion atomic clock with 3× 10- 18 systematic uncertainty. *Physical Review Letters*, 116(6):063001, 2016. (14, 18).

[136] Moustafa Abdel Hafiz, Xiaochi Liu, Stéphane Guérandel, Emeric De Clercq, and Rodolphe Boudot. A cpt-based cs vapor cell atomic clock with a short-term fractional frequency stability of 3 x 10-13 τ-1/2. In *Journal of Physics: Conference Series*, volume 723, page 012013. IOP Publishing, 2016. (14).

[137] Marc Fischer, Nikolai Kolachevsky, Marcus Zimmermann, Ronald Holzwarth, Th Udem, Theodor W Hänsch, M Abgrall, J Grünert, I Maksimovic, S Bize, et al. New limits on the drift of fundamental constants from laboratory measurements. *Physical Review Letters*, 92(23):230802, 2004. (14, 15).

[138] Pierre Waller, Francisco Gonzalez, Stefano Binda, Ilaria Sesia, Irene Hidalgo, Guillermo Tobias, and Patrizia Tavella. The in-orbit performances of giove clocks. *IEEE Transactions on ultrasonics, ferroelectrics, and frequency control*, 57(3), 2010. (14).

[139] John D Prestage and Gregory L Weaver. Atomic clocks and oscillators for deep-space navigation and radio science. *Proceedings of the IEEE*, 95(11):2235–2247, 2007. (14).

[140] Laurent-Guy Bernier, Pascal Rochat, et al. Active hydrogen maser atomic frequency standard, November 17 1998. US Patent 5,838,206. (14).

[141] Till Rosenband, DB Hume, PO Schmidt, Chin-Wen Chou, Anders Brusch, Luca Lorini, WH Oskay, Robert E Drullinger, Tara M Fortier, JE Stalnaker, et al. Frequency ratio of al+ and hg+ single-ion optical clocks; metrology at the 17th decimal place. *Science*, 319(5871):1808–1812, 2008. (15).

[142] Isidor Isaac Rabi. Space quantization in a gyrating magnetic field. *Physical Review*, 51(8):652, 1937. (15).

[143] Norman F Ramsey. A new molecular beam resonance method. *Physical Review*, 76(7):996, 1949. (15).

[144] Norman F Ramsey. Experiments with separated oscillatory fields and hydrogen masers. *Reviews of Modern Physics*, 62(3):541, 1990. (15).

[145] WM Itano, JC Bergquist, JJ Bollinger, JM Gilligan, DJ Heinzen, FL Moore, MG Raizen, and DJ Wineland. Quantum projection noise: Population fluctuations in two-level systems. *Physical Review A*, 47(5):3554, 1993. (18, 30, 30).

[146] George John Dick. Local oscillator induced instabilities in trapped ion frequency standards. Technical report, DTIC Document, 1987. (19, 129).

[147] V Guarrera, R Szmuk, J Reichel, and P Rosenbusch. Microwave-dressed state-selective potentials for atom interferometry. *New Journal of Physics*, 17(8):083022, 2015. (19).

[148] Albert Einstein. *Quantentheorie des einatomigen idealen Gases*. Akademie der Wissenshaften, in Kommission bei W. de Gruyter, 1924. (20).

[149] F. Dafolvo, S. Giorgini, L. P. Pitaevskii, and S. Stringari. Theory of Bose–Einstein condensation in trapped gases. *Rev. Mod. Phys.*, 71:463, 1999. (20, 21, 22, 24, 24, 43, 45, 45).

[150] L. P. Pitaevskii and S. Stringari. *Bose–Einstein condensation*. Oxford University Press, 2003. (20, 21, 24, 29).

[151] CK Hong, Zhe-Yu Ou, and Leonard Mandel. Measurement of subpicosecond time intervals between two photons by interference. *Physical Review Letters*, 59(18):2044, 1987. (20).

[152] Raphael Lopes, Almazbek Imanaliev, Alain Aspect, Marc Cheneau, Denis Boiron, and Christoph I Westbrook. Atomic hong-ou-mandel experiment. *Nature*, 520(7545):66–68, 2015. (20).

[153] Michael Robin Matthews, Brian P Anderson, PC Haljan, DS Hall, CE Wieman, and Eric A Cornell. Vortices in a Bose–Einstein condensate. *Physical Review Letters*, 83(13):2498, 1999. (20).

[154] KW Madison, F Chevy, W Wohlleben, and Jl Dalibard. Vortex formation in a stirred Bose–Einstein condensate. *Physical Review Letters*, 84(5):806, 2000. (20).

[155] Mikhail Egorov, Russell P Anderson, Valentin Ivannikov, Bogdan Opanchuk, Peter Drummond, Brenton V Hall, and Andrei I Sidorov. Long-lived periodic revivals of coherence in an interacting Bose–Einstein condensate. *Physical Review A*, 84(2):021605, 2011. (20, 74).

[156] J. T. M. Walraven. *Quantum Gases - Statistics and Interactions*. lecture course in University of Amsterdam, 2014. (22).

[157] N.N. Bogoliubov. On the theory of superfluidity. *J. Phys. (USSR)*, 11:23, 1947. (23).

[158] N.N. Bogoliubov and D.V. Shirkov. *Introduction to the theory of quantized fields*. John Wiley and Sons, 3rd edition, 1980. (23).

[159] E. P. Gross. Unified theory of interacting bosons. *Phys. Rev.*, 106:161, 1957. (23).

[160] V. L. Ginzburg and L. P. Pitaevskii. On the theory of superfluidity. *J. Exptl. Theoret. Phys.*, 34:1240–1245, 1958. (23).

[161] Chiara Menotti and Sandro Stringari. Collective oscillations of a one-dimensional trapped Bose–Einstein gas. *Physical Review A*, 66(4):043610, 2002. (24, 26).

[162] G. Baym and C. J. Pethick. Ground-state properties of magnetically trapped -condensed rubidium gas. *J. Exptl. Theoret. Phys.*, 76:6, 1996. (24, 27).

[163] A Munoz Mateo and V Delgado. Effective mean-field equations for cigar-shaped and disk-shaped Bose–Einstein condensates. *Physical Review A*, 77(1):013617, 2008. (24, 25).

[164] D. S. Petrov, G. V. Shlyapnikov, and J. T. M. Walraven. Regimes of quantum degeneracy in trapped 1d gases. *Phys. Rev. Lett.*, 85:3745–3749, Oct 2000. (24).

[165] Kunal K. Das. Highly anisotropic Bose–Einstein condensates: Crossover to lower dimensionality. *Phys. Rev. A*, 66:053612, Nov 2002. (24).

[166] L Salasnich, A Parola, and L Reatto. Effective wave equations for the dynamics of cigar-shaped and disk-shaped Bose condensates. *Physical Review A*, 65(4):043614, 2002. (26, 74).

[167] M. Olshanii. Atomic scattering in the presence of an external confinement and a gas of impenetrable bosons. *Phys. Rev. Lett.*, 81:938, 1998. (26).

[168] James Edgar Williams. *The preparation of topological modes in a strongly-coupled two-component Bose–Einstein Condensate*. PhD thesis, Citeseer, 1999. (29, 74).

[169] Robert William Pattinson. *Two-component Bose–Einstein condensates: equilibria and dynamics at zero temperature and beyond*. PhD thesis, Newcastle University, 2014. (29).

[170] Dan M Stamper-Kurn and Masahito Ueda. Spinor gases: Symmetries, magnetism, and quantum dynamics. *Reviews of Modern Physics*, 85(3):1191, 2013. (29).

[171] P Ao and ST Chui. Two stages in the evolution of binary alkali Bose–Einstein condensate mixtures towards phase segregation. *Journal of Physics B: Atomic, Molecular and Optical Physics*, 33(3):535, 2000. (30, 74).

[172] H Pu and NP Bigelow. Properties of two-species condensates. *Physical Review Letters*, 80(6):1130, 1998. (30).

[173] Alice Sinatra and Yvan Castin. Phase dynamics of Bose–Einstein condensates: Losses versus revivals. *The European Physical Journal D-Atomic, Molecular, Optical and Plasma Physics*, 4(3):247–260, 1998. (30, 74).

[174] Alice Sinatra and Yvan Castin. Binary mixtures of Bose–Einstein condensates: Phase dynamics and spatial dynamics. *The European Physical Journal D*, 8(3):319–332, 2000. (30, 35, 74, 78).

[175] Kean Loon Lee, Nils B Jørgensen, I-Kang Liu, Lars Wacker, Jan J Arlt, and Nick P Proukakis. Phase separation and dynamics of two-component Bose–Einstein condensates. *Physical Review A*, 94(1):013602, 2016. (30, 74).

[176] John J Bollinger, Wayne M Itano, David J Wineland, and DJ Heinzen. Optimal frequency measurements with maximally correlated states. *Physical Review A*, 54(6):R4649, 1996. (30).

[177] D Leibfried, Murray D Barrett, T Schaetz, J Britton, J Chiaverini, Wayne M Itano, John D Jost, Christopher Langer, and David J Wineland. Toward heisenberg-limited spectroscopy with multiparticle entangled states. *Science*, 304(5676):1476–1478, 2004. (30).

[178] Yun Li, Yvan Castin, and Alice Sinatra. Optimum spin squeezing in Bose–Einstein condensates with particle losses. *Physical Review Letters*, 100(21):210401, 2008. (30, 33, 104, 105, 120).

[179] FT Arecchi, Eric Courtens, Robert Gilmore, and Harry Thomas. Atomic coherent states in quantum optics. *Physical Review A*, 6(6):2211, 1972. (30).

[180] David J Wineland, John J Bollinger, Wayne M Itano, FL Moore, and DJ Heinzen. Spin squeezing and reduced quantum noise in spectroscopy. *Physical Review A*, 46(11):R6797, 1992. (32, 105, 118).

[181] Y. Li, P. Treutlein, J. Reichel, and A. Sinatra. Spin squeezing in a bimodal condensate: spatial dynamics and particle losses. *Eur. Phys. J. B*, 68:365–381, 2009. (32, 33, 35, 35, 120).

[182] Anders Søndberg Sørensen. Bogoliubov theory of entanglement in a Bose–Einstein condensate. *Physical Review A*, 65(4):043610, 2002. (33, 104).

[183] Alice Sinatra, Jean-Christophe Dornstetter, and Yvan Castin. Spin squeezing in Bose–Einstein condensates: Limits imposed by decoherence and non-zero temperature. *Frontiers of Physics*, 7(1):86–97, 2012. (33, 84, 104, 120).

[184] B Opanchuk, M Egorov, S Hoffmann, AI Sidorov, and PD Drummond. Quantum noise in three-dimensional BEC interferometry. *EPL (Europhysics Letters)*, 97(5):50003, 2012. (33).

[185] Mattias T Johnsson, Graham R Dennis, and Joseph J Hope. Squeezing in Bose–Einstein condensates with large numbers of atoms. *New Journal of Physics*, 15(12):123024, 2013. (33).

[186] PA Altin, Gordon McDonald, Daniel Doering, JE Debs, TH Barter, JD Close, NP Robins, SA Haine, TM Hanna, and RP Anderson. Optically trapped atom interferometry using the clock transition of large 87rb Bose–Einstein condensates. *New Journal of Physics*, 13(6):065020, 2011. (33).

[187] Yun Li. *États comprimés de spin dans un condensat de Bose–Einstein*. PhD thesis, Paris 6, 2010. (35, 104, 105).

[188] Clément Lacroûte. *Développement d'une horloge atomique sur puce à atomes: optimisation de la durée de cohérence et caractérisation préliminaire.* PhD thesis, Université Pierre et Marie Curie-Paris VI, 2010. (37, 37, 39, 41, 52).

[189] Christian Deutsch. *Identical spin rotation effects in an ultracold interacting trapped atomic clock*. PhD thesis, UPMC, 2011. (37, 39, 55, 55, 55, 58, 62, 64, 70, 93).

[190] Dana Z Anderson and Jakob GJ Reichel. Cold atom system with atom chip wall, October 24 2006. US Patent 7,126,112. (38).

[191] J Reichel, W Hänsel, and TW Hänsch. Atomic micromanipulation with magnetic surface traps. *Physical Review Letters*, 83(17):3398, 1999. (38).

[192] S Wildermuth, P Krüger, C Becker, M Brajdic, S Haupt, A Kasper, R Folman, and J Schmiedmayer. Optimized magneto-optical trap for experiments with ultracold atoms near surfaces. *Physical Review A*, 69(3):030901, 2004. (38).

[193] X Baillard, A Gauguet, S Bize, P Lemonde, Ph Laurent, A Clairon, and P Rosenbusch. Interference-filter-stabilized external-cavity diode lasers. *Optics Communications*, 266(2):609–613, 2006. (38).

[194] Th W Hänsch, MD Levenson, and AL Schawlow. Complete hyperfine structure of a molecular iodine line. *Physical Review Letters*, 26(16):946, 1971. (38).

[195] Fernando Ramirez-Martinez, Michel Lours, Peter Rosenbusch, Friedemann Reinhard, and Jakob Reichel. Low-phase-noise frequency synthesizer for the trapped atom clock on a chip. *IEEE transactions on ultrasonics, ferroelectrics, and frequency control*, 57(1), 2010. (39).

[196] Ramon Szmuk. *Atom chips for metrology*. PhD thesis, UPMC, 2015. (39, 94, 124).

[197] Wolfgang Ketterle and NJ Van Druten. Evaporative cooling of trapped atoms. *Advances in atomic, molecular, and optical physics*, 37:181–236, 1996. (42, 43).

[198] Fabrice Gerbier. *Condensats de Bose–Einstein dans un piege anisotrope*. PhD thesis, Universite Paris VI, 2003. (44).

[199] David A Smith, Simon Aigner, Sebastian Hofferberth, Michael Gring, Mauritz Andersson, Stefan Wildermuth, Peter Krüger, Stephan Schneider, Thorsten Schumm, and Jörg Schmiedmayer. Absorption imaging of ultracold atoms on atom chips. *Optics Express*, 19(9):8471–8485, 2011. (51).

[200] G. Reinaudi, T. Lahaye, Z. Wang, and D. Guery-Odelin. Strong saturation absorption imaging of dense clouds of ultracold atoms. *Opt. Lett.*, 32:3143, 2007. (52).

[201] Kenneth Maussang. *Etats comprimes atomiques sur puce a atomes*. PhD thesis, Paris VI, 2010. (56, 59).

[202] Rodney Loudon. *The Quantum Theory of Light, Third Edition (Oxford Science Publications)*. Oxford Science Publications. Oxford University Press, USA, 3 edition, 2000. (59).

[203] C. Ockeloen, A. Tauschinsky, R. Spreeuw, and S. Whitlock. Detection of small atom numbers through image processing. *Phys. Rev. A*, 82:061606, 2010. (61, 62).

[204] F Pereira Dos Santos, H Marion, S Bize, Y Sortais, A Clairon, and Christophe Salomon. Controlling the cold collision shift in high precision atomic interferometry. *Physical Review Letters*, 89(23):233004, 2002. (66).

[205] Claude Cohen-Tannoudji, Jacques Dupont-Roc, and Gilbert Grynberg. *Processus d'interaction entre photons et atomes*. Edp Sciences, 2012. (66).

[206] Mark Kasevich and Steven Chu. Laser cooling below a photon recoil with three-level atoms. *Physical Review Letters*, 69(12):1741, 1992. (67).

[207] AM Kamchatnov and VS Shchesnovich. Dynamics of Bose–Einstein condensates in cigar-shaped traps. *Physical Review A*, 70(2):023604, 2004. (74).

[208] Zachary Dutton and Charles W Clark. Effective one-component description of two-component Bose–Einstein condensate dynamics. *Physical Review A*, 71(6):063618, 2005. (74).

[209] Russell Anderson. *Nonequilibrium dynamics and relative phase evolution of two-component Bose–Einstein condensates*. PhD thesis, Ph. D. thesis, Swinburne University, 2010. (74, 74, 76).

[210] Hillel Tal-Ezer and R Kosloff. An accurate and efficient scheme for propagating the time dependent schrödinger equation. *The Journal of chemical physics*, 81(9):3967–3971, 1984. (75).

[211] Lauri Lehtovaara, Jari Toivanen, and Jussi Eloranta. Solution of time-independent schrödinger equation by the imaginary time propagation method. *Journal of Computational Physics*, 221(1):148–157, 2007. (75).

[212] MD Feit, JA Fleck, and A Steiger. Solution of the schrödinger equation by a spectral method. *Journal of Computational Physics*, 47(3):412–433, 1982. (76).

[213] Lokenath Debnath and Dambaru Bhatta. *Integral transforms and their applications*. CRC press, 2014. (76).

[214] D Kadio and YB Band. Analysis of a magnetically trapped atom clock. *Physical Review A*, 74(5):053609, 2006. (77).

[215] Pierre Lemonde. *Pharao: Étude d'une horloge spatiale utilisant des atomes refroidis par laser, réalisation d'un prototype.* PhD thesis, Université Pierre et Marie Curie, 1997. (82).

[216] Alice Sinatra, Yvan Castin, and Emilia Witkowska. Coherence time of a Bose–Einstein condensate. *Physical Review A*, 80(3):033614, 2009. (84).

[217] MÖ Oktel and LS Levitov. Collective dynamics of internal states in a Bose–Einstein gas. *Physical Review A*, 65(6):063604, 2002. (95).

[218] Giulia Ferrini, Dominique Spehner, Anna Minguzzi, and FWJ Hekking. Effect of phase noise on quantum correlations in Bose–Josephson junctions. *Physical Review A*, 84(4):043628, 2011. (104).

[219] Alice Sinatra. Private communication, 2017. (120, 133).

[220] Yvan Castin and Alice Sinatra. Spatial and temporal coherence of a Bose-condensed gas. In *Physics of Quantum Fluids*, pages 315–339. Springer, 2013. (120, 136).

[221] Konstantin Ott, Sebastien Garcia, Ralf Kohlhaas, Klemens Schüppert, Peter Rosenbusch, Romain Long, and Jakob Reichel. Millimeter-long fiber Fabry-Perot cavities. *Optics Express*, 24(9):9839–9853, 2016. (137).

[222] Jérôme Lodewyck, Philip G Westergaard, and Pierre Lemonde. Nondestructive measurement of the transition probability in a Sr optical lattice clock. *Physical Review A*, 79(6):061401, 2009. (138).

[223] Nobuyasu Shiga and Makoto Takeuchi. Locking the local oscillator phase to the atomic phase via weak measurement. *New Journal of Physics*, 14(2):023034, 2012. (138).

[224] Thomas Vanderbruggen, Ralf Kohlhaas, Andrea Bertoldi, Simon Bernon, Alain Aspect, Arnaud Landragin, and Philippe Bouyer. Feedback control of trapped coherent atomic ensembles. *Physical Review Letters*, 110(21):210503, 2013. (138).

[225] RWP Drever, John L Hall, FV Kowalski, J_ Hough, GM Ford, AJ Munley, and H Ward. Laser phase and frequency stabilization using an optical resonator. *Applied Physics B*, 31(2):97–105, 1983. (138).

[226] G Vallet, E Bookjans, U Eismann, S Bilicki, R Le Targat, and J Lodewyck. A noise-immune cavity-assisted non-destructive detection for an optical lattice clock in the quantum regime. *arXiv preprint arXiv:1703.04609*, 2017. (138).

Résumé

Dans ce manuscrit, nous présentons une étude expérimentale du phénomène de compression de spin dans un condensat de Bose-Einstein de ^{87}Rb, résultant d'une interaction non-linéaire provenant de collisions entre les deux états internes $|F = 1, m_F = -1 >$ et $|F = 2, m_F = 1 >$ de l'état fondamental $5^2S_{1/2}$. Les atomes sont refroidis dans un piège magneto-optique, puis piégés magnétiquement à l'aide de notre puce à atomes jouant le rôle de parois supérieure pour notre enceinte à vide. La puce est aussi utilisée pour émettre le champ radiofréquence permettant le refroidissement évaporatif conduisant à la condensation de Bose-Einstein, ainsi que le champ micro-onde qui réalise le transfert cohérent des atomes d'un état interne à un autre.
L'ensemble atomique est décrit par le Hamiltonien "*one-axis-twisting*" qui contient un terme quadratique en la composante selon l'axe z du vecteur de spin atomique S_z. L'amplitude de cette interaction non-linéaire, initialement très faible, dépend des longueurs de diffusion des états internes considérés, et peut être grandement augmentée en réduisant le recouvrement des fonctions d'onde. C'est pourquoi le système est placé dans une configuration particulière (grand nombre d'atomes et piège anisotrope de type "cigare") pour laquelle les deux états vont alterner des phases de séparation et recombinaison spatiale. L'impact de cette dynamique spatiale sur l'interaction de champ moyen et la cohérence du système est analysé expérimentalement à travers l'étude du contraste et de la fréquence centrale d'un interféromètre de Ramsey.
Théoriquement, lorsque les deux états sont séparés, la distribution de spin se transforme d'une distribution circulaire régie par le bruit de projection quantique, en une ellipse dont le petit axe est inférieur à la limite quantique standard, sous l'effet de l'interaction en S_z^2. Ceci est vérifié expérimentalement en réalisant la tomographie de l'état atomique au moment où les deux modes internes se recombinent. Un paramètre de compression de spin $\xi^2 = -1.3 \pm 0.4$ dB est ainsi obtenu pour 5000 atomes et un contraste de 90%. L'étude des différentes sources d'instabilités a permis d'identifier les pertes atomiques comme limitation principale de la compression de spin et du contraste de l'interféromètre.
Ce travail s'inscrit dans le contexte de la métrologie quantique et représente un pas vers la production d'états comprimés en spin permettant la réalisation d'interféromètres atomiques fonctionnant sous la limite quantique standard. La question de la cohérence d'un condensat bimodal soumis à de nombreuses collisions élastiques et inélastiques est aussi adressée.

Mots Clés

Condensats de Bose-Einstein, puce atomique, compression de spin, metrologie quantique, horloge atomique, intrication.

Abstract

In this manuscript, we present an experimental study of spin squeezing in a spinor Bose-Einstein condensate of ^{87}Rb, arising from a non-linear interaction originating from collisions between the two internal states $|F = 1, m_F = -1 >$ and $|F = 2, m_F = 1 >$ of the $5^2S_{1/2}$ manifold. The atoms are cooled down in a magneto-optical trap and magnetically trapped thanks to our atom-chip which acts as a top wall for our vacuum cell. The chip is also used to emit the radio-frequency field that perform the evaporative cooling leading to Bose-Einstein condensation, and the microwave field used to coherently transfer the atoms from one internal state to another.
The atomic ensemble in a coherent superposition is well described by the so-called *one-axis-twisting* Hamiltonian that contains a term quadratic in the z-component of the spin vector S_z. the strength of this non-linear interaction, initially very weak, depends on the intra- and inter-state s-wave scattering lengths, and can be greatly enhanced by reducing the wave-function spatial overlap between the two states. We therefore place the system in a configuration (high atom number and cigar-shaped trap) for which the two states experience spontaneous relative spatial separation and recombination phases. The impact of this spatial dynamics on the mean field interaction and coherence of the system is experimentally analyzed through the study of the contrast and central frequency of a Ramsey interferometer.
Theoretically, when the two states are separated, the spin noise distribution evolves from a uniform circular distribution defined by the quantum projection noise, to an elliptic one whose small axis is smaller than the standard quantum limit, under the action of the S_z^2 interaction. This is verified experimentally by performing the tomography of the atomic state, when the two internal modes recombine. A squeezing parameter $\xi^2 = -1.3 \pm 0.4$ dB is reached for 5000 atoms and a 90% contrast. The study of the different instability sources highlights the atomic-density-dependent losses as the main limitation for both the noise reduction and the contrast of the interferometer.
This work has been initiated in the context of quantum metrology and represents a step towards the production of spin squeezed states enabling the realization of atom interferometers working below the standard quantum limit. It also addresses the fundamental question of coherence of spinor Bose-Einstein condensates undergoing many elastic and inelastic collisions.

Keywords

Bose-Einstein condensates, atom-chip, spin squeezing, quantum metrology, atomic clock, many-particle entanglement.